

Design Method for Efficient
Concentrated Stator Motors based on
B-H Trajectory Behavior Models

by

Takahiro Kumagai

A dissertation submitted in partial fulfillment
of the requirements for the degree of

DOCTOR OF ENGINEERING

at the

NAGAOKA UNIVERSITY OF TECHNOLOGY

2022

© by Takahiro Kumagai 2022
All Rights Reserved

Acknowledgements

First and foremost, I would like to express my sincere gratitude to my advisor, Professor Jun-ichi Itoh, for providing tremendous levels of support over the years. His enthusiasm and passion keep me always moving forward. He has also provided me many rewarding opportunities to participate in national and international conferences, and also internship program.

I also wish to express my grateful to Professor Kan Akatsu, who is with Yokohama National University, for kindly taking part in the PhD defense as a co-examiner and his interests in this work. I would also like to express my gratitude and appreciation to Emeritus Professor Seiji Kondo, Professor Kiyoshi Ohishi, Professor Toshimasa Miyazaki, Associate Professor Hitoshi Haga, Assistant Professor Yuki Yokokura, and Specially Appointed Lecturer Keisuke Kusaka, who are with the Power Laboratory from Nagaoka University of Technology.

I would also like to extend thanks to Dr. Daisuke Sato and Dr. Masakazu Kato who are with Nagaoka Motor Development Co., Ltd., for teaching me and supporting me.

Further, I warmly thank everybody else in the Power Electronics Laboratory, in particular Dr. Hiroki Watanabe, Mr. Kengo Kawauchi, Mr. Ryoichi Ishibashi, Mr. Koki Yamaguchi, Mr. Takumi Yasuda, and Mr. Taisuke Shioi, and Koki Tokui for their motivating and helpful discussions as well as for the good times we had in the Power Electronics Lab. I would also like to thank to Mrs. Eriko Inamochi who has been making the research activities in Power Electronics Lab. possible from administration side.

Finally, I would like to express my thanks and loves to my family (father, mother, elder-sister, and elder-brother) –especially my wife Kana– for their continued support, patience and encouragement. Their love is the key to the successes in my life. Thank you for helping push me towards this goal.

Nagaoka, March 2022
Takahiro Kumagai

Table of Contents

| | |
|-------------------------|-----|
| Title page | i |
| Acknowledgements | iii |
| Table of Contents | v |
| List of Figures | x |
| List of Tables | xv |

Chapter 1

Introduction

| | |
|--|----|
| 1.1 Background | 1 |
| 1.1.1 Necessity of Efficiency Improvement in Motors | 1 |
| 1.1.2 Advantages of Concentrated Stator Motors and their Drawbacks | 3 |
| 1.1.3 Properties of Soft Magnetic Materials | 6 |
| 1.1.4 Efficiency Improvement of Concentrated Stator Motors | 8 |
| (a) Efficiency Improvement with Material Property | |
| (b) Efficiency Improvement with Mechanical Characteristics | |
| 1.1.5 Difficulties in handling Magnetic Saturation and Iron Loss | 13 |
| (a) Difficulty in handling Magnetic Saturation in Automatic Design | |
| (b) Difficulty in handling Iron Loss in FEM Analysis | |
| (c) Difficulty in handling Iron Loss in Pulse Pattern | |
| 1.2 Research Objectives | 16 |

| | | |
|-------|---|----|
| 1.2.1 | Automatic Design in Considering Magnetic Saturation | 16 |
| 1.2.2 | Improvement of FEM Analysis for Iron Loss | 17 |
| 1.2.3 | Optimal Pulse Pattern for Iron Loss | 18 |
| 1.3 | Thesis Organization | 19 |
| | Bibliography | 23 |

Chapter 2

Efficiency improvement in Concentrated Stator Motors based on B-H Trajectory Behavior Model

| | | |
|-------|---|----|
| 2.1 | Introduction | 27 |
| 2.2 | Torque and Loss | |
| 2.2.1 | Torque | 28 |
| 2.2.2 | Copper loss | 32 |
| 2.2.3 | Iron loss | 33 |
| 2.3 | Efficiency Improvement with Liner model | 39 |
| 2.3.1 | Automatic Design with Permeance Method | 42 |
| 2.3.2 | Permeance Method Compensating Magnetic Saturation | 44 |
| 2.3.3 | FEM Analysis of Iron Loss | 46 |
| 2.3.4 | FEM Analysis of Iron Loss Compensating Hysteresis Loss | 48 |
| 2.3.5 | Optimal Design with FEM | 50 |
| 2.3.6 | Optimal Current Reference | 52 |
| 2.3.7 | Optimal Pulse Pattern | 53 |
| 2.4 | Proposed Efficiency Improvement Method based on B-H Trajectory Behavior Model | 56 |
| 2.4.1 | Proposed Automatic Design considering Magnetic Saturation for Efficient Motor | 56 |
| 2.4.2 | Proposed High Accuracy Iron Loss Calculation with FEM for Efficient Motor | 58 |

| | | |
|-------|---|----|
| 2.4.3 | Proposed Optimal Pulse Pattern of Iron Loss Reduction for Efficient Motor | 58 |
| 2.4.4 | Beneficial Position of Proposed Strategies based on B-H Trajectory Behavior Model | 60 |
| 2.5 | Conclusion | 61 |
| | Bibliography | 62 |

Chapter 3

Automatic design considering magnetic saturation of SRM for high efficiency motor

| | | |
|-------|--|-----|
| 3.1 | Introduction | 67 |
| 3.2 | Proposed Automatic Design Method of Typical Parameters of a Switched Reluctance Motor | |
| 3.2.1 | Decision method of number of phases m , number of stator teeth N_s , number of rotor teeth N_r | 76 |
| 3.2.2 | Decision method of stack thickness L_h | 78 |
| 3.2.3 | Decision method of stator diameter D_s | 86 |
| 3.2.4 | Decision method of number of turns N | 93 |
| 3.2.5 | Decision method of rotor diameter D_r | 96 |
| 3.2.6 | Parameter adjustment by simulation | 97 |
| 3.3 | 0.75kW SRM design example | |
| 3.3.1 | Decision of the number of phases and poles | 101 |
| 3.3.2 | Miniaturization design | 101 |
| 3.3.3 | Adjustment with simulation | 103 |
| 3.3.4 | Validation of designed motor | 104 |
| 3.3.5 | Utility of magnetic saturation | 109 |
| 3.3.6 | Design in different iron core materials | 112 |
| 3.4 | Conclusion | 115 |

| | |
|---|-----|
| Bibliography | 116 |
| | |
| Chapter 4 | |
| Design and Evaluation with Improved High Accuracy Iron Loss Calculation with FEM for High Efficiency Motor made by Blanking Amorphous Alloy Foil | |
| 4.1 Introduction | 118 |
| 4.2 Pre-experimental iron loss evaluation of ring cores | |
| 4.2.1 Experimental preparation | 119 |
| 4.2.2 Measurement results of B-H characteristic | 122 |
| 4.2.3 Experimental results of iron loss characteristic | 124 |
| 4.3 Improvement of accuracy of iron loss analysis in FEA | |
| 4.3.1 Preparation of Play model method based on measured BH trajectory behavior model | 128 |
| 4.3.2 Preparation of Homogenization method | 131 |
| 4.4 Design and Manufacture of SRMs | 132 |
| 4.5 Experimental evaluation of SRMs | |
| 4.5.1 Test system configuration | 138 |
| 4.5.2 Comparison of Analysis Accuracy | 141 |
| 4.5.3 Test procedure | 144 |
| 4.5.4 Measured characteristics of SS-SRM and AA-SRM | 146 |
| 4.5.5 Comparison results between measurement and FEA | 153 |
| 4.6 Conclusion | 157 |
| Bibliography | 158 |

Chapter 5

Optimum Pulse Pattern of iron loss for efficiency improvement for High-Speed IPMSM

| | | |
|-------|--|-----|
| 5.1 | Introduction | 160 |
| 5.2 | Pulse pattern for iron loss reduction in stator core | |
| 5.2.1 | PWM pulse patterns | 161 |
| 5.2.2 | Iron loss evaluation function under PWM | 164 |
| 5.3 | Experimental Verification | |
| 5.3.1 | Verification in inductor | 172 |
| 5.3.2 | Verification in High-speed IPMSM..... | 179 |
| 5.4 | Conclusion | 186 |
| | Bibliography | 187 |

Chapter 6

Conclusion

| | | |
|-----|----------------------------|-----|
| 6.1 | Discussion..... | 188 |
| 6.2 | Future Work..... | 191 |
| | List of Achievements | 192 |

List of Figures

Chapter 1

| | | |
|---------|---|----|
| Fig.1.1 | The estimated global electrical energy demand by end use and electrical energy demand of motor applications by sector | 2 |
| Fig.1.2 | The appearance of the stator with concentrated winding and distributed winding | 3 |
| Fig.1.3 | Stator structure and motor loss | 5 |
| Fig.1.4 | Comparison of N-T characteristic in IPMSM | 5 |
| Fig.1.5 | Maps of non-oriented electrical steel products | 7 |
| Fig.1.6 | The characteristic factor diagram of the motors with concentrated windings for efficiency improvement | 12 |
| Fig.1.7 | The features in the NT characteristic of the motor | 13 |
| Fig.1.8 | The outline of this paper | 22 |

Chapter 2

| | | |
|----------|--|----|
| Fig.2.1 | Image of eddy currents flowing in a steel plate | 35 |
| Fig.2.2 | Image of hysteresis loop | 37 |
| Fig.2.3 | Overview of the efficiency improvement based on linear model. | 41 |
| Fig.2.4 | The conceptual diagram of the normal design and the inverse design | 42 |
| Fig.2.5 | The magnetic circuit of SPMSM | 43 |
| Fig.2.6 | B-H of core material and its approximation curve | 44 |
| Fig.2.7 | SPICE model of nonlinear reluctance | 45 |
| Fig.2.8 | The iron loss curve | 46 |
| Fig.2.9 | Magnetic flux density at the evaluation point | 47 |
| Fig.2.10 | The method of calculating the hysteresis loss by counting the number of hysteresis loops | 48 |
| Fig.2.11 | The minor loops with DC bias | 49 |

| | | |
|----------|---|----|
| Fig.2.12 | The process of optimizing rotor shape | 50 |
| Fig.2.13 | Amplitude of space harmonic components included in gap flux density waveform. | 51 |
| Fig.2.14 | PMSM model about copper loss | 52 |
| Fig.2.15 | Illustration of voltages of low pulse number | 53 |
| Fig.2.16 | Experimental comparison of optimal PWM and Sine-Triangle PWM | 55 |
| Fig.2.17 | The proposed BH trajectory model and the details of each proposed method using it as the core | 59 |
| Fig.2.18 | Comparison between the high efficiency based on the conventional model with linearity and the proposed BH trajectory behavior model | 60 |
| Fig.2.19 | The benefit position of the proposed method | 61 |

Chapter 3

| | | |
|----------|---|-----|
| Fig.3.1 | Output N-T characteristics..... | 68 |
| Fig.3.2 | Dimensions of SRM..... | 69 |
| Fig.3.3 | Inductance distribution, torque characteristic generated when a constant current is applied, and current waveforms at each operating point..... | 70 |
| Fig.3.4 | Contour plots and flux lines of SRM and magnetic circuit model considering local saturation of the pole-tips..... | 72 |
| Fig.3.5 | Proposed design flow of SRM | 75 |
| Fig.3.6 | BH trajectory behavior model..... | 79 |
| Fig.3.7 | Relationship between current amplitude and magnetization characteristic | 81 |
| Fig.3.8 | Positional relationship between stator teeth and rotor teeth..... | 82 |
| Fig.3.9 | Instantaneous maximum torque..... | 84 |
| Fig.3.10 | Current waveforms under base speed | 87 |
| Fig.3.11 | Relationship between speed and current RMS value | 87 |
| Fig.3.12 | Stator slot of SRM | 88 |
| Fig.3.13 | Cross section of stator tooth and winding of SRM | 90 |
| Fig.3.14 | Procedure of setting control parameters..... | 99 |
| Fig.3.15 | Relationship between rotor diameter D_r and motor volume V_{vol} | 101 |
| Fig.3.16 | Number of trials and average torque and current RMS value..... | 103 |

| | | |
|----------|--|-----|
| Fig.3.17 | Cross section of designed SRM | 104 |
| Fig.3.18 | Calculated back EMF of designed SRM at base speed..... | 105 |
| Fig.3.19 | Simulation results of currents and torques at operating points (A) and (B)..... | 107 |
| Fig.3.20 | Map of current density and copper loss. | 108 |
| Fig.3.21 | Current paths at operating point (A) and point (B) under different magnetic saturation level..... | 110 |
| Fig.3.22 | Relationship between magnetic saturation level α_{sat} and motor volume. | 111 |
| Fig.3.23 | B-H characteristics of 35H300, 2605SA1, and 35JNE300 .. | 112 |
| Fig.3.24 | Current paths at operating point (A) and point (B) under different magnetic material | 114 |

Chapter 4

| | | |
|----------|--|-----|
| Fig.4.1 | Photograph of ring-cores made with the processing methods as shown in Table 4.1. | 120 |
| Fig.4.2 | Diagrams of measurement setup for ring-core..... | 121 |
| Fig.4.3 | Measured B-H characteristics at a frequency of 50Hz. | 123 |
| Fig.4.4 | Measured iron loss characteristics at 1.0T. | 124 |
| Fig.4.5 | Measured BH trajectory behavior model of AA-B..... | 129 |
| Fig.4.6 | Diagram of play model..... | 130 |
| Fig.4.7 | Photograph of 70W-SRM made of blanked amorphous alloy foil. | 133 |
| Fig.4.8 | Effect of airgap length | 135 |
| Fig.4.9 | Measurement system for test SRM..... | 139 |
| Fig.4.10 | Diagrams of measurement setup for the iron loss in the completely stopped state | 141 |
| Fig.4.11 | Comparison of the experimental and analytical values of the iron loss..... | 143 |
| Fig.4.12 | The speed and the torque meter output during the experiment (Step1~Step6)..... | 145 |
| Fig.4.13 | Efficiency characteristics of SS-SRM and AA-SRM in all output range at 10000r/min. | 147 |
| Fig.4.14 | Motor loss comparison between SS-SRM and AA-SRM in all | |

| | | |
|----------|---|-----|
| | output range at 10000r/min.ffff..... | 148 |
| Fig.4.15 | Motor loss comparison between SS-SRM and AA-SRM of rated power (70W) at 10000r/min..... | 149 |
| Fig.4.16 | Efficiency characteristics of SS-SRM and AA-SRM in all speed range at 1p.u. torque..... | 151 |
| Fig.4.17 | Iron loss characteristics of SS-SRM and AA-SRM in all speed range at 1p.u. torque..... | 152 |
| Fig.4.18 | Comparison results of measurement and FEA in all output range at 10000r/min..... | 154 |
| Fig.4.19 | Iron loss separation results of rated power (70W) at 10000r/min..... | 156 |

Chapter 5

| | | |
|----------|---|-----|
| Fig.5.1 | Phase voltage waveforms and line-to-line voltage waveform of synchronous PWM (1/4 cycle). | 162 |
| Fig.5.2 | Transition modes of space vector. | 163 |
| Fig.5.3 | Iron loss distribution and separation | 165 |
| Fig.5.4 | Relationship between line-to-line voltage waveform and magnetic flux density waveform and BH trajectory. | 167 |
| Fig.5.5 | Configuration of the system to measure iron loss of test inductor. | 172 |
| Fig.5.6 | Photograph of inductor. | 173 |
| Fig.5.7 | Correlation coefficient between evaluation value and iron loss, current THD of test inductor. | 175 |
| Fig.5.8 | U-V line-to-line voltage and phase current waveforms. | 177 |
| Fig.5.9 | Iron loss of test inductor..... | 178 |
| Fig.5.10 | Configuration of IPMSM drive system..... | 179 |
| Fig.5.11 | Model of test motor: concentrated winding IPMSM..... | 180 |
| Fig.5.12 | Correlation coefficient between evaluation value and iron loss, current THD of test motor. | 182 |
| Fig.5.13 | U-V line-to-line voltage and phase current waveforms. | 184 |
| Fig.5.14 | Iron loss of test motor | 185 |

List of Tables

Chapter 2

| | | |
|-----------|--|----|
| Table 2.1 | The structure of a synchronous motor and its characteristics in terms of inductance variation and torque generation mechanism..... | 29 |
| Table 2.2 | The summarization of the results of the torque and loss characteristics | 38 |

Chapter 3

| | | |
|-----------|---|-----|
| Table 3.1 | Combinations of phase-numbers and pole-numbers..... | 76 |
| Table 3.2 | Motor parameters of SRM | 84 |
| Table 3.3 | Design requirements and constraints. | 100 |
| Table 3.4 | Design parameters | 104 |
| Table 3.5 | Design parameters | 113 |

Chapter 4

| | | |
|-----------|---|-----|
| Table 4.1 | Specifications of ring-cores..... | 120 |
| Table 4.2 | Magnetic flux density at 7500A/m and permeability around 0A/m..... | 123 |
| Table 4.3 | Coefficients of the Steinmetz equation..... | 126 |
| Table 4.4 | Characteristic of 20HX1300 and 2605SA1 | 131 |
| Table 4.5 | Specifications of test SRMs | 133 |
| Table 4.6 | Cost comparison in different processing methods excluding the cost of molds and equipment | 136 |
| Table 4.7 | Cost comparison of blanking processing in different materials | 136 |
| Table 4.8 | The operation of load motor and test motor at each step ... | 145 |

Chapter 5

| | | |
|-----------|--|-----|
| Table 5.1 | Specifications of test inductor. | 173 |
| Table 5.2 | Switching patterns of carry-synchronous PWM and proposed PWM in test inductor..... | 176 |
| Table 5.3 | Specifications of test motor. | 180 |
| Table 5.4 | Switching patterns of carry-synchronous PWM and proposed PWM in test motor | 183 |

Chapter 1

Introduction

1.1. Background

1.1.1 Necessity of Efficiency Improvement in Motors

The development of the science and technology has improved our standard of living. On the other hand, the problem of the global warming has become more serious as a sacrifice of the development of the science and technology. The global average surface temperature increased by 0.85°C from 1880 to 2012 according to the fifth assessment report of Intergovernmental Panel on Climate Change (IPCC) [1-1]. The report has pointed out that there is a high possibility (more than 95%) that the human activity has been the dominant factor in the warming observed since the mid-20th century. In addition, the greenhouse gases such as the atmospheric carbon dioxide (CO_2), methane (CH_4), and nitrous oxide (N_2O) have increased to the unprecedented levels over the past 800,000 years.

Fig.1.1 shows the estimated global electrical energy demand by end use and electrical energy demand of the motor applications by sector [1-2]. Note that the annual global electrical energy demand of the total of all sectors is 15700TWh. As shown in Fig.1.2, the electric motors are the biggest consumer. Around the 46% of the global electricity demand is from the electric motor. On the other word, the estimated global electrical energy

demand of the motors reaches to 7200TWh per year. The electric motors are used in a variety of sectors. The highest portion of the electrical energy demand for the motor applications is the industrial sector of 60.27%. The commercial sector follows at 20.55% and the residential sector follows at 12.33%.

The annual electrical energy is 7.4 TWh in the case of the power generation at a nuclear power plant with a capacity of 100 kW (assume 85% facility utilization) [1-3]. In other words, if the efficiency of the world's electrical motors were improved by 0.1%, the power consumption of one nuclear power plant is reduced. This means that the amount of the electricity consumed by the electrical motors is significant. Therefore, it is necessary to improve the efficiency of the electrical motors.

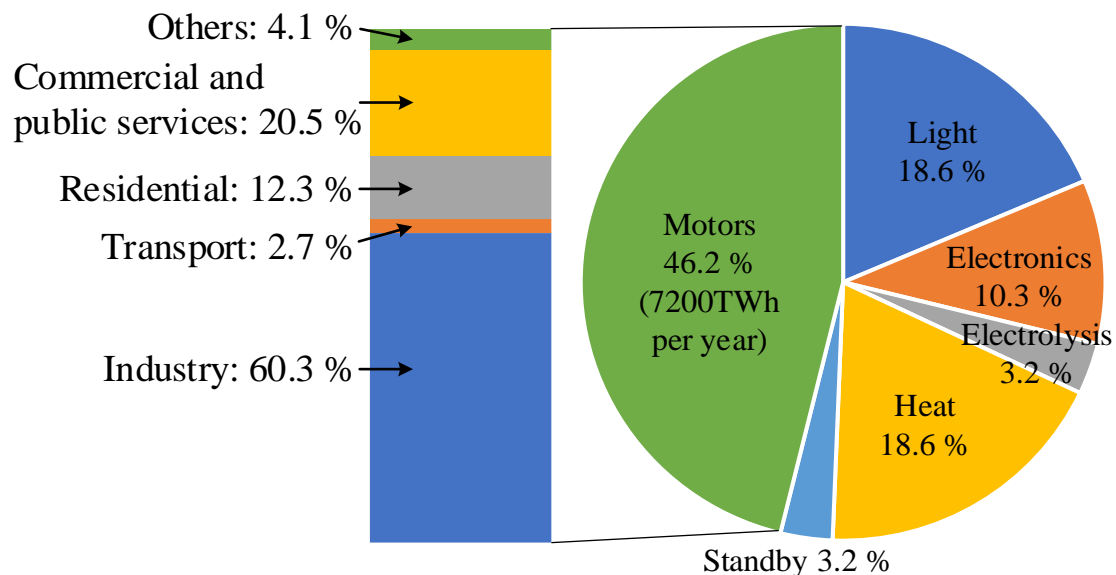


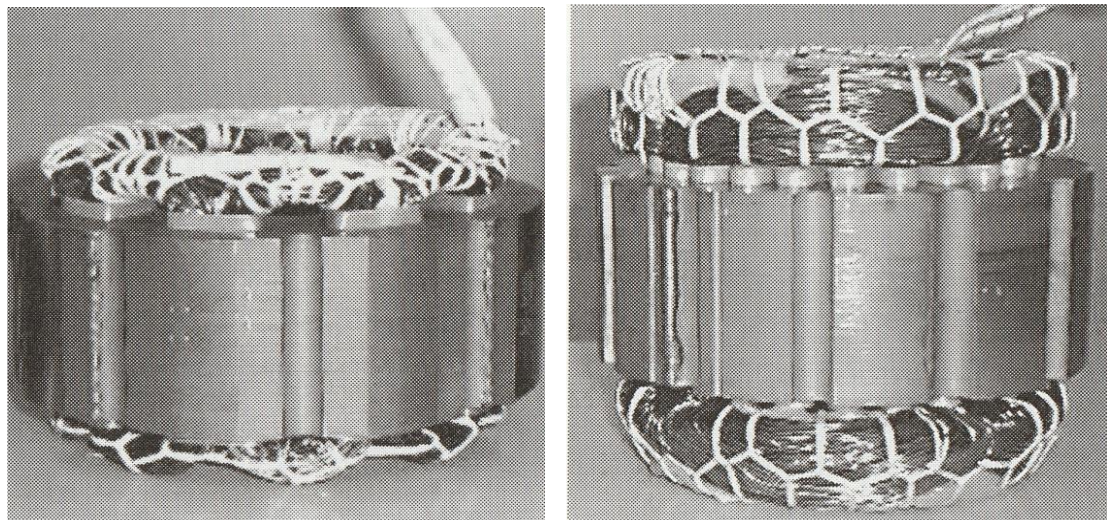
Fig.1.1 The estimated global electrical energy demand by end use and electrical energy demand of motor applications by sector (2006). The annual global electrical energy demand of the total of all sectors is 15700TWh. That of the motors is 7200TWh.(Adapted from [1-2] INTERNATIONAL ENERGY AGENCY: “Energy-Energy-Efficiency Policy Opportunities for Electric Motor-Driven Systems”)

1.1.2 Advantages of Concentrated Stator Motors and their Drawbacks

Fig.1.2 shows the appearance of the stators with the concentrated winding and the distributed winding [1-4]. The concentrated windings have following advantages:

- (i) further miniaturization
- (ii) efficiency improvement
- (iii) resource saving
- (iv) efficient winding operations

thanks to the reduction of the coil-end and the simplicity of the structure. In particular, the concentrated windings are applied into the permanent magnet synchronous motors (PMSMs)[1-4]-[1-6] and the switched reluctance motors (SRMs)[1-7]-[1-9].



(a) Concentrated winding

(b) Distributed winding

Fig.1.2 The appearance of the stator with concentrated winding and distributed winding (Adapted from [1-4] Y. Takeda, N. Matsui, S. Morimoto, and Y. Honda: “Design and control of Interior Permanent Magnet Synchronous Motor”, Ohmsha (2016))

Despite the outstanding advantages explained above, the concentrated windings have following drawbacks:

- (i) large iron loss
- (ii) large magnetic saturation
- (iii) low maximum torque (which is specific issue in IPMSM)

where (i) occurs due to the large harmonics of magnetic flux density distribution. On the other hand, (ii) is because the magnetic flux concentrates into one slot. (iii) is due to the low winding coefficient of 0.866 in the concentrated stator IPMSM compared with that of the distributed stator IPMSM which has the winding coefficient of 0.966-1.000. The low winding coefficient is because the winding pitch has to be an electric angle of 120 degrees. However, several studies [1-10]-[1-12] have improved the winding coefficient to 0.951 by devising a slot combination. Therefore, the problem of (iii) the low maximum torque is no longer serious in the concentrated stator motor. However, the problem of (i) the large iron loss and (ii) the large magnetic saturation still remains in the concentrated stator motor. The specific examples of the problems of (i) and (ii) are followings.

Fig.1.3 shows the stator structure and the motor loss [1-4]. These results assume the compressor motors for air conditioners and refrigerators. The resistance of the concentrated winding is much lower than that of the distributed winding. As a result, the copper loss is reduced. On the other hand, the change of the magnetic flux density in the stator core in the concentrated winding is larger than that in the distributed winding. As a result, the iron loss is increased [1-4]. The problem of (i) is serious in the high output.

Fig.1.4 shows the comparison of N-T characteristic in IPMSM [1-4]. These results assume the motors for electric vehicles. The q-axis inductance of the centralized winding is smaller than that of the distributed winding. This is because the local large magnetic saturation occurs due to the concentrated magnetic flux into one slot. Therefore, the reluctance torque cannot be used effectively in addition to the problem of (iii) low maximum torque. Therefore, the overall performance of the constant output

characteristics is inferior. Due to these problems, it seems that the concentrated stator IPMSM are not adapted in the motors for the electric vehicles requiring a wide range of N-T characteristics. In the SRM with only the reluctance torque, the problem of (ii) large magnetic saturation is also serious in terms of the decrease in the maximum torque.

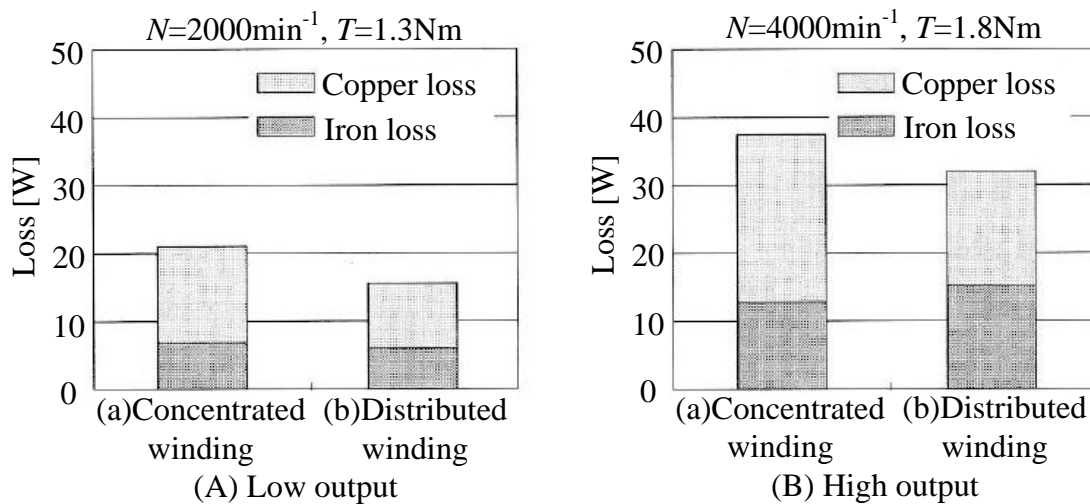


Fig.1.3 Stator structure and motor loss (Adapted from [1-4] Y. Takeda, N. Matsui, S. Morimoto, and Y. Honda: “Design and control of Interior Permanent Magnet Synchronous Motor”, Ohmsha (2016))

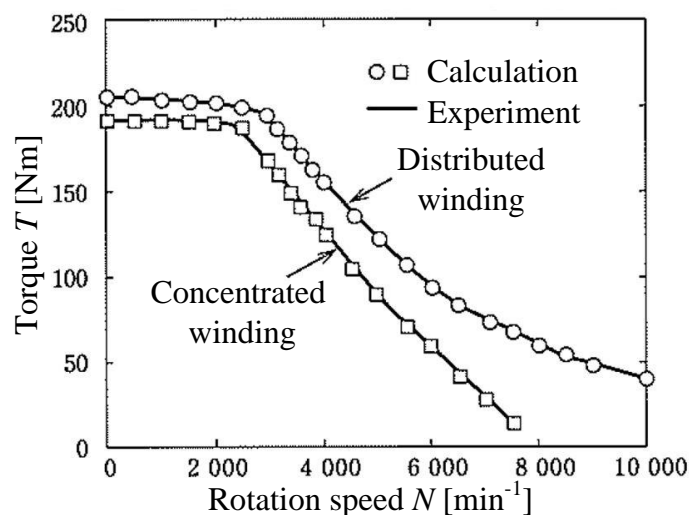


Fig.1.4 Comparison of N-T characteristic in IPMSM (Adapted from [1-4] Y. Takeda, N. Matsui, S. Morimoto, and Y. Honda: “Design and control of Interior Permanent Magnet Synchronous Motor”, Ohmsha (2016))

1.1.3 Properties of Soft Magnetic Materials

As explained in Section 1.1.2, the iron loss and magnetic saturation are major problems in the concentrated stator motor. In recent year, those problems are resolved thanks to the advanced soft magnetic materials [1-13]-[1-18]. Therefore, the combination of the copper loss and iron loss reduction is expected to be higher efficiency improvement by adopting the concentrated winding and the low iron loss material.

Fig. 1.5 shows the maps of the non-oriented electrical steel products [1-19]. The characteristics of the electrical steels are mainly characterized by the saturation magnetic flux density (e.g., B_{50} : the magnetic flux density at a magnetizing force of 5000 A/m) and the iron loss (e.g., $W_{15/50}$: the iron loss at a magnetic flux density amplitude of 1.5T and a frequency of 50 Hz). In general, the materials with the low iron loss improve the efficiency of the motor. On the other hand, the materials with the high saturation flux density increase the torque of the motor.

In general, the saturation magnetic flux density and the iron loss are determined by the amount of Si contained in the electrical steels. In the low Si material, the iron loss is large, but the saturation magnetic flux density becomes large. On the other hand, in the high Si material, the saturation magnetic flux density is small, but the iron loss becomes small. There is a trade-off relationship between the saturation flux density and the iron loss. Therefore, in order to achieve the high efficiency, it is important to utilize the properties of the electrical steels according to the material characteristics such as the saturation flux density and the iron loss.

In recent years, the new materials with the higher magnetic flux density and the same iron loss have been developed. These new materials realize the motors with the higher efficiency and the larger torque than ever before. As those new electrical steels are expected to be practical use, it is necessary to

establish the efficiency and high torque improvement technique by maximizing the magnetic properties of the iron core material.

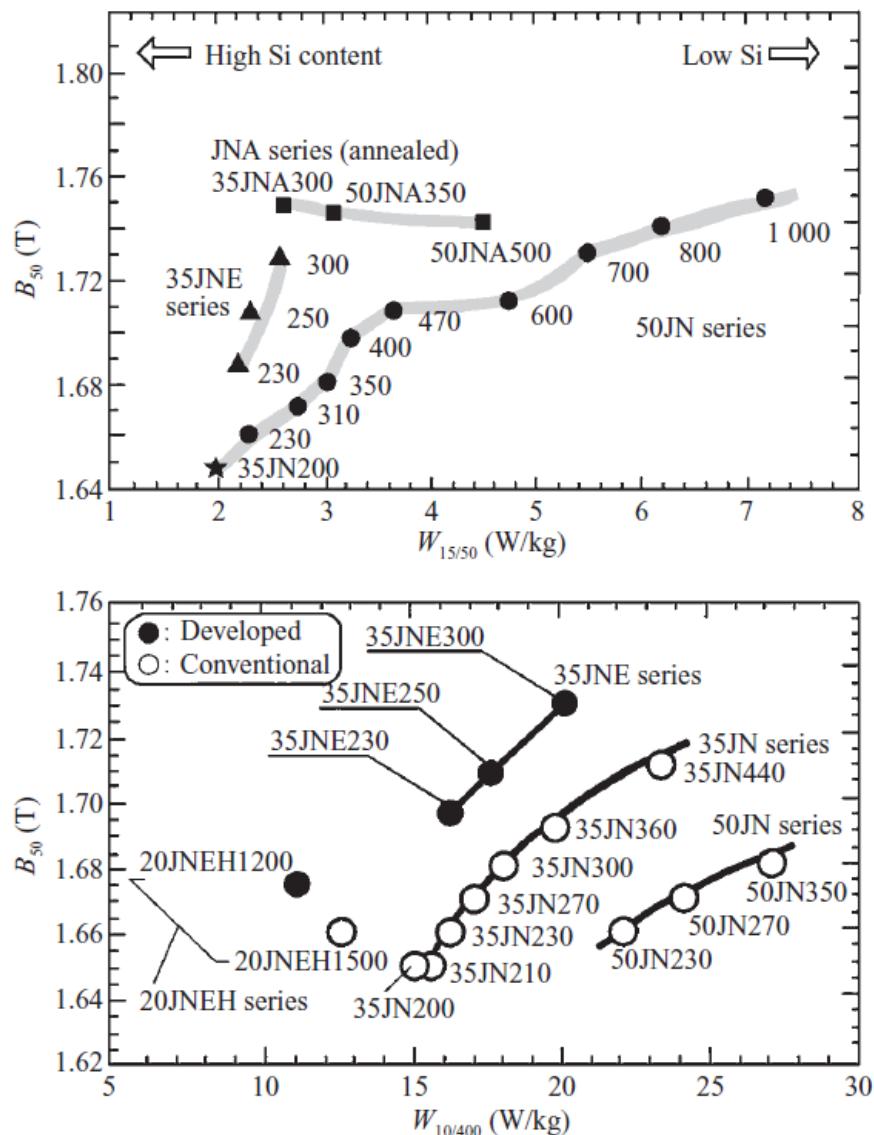


Fig.1.5 Maps of non-oriented electrical steel products (Adapted from [1-19] K. Sadahiro, S. Gotoh, and S. Uenosono: "Soft magnetic Materials of JFE Steel Group", JFE Technical Report, No.8, p1-p6 (2005))

1.1.4 Efficiency Improvement of Concentrated Stator Motors

Fig. 1.6 shows the characteristic factor diagram of the concentrated stator winding motors for the efficiency improvement. This section describes the main aspects of increasing the efficiency of the electric motors (a) with a material property and (b) with a mechanical characteristic.

(a) Efficiency Improvement with Material Property

In order to improve the efficiency by the material properties (BH curve and iron loss), it is important not only to improve the inherent physical properties of the material but also to manage the degree of the magnetization of the material. The consideration of the trade-off between torque, copper loss, and iron loss is important in managing the degree of the magnetization. In general, the increase of the magnetic flux density B or the magnetic field force H results in the increase of the torque. However, the increase of B also results in the increase of the iron loss, and the increase of H also results in the increase of the copper loss. The degree of the magnetization is managed by the design and the drive.

First, the improvement with the inherent physical properties of the material is explained. In order to achieve the high torque/copper loss, a high saturation magnetic flux density is required [1-20]. On the other hand, in order to achieve the high torque/iron loss, a low residual magnetic field, a thin thickness, and a high resistivity are required [1-21].

Next, the magnetization management with the design is explained. In order to achieve the high torque/copper loss, the air gap surface has to be widened, which is achieved by increasing the rotor diameter and the thickness [1-22]. On the other hand, in order to achieve the high torque/iron loss, the core cross-sectional area has to be widened for the reduction of the magnetic flux density, which is achieved by increasing the thickness [1-22].

In addition, in order to optimally manage the magnetization of the material, the permeance method [1-23]-[1-25] or electromagnetic field method (FEM) analysis [1-26]-[1-28] are used in order to evaluate the degree of the magnetization. The permeance analysis does not require a high accuracy. However, it is important to apply the permeance method in order to manage the magnetization easily. In addition, the magnetic saturation has to be considered due to its significant impact on the losses and the size. On the other hand, FEM analysis requires a high accuracy to consider the material characteristic. It is important to consider the material characteristic which degraded by processing. In addition, it is important to accurately evaluate the non-sinusoidal magnetic flux which is generated at the various locations.

Next, the magnetization management with the drive is explained. In order to achieve a high torque/iron loss ratio and a high torque/copper loss, it is necessary to optimize the magnetic flux waveform [1-29] and the current waveform [1-30] respectively.

(b) Efficiency Improvement with Mechanical Characteristics

In order to reduce the copper loss, the occupancy rate of the winding has to be high. The flat wire is used in order to improve the occupancy rate. In the round wire coils of the circular coil cross-section, the occupancy rate becomes low due to the unnecessary gaps. The flat wire is less to have unnecessary gaps, thus improving the occupancy rate. A split iron core is also effective because the winding is wound directly on the split core.

There are two main methods for reducing the iron loss: reducing classical eddy current loss and reducing hysteresis loss. In reducing classical eddy current loss, the insulation in the lamination process is important. In the mass production of the electric motors, the electrical steels are generally blanked into the shape of a motor and then laminated them. In the lamination of the

electrical steels, a caulking or a welding are usually performed. However, the short-circuits between the layers of the electrical steels occur in the caulking and welding areas. This results in increase of the eddy current loss. Therefore, a lamination method with impregnation lamination has been developed. In impregnation lamination, the core is dipped in impregnating adhesive, which is a low-viscosity liquid. The adhesive is allowed to soak into the small gaps between the layers, filling the layers with adhesive and adhering them together. This method prevents short-circuits between layers and reduces eddy current losses. On the other hand, in the case of small-volume production, a wire cutting is used. In the wire cutting process, the cut surface melts due to heat. This causes short circuit between layers. In this case, the etching method of the surface using the corrosive effect of chemicals has been developed. The stacked short-circuited cutting surface is removed. This results in reduction of the eddy current loss. In order to reduce the hysteresis loss, it is effective to disperse the stress on the core that occurs during the production process. In the lamination by the caulking or the welding, the stress on the core is concentrated at a single point. As a result, the residual stress in the vicinity deteriorates the hysteresis characteristics. The impregnated lamination is also effective in reducing the hysteresis loss because the stress is dispersed.

There are two methods for reducing the mechanical loss: reducing a wind loss and reducing a bearing loss. The wind loss generated by the cooling fan is reduced by making the cooling fan smaller. Therefore, it is necessary to reduce the loss generated by the electric motor and to reduce the air volume required for cooling. The improvement of bearings is an effective way to reduce the bearing loss.

In this paper, (a) efficiency improvement with material property is focused. As mentioned in chapter 1.2.2, the new materials with the higher magnetic flux density for the same iron loss have been developed. These new

materials realize the motors with the higher efficiency and the larger torque than ever before. As those new electrical steels are expected to be practical use, it is necessary to establish the efficiency and high torque improvement technique by maximizing the magnetic properties of the iron core material.

1.1.5 Difficulties in handling Magnetic Saturation and Iron Loss

Loss

In the previous chapters, first, the properties of the materials, such as saturation flux density and iron loss are described, then the efficiency advantages of concentrated synchronous motors are described, and finally the purpose of this paper is described. While the copper loss is dramatically reduced in a concentrated synchronous motor, a large iron loss occurs due to the rapid fluctuations in the magnetic flux density. Therefore, it is necessary to improve the efficiency by taking advantage of the material characteristics. Then, the specific issue is discussed in this section.

Fig.1.7 shows the features in the NT characteristic of the motor. Note that the constant power characteristic is assumed. The typical operating points for a motor are (A) the maximum torque region and (B) the maximum speed region.

In order to improve the efficiency by taking advantage of the material characteristics, there are three difficulties: (a) in handling the magnetic saturation in the automatic design, (b) in handling the iron loss in FEM analysis, and (c) in handling the iron loss in the pulse pattern.

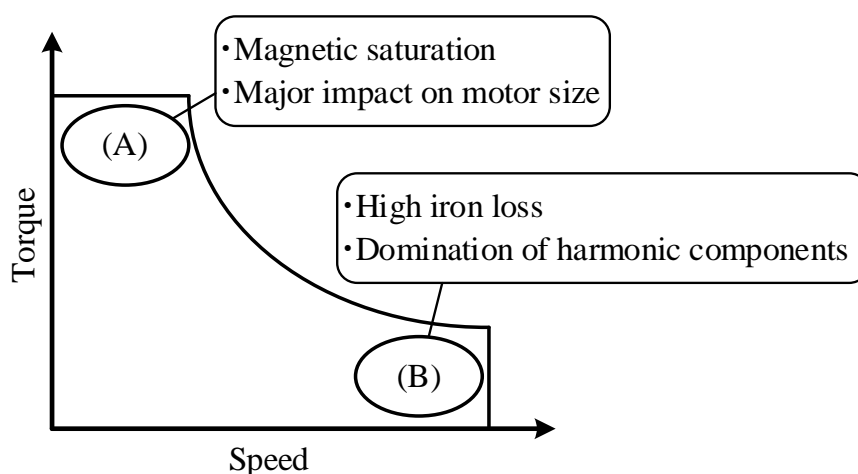


Fig.1.7 The features in the NT characteristic of the motor

(a) Difficulty in handling Magnetic Saturation in Automatic Design

In (A) the maximum torque region, the greatest magnetic saturation occurs in the material. In general, the motor size is determined by the maximum torque. Therefore, the degree of the magnetic saturation has a great influence on the motor size. There are two methods to determine the motor size: one is a design based on the output equation, and the other is an automatic design based on the permeance method. In the design based on the output equation, the size is determined from the output coefficient based on the past designed motors. However, the design method based on the past designed motors leads to larger motors and lower efficiency in the situation that the new electrical steels are being developed as mentioned in Section 1.1.2. On the other hand, in the design based on the permeance method, the motor size is automatically determined based on the input parameters such as the desired efficiency (in other words, the allowable loss). However, in the permeance method of the automatic design, each dimension is determined from the theoretical equation of the motor parameters ignoring the magnetic saturation. This is because the magnetic saturation leads to nonlinearity in the magnetoresistance in the permeance method. This nonlinearity makes the formulation difficult. However, the degree of the magnetic saturation has a great influence on the motor size. Therefore, the major problem is to handle magnetic saturation in the automatic design method based on the permeance method.

(b) Difficulty in handling Iron Loss in FEM Analysis

In (B) the maximum speed region, the largest iron loss occurs in the material. As mentioned in Section 1.1.2., the significant reduction of the iron loss by the low iron loss materials is expected with the development of new electrical steels. In this situation, it is important for the design stage to

estimate how much iron loss is reduced by the applied electrical sheet. In order to design the detailed dimensions with consideration of the iron loss, it is common to use finite element method (FEM) analysis. Since the design with FEM analysis is the final stage, very high accuracy is required. However, it is known that the iron loss is also affected by the processing of the material. In addition, the magnetic flux density fluctuation is very complicated and steep in the concentrated winding motor. Therefore, the calculation of the iron loss is much more difficult than that for distributed winding motor. Therefore, the accurate calculation of the iron loss in the detailed design method based on FEM analysis is a major problem.

(c) Difficulty in handling Iron Loss in Pulse Pattern

In (B) the maximum speed region, the harmonic component due to the switching is increased since the electrical frequency is increased. The harmonic component has a significant effect on the iron loss. Therefore, it is necessary to reduce the iron loss by using the optimal pulse patterns. The evaluation function of the iron loss is important for optimizing the pulse pattern. In contrast to the copper loss, the iron loss does not allow the frequency superposition. Therefore, the derivation of the evaluation function is very difficult. Therefore, the derivation of the evaluation function of the iron loss for the pulse pattern is a major problem.

1.2. Research Objectives

The purpose of this research is to improve the motor efficiency with by handling the magnetic saturation and the iron loss in the materials based on the proposed BH trajectory behavior model. The BH trajectory behavior model estimates and calculates the magnetic saturation and the iron loss from the BH trajectory that the core material follows when excited from the outside. The application of the BH trajectory behavior model varies depending on the purpose of application (simplicity or accuracy). However, all methods of applying the BH trajectory behavior model consider the material properties more accurately than the conventional linear methods.

1.2.1 Automatic Design in Considering Magnetic Saturation

The purpose of the method is an automatic design of typical parameters such as number of phases, number of poles, stack thickness, stator outer diameter, rotor outer diameter, and number of turns of a SRM from the requirement of the N-T characteristic. SRM utilizes the magnetic saturation region actively. In particular, a specific parameter related to the magnetic saturation is defined based on the proposed BH trajectory behavior model. As a result, it is achieved to arbitrarily determine how much to use the magnetic properties of the iron core material. In the proposed method, the typical motor parameters in order to realize a miniaturized volume which satisfies an input N-T characteristic are obtained by setting the parameter related to magnetic saturation, maximum electrical frequency, maximum current density, maximum copper loss, conductor slot fill factor, magnetic properties of material, and input voltage. In this method, the efficiency improvement is achieved by setting the constant of the lower allowable copper loss. Note that the efficiency improvement has the sacrifice of increasing motor volume. However, the sacrificial increase of the motor volume is minimized in this method.

1.2.2 Improvement of FEM Analysis for Iron Loss

The purpose of this method is to estimate the iron loss accurately based on the proposed BH trajectory behavior model with FEM analysis. In addition, a high efficiency motor is designed using the improved FEM analysis. In particular, this paper deals with amorphous alloys, which have attracted attention as low iron loss materials in recent years. The amorphous alloys are thin and have high electrical resistivity, which results in low eddy current loss. In addition, the amorphous alloys are characterized by low hysteresis loss because they do not have a crystalline structure. Normally, for the mass-production of the motors, the motor cores are manufactured by blanking the electrical steels. On the other hand, it is known that the distortion and the residual stress generated in the electrical steels during blanking process deteriorates the magnetization characteristics. It is important to quantitatively understand the impact of these factors on the motor performance. Conventionally, the iron loss analysis is performed by multiplying the iron loss value calculated from the iron loss curves by the building factor (BF) values. However, the BF values are based on the knowledge obtained for the general electrical steels. Therefore, it is impossible that the iron loss is analyzed accurately for the amorphous alloys. Therefore, in this study, the analysis that does not rely on the BF values is used to obtain a characterization of the iron loss characteristics of the blanked amorphous alloy.

1.2.3 Optimal Pulse Pattern for Iron Loss

The purpose of this method is to derive the evaluation function of the iron loss based on the proposed BH behavior model. In addition, the pulse pattern is optimized based on the evaluation function in order to reduce the iron loss. The iron loss increases as the drive frequency increases. Therefore, the ratio of iron loss to the total loss increases especially at high speed rotation. Therefore, the target of the iron loss reduction is the high-speed light-load region. Conventionally, the iron loss is calculated by using the harmonic analysis results of the magnetic flux density at each part of the iron core obtained by FEM method and the iron loss curve. However, FEM analysis considering the carrier harmonics is time-consuming. The optimization of the pulse pattern is not practical because it requires the optimization of the multiple switching timings. In addition, the iron loss does not have a simple superposition of each frequency component. Therefore, in this study, the evaluation function for iron loss is derived without relying on the harmonic analysis, which is easy to calculate the iron loss accurately.

1.3. Thesis Organization

Fig.1.7 shows the outline of this paper. This paper consists of six chapters. The contents of each chapter are as follows.

In Chapter 1, as the research background, the necessity of improving the motor efficiency of the electric energy was explained based on the current status of the global warming and the electrical energy demand of the motors. In addition, the characteristics of the soft magnetic materials which greatly affect the motor efficiency were also explained from the viewpoint of the trade-off between maximum magnetic flux density and iron loss and new developed materials. In addition, the advantages of the concentrated winding synchronous motor were explained from the aspect of the motor efficiency. In addition, the method in order to improve the motor efficiency was explained. In addition, the necessity of increasing the efficiency by taking advantage of the material characteristics was explained. Next, the problems of the magnetic saturation and the iron loss, which are the problems in utilizing the material properties, were explained. Finally, the purpose of this paper was explained.

Chapter 2 begins with a basic explanation of the torque and the loss, which affect the efficiency of the motors. It also explains the conventional linear model-based efficiency improvement technology based on the explained torque and loss fundamentals. After that, the problems in handling magnetic saturation and iron loss based on the linear model are explained in detail. The proposed BH trajectory behavior model estimates and calculates the torque under magnetic saturation, where the linearity is lost, and the hysteresis loss, where the frequency superposition is not valid, by considering the material properties in detail. Finally, a comparison is conducted between the conventional high efficiency technology based on the linear model and the proposed high efficiency technology based on the BH trajectory model to show the position of this paper.

In Chapters 3 to 5, the specific applications of the BH trajectory behavior model described in Chapter 2 are presented and its characteristics and performance are discussed. The superiority and usefulness of the BH trajectory behavior model for improving the efficiency considering the magnetic saturation and the iron loss are verified by simulations and experiments.

Chapter 3 describes the automatic design method for high-efficiency motors with consideration of the magnetic saturation using the BH trajectory behavior model. First, the geometrical parameters and the input constants for the automatic design of the high-efficiency motor are explained. Next, the procedure to apply the proposed BH trajectory behavior model into the permeance method is explained. Then, the torque and the loss are formulated as functions of the shape parameters based on the proposed permeance method. The derived theoretical equations are summarized, and an automatic design method using the rotor diameter as a degree of freedom is proposed and validated. In addition, the effect of the magnetic saturation considered by the BH trajectory behavior model is discussed. In order to confirm that the design method considers the material characteristics, the design examples using the materials with different saturation magnetic flux densities are presented.

In Chapter 4, a method for accurate FEM analysis of iron loss using a BH trajectory behavior model and a design method for high-efficiency motors based on the analysis are explained. In particular, by applying the method into a blanked amorphous material, the problem of degradation due to the blanking during the mass production is quantitatively demonstrated. First, a simple experiment using a ring core is performed to quantitatively show the effect of the processing degradation due to the blanking. Next, the BH trajectory behavior model is multiplied by the algorithm implemented in

the FEM analysis software to realize highly accurate iron loss analysis. Using the accurate iron loss analysis, a high-efficiency motor utilizing blanked amorphous material is designed and prototyped. The efficiency and the loss of the prototype motor are evaluated. In addition, the superiority of the designed motor is explained. Finally, the accuracy of the iron loss analysis is verified to validate the proposed method.

In Chapter 5, a highly efficient pulse pattern using the iron loss evaluation function derived from the BH behavior model is explained. First, the assumption of the pulse pattern is explained in order to optimize the pulse pattern. Next, the procedure to apply the proposed BH trajectory behavior model into the derivation of the iron loss evaluation function under PWM is explained. Then, the optimal pulse pattern is derived based on the proposed iron loss evaluation function. The validity of the derived pulse pattern is explained by the experiments using the inductor and the motor. In addition, the current THD is also evaluated to explain that the proposed method is different from the conventional linear model-based method.

Chapter 6 summarizes the usefulness of this thesis and the efficiency improvement technique applying the BH trajectory behavior model proposed in each chapter. In addition, the future issues are summarized.

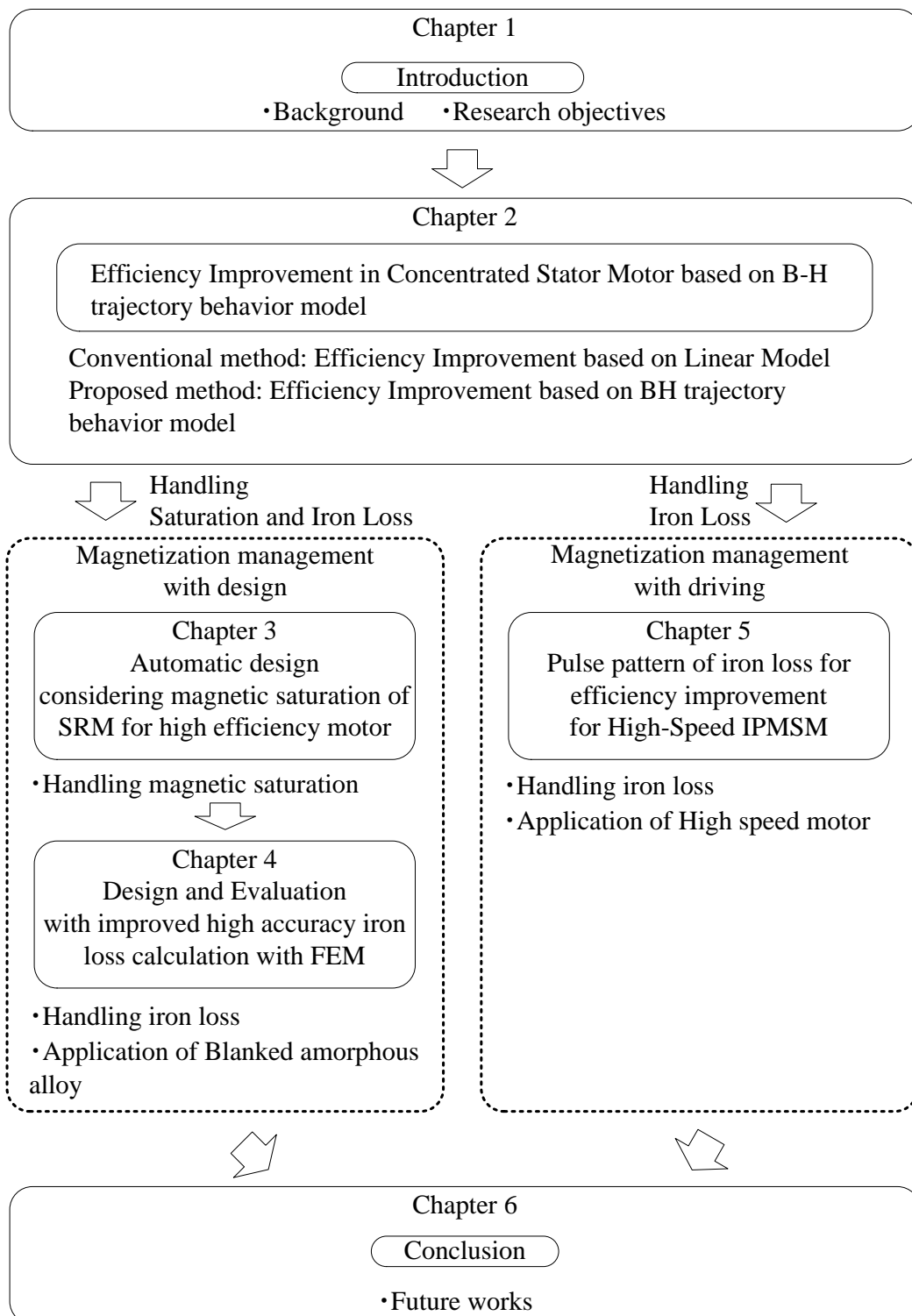


Fig. 1.8. The outline of this paper

Bibliography

- [1-1] IPCC Working Group III, AR5 Climate Change 2014: Mitigation of Climate Change.
[Online]Available:
https://www.ipcc.ch/site/assets/uploads/2018/02/ipcc_wg3_ar5_full.pdf
- [1-2] INTERNATIONAL ENERGY AGENCY: “Energy-Energy-Efficiency Policy Opportunities for Electric Motor-Driven Systems”
- [1-3] Official home page of KYUSHU ELECTRONIC POWER CO., INC.
[Online]Available:
http://www.kyuden.co.jp/effort_renewable-energy_photovoltaic_faq.html
- [1-4] Y. Takeda, N. Matsui, S. Morimoto, and Y. Honda: “Design and control of Interior Permanent Magnet Synchronous Motor”, Ohmsha (2016)
- [1-5] H. Koharagi, M. Sasaki, M. Senoh, and K. Noma: “Investigation of Brushless DC Motors with Concentrated Windings for Air Conditioners”, The Paper of Technical Meeting on Rotating Machinery, IEEJ, RM-01-64 (2001) (in Japanese)
- [1-6] H. Murakami, Y. Honda, S. Morimoto, and Y. Takeda: “A Study of Rotor Design for IPMSM with Concentrated Winding Considering the Iron Loss”, T. IEE Japan, Vol.121-D, No.5, pp.597–603 (2001-5) (in Japanese)
- [1-7] T. Aizawa, T. Ohno, and K. Sawa: “A Study on Design of Switched Reluctance Motor”, The Papers of Technical Meeting on Rotating Machinery, IEEJ, RM-97-12 (1997) (in Japanese)
- [1-8] K. Kiyota and A. Chiba: “Design of Switched Reluctance Motor Competitive to 60-kW IPMSM in Third-Generation Hybrid Electric Vehicle”, IEEE Transactions on Industry Applications, vol. 48, no. 6, pp. 2303-2309 (2012)
- [1-9] K. Kiyota, T. Kakishima, H. Sugimoto, and A. Chiba: “Comparison of the Test Result and 3D-FEM Analysis at the Knee Point of a 60 kW SRM for a HEV”, IEEE Transactions on Magnetics, vol. 49, no. 5, pp. 2291-2294 (2013)
- [1-10] K. Akatsu, S. Wakui:” A Design Method of Fractional-Slot Concentrated Winding SPMSM Using Winding factor and

- Inductance factor”, IEEJ Transactions on Industry Applications, Vol.217, No.11, pp.1171-1179 (2007) (in Japanese)
- [1-11] A.M. EL-Refaie, T.M. Jahns, P.J. McCleer, and J.W. McKeever: “Experimental Verification of Optimal Flux Weakening in Surface PM Machines Using Concentrated Windings”, IEEE Transaction on Industrial Application, Vol.42, No.2, pp.443–453 (2006)
- [1-12] P. Ponomarev, P. Lindh, J. Pyrhonen:”E-ect of Slot-and-Pole Combination on the Leakage Inductance and the Performance of Tooth-Coil Permanent-Magnet Synchronous Machines,” IEEE Transaction on Industrial Electronics, vol. 60, no. 10, pp. 4310-4317, (2013)
- [1-13] R. Kolano, A. Kolano-Burian, K. Krykowski, J. Hetmańczyk, M. Hreczka, M. Polak, and Jan Szynowski “Amorphous soft magnetic core for the stator of the high-speed PMSM motor with half-open slots,” IEEE Transactions on Magnetics, vol. 52, no. 6, no. 2003005 (2016)
- [1-14] S. Okamoto, N. Denis, Y. Kato, M. Ieki, and K. Fujisaki, “Core loss reduction of an interior permanent-magnet synchronous motor using amorphous stator core,” IEEE Transactions on Industry Applications, vol. 52, no. 3, pp. 2261–2268 (2016)
- [1-15] D.-K. Hong, D. Joo, B.-C. Woo, Y.-H. Jeong, and D.-H. Koo, “Investigations on a super high speed motor-generator for microturbine applications using amorphous core,” IEEE Transactions on Magnetics, vol. 49, no. 7, pp. 4072–4075 (2013)
- [1-16] T. Fan, Q. Li, and X. Wen, “Development of a high power density motor made of amorphous alloy cores,” IEEE Transactions on Industrial Electronics, vol. 61, no. 9, pp. 4510–4518 (2014)
- [1-17] W. Tong, S. Dai, S. Wu, and R. Tang, “Performance Comparison Between an Amorphous Metal PMSM and a Silicon Steel PMSM,” IEEE Transactions on Magnetics, vol. 55, no. 6, no. 8102705 (2014)
- [1-18] M. Dems and K. Komez, “Performance characteristics of a high-speed energy-saving induction motor with an amorphous stator core,” IEEE Transactions on Industrial Electronics, vol. 61, no. 6, pp. 3046–3055 (2014)
- [1-19] K. Sadahiro, S. Gotoh, and S. Uenosono: “Soft magnetic Materials of JFE Steel Group”, JFE Technical Report, No.8, p1-p6 (2005)

- [1-20] Yuya Ako, Yasuhito Takahashi, Koji Fujiwara, Takehiro Jikumaru: “Improvement of Power Density of Surface Permanent Magnet Synchronous Motor by Applying Permendur to Stator Core”, The Papers of Technical Meeting on Rotating Machinery, IEEJ, SA-18-031, RM-18-031 (2018)
- [1-21] R. Tang, W. Tong, and X. Han, “Overview on amorphous alloy electrical machines and their key technologies,” Chinese Journal of Electrical Engineering, vol. 2, no. 1, pp. 1–12 (2016)
- [1-22] JSOL: “Introduction to Permanent Magnet Synchronous Motor Design”, JSOL Corporation (2016)
- [1-23] Z. Q. Zhu, D. Howe, E. Bolte, and B. Ackermann, “Instantaneous magnetic field distribution in brushless permanent magnet DC motors. I. Open-circuit field”, IEEE Trans. Magn., Vol.29, No.1, pp.124-135 (1993)
- [1-24] T. Kosaka and N. Matsui, “Simplified Analysis and Evaluation of Drive Characteristic of Fully-Pitched Winding Reluctance Motors”, IEEJ Trans. IA, Vol.119, No.10, pp.1165-1170 (1999) (in Japanese)
- [1-25] B. Sheikh-Ghalavand, S. Vaez-Zadeh and A. H. Isfahani, “An Improved Magnetic Equivalent Circuit Model for Iron-Core Linear Permanent-Magnet Synchronous Motors”, IEEE Trans. Magn., Vol.46, No.1, pp.112-120 (2010)
- [1-26] K. Yamazaki, Y. Seto, and M. Tanida, “Iron Loss Analysis of IPM Motor Considering Carrier Harmonics”, IEEJ Trans. IA, Vol.125, No.7, pp.758-766 (2005) (in Japanese)
- [1-27] K. Narita, T. Yamada, Y. Sakashita, and K. Akatsu, “Coupled Analysis Technique Involving Magnetic-Field-Control/Circuit Simulation and Loss Estimation for Permanent Magnet Synchronous Machine” , IEEJ Trans. IA, Vol.131, No.11, pp.1309-1315 (2011) (in Japanese)
- [1-28] T. Okitsu, D. Matsushashi and K. Muramatsu, “Method for Evaluating the Eddy Current Loss of a Permanent Magnet in a PM Motor Driven by an Inverter Power Supply Using Coupled 2-D and 3-D Finite Element Analyses”, IEEE Trans. Magn., Vol.45, No.10, pp.4574-4577 (2009)
- [1-29] T. Sun, J. Wang, and X. Chen, “Maximum torque per ampere (MTPA) control for interior permanent magnet synchronous machine drives based on virtual signal injection,” IEEE Trans. Power Electron., vol.

30, no. 9, pp. 5036–5045, Sep. 2015.

- [1-30] S. Jung, J. Hong and K. Nam, Current Minimizing Torque Control of the IPMSM Using Ferraris Method, IEEE Trans. Power Electron., vol. 28, no. 12, pp. 5603-5617, Dec.2013.

Chapter 2

Efficiency improvement in Concentrated Stator Motors based on B-H Trajectory Behavior Model

2.1 Introduction

This chapter describes the efficiency improvement in the synchronous motors with the concentrated stator windings based on the B-H trajectory behavior model. This chapter begins with a basic explanation of the torque and the loss, which affect the efficiency of the motors. It also explains the conventional linear model-based efficiency improvement technology based on the explained torque and loss fundamentals. After that, the problems in handling the magnetic saturation and the iron loss based on the linear model are explained in detail. The proposed B-H trajectory behavior model estimates and calculates the torque under the magnetic saturation, where the linearity is lost, and the hysteresis loss, where the frequency superposition is not valid, by considering the material properties in detail. Finally, a comparison is conducted between the conventional high efficiency technology based on the linear model and the proposed high efficiency technology based on the B-H trajectory model to show the position of this paper.

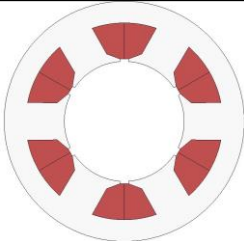
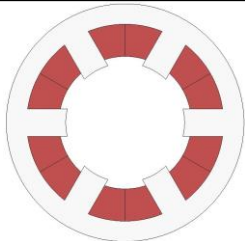
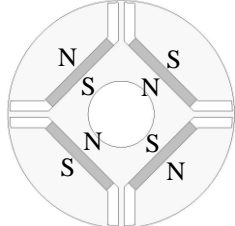
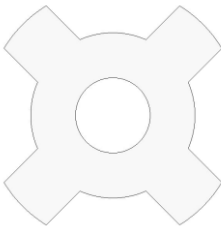
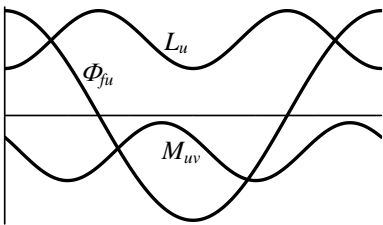
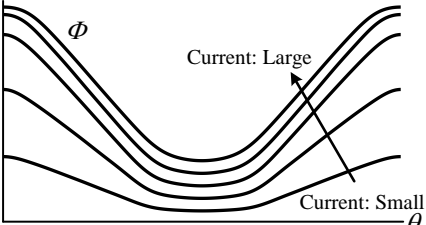
2.2 Torque and Loss

This section describes the torque and the losses of the motor. The efficiency of the motor depends on not only the losses of the motor but also the torque (output) of the motor. Therefore, the torque and the loss of the motor are closely related to the motor's efficiency.

2.2.1 Torque

Table 2.1 shows the structure of a synchronous motor and its characteristics in terms of inductance variation and torque generation mechanism. The motor generates torque by converting the magnetic energy stored in space into mechanical energy. The change of magnetic energy is caused by the change of self-inductance and mutual inductance with the position of rotation. The way the inductance changes depends on the structure and winding method of the rotor and stator. In the IPMSM, the interlinkage flux, self-inductance, and mutual inductance of the permanent magnets change. The torque at which energy conversion takes place due to changes in the interlinkage flux of the permanent magnet is called the magnet torque. On the other hand, the torque generated by the change in magnetic energy due to the change in self-inductance and mutual inductance is called reluctance torque. In the SRM, only the self-inductance changes. Therefore, the torque of the SRM is only the reluctance torque, which is the torque generated by the conversion of the magnetic energy change caused by the self-inductance change [2-1]. In general, IPMSM has weak magnetic saturation and SRM has strong magnetic saturation. This is because the magnetic flux is concentrated on the opposite portion between the stator pole and the rotor pole in order to obtain the reluctance torque in SRM. As a result, local magnetic saturation occurs in the motor core.

Table. 2.1. The structure of a synchronous motor and its characteristics in terms of inductance variation and torque generation mechanism

| Motor type | IPMSM | SRM |
|---|---|---|
| Stator configuration |  |  |
| Rotor configuration |  |  |
| Inductance and interlinkage flux distribution |  |  |
| Torque generation mechanism | Change in armature chain flux of permanent magnet + change in self-inductance + change in mutual inductance | Change in self-inductance |
| Characteristic | Sinusoidal distribution + Weak saturation | Non-sinusoidal distribution + Strong saturation |
| Torque equation | Constant value and few parameters | Instantaneous value and many parameters |

First, IPMSM's torque is explained. The direction of the N-pole of the permanent magnet is defined as the d-axis. In addition, the direction $\pi/2$ from the d-axis is defined as the q-axis, and the advance angle of the d-axis taken clockwise with respect to the U-phase winding is θ . The distribution of inductance and the stranded magnetic flux of IPMSM is expressed by the following equation.

$$\left\{ \begin{array}{l} L_u = l_a + L_a - L_{as} \cos 2\theta \\ L_v = l_a + L_a - L_{as} \cos\left(2\theta + \frac{2}{3}\pi\right) \dots\dots\dots (2.1) \\ L_w = l_a + L_a - L_{as} \cos\left(2\theta - \frac{2}{3}\pi\right) \end{array} \right.$$

$$\left\{ \begin{array}{l} M_{uv} = -\frac{1}{2}L_a - L_{as} \cos\left(2\theta - \frac{2}{3}\pi\right) \\ M_{vw} = -\frac{1}{2}L_a - L_{as} \cos 2\theta \dots\dots\dots (2.2) \\ M_{wu} = -\frac{1}{2}L_a - L_{as} \cos\left(2\theta + \frac{2}{3}\pi\right) \end{array} \right.$$

$$\left\{ \begin{array}{l} \Phi_{fu} = \Phi_f \cos \theta \\ \Phi_{fv} = \Phi_f \cos\left(\theta - \frac{2}{3}\pi\right) \dots\dots\dots (2.3) \\ \Phi_{fw} = \Phi_f \cos\left(\theta + \frac{2}{3}\pi\right) \end{array} \right.$$

where L_u , L_v , and L_w are the self-inductance of each phase, and M_{uv} , M_{vw} , and M_{wu} are the mutual inductance between each phase. In addition, θ is the rotor position, l_a is the leakage inductance, L_a is the average value of the effective inductance, and L_{as} is the amplitude of the effective inductance. where Φ_{fu} , Φ_{fv} , and Φ_{fw} are armature chain fluxes due to permanent magnets. In addition, Φ_f is the maximum value of armature chain flux due to permanent magnets.

The torque of a PMSM can be expressed by the following equation.

$$T = p_f \left\{ \Phi_{fa} i_q + (L_d - L_q) i_d i_q \right\} \dots\dots\dots (2.4)$$

where

$$L_d = l_a + \frac{3}{2}(L_a - L_{as}), \quad L_q = l_a + \frac{3}{2}(L_a + L_{as}), \quad \Phi_{fa} = \sqrt{\frac{3}{2}} \Phi_f \dots (2.5)$$

The first term in the above equation is the magnet torque and the second term is the reluctance torque. As shown in this equation, there is a linearity in this magnet torque. This is because magnetic saturation is not considered in PMSM. When magnetic saturation is not considered, the magnetic circuit method is easily applied. An example of the application of the magnetic circuit method will be described later.

Next, SRM's torque is explained. In general, SRMs have magnetic saturation properties. Various models of the interlinkage flux to consider the magnetic saturation have been proposed. One of the most popular method is approximation method with Fourier series with the parameters as a function of motor current by considering the magnetic saturation. In this method, flux linkage characteristics considering the magnetic saturation can be expressed by the following equation.

$$\Phi = \sum_{n=1}^N \left(\sum_{m=1}^M k_{nm} i^m \right) \cos(nN_r \theta_m) \dots\dots\dots (2.6)$$

where k_{nm} is the m -th order coefficient of the polynomial function with respect to the current in the n -th order coefficient of the discrete Fourier series with respect to the rotor position. In addition, N and M are the highest order of the coefficient and N_r is the number of rotor poles.

The torque of a SRM can be expressed by the following equation [2-1].

$$T = \sum_{n=1}^N \left(\sum_{m=1}^M k_{nm} \frac{i^{m+1}}{m+1} \right) (-nN_r \sin(nN_r \theta_m)) \dots\dots\dots (2.7)$$

The term in the above equation is the reluctance torque. As shown in this equation, there is a nonlinearity in the reluctance torque. This is because

magnetic saturation is generally considered in SRM. When magnetic saturation is considered, it is not easy to apply the magnetic circuit method into SRM.

2.2.2 Copper loss

Copper loss is the Joule loss caused by the current flowing through the windings of an electric motor. In general, the resistance of wiring is small and is often ignored. However, the winding of an electric motor can be several meters to several tens of meters long. Therefore, the resistance becomes so large, which cannot be ignored. The copper loss is proportional to the winding resistance and increases in proportion to the square of the current flowing. Therefore, the copper loss is expressed by the following equation.

$$W_c = RI_{RMS}^2 \dots\dots\dots (2.8)$$

where W_c is the copper loss, R is winding resistance, and I_{RMS} is the root mean square (RMS) of the current. The current RMS value is expressed by the following equation.

$$I_{RMS} = \sqrt{\frac{1}{T} \int_0^T i(t)^2 dt} \dots\dots\dots (2.9)$$

Where T is the period and i is the current.

First, assume that the current is an ideal sine wave. Therefore, the current is expressed by following equation.

$$i(t) = I_1 \sin(2\pi f_1 t) \dots\dots\dots (2.10)$$

where I_1 is the amplitude of fundamental waveform and f_1 is the frequency. By substituting equation (2.10) into equation (2.9), the following equation is obtained.

$$I_{RMS} = \sqrt{\frac{1}{T} \int_0^T i(t)^2 dt} = \frac{1}{\sqrt{2}} I_1 \dots\dots\dots (2.11)$$

By substituting equation (2.11) into equation (2.8), the following equation is obtained.

$$W_c = RI_{RMS}^2 = \frac{1}{2} RI_1^2 \dots\dots\dots (2.12)$$

Next, assume that the current is a non-sine wave. Therefore, the current is expressed by following equation.

$$i(t) = \sum_{n=1}^N I_n \sin(2\pi f_1 n t) \dots\dots\dots (2.13)$$

where I_n is the amplitude of n-th harmonic components. By substituting equation (2.13) into equation (2.9), the following equation is obtained.

$$I_{RMS} = \sqrt{\frac{1}{T} \int_0^T i(t)^2 dt} = \frac{1}{\sqrt{2}} \sqrt{\sum_{n=1}^N I_n^2} \dots\dots\dots (2.14)$$

By substituting equation (2.14) into equation (2.8), the following equation is obtained.

$$W_c = RI_{RMS}^2 = \frac{1}{2} R \sum_{n=1}^N I_n^2 \dots\dots\dots (2.15)$$

As shown in equation (2.15), the current RMS value is mathematically a superposition of each frequency component. Therefore, the copper loss increased by the harmonic components of current and voltage is called harmonic copper loss. By increasing the switching frequency, the amplitude of the switching frequency component I_n is reduced. Therefore, increasing the switching frequency is effective in reducing the copper loss.

2.2.3 Iron loss

Iron loss is the loss generated in stator iron cores, rotor iron cores, and permanent magnets. It is a general term for hysteresis loss generated by changes in magnetization energy in iron cores and eddy current loss (Joule loss) generated by eddy currents flowing in iron cores and permanent magnets. The hysteresis loss increases in proportion to the frequency of the magnetic flux density in the iron core. On the other hand, eddy current loss increases in proportion to the square of the magnetic flux density frequency. Both losses increase as the amplitude of the magnetic flux density increases

and vary greatly depending on the characteristics of the electromagnetic steel sheet used as material.

First, eddy current loss is explained. Eddy current loss (Joule loss) generated by eddy currents flowing in iron cores and permanent magnets.

Fig. 2.1 shows image of eddy currents flowing in a steel plate. r is resistivity, d is thickness, h is width, l is depth, and ϕ is flux. As shown in Fig. 2.1, when magnetic flux ϕ crosses the steel plate in the direction of the orange arrow, eddy currents flow on the surface of the steel plate as shown by the red arrow in the figure. The magnetic flux ϕ that crosses the area xh from the center to the part of the thickness direction x is expressed by the following equation using the magnetic flux density.

$$\phi = B(t)hx \dots\dots\dots (2.16)$$

When a strip of minute thickness dx (dotted line in Fig. 2.1) is cut out of the steel plate, the electromotive force e induced in the strip is expressed by the following equation.

$$e = -\frac{d\phi}{dt} = -\frac{dB(t)}{dt}hx \dots\dots\dots (2.17)$$

The surface resistance r of the strip is expressed by the following equation if paying attention to the direction of the eddy current.

$$r = \rho \frac{h}{ldx} \dots\dots\dots (2.18)$$

Therefore, the magnitude of the eddy current flowing in the strips, di , is expressed by the following equation.

$$di = \frac{e}{r} = -\frac{dB(t)}{dt} \frac{lx}{\rho} dx \dots\dots\dots (2.19)$$

Since the power consumption edi due to the eddy current di flowing in the strips is expressed in the following equation, the power consumption p of the entire steel sheet is expressed in the following equation.

$$p(t) = \int edi = 2 \int_0^{d/2} \frac{dB(t)}{dt} hx \frac{dB(t)}{dt} \frac{lx}{\rho} dx = \left(\frac{dB(t)}{dt} \right)^2 \frac{hld^3}{12\rho} \dots\dots (2.20)$$

The average power consumed by a steel plate is expressed by the following equation.

$$\bar{p} = \frac{1}{T} \int_0^T p(t) dt = \frac{hld^3}{12\rho} \frac{1}{T} \int_0^T \left(\frac{dB(t)}{dt} \right)^2 dt \dots\dots\dots (2.21)$$

Since all of the power consumed by eddy currents is converted into heat loss, the amount of heat generated per unit volume. Then, the eddy current loss is expressed by the following equation.

$$W_{eddy} = \frac{\bar{p}}{hld} = \frac{d^2}{12\rho} \frac{1}{T} \int_0^T \left(\frac{dB(t)}{dt} \right)^2 dt \dots\dots\dots (2.22)$$

First, assume that the flux density is an ideal sine wave. Therefore, the flux density is expressed by following equation.

$$B(t) = B_1 \sin(2\pi f_1 t) \dots\dots\dots (2.23)$$

where B_1 is the amplitude of fundamental waveform and f_1 is the frequency.

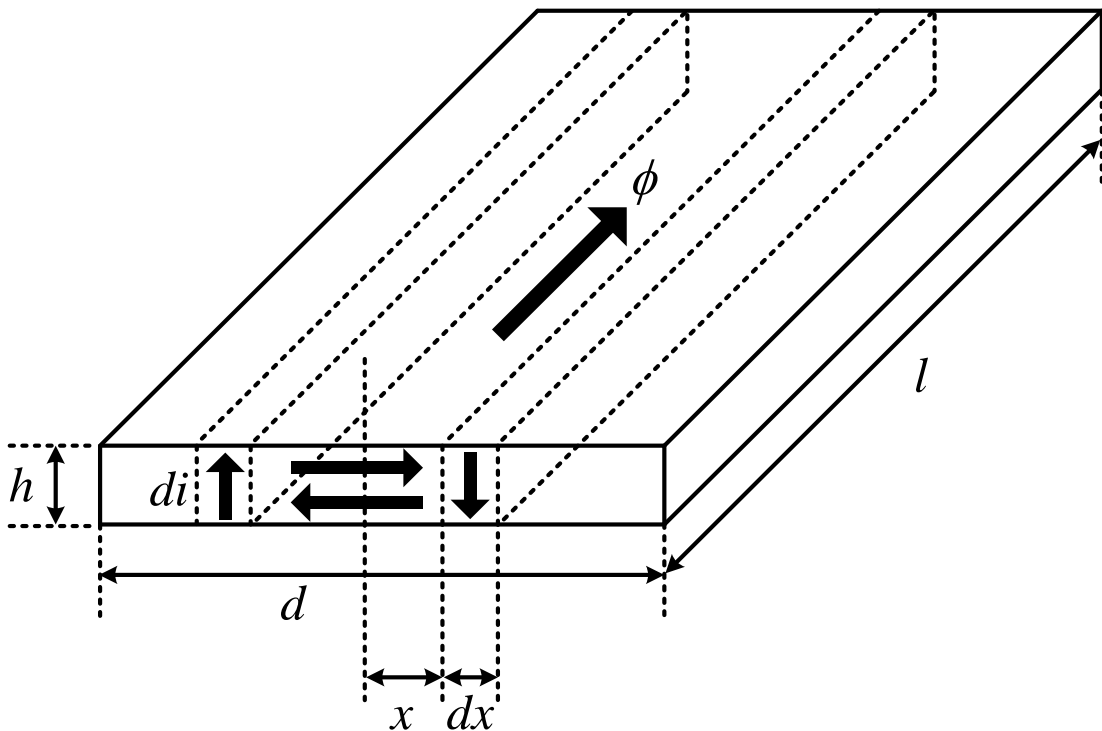


Fig. 2.1. Image of eddy currents flowing in a steel plate

By substituting equation (2.23) into equation (2.22), the following equation is obtained.

$$W_{eddy} = \frac{d^2}{12\rho} \frac{1}{T} \int_0^T \left(\frac{dB(t)}{dt} \right)^2 dt = \frac{\pi^2}{6\rho} f^2 B_1^2 d^2 \dots\dots\dots (2.24)$$

Next, assume that the current is a non-sine wave. Therefore, the flux density is expressed by following equation.

$$B(t) = \sum_{n=1}^N B_n \sin(2\pi f_1 nt) \dots\dots\dots (2.25)$$

where B_n is the amplitude of n-th harmonic components. By substituting equation (2.25) into equation (2.22), the following equation is obtained.

$$\begin{aligned} W_{eddy} &= \frac{d^2}{12\rho} \frac{1}{T} \int_0^T \left(\frac{dB(t)}{dt} \right)^2 dt \\ &= \frac{d^2}{12\rho} \frac{1}{T} \int_0^T \left(2\pi f_1 \sum_{n=1}^N n B_n \sin(2\pi f_1 nt) \right)^2 dt \dots\dots\dots (2.26) \\ &= \frac{\pi^2}{6\rho} d^2 \sum_{n=1}^N (nf_1)^2 B_n^2 \end{aligned}$$

As shown in equation (2.26), the eddy current losses are frequency weighted, and it can be seen that the superposition of the frequency components is mathematically valid. By increasing the switching frequency, the amplitude of the switching frequency component I_n would be lower. On the other hand, by increasing the switching frequency, the order n of the frequency becomes higher. Therefore, increasing the switching frequency is not effective to reduce the eddy current loss. This is distinctly different from copper loss.

Next, hysteresis loss is explained. Hysteresis loss generated by changes in magnetization energy in iron cores.

Fig. 2.1 shows the image of hysteresis loop. An alternating magnetic field (a magnetic field that repeatedly changes in magnitude and direction with time) is generated, and the hysteresis of the iron core causes the magnetic

flux density B to draw a hysteresis loop. The hysteresis loss is the area enclosed by the hysteresis loop. When the frequency of the alternating magnetic field is f [Hz], the hysteresis loop rotates f times in one second, so the hysteresis loss W_{hys} is expressed by the following equation.

$$W_{hys} = K(B(t))f \dots\dots\dots (2.27)$$

In general, if any minor loop does not occur, the hysteresis loss depends on the flux density amplitude B_{max} . Therefore, if there are no minor loops, the equation can be rewritten as

$$W_{hys} = K(B_{max})f \dots\dots\dots (2.28)$$

However, in general, superposition of frequency components is not feasible for hysteresis loss.

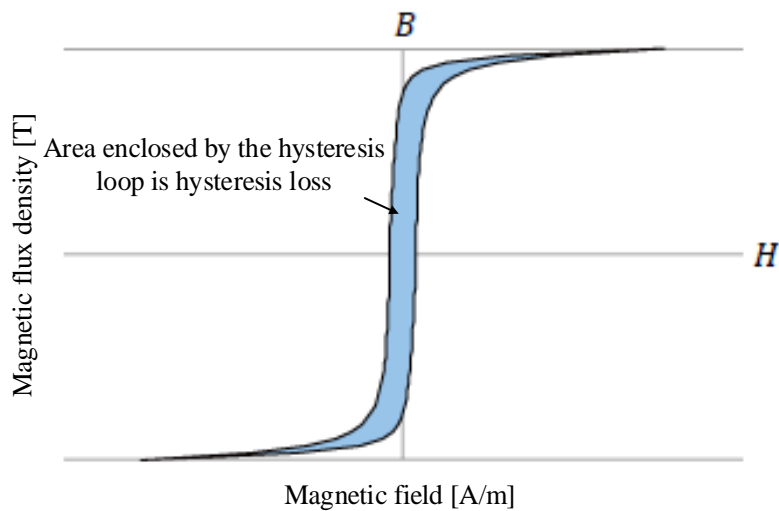


Fig. 2.2 Image of hysteresis loop (Adapted from [2-2] JSOL Official site, <https://www.jmag-international.com/jp/>)

Table 2.2 summarizes the results of the torque and the loss characteristics. There is a linearity in the torque of the PMSM, the copper loss, and the eddy current loss of the iron loss. On the other hand, there is no linearity in the torque of the SRM and the hysteresis loss of the iron loss.

Table. 2.2 The summarization of the results of the torque and loss characteristics

| |
|--|
| <div style="border: 1px solid black; border-radius: 10px; padding: 5px; width: fit-content; margin: 0 auto;">Torque calculation</div> <p style="margin-top: 10px;">Torque equation in IPMSM (not considering saturation)</p> $T = p_f \left\{ \Phi_{fa} i_q + (L_d - L_q) i_d i_q \right\}$ <p style="text-align: center; margin: 5px 0;"><u>Torque (=magnet torque in PMSM) has linearity</u></p> <p style="margin-top: 10px;">Torque equation in SRM (considering saturation)</p> $T = \sum_{n=1}^N \left(\sum_{m=1}^M k_{nm} \frac{i^{m+1}}{m+1} \right) (-nN_r \sin(nN_r \theta_m))$ <p style="text-align: center; margin: 5px 0;"><u>Torque (=reluctance torque in SRM) does not have linearity</u></p> |
| <div style="border: 1px solid black; border-radius: 10px; padding: 5px; width: fit-content; margin: 0 auto;">Copper loss calculation</div> <p style="margin-top: 10px;">If current is defined by</p> $i(t) = I_1 \sin(2\pi f_1 t) + I_2 \sin(2 \cdot 2\pi f_1 t) + \dots + I_n \sin(n \cdot 2\pi f_1 t)$ <p style="margin-top: 10px;">Copper loss is calculated by</p> <div style="text-align: center; margin: 5px 0;"> </div> $W_c = \frac{1}{2} R I_1^2 + \frac{1}{2} R I_2^2 + \dots + \frac{1}{2} R I_n^2$ <p style="text-align: center; margin: 5px 0;"><u>The copper loss has linearity</u></p> |
| <div style="border: 1px solid black; border-radius: 10px; padding: 5px; width: fit-content; margin: 0 auto;">Iron loss calculation</div> <p style="margin-top: 10px;">If current is defined by</p> $B(t) = B_1 \sin(2\pi f_1 t) + B_2 \sin(2 \cdot 2\pi f_1 t) + \dots + B_n \sin(n \cdot 2\pi f_1 t)$ <div style="display: flex; justify-content: center; align-items: center; margin: 10px 0;"> <div style="text-align: center; margin-right: 10px;"> </div> <div style="text-align: left;"> <p>Eddy current loss: $W_{eddy} = K_{eddy} B^2 f^2$</p> <p>Hysteresis loss: $W_{hys} = K_{hys} (B(t)) f$</p> </div> </div> $W_{eddy} = K_{eddy} B_1^2 (f_1)^2 + K_{eddy} B_2^2 (2f_1)^2 + \dots + K_{eddy} B_n^2 (nf_1)^2$ <p style="margin-top: 5px;">$W_{hys} = \text{unknown}$</p> <p style="text-align: center; margin: 5px 0;"><u>The eddy current loss has linearity,</u> <u>however hysteresis loss does not have linearity</u></p> |

2.3 Efficiency Improvement with Liner Model

In order to improve the efficiency of a motor, it is important to model the torque and the loss of the motor. These models are derived by assuming that the linearity is valid in the model. Linearity means that the superposition principle is valid. The superposition principle means that the response returned by the system when two or more inputs are given simultaneously is the sum of the responses returned when each input is added alone. If a response $f(x_n)$ is returned for an input x_n , then the following equation holds.

$$f(x_1 + x_2 + \dots + x_n) = f(x_1) + f(x_2) + \dots + f(x_n) \dots\dots\dots (2.29)$$

Many physical systems are regarded as models with linearity. The linearity of the model is very useful because it is easy to analyze the characteristic mathematically. Therefore, there are many examples where the superposition principle is applied into the expression for torque and loss. Fourier analysis and magnetic circuit method are mathematical techniques for the model with a linearity.

Fourier analysis is one of the data analysis methods, which is generally used to convert time domain data into frequency domain. The Fourier series is given by the following equation.

$$f(t) \sim \frac{a_0}{2} + \sum_{n=1}^{\infty} (a_n \cos nt + b_n \sin nt) \dots\dots\dots (2.30)$$

where

$$a_k = \frac{1}{\pi} \int_{-\pi}^{\pi} f(t) \cos kt dt \dots\dots\dots (2.31)$$

$$b_k = \frac{1}{\pi} \int_{-\pi}^{\pi} f(t) \sin kt dt \dots\dots\dots (2.32)$$

Complex periodic functions and periodic signals are represented by sums of periodic functions of simple forms.

In the permeance method, the magnetomotive force and magnetic flux are treated in the same way as the relationship between voltage and current in an electric circuit. Therefore, it is possible to analyze magnetic phenomena inside motor. The magnetoresistance of a magnetically uniform magnetic circuit element is expressed as follows

$$R = \frac{l}{\mu S} \dots\dots\dots (2.33)$$

where l is the element length, μ is the magnetic permeability, and S is the cross-sectional area. Magnetoresistance is a result of the superposition principle. If the magnetoresistances R_1 , R_2 , and R_n are arranged in series, the composite magnetoresistance is expressed as follows

$$R = R_1 + R_2 + \dots + R_n = \sum_{n=1}^n R_n \dots\dots\dots (2.34)$$

The multiple magnetic circuit elements in a motor are considered separately. On the other hand, the magnetic flux is expressed as

$$\phi = \frac{1}{S_n} \frac{Ni}{\sum R_n} \dots\dots\dots (2.35)$$

where N is the number of turns, i is current. Complex motor geometries is represented by a simple sum of magnetoresistances. (in this explanation, the parallel case is assumed).

Fig. 2.3 shows an overview of the efficiency improvement based on linear model. The use of the Fourier analysis in order to increase the efficiency is an effective for reducing the copper loss and the eddy current loss. This is because the frequency superposition is valid for the copper loss and the eddy current loss as explained in the previous chapter. The Fourier analysis is used in order to reduce the loss by focusing on each harmonic. In addition, the use of the Permeance method in order to increase the efficiency is effective when the material is not magnetically saturated. This is because each magnetic circuit element is considered independently when the circuit is not magnetically saturated. The independent magnetic circuit elements are easy in order to design the parameters for the high efficiency. The specific examples of the efficiency improvement using the Fourier analysis and the permeance method are described at the following chapter.

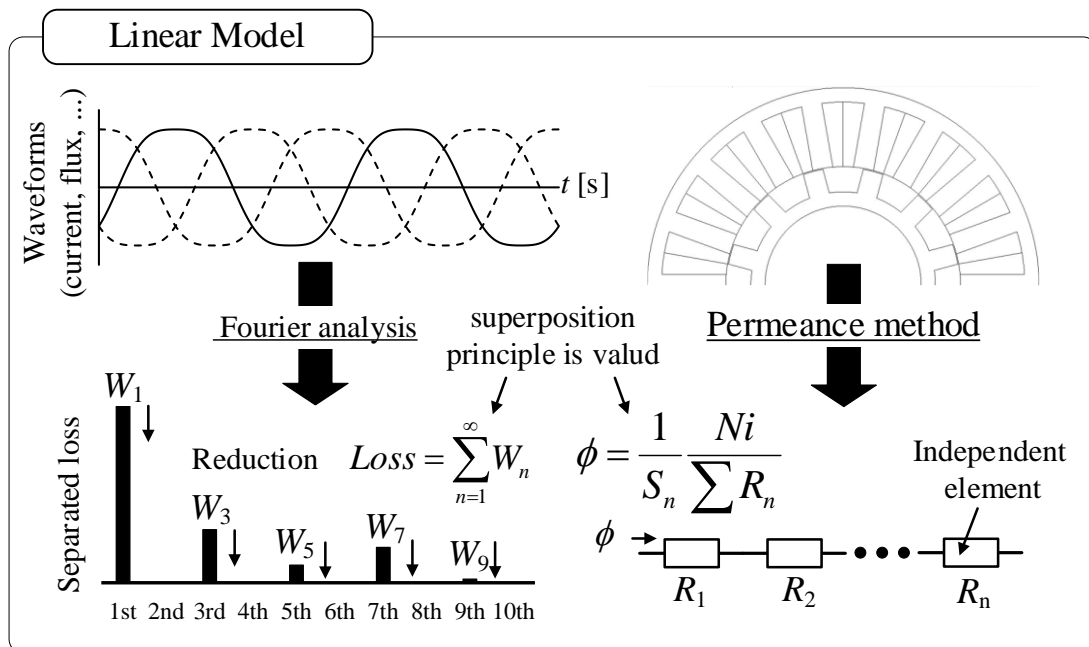


Fig. 2.3 Overview of the efficiency improvement based on linear model.

2.3.1 Automatic Design with Permeance Method[2-3]-[2-5]

Fig.2.4 shows the conceptual diagram of the normal design and the inverse design. The inverse motor design which directly decides motor configurations from the required characteristics is absolutely imperative to achieve a fast motor design.

A simple calculation method is proposed for automatic design to derive the motor geometry that fully satisfies the required output characteristics and minimizes the volume. The input constants are the maximum value of the N-T characteristics, the allowable losses, and the maximum ratings of the materials and devices used. In addition, by deriving the motor shape parameters to realize them, the corresponding shape can be derived even when the N-T characteristics change. Then, each output variable is theoretically developed and completely formulated, and all variables are expressed as a function of rotor radius, which enables easy volume minimization.

An important part of this method is the derivation of theoretical equations for each shape parameter. For this purpose, it is necessary to formulate the torque equation and other equations using the shape parameters.

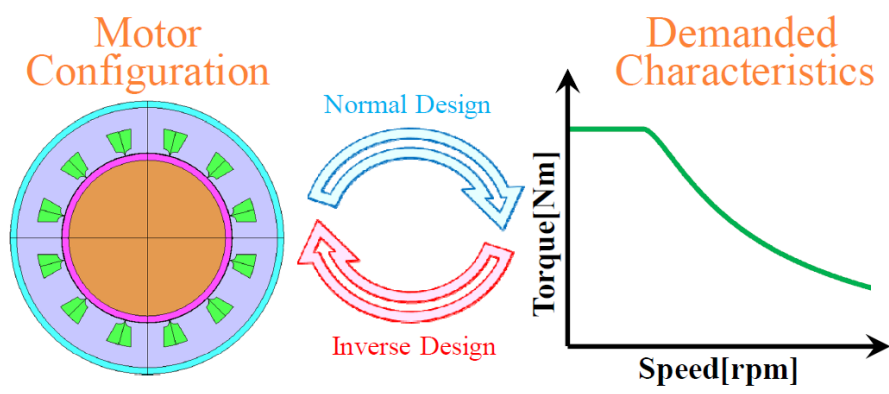


Fig.2.4 The conceptual diagram of the normal design and the inverse design (Adapted from [2-3] T. Yamada, K. Akatsu: “Automatic Design Method Considering the Frequently Used Area of a PMSM for an HEV”, ICEMS, pp1-6 (2012))

Fig.2.5 shows the magnetic circuit of SPMSM. In order to formulate the torque equation expressed by equation (2.4) in terms of shape parameters, the motor parameters such as ψ , L_d , and L_q are required. For example, ψ is expressed by following

$$\psi = \sqrt{\frac{3}{2}} N_t |\phi| = \sqrt{\frac{3}{2}} N_t \sqrt{3} B_g \left(r_r + \frac{1}{2} l_g \right) \frac{l_s}{P} \dots\dots\dots (2.36)$$

Where N_t is the number of turns, B_g is the magnetic flux density of the air gap, and the others are the motor diameters. In the literature, B_g is formulated as a shape parameter based on the magnetic circuit shown in Figure 2.8. In addition, by organizing these formulated parameters and rewriting them as a function of rotor diameter, a clear automatic design method is realized.

In these methods, the magnetic saturation of the core is neglected. In other words, the magnetoresistance of the core is assumed to be sufficiently lower than the magnetoresistance of the air gap. However, it is effective to magnetically saturate the core from the viewpoint of resource saving. In particular, SRMs are designed and controlled to actively utilize the saturation region. Therefore, it is not appropriate to use theoretical equations that ignore magnetic saturation.

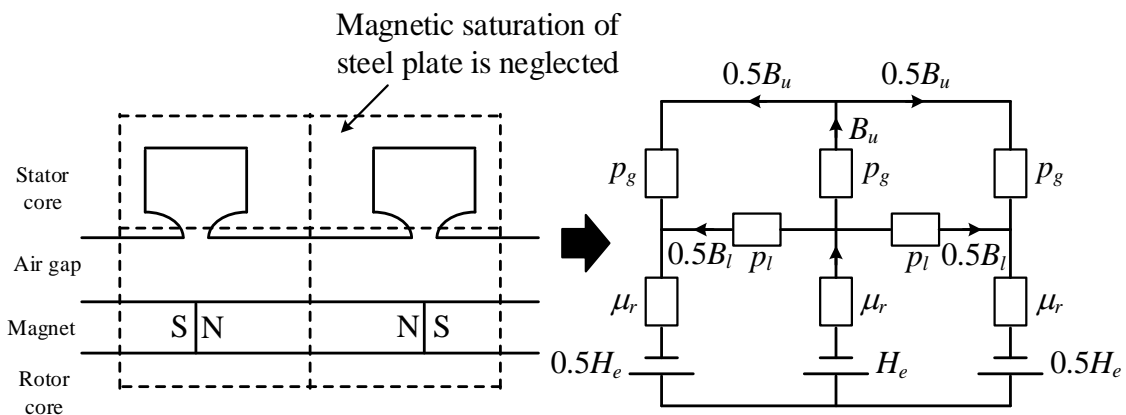


Fig. 2.5 The magnetic circuit of SPMSM

2.3.2 Permeance Method Compensating Magnetic Saturation[2-6]-[2-8]

Fig. 2.6 shows the B-H of core material and its approximation curve. As a promising method to compensate the effect of the magnetic saturation in the permeance method, there is a method with polynomial approximation of the B-H characteristic. In order to consider the nonlinearity of the magnetization properties, the curve is approximated by the following polynomial equation

$$H = \alpha_1 B + \alpha_n B^n \dots\dots\dots (2.37)$$

where α_1 and α_n are approximation coefficients. After this approximation, the permeance method is applied. Then, the magnetoresistance is expressed as follows

$$R_m = \frac{\alpha_1 l}{S} + \frac{\alpha_n l}{S^n} \phi^{n-1} \dots\dots\dots (2.38)$$

where S and l are the cross-sectional area and magnetic path length of the element, ϕ is the magnetic flux. With these methods, magnetic saturation is considered in the permeance method.

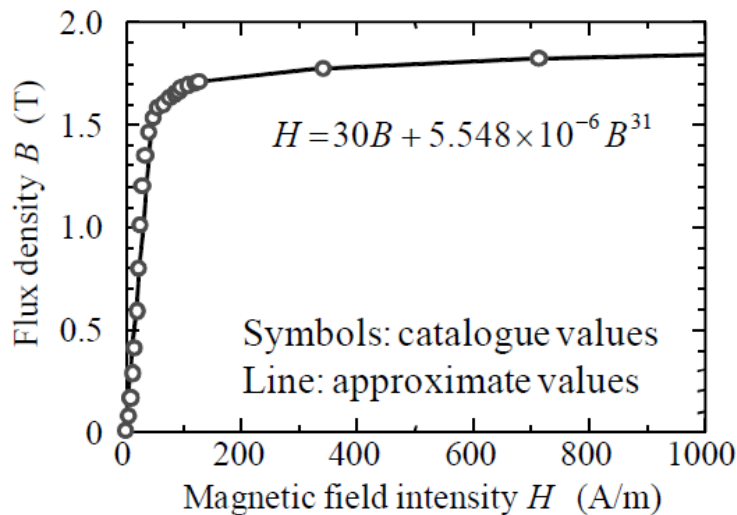


Fig. 2.6 B-H of core material and its approximation curve (Adapted from [2-6] Kenji Nakamura and Osamu Ichinokura: “Reluctance Network Based Dynamic Analysis in Power Magnetics”, IEEJ Transactions on Fundamentals and Materials, Vol. 128, No.8 pp.506-510(2008))

Fig.2.7 illustrates the SPICE model of nonlinear reluctance. As shown from the above equation, the linearity of the magneto-resistance has been lost. In this method, the magnetic flux ϕ must be calculated by the Runge-Kutta method or some other method. Instead of Runge-Kutta method, general purpose circuit simulators like “PLECS” or “SPICE” are used. As shown in the figure, the linear term is expressed as the linear resistance and the nonlinear one is represented by the nonlinear controlled voltage source.

However, the theoretical equation becomes more complicated when the torque and loss are expressed in the theoretical equation of the motor shape. It is not easy to establish an automatic design method from a complicated theoretical equation. Therefore, it is not effective to use such polynomial approximation to consider magnetic saturation in the automatic design method.

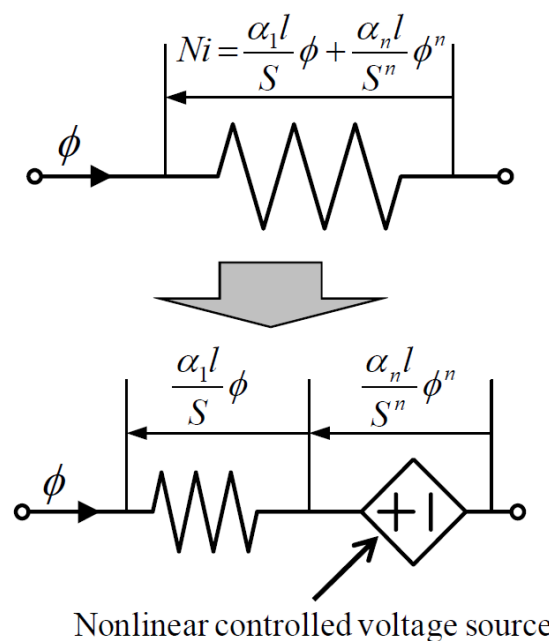


Fig. 2.7. SPICE model of nonlinear reluctance (Adapted from [2-6] Kenji Nakamura and Osamu Ichinokura: “Reluctance Network Based Dynamic Analysis in Power Magnetics”, IEEJ Transactions on Fundamentals and Materials, Vol. 128, No.8 pp.506-510(2008))

2.3.3 FEM Analysis of Iron Loss [2-2], [2-9]-[2-12]

Fig. 2.8 shows the iron loss curve. In the iron loss curve, the horizontal axis is the magnetic flux density and the vertical axis is the iron loss density, which is given for each frequency. The iron loss curve is commonly used as a method to analyze iron loss by electromagnetic field analysis. The iron loss curve is given by the following equation.

$$W_i \Delta vol. = p(f, B) \dots\dots\dots (2.39)$$

where the left side shows the iron loss density, and the right side shows that it is a function of frequency and magnetic flux density.

Fig.2.9(a) shows the magnetic flux density at the evaluation point, whereas Fig.2.9(b) shows the its harmonic analysis results. The time variation of the magnetic flux density in the core is obtained by FEM analysis. However, in the case of a motor, the time variation of the magnetic flux density is not sinusoidal. In general, this non-sinusoidal magnetic flux density waveform is decomposed into frequencies by Fourier analysis. As a result, the magnetic flux density waveform $B(t)$ at the evaluation point (r, θ, z) can be expressed as following equation.

$$B(t, r, \theta, z) = \frac{a_0(r, \theta, z)}{2} + \sum_{n=1}^{\infty} (a_n(r, \theta, z) \cos nt + b_n(r, \theta, z) \sin nt) \quad (2.40)$$

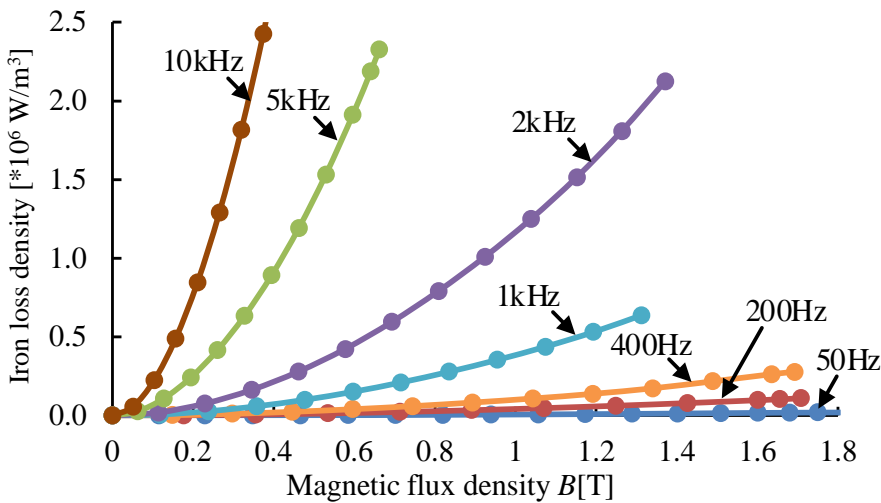


Fig. 2.8 The iron loss curve

In addition, the n th-order magnetic flux density amplitude is expressed as following equation.

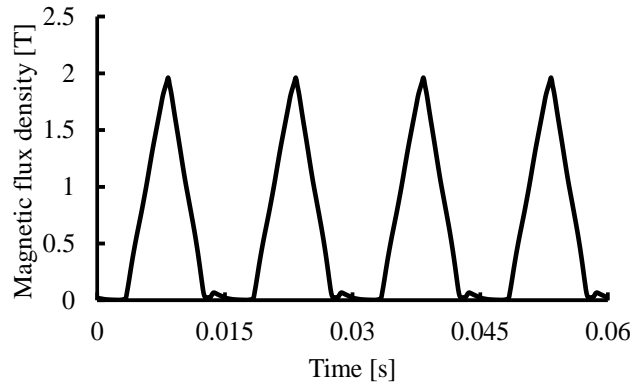
$$B_n(r, \theta, z) = \sqrt{a_n(r, \theta, z)^2 + b_n(r, \theta, z)^2} \dots\dots\dots (2.41)$$

If the superposition of the frequency components is valid for the iron loss, the iron loss per unit volume at the evaluation point (r, θ, z) can be expressed as following equation.

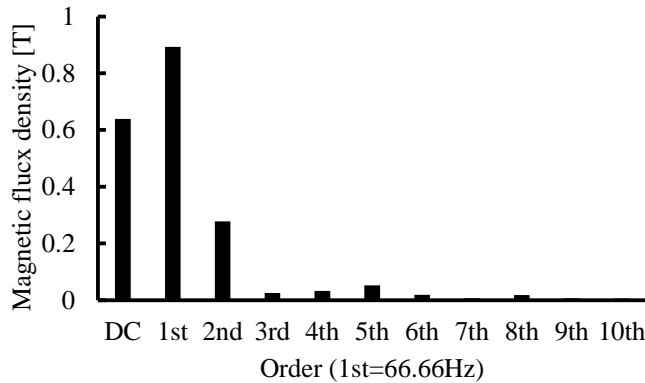
$$W_i(r, \theta, z)drd\theta dz = \sum_{n=1}^{\infty} p(f_n, B_n(r, \theta, z)) \dots\dots\dots (2.42)$$

In the actual calculation, this decomposition is performed for all the elements (mesh). Then multiply by the volume of the element to get the loss for each element.

$$W_i = \iiint_{Vol} W_i drd\theta dz = \iiint_{Vol} \sum_{n=1}^{\infty} p(f_n, B_n(r, \theta, z)) drd\theta dz \dots\dots\dots (2.43)$$



(1) Magnetic flux density



(b) Harmonic analysis results

Fig. 2.9 Magnetic flux density at the evaluation point

These discussions assume that iron loss is a result of frequency superposition. As explained in the previous section, iron loss (especially hysteresis loss) does not allow for frequency superposition. Therefore, these methods are expected to produce errors. The calculation of losses in electromagnetic field analysis requires high accuracy. This is because it is the final step in the design process.

2.3.4 FEM Analysis of Iron Loss Compensating Hysteresis Loss

[2-2], [2-13]-[2-15]

Fig.2.10 illustrates the method of calculating the hysteresis loss by counting the number of hysteresis loops. As a promising method to consider the hysteresis loss, there is a method of counting the number of hysteresis loops [2-13]. In this method, the number of extremes of the magnetic flux density waveform are counted. Then, starting from one pole value, if a second pole value is found, there is one loop. The difference between the two extremes is the amplitude B_j of the loop, and the loss $W(B_j)$ corresponding to that loop is calculated from the iron loss characteristic data. This is applied for all the loops that appear in the waveform, and then added together to calculate the hysteresis loss. The hysteresis loss can be expressed as follows

$$W_{hys} = W_{hys}(B_1) + W_{hys}(B_2) + \dots + W_{hys}(B_n) \dots\dots\dots (2.44)$$

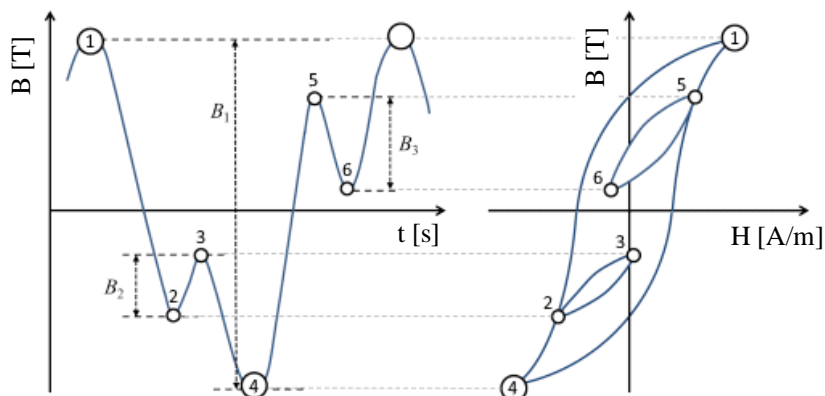


Fig.2.10. The method of calculating the hysteresis loss by counting the number of hysteresis loops (Adapted from [2-2] JSOL Official site, <https://www.jmag-international.com/jp/>)

Fig.2.11 shows the minor loops when the DC bias B_{dc} of the magnetic flux density is 0 T, 0.5 T, 1 T, and an AC component of 0.1 T is superimposed on it for 50A470. As shown in Fig.2.15, the area of the loop increases as the bias increases. However, in the conventional method, the area of the loop is calculated to be the same regardless of the size of the DC bias as long as the amount of change in magnetic flux density is the same. In other words, the value with zero bias, which is the state of measurement of iron loss characteristics, is applied. Therefore, hysteresis loss cannot be accurately evaluated using these advanced methods

A method of correcting the calculated value by using the building factor (BF value) has also been proposed [2-14][2-15]. However, it is known that the BF value varies depending on the material, operating point, and driving method. Therefore, when using this method, it is necessary to build a prototype motor and experimentally determine the BF value at each operating point and each driving method. This is very time-consuming.

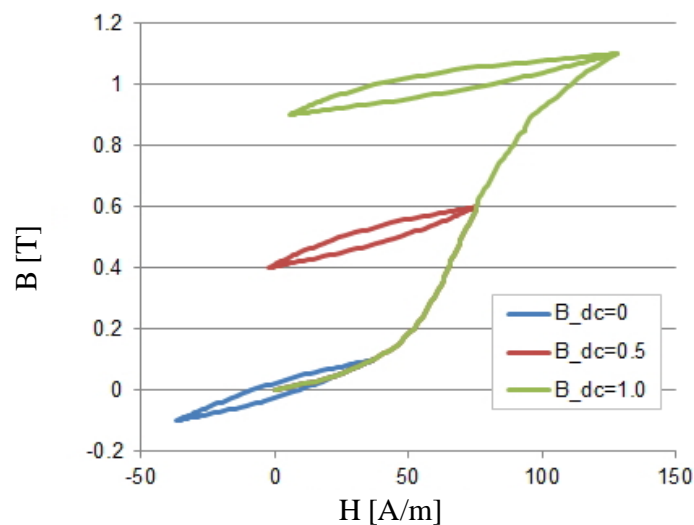


Fig. 2.11 The minor loops with DC bias (Adapted from [2-2] JSOL Official site, <https://www.jmag-international.com/jp/>)

2.3.5 Optimal Design with FEM [2-16]

Fig.2.12 shows the process of optimizing rotor shape. In the previous section, the automatic design method by permeance was explained. In contrast, there is a design method using FEM analysis. To design by FEM analysis, it is necessary to calculate and optimize the evaluation function in a practically acceptable calculation time. In the literature, the value of the iron loss is not directly adopted as the objective function in the optimization calculation. Instead, an approximate evaluation function for iron loss expressed by the harmonic components of the gap flux density is derived.

$$W = \sum_{n=1}^{\infty} (kB_k)^2 \dots\dots\dots (2.45)$$

where k is the spatial harmonic order of the gap flux density waveform, and B_k is the k th order spatial harmonic flux density. In the literature, the motor shape is optimized with minimization of this equation.

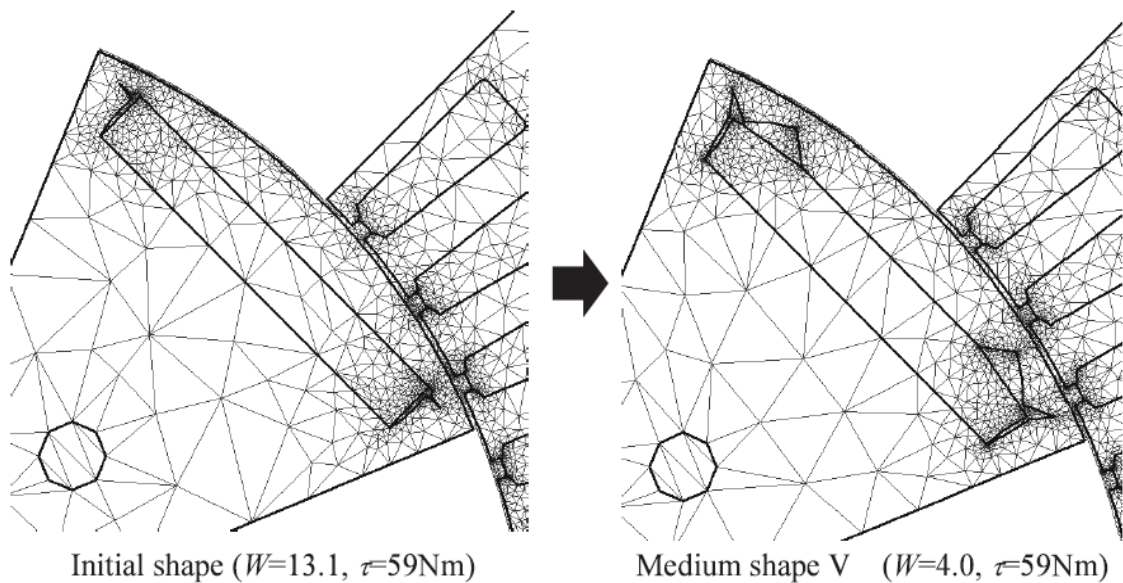


Fig.2.12 The process of optimizing rotor shape (Adapted from [2-16] K. Yamazaki, S. Ohki, A. Nezu, T. Ikemi: “Development of Interior Permanent Magnet Motors Reducing Harmonic Iron Losses under Field Weakening Control”, IEEJ Journal Industry Applications, vol. 127, no. 8, pp. 837-843 (2007) (in Japanese))

Fig.2.13 shows the gap flux density waveform and the contained harmonic flux density components. As shown in Fig.2.16, the magnetic flux density waveform approached a sinusoidal shape from a trapezoidal wave shape.

The evaluation function used in this method is the evaluation function of eddy current loss explained in section 2.2.3. Therefore, this method also neglects the hysteresis loss. In addition, Fourier analysis is required for these calculations. Fourier analysis complicates the optimization process.

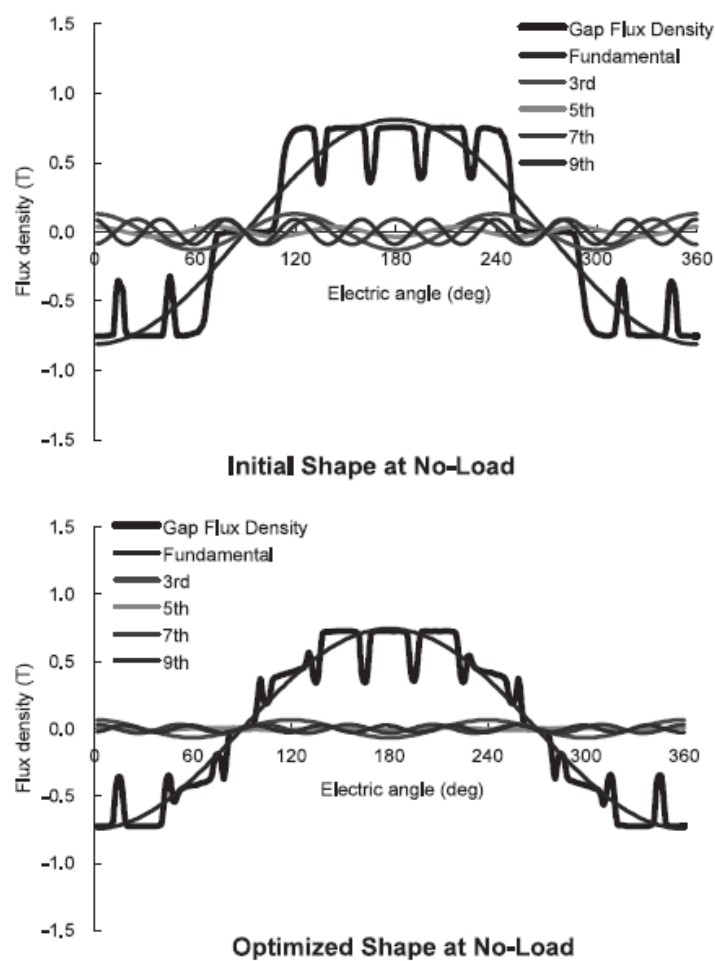


Fig.2.13 Amplitude of space harmonic components included in gap flux density waveform. (Adapted from [2-16] K. Yamazaki, S. Ohki, A. Nezu, T. Ikemi: “Development of Interior Permanent Magnet Motors Reducing Harmonic Iron Losses under Field Weakening Control”, IEEJ Journal Industry Applications, vol. 127, no. 8, pp. 837-843 (2007) (in Japanese))

2.3.6 Optimal Current Reference[2-17]

Fig.2.14 shows the equivalent circuit for the copper loss of a PMSM. where for the three-phase case, the current and EMF are given by

$$i_j(t) = \sum_{k=1}^{\infty} I_k \sin \left[k \left\{ \omega_e t + \frac{2\pi}{3} (j-1) \right\} + \alpha_k \right] \dots\dots\dots (2.46)$$

$$e_j(t) = \sum_{k=1}^{\infty} E_k \sin \left[v \left\{ \omega_e t + \frac{2\pi}{3} (j-1) \right\} + \beta_k \right] \dots\dots\dots (2.47)$$

where I_k and E_v are the Fourier coefficients, and α_k and β_v at each order are the phase differences. In this circuit, it is assumed that constant power is consumed by the load (voltage source). The copper loss is minimum when the waveforms of the current is the same as that of EMF. Therefore, the following equation is valid.

$$\begin{cases} I_j = kE_j \\ \beta_j = \alpha_j \end{cases} \dots\dots\dots (2.48)$$

This is the case when the total power factor is 1. In this method, magnetic saturation is also ignored. Therefore, current waveform optimization based on the principle of superposition of frequency components is effective, as in this method.

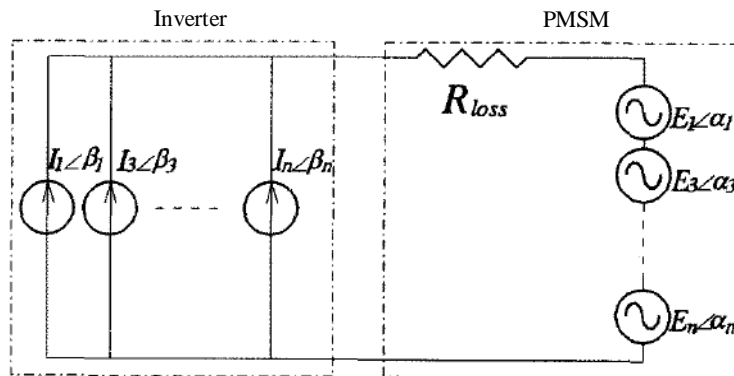


Fig. 2.14 PMSM model about copper loss(Adapted from [2-17] Takeshi Chigiri, Takeshi Shimada, Tadaaki Watanabe, Osamu Ichinokura, Toshimasa Jinzenji: “Current control method for zero torque ripple and maximum efficiency of brushless dc motor” , IEEJ Journal Industry Applications, vol. 116, no. 12, pp. 1276-1282 (1996) (in Japanese))

2.3.7 Optimal Pulse Pattern[2-18]-[2-29]

In order to optimize the pulse pattern, an evaluation function is needed. In many cases, the current THD or voltage THD is often employed as the evaluation function.

Fig.2.15 shows a typical voltage waveform having only a few switching transitions in each cycle. $\alpha_1, \alpha_2, \dots, \alpha_N$ are the switching angles for Nth switching. Each switching timing is optimized in order to minimize the evaluation function of loss. Total harmonic distortion (THD) is commonly used as the evaluation function. In general, THD based on the current waveform and THD based on the voltage waveform are adopted. In both cases, THD is an evaluation function for reducing current harmonics.

The THD based on the current [2-19]-[2-25] is expressed as follows

$$I_{THD} = \sqrt{\frac{I_{RMS}^2 - I_1^2}{I_1^2}} = \sqrt{\frac{\sum_{n=6k \pm 1} I_n^2}{I_1^2}} \quad k = 1, 2, 3, \dots \dots \dots (2.43)$$

where I_{RMS} is the RMS line current, I_1 is RMS fundamental line current, and I_n is the n-th order harmonic RMS current. This implies the current RMS value I_{RMS} for the current fundamental I_1 . Therefore, by adopting this THD as an evaluation function and optimizing the pulse pattern, the copper loss is minimized for the fundamental amplitude I_1 .

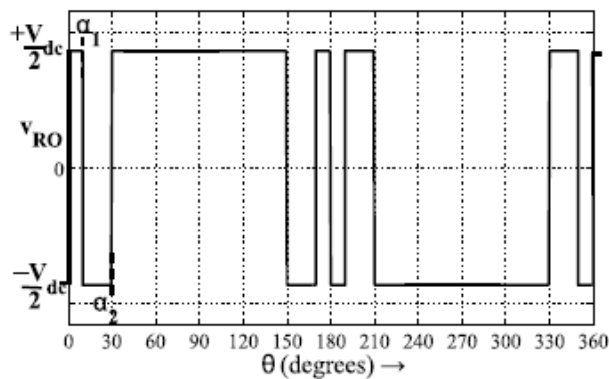


Fig. 2.15 Illustration of voltages of low pulse number (Adapted from [2-18] A, Tripathi and G. Narayanan: “Investigations on Optimal Pulse-Width Modulation to Minimize Total Harmonic Distortion in the Line Current”, IEEE Transactions on Industry Applications, Vol. 53, No.1, pp1-pp10 (2017))

On the other hand, the THD based on the voltage waveform can also be used as an evaluation function. This is because the current waveform changes in a complicated manner depending on the motor constant, speed, and other conditions. By using the voltage-based THD, THD is formulated directly as a function of switching timing. The evaluation function of THD based on voltage waveform [2-18],[2-26]-[2-29] can be expressed as follows

$$V_{WTHD} = \sqrt{\frac{\sum_{n=6k\pm 1} V_n^2/n^2}{V_1^2}} \quad k = 1, 2, 3, \dots \dots \dots (2.44)$$

where, V_1 is the peak fundamental voltage and V_n is the peak n^{th} harmonic voltage. where V_1 is the voltage fundamental and V_n is the n th order voltage harmonics. This is commonly referred to as weighted THD. In this case, V_n can be expressed by the following equation from Fourier analysis

$$V_n = \left(\frac{2V_{dc}}{n\pi} \right) \left\{ 1 + \sum_{i=1}^N (-1)^i 2 \cos(n\alpha_i) \right\} \dots \dots \dots (2.45)$$

where V_{dc} is the DC bus voltage; $\alpha_1, \alpha_2, \dots, \alpha_N$ are the N switching angles in a quarter cycle. This is based on the idea that higher-order voltage harmonics have little effect on the RMS value of current in a motor with an integrating element such as inductance.

Fig.2.16 shows experimental comparison of optimal PWM and Sin-Triangle PWM in terms of (a) V_{WTHD} (b) I_{THD} and (c) no-load P_{Loss} . Note that the optimal PWM is introduced by minimizing the evaluation function V_{WTHD} . As can be seen from the figure, the optimal PWM with the minimum weighted voltage THD reduces the weighted THD significantly more than the sin-triangle PWM. As a result, the current THD is also reduced. And, thanks to the reduction in current THD, losses are also reduced. Note that these results were obtained at a very low fundamental frequency of 45 Hz. Therefore, copper loss is considered to be the dominant loss. As a result, the reduction of copper loss is considered to have a significant effect on the improvement of loss.

In before results, the loss is reduced with optimal pulse pattern. However, the fundamental frequency is very low. In other words, it seems that iron loss is hardly included in the loss. All of the methods focus only on reducing copper loss, and do not consider iron loss. The iron loss increases as the drive frequency increases. In particular, it accounts for a large percentage of the total loss at high speeds. Therefore, these methods will be problematic at high speeds.

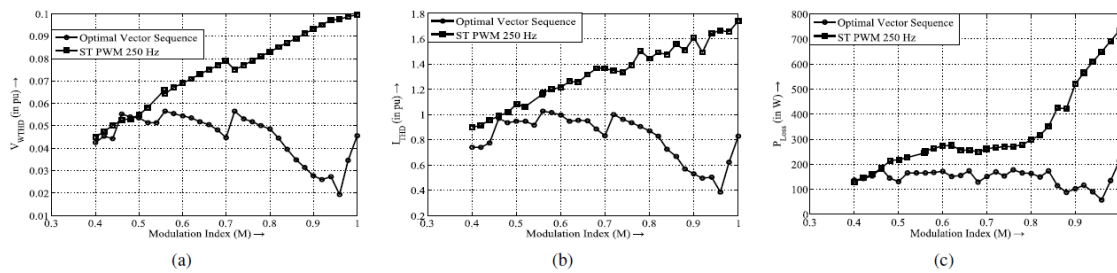


Fig. 2.16. Experimental comparison of optimal PWM and Sine-Triangle PWM in terms of (a) V_{WTHD} (b) I_{THD} and (c) no-load P_{Loss} . Note that the fundamental frequency is 45Hz. (Adapted from [2-18] A, Tripathi and G. Narayanan: “Investigations on Optimal Pulse-Width Modulation to Minimize Total Harmonic Distortion in the Line Current”, IEEE Transactions on Industry Applications, Vol. 53, No.1, pp1-pp10 (2017))

2.4 Proposed Efficiency Improvement Method based on B-H Trajectory Behavior Model

In the previous section, the problems of the high efficiency method based on the linear model due to the non-linearity of the magnetic saturation and the iron loss are confirmed. In this section, the solution of these problems and improvement method of the motor efficiency are explained.

Fig.2.17 shows the proposed B-H trajectory behavior model and the details of each proposed method using the model. It has been a problem how to handle the magnetic saturation and the iron loss of the materials. Therefore, the B-H trajectory behavior model which considers both the magnetic saturation and the iron loss is introduced. The B-H trajectory behavior model shown in the Fig.2.17 consists of a group of the measured major loops with the different magnetic flux density amplitudes. The B-H trajectory behavior model has the individual characteristics depending on the material (depending on not only the material type but also the processing method). This is the core of each proposed method.

2.4.1 Proposed Automatic Design considering Magnetic Saturation for Efficient Motor

The proposed method for automatic design method considering the magnetic saturation is described. The proposed automatic design method is based on the permeance method as before. However, the influence of the magnetic saturation is considered in the permeance method. In general, since the motor has an air gap, the loss (area in hysteresis loop) of the material has a small effect on the field. Therefore, first, the B-H trajectory model is approximated by setting the area (loss) in the above B-H trajectory model to zero, which is easy to handle. Next, the B-H trajectory model is approximated by dividing the non-saturated region and the saturated region

and approximating them so that the model is easily applied into the permeance method. Finally, this B-H trajectory model is applied into the permeance method in order to introduce the variable magnetoresistance into the automatic design. Thanks to the variable magnetoresistance, the automatic design considering the magnetic saturation is achieved. A new contribution is the simple design of the efficient motors considering the magnetic saturation, i.e. effectively utilizing the magnetic properties of the iron core. This automatic design method is realized by utilizing the variable reluctance approximately derived from the B-H trajectory behavior model.

2.4.2 Proposed High Accuracy Iron Loss Calculation with FEM for Efficient Motor

The proposed method for calculating the iron loss with high accuracy using FEM analysis is described. In the proposed method, the arbitrary hysteresis loops are represented by multiplying the several hysteron with the different widths by a shape function. The hysteresis loss is calculated from the area of the represented hysteresis loops in order to reproduce the characteristics such as DC superposition. In particular, the ring core was made with the same material and processing method used in the motor. In addition, the B-H trajectory model was measured and created based on the characteristics measured by the ring core. This enables extremely the accurate iron loss analysis considering the degradation of the processing. A new contribution is the detailed design of the efficient motors by accurate FEM analysis without the pre-evaluation using the prototype motors. This detailed design is realized by utilizing the implemented B-H trajectory behavior model in the FEM simulator.

2.4.3 Proposed Optimal Pulse Pattern of Iron Loss Reduction for Efficient Motor

The proposed optimal pulse pattern in order to reduce the iron loss is described. In particular, the evaluation function of the iron loss when the pulse pattern is applied is important in this method. The evaluation function of the iron loss is derived from the relationship between the maximum flux density amplitude and the iron loss (area), which is calculated from the B-H trajectory model. In addition, it is focused that the fact that the line voltage of the synchronous PWM is unipolar at half cycle and no minor loop is generated. Then, the iron loss is evaluated from the maximum magnetic flux density amplitude, which is calculated from the time integral of the voltage. Therefore the evaluation of the THD of the voltage and current is not needed. The method makes it possible to derive the easy and highly accurate evaluation function for the iron loss. A new contribution is the efficient driving by the optimum pulse pattern derived from the principle of the iron loss generation. This pulse pattern is derived to minimize the area (iron loss) in the B-H trajectory behavior model.

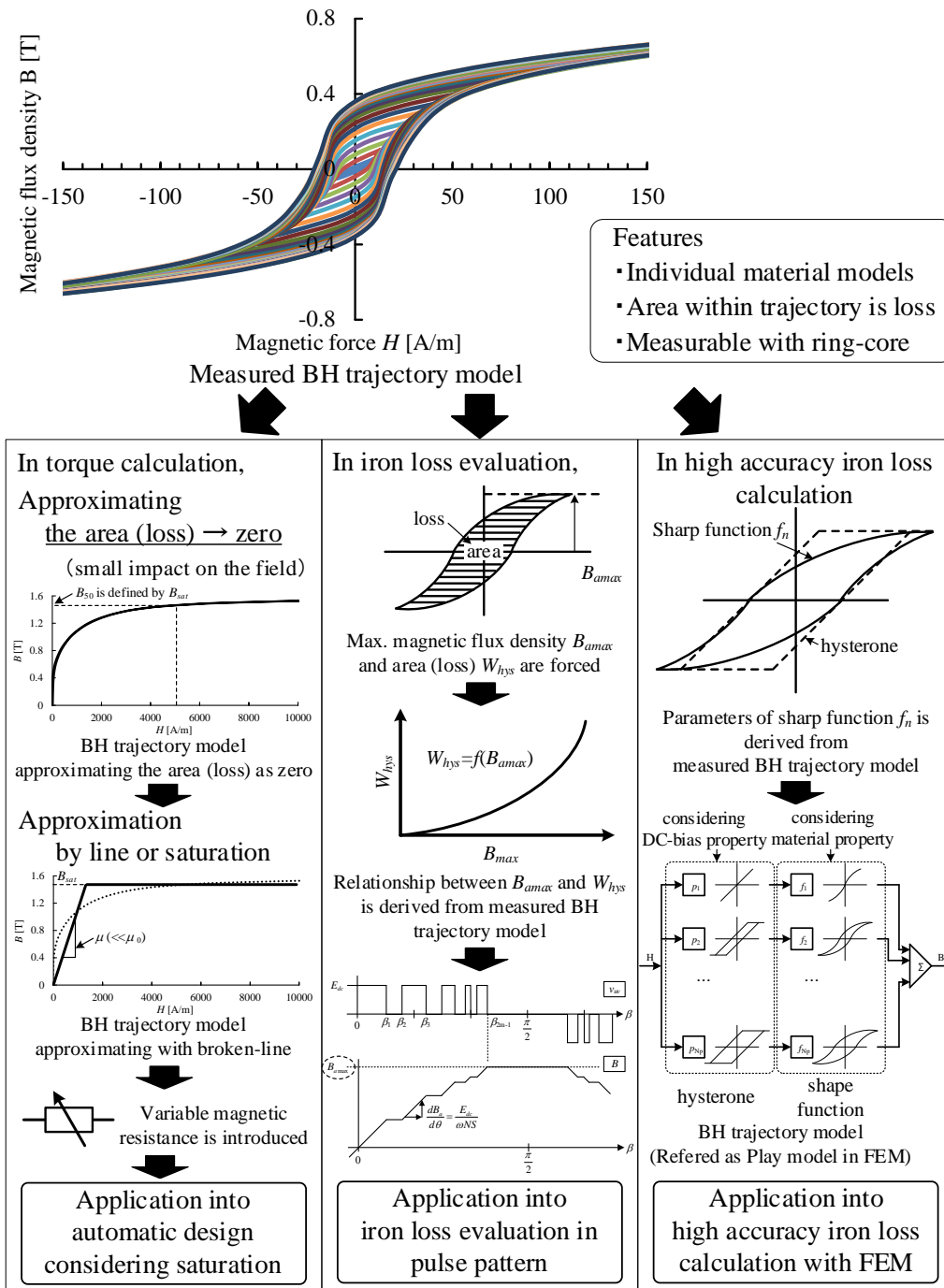


Fig.2.17 The proposed B-H trajectory model and the details of each proposed method using it as the core

Fig.2.18 shows a comparison between the efficiency improvement based on the conventional model with linearity and the proposed B-H trajectory behavior model. Conventional methods applied the technique of Fourier analysis to hysteresis loss. However, the principle of the superposition does not hold for hysteresis loss. As a result, there were errors between the model and the real. In addition, the magnetic saturation was not considered in the motor design. Therefore, there was a limit to its application. In the proposed method, the hysteresis loss is calculated as the area of the B-H trajectory. In the proposed method, the hysteresis loss is calculated as the area of the B-H trajectory. Therefore, there is no error between the model and the real. In addition, the variable magnetoresistance is introduced in the motor design. Therefore, the magnetic saturation is considered. As a result, the proposed method is applied into the SRM which has the saturation characteristic.

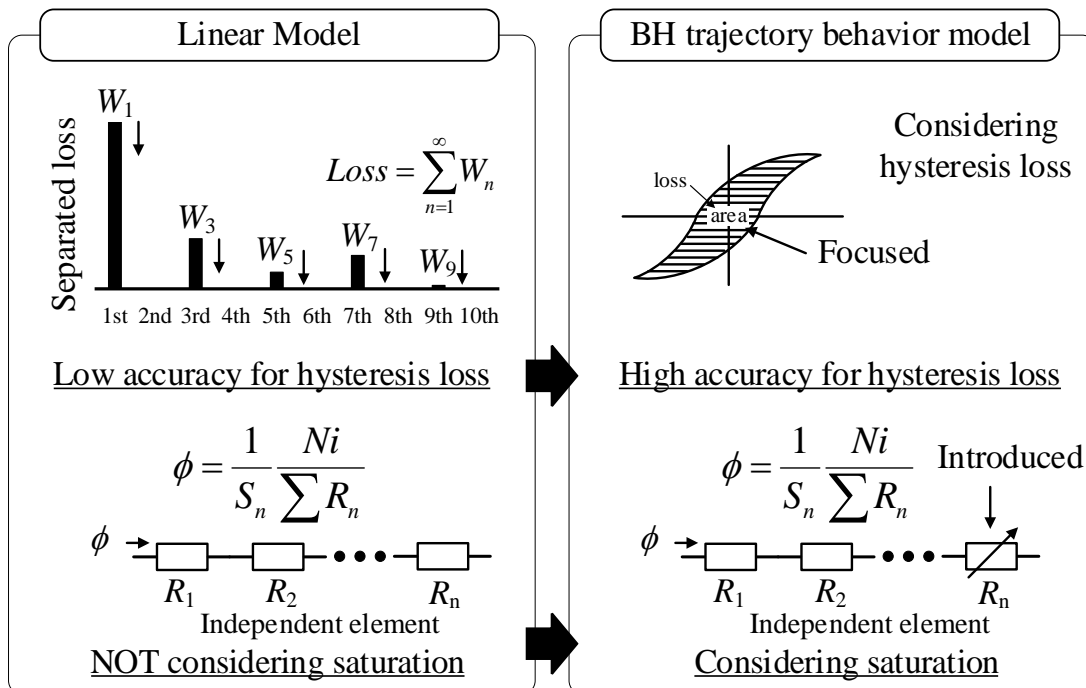


Fig.2.18 Comparison between the high efficiency based on the conventional model with linearity and the proposed B-H trajectory behavior model

2.4.4 Beneficial Position of Proposed Strategies based on B-H Trajectory Behavior Model

Fig.2.22 shows the benefit position of the proposed method. The conventional linear model method for increasing the efficiency is inaccurate mainly due to the iron loss and the magnetic saturation. In other words, the expected efficiency improvement results may not be obtained. In addition, the efficiency improvement method that compensates the linear model with correction coefficients such as the BF value requires the many processes such as the evaluation of actual equipment in order to determine the accurate correction coefficients. On the other hand, in the proposed method, the iron loss and the magnetic saturation is considered only from the B-H trajectory behavior model. Therefore, both user-friendliness and accuracy are achieved.

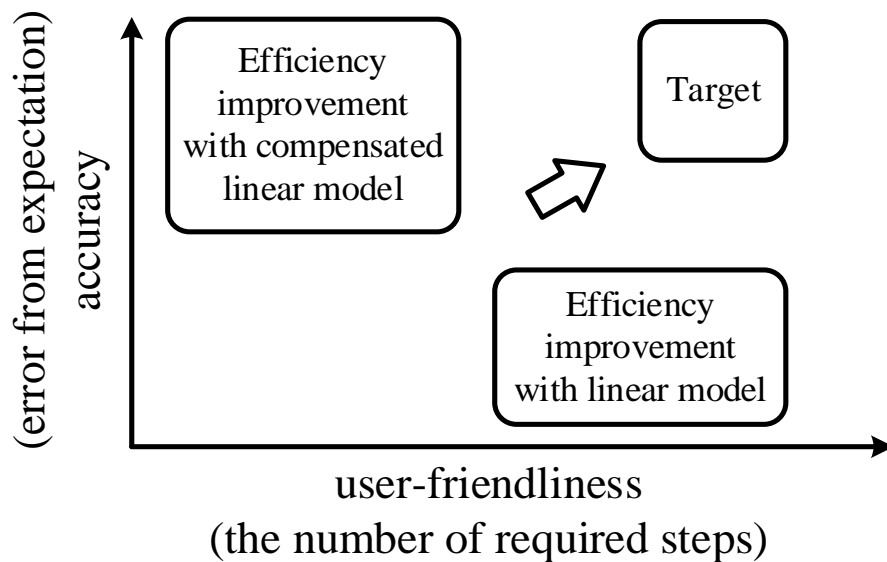


Fig.2.19 The benefit position of the proposed method

2.5 Conclusion

This chapter described the efficiency improvement in synchronous motors with concentrated stator windings based on B-H trajectory behavior model. This chapter began with a basic explanation of torque and loss, which affect the efficiency of motors. It also explained the conventional linear model-based efficiency improvement technology based on the explained torque and loss fundamentals. After that, the problems in handling magnetic saturation and iron loss based on the linear model were explained in detail. The proposed B-H trajectory behavior model estimates and calculates the torque under magnetic saturation, where linearity is lost, and the hysteresis loss, where frequency superposition is not valid, by considering the material properties in detail. Finally, a comparison was conducted between the conventional high efficiency technology based on the linear model and the proposed high efficiency technology based on the B-H trajectory model to show the position of this paper.

Bibliography

- [2-1] M. Morimoto, Y. Takeda, N. Matsui, K. Ohyama, S. Morimoto, Y. Honda, H. Dohmeki, and T. Kosaka: Reluctance Torque Assisted Motors, p171-173, The Institute of Electrical Engineers of Japan (2016) (in Japanese)
- [2-2] JSOL Official site, <https://www.jmag-international.com/jp/>
- [2-3] T. Yamada, K. Akatsu: “Automatic Design Method Considering the Frequently Used Area of a PMSM for an HEV”, ICEMS, pp1-6. (2012)
- [2-4] K. Akatsu, S. Wakui, and M. Arimitsu: “Automatic Design Method for PM Motor which satisfies the Output NT Requirements”, IEEJ Journal Industry Applications, vol. 124, no. 9, pp. 946-955 (2004) (in Japanese)
- [2-5] N. Kariya and K. Akatsu: “Automatic Design Method for PMSM”, ppY-76, (2014)
- [2-6] Kenji Nakamura and Osamu Ichinokura: “Reluctance Network Based Dynamic Analysis in Power Magnetics2, IEEJ Transactions on Fundamentals and Materials, Vol. 128, No.8 pp.506-510(2008)
- [2-7] K. Nakamura, K. Kimura, O. Ichinokura:” Simple Magnetic Circuit Model of Switched Reluctance Motor Considering Magnetic Saturation”, Vol.28 No.4 pp.602-606(2004)
- [2-8] O. Ichinokura, K. Tajima, K. Nakamura, and Y. Yoshida: Dynamic analysis of electric motor using magnetic circuit model, p185, Kagakujiyoho shuppan Co., Ltd. (2016) (in Japanese)
- [2-9] K. Yamazaki, Y. Haruishi, and T. Ara: “Harmonic torque calculation of induction motors using electromagnetic field analysis”, IEEJ-Trans. IA, Vol.124, No.11, pp.1155–1163 (2004-11) (in Japanese)
- [2-10] K. Yamazaki, Y. Seto, and M. Tanida: “Iron loss analysis of IPM motor considering carrier harmonics”, IEEJ-Trans. IA, Vol.125, No.7, pp.758–766 (2005-7) (in Japanese)
- [2-11] K. Yamazaki and Y. Abe: “Loss Analysis of Induction Motors Considering Carrier Harmonics of PWM Inverters”, IEEJ Journal of Industry Applications, Vol.126, No.4 pp.404-412 (2006)

- [2-12] K. Yamazaki and T. Abe: “Loss Analysis of IPM Motors Considering Carrier Harmonics -Calculation of Eddy Current Loss in Permanent Magnet Using 3-D Finite Element Method-”, IEEJ Journal Industry Applications, vol. 127, no. 1, pp. 87-94 (2007) (in Japanese)
- [2-13] K. Yamazaki: “Loss Calculation of Induction Motors Considering Harmonic Electromagnetic Fields in Stator and Rotor”, IEEJ Journal Industry Applications, vol. 123, no. 4, pp. 392-400 (2003) (in Japanese)
- [2-14] T. Kakishima, K. Kiyota, H. Sugimoto, A. Chiba: “Reduction of Iron Loss Error between Full Load Test and Simulation of a 60 kW SRM for HEV”, IEE-Japan Industry Applications Society Conference, Y102 (2013)
- [2-15] Takanori Suzuki, Shinya Ito, Naoki Tanaka, Akira Chiba, Tadashi Fukao, Hironori Ninomiya: “Development of High Efficiency Switched Reluctance Motor”, IEEJ Journal Industry Applications, vol. 126, no. 4, pp. 511-518 (2006) (in Japanese)
- [2-16] K. Yamazaki, S. Ohki, A. Nezu, T. Ikemi: “Development of Interior Permanent Magnet Motors Reducing Harmonic Iron Losses under Field Weakening Control”, IEEJ Journal Industry Applications, vol. 127, no. 8, pp. 837-843 (2007) (in Japanese)
- [2-17] Takeshi Chigiri, Takeshi Shimada, Tadaaki Watanabe, Osamu Ichinokura, Toshimasa Jinzenji: “Current control method for zero torque ripple and maximum efficiency of brushless dc motor” , IEEJ Journal Industry Applications, vol. 116, no. 12, pp. 1276-1282 (1996) (in Japanese)
- [2-18] A. Tripathi and G. Narayanan: “Investigations on Optimal Pulse-Width Modulation to Minimize Total Harmonic Distortion in the Line Current”, IEEE Transactions on Industry Applications, Vol. 53, No.1, pp1-pp10 (2017)
- [2-19] L. Liyi, G. Tan, J. Liu, and B. Kou, “An optimal pulse width modulation method for high-speed permanent magnet synchronous motor,” in Proc. IEEE Intl. Conf. on Inf. Science and Tech., 2013, Mar 2013, pp. 237–244.

- [2-20] W. Yongqing, Q. Mingzhong, and Z. Xiaofeng, "Optimized control scheme of hybrid inverters in high power drives," in Proc. IEEE Pow. Engg. And Auto. Conf. (PEAM), Sept 2012, pp. 1–4.
- [2-21] A. Tripathi and G. Narayanan, "Investigations on optimal pulse-width modulation to minimize total harmonic distortion in the line current," in Proc. IEEE India Int. Conf. on Pow. Electron. (IICPE), 2014, pp. 1–6.
- [2-22] N. Yosefpoor, S. Fathi, N. Farokhina, and A. Abyaneh, "Thd minimization applied directly on the line-to-line voltage of multilevel inverters," IEEE Trans. Ind. Electron., vol. 59, no. 1, pp. 373–380, Jan 2008.
- [2-23] A. Tripathi and G. Narayanan, "Optimal pulse width modulation of voltage-source inverter fed motor drives with relaxation of quarter wave symmetry condition," in Proc. IEEE Intl. Conf. Electron., Comp. and Comm. Technology (CONECCT), 2014, Jan 2014, pp. 1–6.
- [2-24] G. Buja and G. Indri, "Optimal pulse-width modulation for feeding ac motors," IEEE Trans. Ind. Appl., vol. IA-13, no. 1, pp. 38–44, Jan/Feb 1977.
- [2-24] G. Buja and G. Indri, "Optimal pulse-width modulation for feeding ac motors," IEEE Trans. Ind. Appl., vol. IA-13, no. 1, pp. 38–44, Jan/Feb 1977.
- [2-25] F. Zach and H. Ertl, "Efficiency optimal control for ac drives with pwm inverters," IEEE Trans. Ind. Appl., vol. IA-21, no. 4, pp. 987–1000, Jul/Aug 1985.
- [2-26] A. Tripathi and G. Narayanan, "Investigations on optimal pulse-width modulation to minimize total harmonic distortion in the line current," in Proc. IEEE India Int. Conf. on Pow. Electron. (IICPE), 2014, pp. 1–6.
- [2-27] A. Tripathi and G. Narayanan, "Optimal pulse width modulation of voltage-source inverter fed motor drives with relaxation of quarter wave symmetry condition," in Proc. IEEE Intl. Conf. Electron., Comp. and Comm. Technology (CONECCT), 2014, Jan 2014, pp. 1–6.
- [2-28] D. Holmes and T. Lipo, Pulse width modulation for power converters: principles and practice. John Wiley & Sons, 2003.

- [2-29] W. Chen, H. Sun, X. Gu, and C. Xia, “Synchronized space-vector pwm for three-level vsi with lower harmonic distortion and switching frequency,” *IEEE Trans. Pow. Electron.*, vol. 31, no. 9, pp. 6428–6441, Sept 2016.

Chapter 3

Automatic design considering magnetic saturation of SRM for high efficiency motor

3.1 Introduction

This chapter describes an automatic design method for high-efficiency motors with the consideration of the magnetic saturation using the B-H trajectory behavior model. First, the geometrical parameters and the input constants of the automatic design of the high-efficiency motor are explained. Next, the procedure to apply the proposed B-H trajectory behavior model into the permeance method is explained. Then, the torque and the loss are formulated as functions of the shape parameters based on the proposed permeance method. The organization of the derived theoretical equations of the torque and the loss leads to an automatic design based on the optimization of the rotor diameter as a flexibility. In addition, the effect of the magnetic saturation considered from the B-H trajectory behavior model is discussed. In order to confirm the consideration of the material characteristics in the proposed method, the several design examples are presented using the three materials with the high/middle/low saturation magnetic flux densities.

3.2 Proposed Automatic Design Method of Typical Parameters of a Switched Reluctance Motor

Fig.3.1 shows an example of the speed-torque characteristic (N-T characteristic). In this study, the design method of the motor satisfying the required N-T characteristics is proposed. The N-T characteristics required from the user are determined by the rated output P_{out} , the maximum speed ω_{max} , and the base speed ω_{base} . The maximum torque $T_{max}(=P_{out}/\omega_{base})$ and the torque at maximum speed $T_{\omega_{max}}(=P_{out}/\omega_{max})$ are uniquely determined from these required parameters.

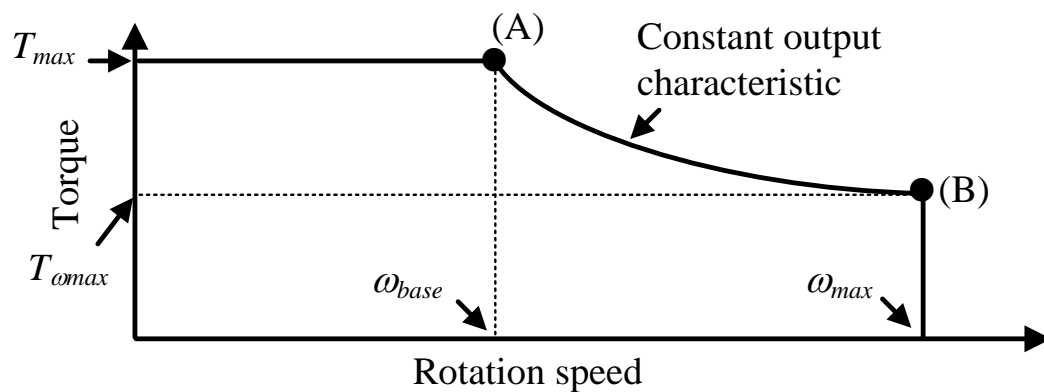


Fig. 3.1. Output N-T characteristics

Fig.3.2 shows the geometry of the SRM assumed in this paper. This paper designs the number of phases m , the number of the stator teeth N_s , the number of the rotor teeth N_r , the rotor diameters D_r , the stator diameters D_s , the thickness L_h , and the number of turns N of the SRM satisfying the required N-T characteristics. The air gap length l_g is treated as a constant because it is determined by the structural constraint. The pole widths of the stator t_s and rotor t_r , which are details of the motor shape, are determined from the respective pole arc angles β_s and β . These parameters are determined from the design range of Corda's triangle [3-1]. The back yoke width y_s , the rotor slot depth d_r , and the shaft diameter r_{sh} are also determined based on the literature [3-1] in order to avoid the extreme magnetic saturation. These details of the motor shape also have some effect on the motor volume. However, when these details are determined at the same time as the determination of the motor size, the design period is prolonged due to the complication of the design flow. Therefore, in this paper, the values introduced as the recommended values in the literature [3-1] and [3-2] are adopted.

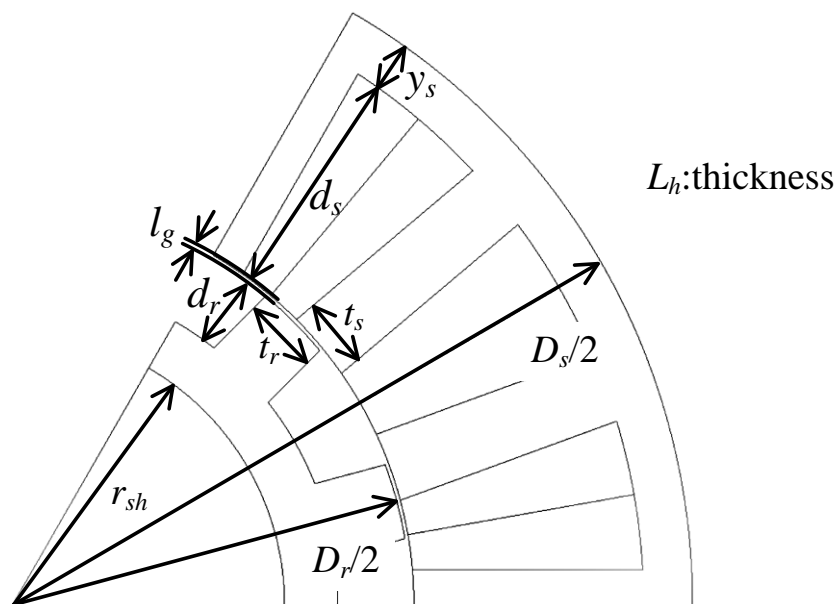


Fig. 3.2. Dimensions of SRM

Fig.3.3 shows the inductance distribution, the torque characteristics, and the current waveforms at each operating point of the SRM. In this paper, the trapezoidal wave driving, which is excellent for torque control, is used when the rotation speed is below ω_{base} . In addition, the single pulse driving, which maximizes the use of DC voltage, is used when the rotation speed is above ω_{base} . The trapezoidal wave driving is a method to control the current wave height to a constant value. It is necessary to determine the current amplitude I_{max} , the applied voltage start angle θ_{on} , and the commutation angle θ_c . The

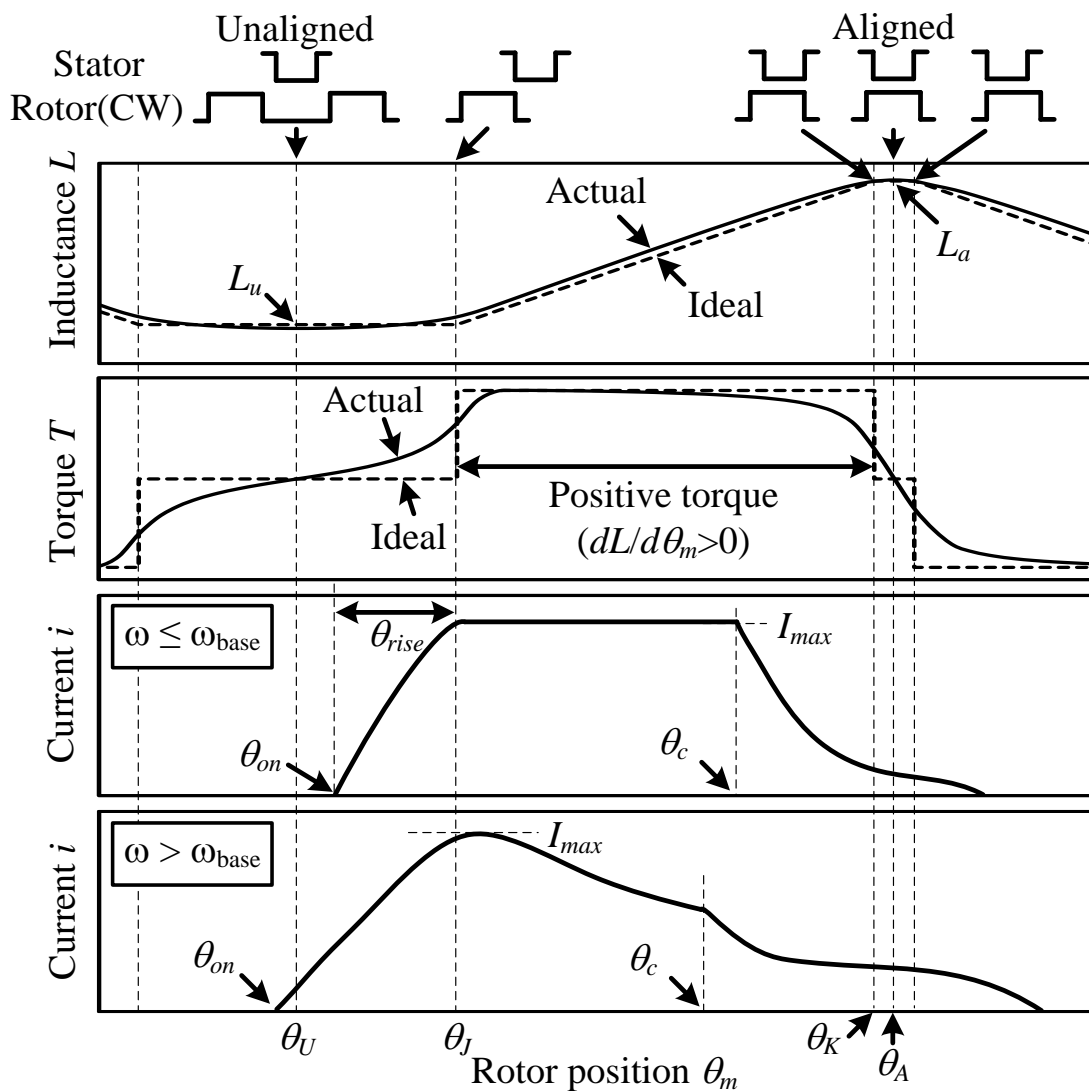
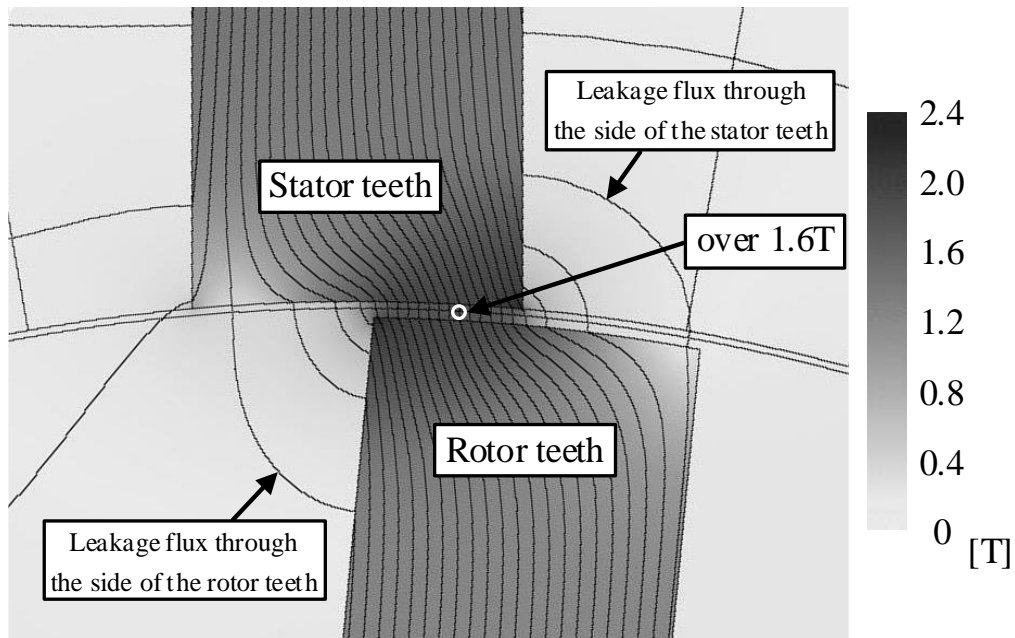


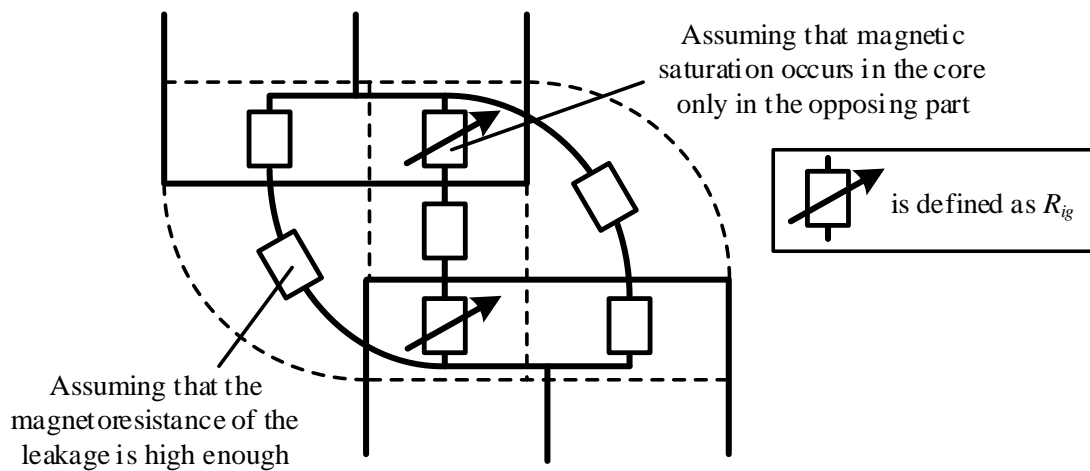
Fig. 3.3. Inductance distribution, torque characteristic generated when a constant current is applied, and current waveforms at each operating point (Actual: including fringing, Ideal: excluding fringing)

current amplitude I_{max} is determined in order to satisfy the required N-T characteristics and to minimize the current amplitude. On the other hand, dwell = $\theta_c - \theta_{on}$ is kept to a constant for θ_c and θ_{on} , and only θ_{on} is adjusted for simplicity.

Fig.3.4(a) shows the contour plot of the magnetic flux density distribution and the flux lines, whereas Fig.3.4(b) shows the magnetic circuit model considering the local saturation of the pole-tips. In this paper, in order to simplify the derivation of the torque equation, the leakage flux flowing on the side of the teeth shown in the Fig. 3.4(a) is ignored. The magnetoresistance of the core is also ignored until the magnetic saturation occurs. In general, the local magnetic saturation occurs at the tip of the pole since the magnetic flux density becomes high at the aligned part of the stator pole and the rotor pole [3-5]. Therefore, the saturation magnetic flux density is assumed to be reached only at the aligned part in the core.



(a) Contour plots and flux lines of SRM



(b) Magnetic circuit model considering local saturation of the pole-tips

Fig. 3.4. Contour plots and flux lines of SRM and the magnetic circuit model considering the local saturation of the pole-tips

Fig.3.5 shows the design algorithm that satisfies the required N-T characteristics considering the magnetic saturation. In the proposed design algorithm, the rotor diameter D_r is determined as a flexibility in order to downsize the motor. On the other hand, the other motor dimensions are determined from the input constants. In this study, the input constants are the rated output P_{out} , the maximum speed ω_{max} , the base speed ω_{base} , the supply voltage V_{dc} , the magnetic saturation level α_{sat} , the maximum allowable electric frequency f_{e_max} , the maximum allowable current density J_{rms_max} , the maximum allowable copper W_{c_max} , the winding occupancy in the slot k_s , and the saturation flux density B_{sat} . The motor dimensions are derived from the following input constants and the optimization conditions, respectively, in the sections of this chapter.

Section 3.2.1

Decision parameters: Number of phases m ,
 number of status lots N_s ,
 number of rotor teeth N_r

Constants: operating point (B) of Fig.3.1,
 allowable maximum electric frequency f_{e_max}

Section 3.2.2

Decision parameters: Stack thickness L_h

Constants: operating point (A) of Fig.3.1,
 magnetic saturation level α_{sat}

Section 3.2.3

Decision parameters: Stator diameter D_s

Constants: operating point (A) of Fig.3.1,
 allowable maximum current density J_{rms_max} ,
 allowable maximum copper loss W_{c_max} ,
 winding occupancy in slot k_s

Section 3.2.4

Decision parameters: Number of turns N

Constants: operating point (A) or operating point (B) of Fig.3.1,
supply voltage V_{dc}

Section 3.2.5

Decision parameters: Rotor diameter D_r

Optimization condition: Volume minimization

In addition, α_{Tmax} , α_{max} , and α_{RMS} are the adjustment parameters by FEM and permeance analysis in order to satisfy the required N-T characteristics, the allowable maximum current density, and the allowable maximum copper loss.

These parameters are adjusted in the following flow: first, the simulation model is created based on the tentatively determined α_{Tmax} , α_{max} , and α_{RMS} , next, the average torque T_{max_ave} and current I_{RMS_sim} at operating point (A) and the average torque $T_{\omega max_ave}$ at operating point (B) are analyzed, finally, α_{Tmax} , α_{max} , and α_{RMS} are updated based on these analyzed value. The details of how to set the control variables for the analysis are described in Section 3.2.6.

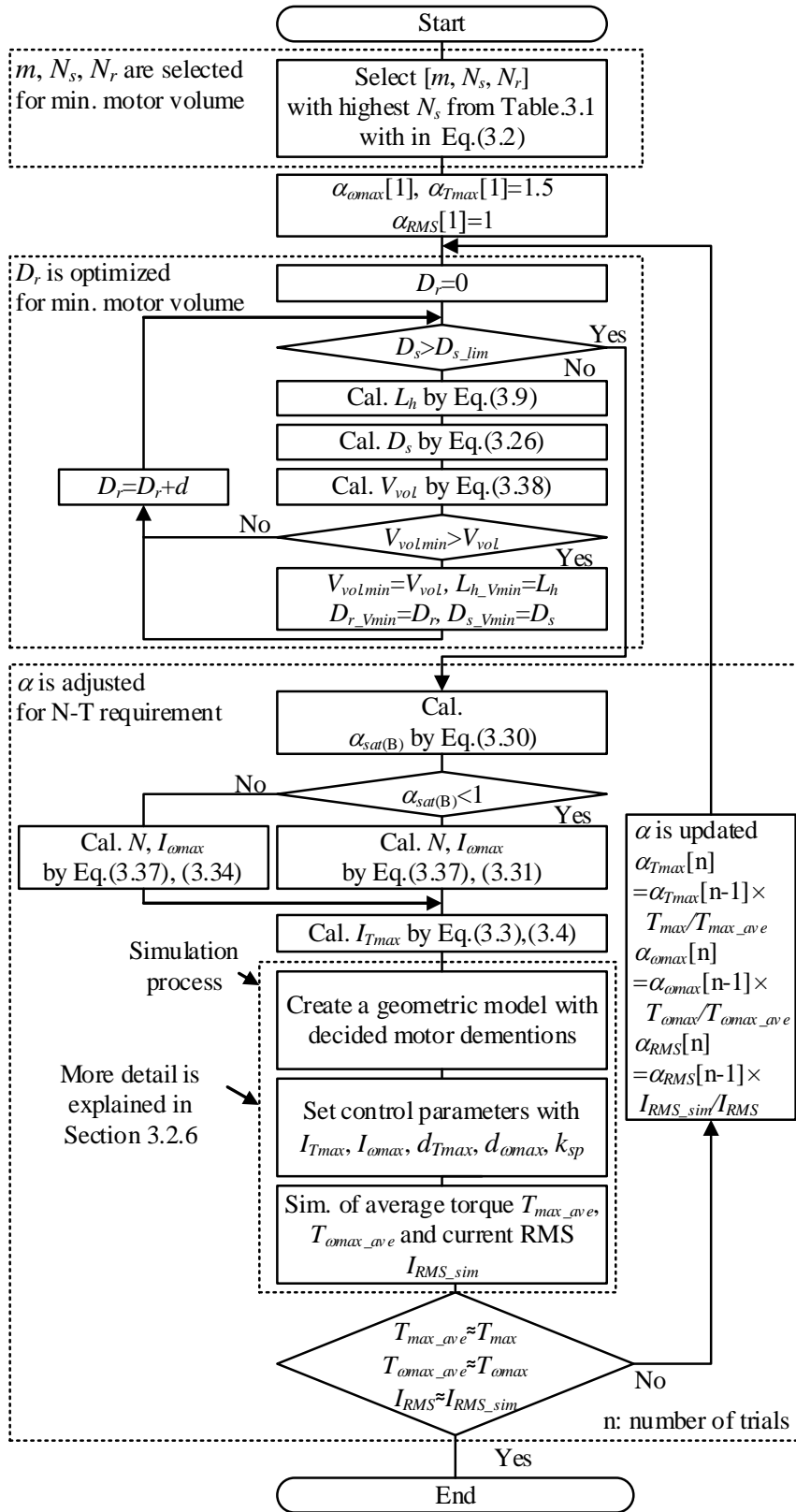


Fig. 3.5. Proposed design flow of SRM.

3.2.1 Decision method of number of phases m , number of stator teeth N_s , number of rotor teeth N_r

This section describes the design method for the combination of the number of phases m and the number of status lots N_s /the number of rotor teeth N_r . In general, the selection of higher N_s leads to the miniaturization of the motor volume thanks to the reduction of the stator yoke thickness and the coil-end length [3-6]. Therefore, the combination of m and N_s/N_r in order to maximize N_s is selected within the range where the electric frequency f_e at the maximum rotation speed ω_{max} does not exceed the allowable maximum electric frequency f_{e_max} . The allowable maximum electric frequency is determined by the processing speed of the controller and the switching frequency.

Table 3.1 shows the common combinations of the number of phases and poles and examples of their applications. Those with a low number of poles are used for from the low to the medium capacity applications. On the other hand, those with a large number of poles are used for from the medium to the large capacity applications. It is reported that the inductance ratio λ (the ratio of the aligned inductance to the unaligned inductance) deteriorates from the 3-phase 18/12 and the 4-phase 16/12 types [3-1].

Table 3.1. Combinations of phase-numbers and pole-numbers

| | m | N_s | N_r | λ [3-1] | Example of application |
|---|--------|-------|-------|-----------------|-------------------------------|
| Selection of highest N_s within eq.(3.2) | 3 | 6 | 4 | High | supercharger[3-7] |
| | 4 | 8 | 6 | High | servo[3-8] |
| | 3 | 12 | 8 | High | pump[3-9] |
| | 4 | 16 | 12 | Low | unmanned aerial vehicle[3-10] |
| | 3 | 18 | 12 | Low | electric vehicle[3-11] |
| Not covered | Higher | | Lower | | electric vehicle[3-12] |

λ : inductance ratio = unsaturated aligned inductance / unaligned inductance

The electrical frequency at the maximum speed ω_{max} is expressed by Eq.(3.1).

$$f_e = \frac{\omega_{max}}{2\pi} N_r \dots\dots\dots (3.1)$$

where the maximum electrical frequency f_e has to be less than or equal to the allowable maximum electrical frequency f_{e_max} . Solving for $f_{max} \leq f_{e_max}$, the constant for the number of the rotor teeth N_r is obtained as Eq.(3.2).

$$N_r \leq \frac{2\pi f_{e_max}}{\omega_{max}} \dots\dots\dots (3.2)$$

As long as the above condition is satisfied, any combination of the number of phases and poles shown in Table 3.1 can be used in order to control the SRM. Although the larger number of the stator teeth N_s leads the smaller volume, the magnetic flux flowing through the sides of the teeth becomes large, which increases the unaligned inductance L_u . The increase of L_u prolongs the period required to raise the actual current to the current command value (θ_{rise} in Fig.3.3). In addition, the deterioration of the inductance ratio λ due to the increase of L_u leads to the decrease of torque/current ratio. In this thesis, the magnetic flux flowing into the side of the teeth is ignored for simplicity. Therefore, the optimum design including the magnetic flux flowing into the side of the teeth is impossible. In reference [3-1], it is reported that the magnetic flux flowing into the sides of the teeth is small in the SRMs with relatively low number of poles such as the 3-phase 12/8 type or less. On the other hand, it is reported that the magnetic flux flowing into the teeth side becomes larger and the inductance ratio λ worsens in the multi-pole SRMs such as the 4-phase 16/12 or the 3-phase 18/12. Therefore, as a limit of this design method ignoring the magnetic flux flowing into the teeth sides, the 3-phase 18/12 type is chosen for the SRM design in Chapter 3. As shown in Table 3.1, since the SRMs with relatively low poles are used in from the low to medium capacities, the proposed design method is targeted for the low and the medium capacity SRMs.

3.2.2 Decision method of stack thickness L_h

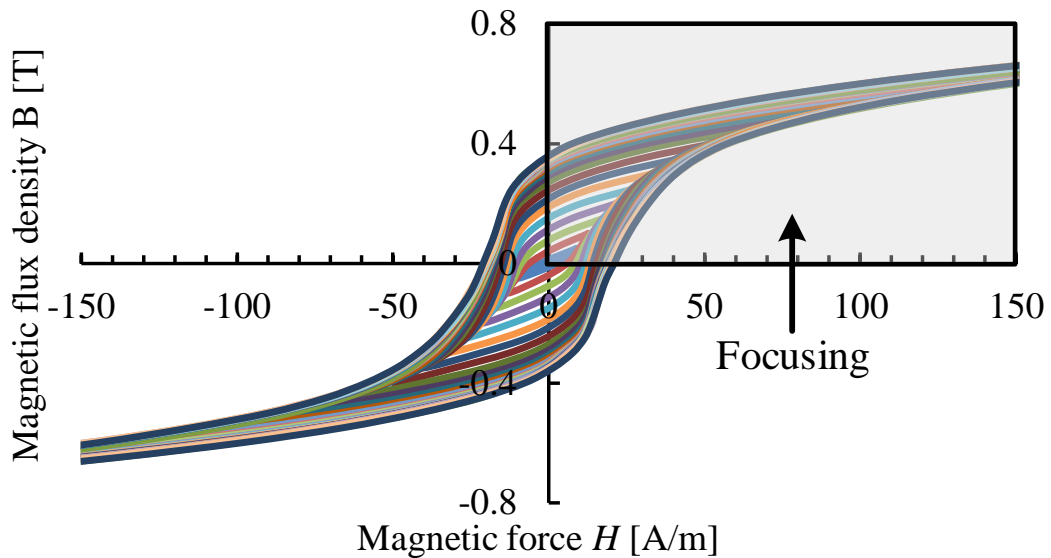
This section describes the design method of the stack thickness L_h of the motor. Since the rotor diameter D_r is given as a flexibility, L_h determines the size of the rotor, i.e., the area of the gap. L_h is derived from the operating point (A) [T_{max} , ω_{base}] in Fig.3.1 and the saturation level α_{sat} .

Fig.3.6(a) shows the B-H characteristic, whereas Fig.3.7(b) shows approximated B-H characteristic. The calculation of the magnetic flux is required to calculate the torque. The calculation is based on the magnetic circuit shown in Fig.3.4(b). Here, the magnetoresistance R_{ig} needs to be formulated, which considers the magnetic saturation shown in the fig.3.4(b). The B-H characteristic shown in Fig.3.6(a) is used to formulate the magnetoresistance R_{ig} . In the model with an air gap, the effect of losses on the field can be assumed to be small. Therefore, the area (loss) of the B-H characteristic is assumed to be zero (solid line in Fig.3.6(b)). Then, the approximated B-H characteristic is further approximated by an angular approximation in order to apply the automatic design method (dotted line in Fig.3.6(b)). In order to approximate, the current when the magnetic saturation occurs is required. The core becomes magnetically saturated when the magnetic flux density in the air gap reaches the saturation flux density B_{sat} . The saturation current I_{sat} is expressed by the Eq.(3.3) [3-1].

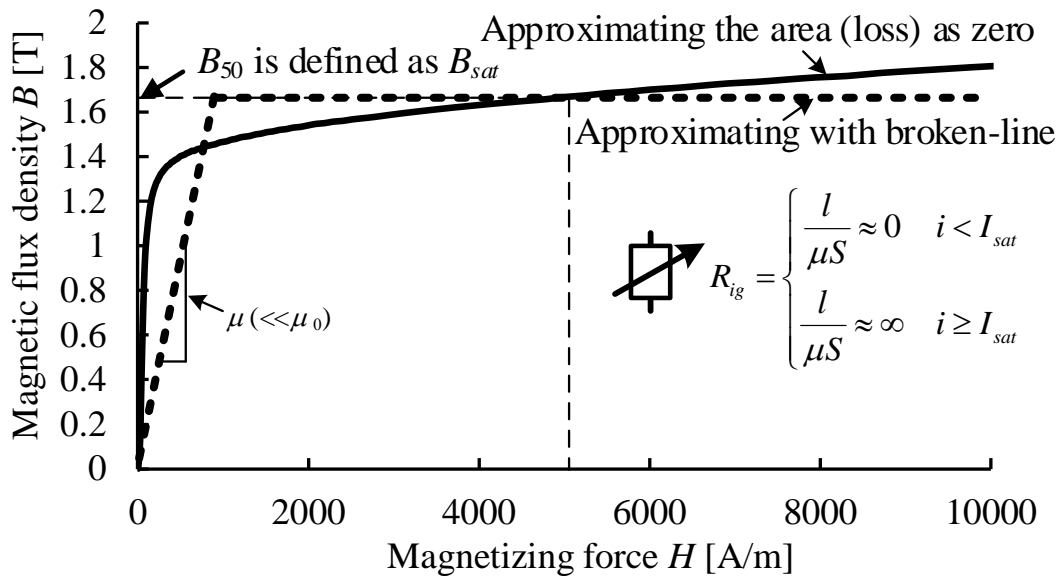
$$I_{sat} = \frac{B_{sat} l_g}{N \mu_0} \dots\dots\dots (3.3)$$

where l_g is the air gap length, N is the number of turns per teeth, and μ_0 is the vacuum permeability. As shown in the B-H characteristic of the electromagnetic steel sheet in Fig.3.6, the magnetic flux density of an electromagnetic steel sheet does not remain constant even after magnetic saturation. The saturation flux density B_{sat} cannot be uniquely determined due to the nonlinearity. This paper adopts the value of B_{50} (the magnetic flux density at a magnetizing force of 5000 A/m), which is used in the JIS standard to indicate the magnetic properties of non-directional

electromagnetic steel sheets, as B_{sat} for simplicity. Although the approximation accuracy is lower than when the nonlinearity of the B-H characteristic is considered, the design flow reflects the typical magnetization characteristics of the electromagnetic steel sheet. The magnetic flux density in the air gap at I_{sat} and B_{50} exceeds 1.6 T (Fig.3.6),



(a) B-H characteristic of the electromagnetic steel sheet



(b) B-H curve assuming the area (loss) as zero and BH characteristic approximating with broken-line

Fig. 3.6. B-H trajectory behavior model

which is much larger than the magnetic flux density in the air gap at PMSM and IM [3-2]. As shown in Fig.3.4, the magnetic flux is concentrated in the area where the stator teeth and the rotor teeth face each other, and the magnetic resistance is small. As a result, the magnetic flux density in the air gap is about 0.5 T in the IM, whereas that in SRM is very high, exceeding 1.6 T.

Fig.3.7 shows the relationship between the magnetization characteristics of SRM and the current amplitude. The current path in Fig.3.7 is the trajectory drawn by the current and the interlinkage flux from the start of excitation to the end of excitation of the stator winding. Here, the magnetic saturation level α_{sat} is defined as Eq.(3.4).

$$\alpha_{sat} = \frac{I_{Tmax}}{I_{sat}} \dots\dots\dots (3.4)$$

where I_{Tmax} is the amplitude of the current in trapezoidal wave drive at the operating point (A) (equivalent to I_{max} in Fig.3.3). The amplitude of the actual current I_{max} is controlled to I_{Tmax} by the current hysteresis control. Since the magnetic saturation level α_{sat} in the Eq.(3.4) is assumed to be an input constant, I_{Tmax} is uniquely determined as the value of I_{sat} multiplied by α_{sat} . As shown in Fig.3.7, the larger the magnetic saturation level α_{sat} , the larger the magnetic saturation region in the magnetization characteristics can be used. Therefore, α_{sat} is a guideline for how much of the magnetic saturation region of the iron core material can be used. Also, since the area of the current path in the magnetization characteristics (Fig.3.7) is proportional to the average torque, the larger α_{sat} results in the less iron core material to output the same torque.

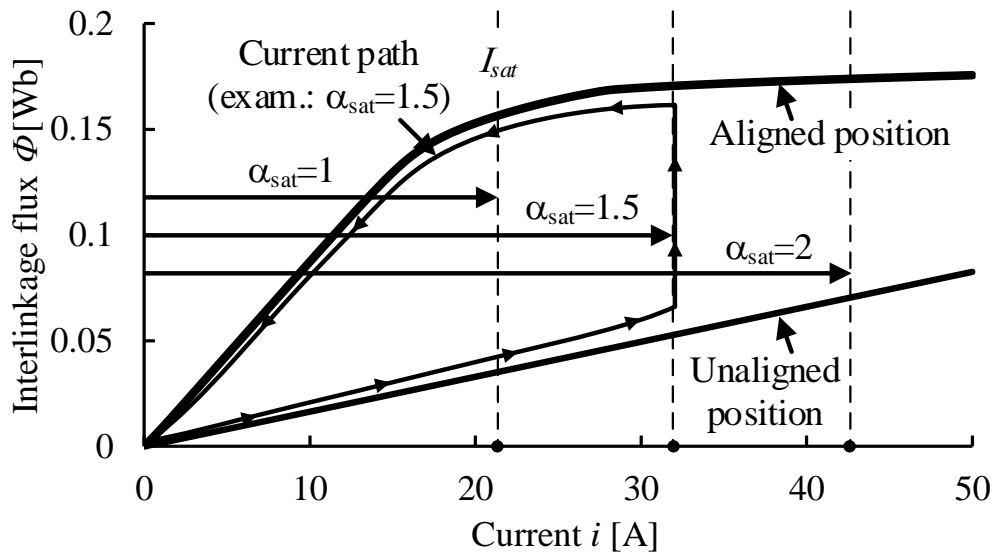


Fig. 3.7. Relationship between current amplitude and magnetization characteristic

Fig.3.8 shows the positional relationship between the stator teeth and the rotor teeth. Since the torque is expressed as the change in the magnetic co-energy with respect to the change in the rotor position, it is necessary to formulate the interlinkage flux Φ . When the current i is smaller than the saturation current I_{sat} and the magnetic saturation does not occur in the core, the interlinkage flux is expressed by Eq.(3.5).

$$\Phi_{line}(i, \theta_m) = \frac{N_s}{m} \frac{N^2 i \mu_0}{l_g} L_h \left(\frac{D_r}{2} \right) \beta(\theta_m) \dots\dots\dots (3.5)$$

where $\beta(\theta_m)$ is the angle between the rotor teeth and the stator teeth (Fig.3.8). On the other hand, when the current i is larger than the saturation current I_{sat} and the magnetic saturation occurs in the core, the interlinkage flux is expressed by Eq.(3.6).

$$\Phi_{sat}(i, \theta_m) = \frac{N_s}{m} N B_{sat} L_h \left(\frac{D_r}{2} \right) \beta(\theta_m) \dots\dots\dots (3.6)$$

If the leakage flux is neglected, the torque is generated only in the torque zone ($[\theta_j, \theta_k]$ section in Fig.3.3), where $\beta(\theta_m)$ varies positively with the change in θ_m . In the torque zone, when the current i is smaller than the saturation current I_{sat} and the magnetic saturation does not occur, the instantaneous maximum torque is expressed by Eq.(3.7) from Eq.(3.5).

$$T_{out_max} = \frac{\partial}{\partial \theta_m} \int_0^i \Phi_{line} di = \frac{N_s}{m} \frac{1}{2} \frac{N^2 \mu_0 L_h \left(\frac{D_r}{2} \right)}{l_g} i^2 \dots\dots\dots (3.7)$$

On the other hand, in the torque zone, when the current i is larger than

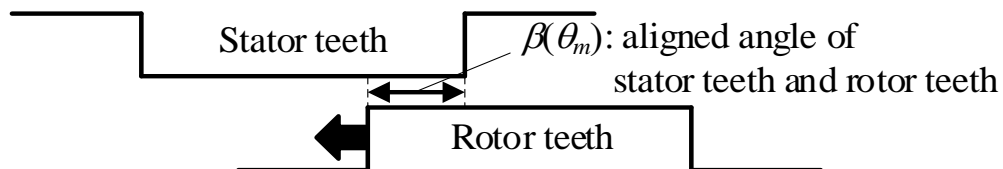


Fig. 3.8. Positional relationship between stator teeth and rotor teeth

the saturation current I_{sat} and the magnetic saturation occurs, the instantaneous maximum torque is expressed as Eq.(3.8) from equations Eq.(3.3)-Eq.(3.6).

$$\begin{aligned}
 T_{out_max} &= \frac{\partial}{\partial \theta_m} \left(\int_0^{I_{sat}} \Phi_{line} di + \int_{I_{sat}}^{I_{Tmax}} \Phi_{sat} di \right) \\
 &= \frac{N_s}{m} NB_{sat} L_h \left(\frac{D_r}{2} \right) \left(I_{Tmax} - \frac{1}{2} I_{sat} \right) \dots\dots\dots (3.8) \\
 &= \frac{N_s}{m} \left(\frac{D_r}{2} \right) L_h \frac{B_{sat}^2 l_g}{\mu_0} \left(\alpha_{sat} - \frac{1}{2} \right)
 \end{aligned}$$

Note that Eq.(3.8) assumes magnetic saturation level $\alpha_{sat} \geq 1$. In Eq.(3.8), the instantaneous maximum torque is proportional to l_g , because Eq.(3.8) does not take losses into account. As the l_g becomes wider, the more current is required to obtain the same torque, which results in the more copper loss. As a result, the torque decreases with increase of l_g . The reason why the copper loss increases when the gap is widened is that the magnetoresistance of the air gap increases and the magnetomotive force required to obtain the same torque becomes larger.

Table 3.2 shows the motor parameters of the SRM used in the verification. A three-phase 18/12 type motor, which is the limit of this design method, is used for the verification. The inductance ratio is 5.32.

Fig.3.9 shows a comparison between the theoretical instantaneous maximum torque T_{out_max} calculated from Eq.(3.7) and Eq.(3.8) and from the electromagnetic field analysis. Note that the instantaneous maximum torque T_{out_max} is obtained when the motor is rotated at a constant current flow. Fig.3.9 shows that the electromagnetic field analysis results of T_{out_max} and that from Eq.(3.7) and Eq.(3.8) are almost same. Because of the large torque ripple in the SRM, the average torque is smaller than the instantaneous maximum torque expressed by Eq.(3.7) and Eq.(3.8). The ratio of the maximum torque to the average torque at the operating point (A) is defined

Table 3.2. Motor parameters of SRM

| | | |
|-------------------------------|-----------------|-----------------------|
| Output power | P_{out} | 0.75kW |
| Maximum speed | ω_{max} | 5000min ⁻¹ |
| Base speed | ω_{base} | 3000min ⁻¹ |
| Phase-numbers and pole-number | m, N_s, N_r | 3phase 18/12 type |
| Input voltage | V_{dc} | 48V |
| Resistance | R | 12 |
| Inductance ratio | λ | 5.32(=8.74mH/1.64mH) |
| Maximum current amplitude | I_{Tmax} | 34.1 A |

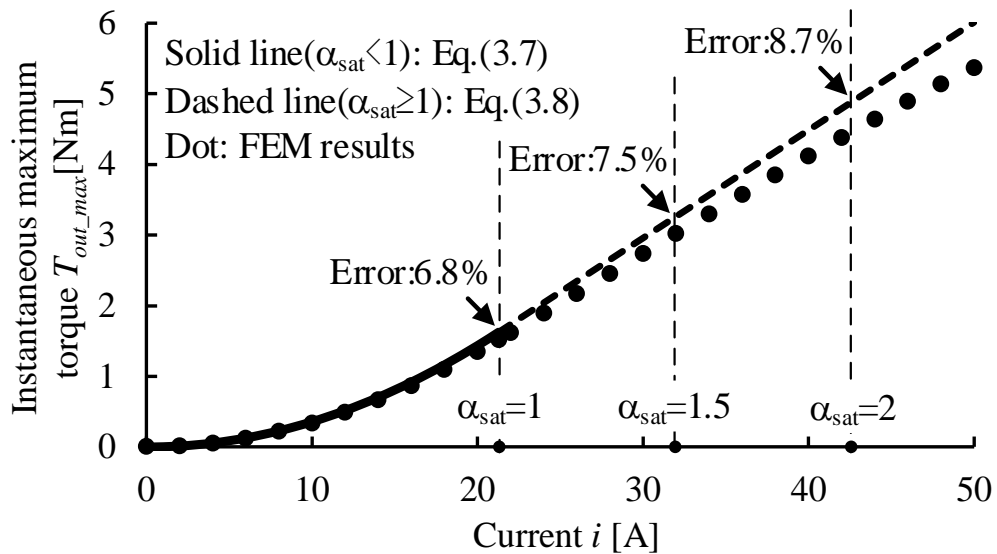


Fig. 3.9. Instantaneous maximum torque

as $\alpha_{T_{max}} = T_{max_max} / T_{max}$. At the operating point (A), the current i is larger than the saturation current I_{sat} , and magnetic saturation occurs in the core. Then, by setting $T_{max_max} = \alpha_{T_{max}} T_{max}$ in Eq.(3.8) and transforming the equation, the stack thickness of the motor L_h is expressed as Eq.(3.9).

$$L_h = \frac{2m\mu_0\alpha_{T_{max}}T_{max}}{N_s D_r B_{sat}^2 l_g (\alpha_{sat} - \frac{1}{2})} \dots\dots\dots (3.9)$$

Eq.(3.9) shows that the larger the α_{sat} leads the smaller stack thickness. In other words, Eq.(3.9) shows that the motor can be made smaller by actively using the saturation region of the magnetic material. Since it is difficult to determine $\alpha_{T_{max}}$ mathematically, it is determined by FEM and the permeance analysis. The specific method is described in section 3.2.6.

3.2.3 Decision method of stator diameter D_s

In this section, determine method of the stator diameter D_s is explained. Stator diameter D_s determines only the length of the teeth, i.e., the slot area of the windings because the rotor diameter D_r is given as a degree of freedom. In this paper, as in Reference [3-3], the slot area is derived so that both the maximum allowable current density J_{rms_max} and the maximum allowable copper loss W_{c_max} are satisfied at the operating point (A) $[T_{max}, \omega_{base}]$ in Fig.3.1 with the set winding occupancy k_s . Note that J_{rms_max} and W_{c_max} are determined by the assumed cooling method.

Fig.3.10 shows the rotation speed and the actual current waveform when a pulsed current of current amplitude I_{max} is given to the command. In addition, Fig.3.11 shows the relationship between the rotation speed and the current RMS value in that case. In this paper, trapezoidal wave driving is used when the rotation speed is less than base speed ω_{base} . Assuming that the current waveform is an ideal pulse-shaped current with current amplitude I_{Tmax} , the current RMS value $I_{RMS_com.}$ is expressed by Eq.(3.10).

$$I_{RMS_com.} = \sqrt{\frac{1}{T} \int_0^{Td_{Tmax}} I_{Tmax}^2 dt} = I_{Tmax} \sqrt{d_{Tmax}} \dots\dots\dots (3.10)$$

where d_{Tmax} is the ratio of the electric period to the pulse width dwell. In this paper, the pulse width is assumed to be constant and $d_{Tmax}=1/3$ is adopted. From Fig.3.10 and Fig.3.11, at low-speed range, the current waveform agree with the pulse wave with the very high accuracy. In the medium speed range, the current RMS value decreases due to the slowing down of the current rise. On the other hand, the current RMS value increases due to the slowing down of the current fall. The balance between these increases and decreases determines the current RMS value. Here, the RMS value I_{RMS} of the actual current in the ω_{base} when a pulse-like current with current amplitude I_{max} is given to the command is defined as in Eq.(3.11).

$$I_{RMS} = \alpha_{RMS} I_{RMS_com.} = \alpha_{RMS} I_{Tmax} \sqrt{d_{Tmax}} \dots\dots\dots (3.11)$$

where α_{RMS} is the ratio of the actual current RMS value I_{RMS} to the current RMS value I_{RMS_com} . which is calculated assuming an ideal pulse-like current. When the balance between the increase and decrease of the RMS current due to the rise and fall of the current is the same, the α_{RMS} will be 1. However, when only the falling edge of the current is greatly affected by magnetic

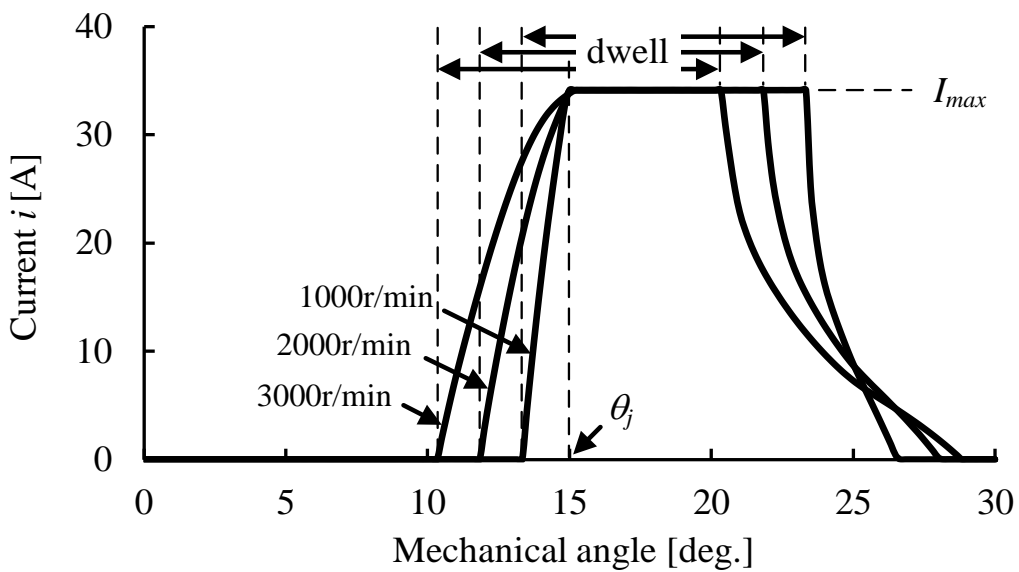


Fig. 3.10. Current waveforms under base speed: 3000min^{-1} ($d_{Tmax}=1/3$)

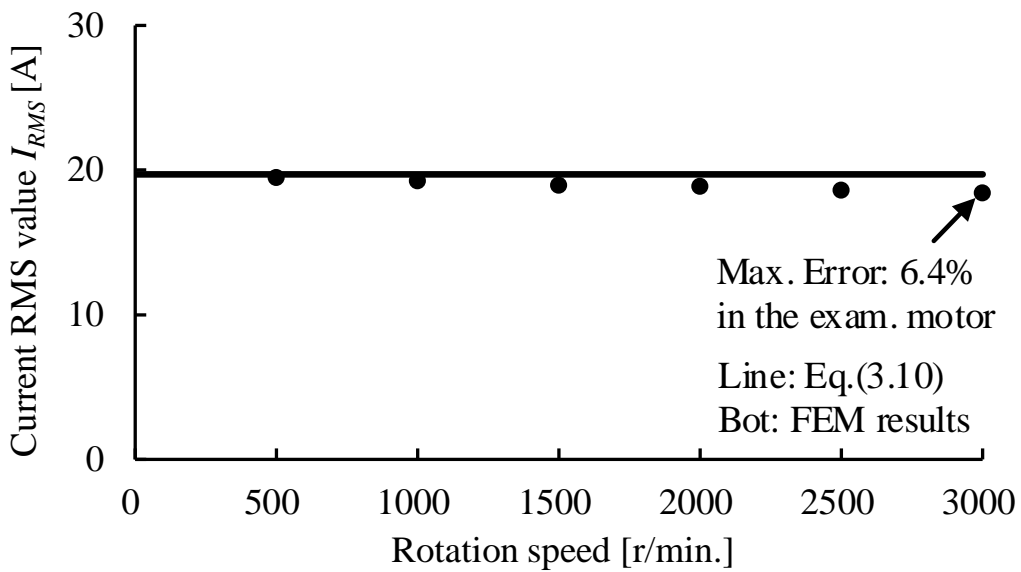


Fig. 3.11. Relationship between speed and current RMS value ($d_{Tmax}=1/3$)

saturation, these balances are broken and α_{RMS} is not equal to 1. Because the rise and fall of the current are open-loop, it is difficult to estimate the value of α_{RMS} from the simple magnetization property model used in this paper. Therefore, the α_{RMS} is determined by FEM and permeance analysis. The specific method is described in Section 2.2.6.

Fig.3.12 shows the stator slot in the SRM. The slot space is the fan-shaped part which width is the slot depth d_s and which central angle is $2\pi/N_s$ minus the stator teeth part, and the slot area per coil is half of it,. Thus, slot area per coil is expressed by Eq.(3.12).

$$\begin{aligned}
 S_{slot} &= \frac{1}{2} \left[\frac{\pi}{N_s} \left\{ \left(\frac{D_r}{2} + l_g + d_s \right)^2 - \left(\frac{D_r}{2} + l_g \right)^2 \right\} - 2d_s \left(\frac{D_r}{2} + l_g \right) \sin \left(\frac{\beta_s}{2} \right) \right] \\
 &= \frac{\pi}{2N_s} d_s^2 + \left(\frac{\pi}{N_s} - \sin \left(\frac{\beta_s}{2} \right) \right) \left(\frac{D_r}{2} + l_g \right) d_s
 \end{aligned}
 \tag{3.12}$$

where β_s is the stator pole arc and d_s is the slot depth.

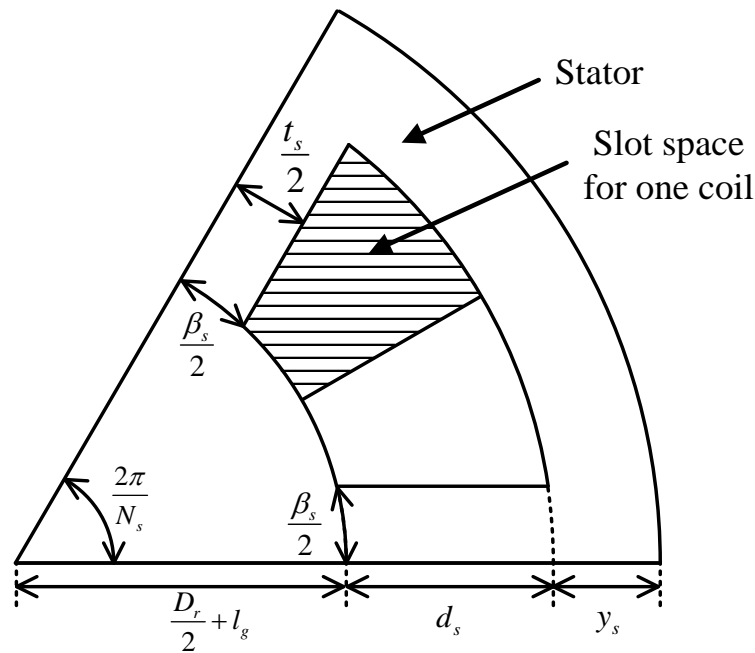


Fig. 3.12. Stator slot of SRM

(i) When using the maximum allowable current density

First, determine method of the coil space from the maximum allowable current density J_{rms_max} is explained. The required slot space S_{slot_J} per coil is expressed by Eq.(3.3), Eq.(3.4) and Eq.(3.11) to Eq.(3.13).

$$S_{slot_J} = \frac{S_{coil}}{k_s} = \frac{N\alpha_{RMS}I_{T\max}\sqrt{d_{T\max}}}{k_s J_{rms_max}} = \frac{\alpha_{RMS}\sqrt{d_{T\max}}}{k_s J_{rms_max}} \frac{\alpha_{sat}B_{sat}l_g}{\mu_0} \dots (3.13)$$

where S_{coil} is the conductor area (copper core wire area) in the slot. By solving for $S_{slot} \geq S_{slot_J}$ from equations Eq.(3.12) and Eq.(3.13), the conditional equation that the slot depth d_s must satisfy is derived in Eq.(3.14).

$$A_J d_s^2 + B_J d_s + C_J \geq 0 \dots\dots\dots (3.14)$$

where

$$A_J = \frac{\pi}{2N_s}$$

$$B_J = \left(\frac{\pi}{N_s} - \sin\left(\frac{\beta_s}{2}\right)\right)\left(\frac{D_r}{2} + l_g\right) \dots\dots\dots (3.15)$$

$$C_J = -\frac{\alpha_{RMS}\sqrt{d_{T\max}}}{k_s J_{rms_max}} \frac{\alpha_{sat}B_{sat}l_g}{\mu_0}$$

Therefore, when using the maximum allowable current density, the conditional equation to be satisfied by the slot depth d_s is expressed by Eq.(3.16).

$$d_s \geq \frac{-B_J + \sqrt{B_J^2 - 4A_J C_J}}{2A_J} \equiv d_{s_J} \dots\dots\dots (3.16)$$

Note that the smallest slot depth that satisfies the condition of maximum allowable current density is defined as d_{s_J} .

(ii) When using the maximum allowable copper loss

Next, determine method of the coil space from the maximum allowable copper loss W_{c_max} is explained. Note that the torque is determined from ampere-turns. In addition, the slot area that considering the copper loss is determined by the square of ampere-turns, it is derived from the square of the maximum torque regardless of the number of turns N .

Fig.3.13 shows a cross-sectional view of the stator teeth and windings. As described in section 3.2.2, the larger the magnetic saturation level α_{sat} , the thinner the product thickness. Thus, the increase in copper loss due to the coil-end effect is a concern. Therefore, the effect of the coil end is formulated. In this paper, the coil end length L_{end} is defined as the height of one side of the winding that protrudes axially from the slot. Assuming that the coil end length is constant regardless of the part, the relationship between the coil end L_{end} , slot depth d_s , and slot area S_{slot} per coil is expressed by Eq.(3.17)..

$$L_{end} d_s = S_{slot} \dots\dots\dots (3.17)$$

Therefore, from Eq.(3.12) and Eq.(3.17), the coil end L_{end} is expressed by

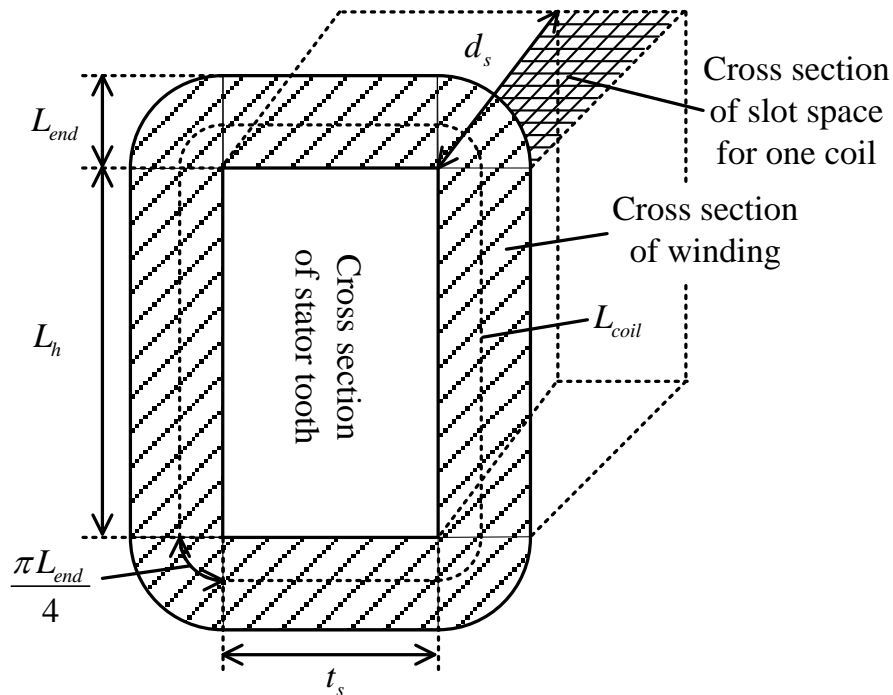


Fig. 3.13. Cross section of stator tooth and winding of SRM

Eq.(3.18).

$$L_{end} = \frac{\pi}{2N_s} d_s + \left(\frac{\pi}{N_s} - \sin\left(\frac{\beta_s}{2}\right) \right) \left(\frac{D_r}{2} + l_g \right) \dots\dots\dots (3.18)$$

The average coil length L_{coil} in one turn shown in Fig.3.13 is expressed by Eq.(3.19) [3-11].

$$L_{coil} = 2L_h + 2t_s + \pi L_{end} \dots\dots\dots (3.19)$$

Therefore, the winding resistance R_{coil} per phase is given by Eq.(3.20).

$$R_{coil} = \frac{N_s \rho_R L_{coil} N}{m k_s S_{slot} / N} \dots\dots\dots (3.20)$$

where ρ_R is the electrical resistivity of the conductor. Therefore, the copper loss is expressed by Eq.(3.21) from equations Eq.(3.11) and Eq.(3.20).

$$W_c = m R_{coil} I_{RMS}^2 = N_s \frac{\rho_R L_{coil}}{k_s S_{slot}} \left(\alpha_{sat} \frac{B_{sat} l_g}{\mu_0} \alpha_{RMS} \sqrt{d_{Tmax}} \right)^2 \dots\dots\dots (3.21)$$

By solving for $W_c \leq W_{c_max}$ from Eq.(3.18) to Eq.(3.21), the conditional equation to be satisfied by the slot depth d_s is derived by Eq.(3.22).

$$A_C d_s^2 + B_C d_s + C_C \geq 0 \dots\dots\dots (3.22)$$

where

$$\begin{aligned} A_C &= \frac{\pi}{2N_s} \\ B_C &= \left(\frac{\pi}{N_s} - \sin\left(\frac{\beta_s}{2}\right) \right) \left(\frac{D_r}{2} + l_g \right) - \frac{\pi^2}{2N_s} \frac{N_s \rho_R}{k_s W_{c_max}} \left(\alpha_{sat} \frac{B_{sat} l_g}{\mu_0} \alpha_{RMS} \sqrt{d_{Tmax}} \right)^2 \\ C_C &= - \left\{ 2L_h + 2t_s + \pi \left(\frac{\pi}{N_s} - \sin\left(\frac{\beta_s}{2}\right) \right) \left(\frac{D_r}{2} + l_g \right) \right\} \\ &\quad - \frac{N_s \rho_R}{k_s W_{c_max}} \left(\alpha_{sat} \frac{B_{sat} l_g}{\mu_0} \alpha_{RMS} \sqrt{d_{Tmax}} \right)^2 \end{aligned} \dots\dots\dots (3.23)$$

Therefore, the conditional equation in order to be satisfied by the slot depth d_s when using the maximum allowable copper loss is expressed by

Eq.(3.24).

$$d_s \geq \frac{-B_c + \sqrt{B_c^2 - 4A_c C_c}}{2A_c} \equiv d_{s_c} \dots\dots\dots (3.24)$$

Note that the smallest slot depth that satisfies the condition of maximum allowable copper loss is defined as d_{s_c} .

When the above conditions are satisfied at the same time, the conditions of less than the maximum allowable current density and less than the maximum allowable copper loss are always satisfy. However, when the slot depth is larger than necessary, the volume becomes larger. Therefore, in order to reduce the size of the SRM, the minimum slot depth that satisfies the conditions of Eq.(3.16) and Eq.(3.24) at the same time should be selected. In other words, the slot depth should be selected the larger of d_{s_J} and d_{s_c} , which is defined as follows.

- d_{s_J} : the smallest slot depth that satisfies the condition of the maximum allowable current density in Eq.(3.16)
- d_{s_c} : the smallest slot depth that satisfies the condition of the maximum allowable copper loss in Eq.(3.24)

Therefore, the slot depth d_s is expressed as Eq.(3.25).

$$d_s = \max(d_{s_J}, d_{s_c}) \dots\dots\dots (3.25)$$

On the other hand, the stator diameter D_s is the sum of the rotor diameter, air gap length, yoke thickness, and slot depth. Thus. That is expressed by Eq.(3.26).

$$D_s = 2 \left\{ \frac{D_r}{2} + l_g + m_s \left(\frac{D_r}{2} + l_g \right) \sin \left(\frac{\beta_s}{2} \right) + d_s \right\} \dots\dots\dots (3.26)$$

where m_s is the ratio of stator yoke thickness to (stator tooth width/2). In general, m_s should be 1.2-1.4 in order to suppress the extreme magnetic saturation of the stator back yoke [3-1].

3.2.4 Decision method of number of turns N

This section explains selection methods of the number of turns N . The number of turns N is determined so that the desired output is obtained with the trapezoidal wave drive at the operating point (A) $[T_{max}, \omega_{base}]$ and single pulse drive at the operating point (B) $[T_{\omega max}, \omega_{max}]$ in Fig.3.1.

When the trapezoidal wave is applied at a rotation speed lower than the base speed ω_{base} , the number of turns must be determined so that the velocity electromotive force V_{emf} is lower than the input voltage V_{dc} at the operating point (A). The velocity electromotive force at the base speed ω_{base} is expressed as Eq.(3.27) from Eq.(3.6).

$$V_{emf} = \frac{\partial \Phi_{sat}}{\partial \theta_m} \omega_{base} = \frac{N_s}{m} N B_{sat} L_h \left(\frac{D_r}{2} \right) \omega_{base} \dots\dots\dots (3.27)$$

Therefore, by solving $V_{emf} \leq V_{dc}$, the conditional equation for the number of turns N is derived as Eq.(3.28).

$$N \leq \frac{m V_{dc}}{N_s B_{sat} L_h \left(\frac{D_r}{2} \right) \omega_{base}} \equiv N_{(A)} \dots\dots\dots (3.28)$$

Note that the maximum number of turns N which satisfies $V_{emf} \leq V_{dc}$ is defined as $N_{(A)}$.

On the other hand, in the case of the single-pulse drive with the rotation speed above the base speed ω_{base} , the number of turns must be determined to reach the desired interlinkage flux at the operating point (B) with a predetermined voltage application width. In single-pulse drive, the interlinkage flux becomes maximum at the rotation angle θ_c . the maximum interlinkage flux Φ_{max} is expressed by Eq.(3.29).

$$\Phi_{max} = \frac{1}{\omega_{max}} \int_{\theta_c}^{\theta_{om}} V_{dc} d\theta = \frac{V_{dc}}{\omega_{max}} \frac{2\pi}{N_r} d_{\omega max} \dots\dots\dots (3.29)$$

where $d_{\omega max}$ is the ratio of the electric period to the pulse width dwell and V_{dc} is the supply voltage. In this thesis, $d_{\omega max}=0.5$, which is the limit of pulse

width in single pulse drive [3-13], is adopted as the initial value in order to utilize most of the DC voltage at the operating point (B). Since the equation will differ depending on whether the required current $I_{\omega max}$ has reached the saturation current or not at the operating point (B), it is necessary to derive an equation that indicates whether the current is in the saturation region or not. From Eq.(3.8), the magnetic saturation level $\alpha_{sat(B)}$ at operating point B is expressed as Eq.(3.30).

$$\alpha_{sat(B)} = \frac{\alpha_{\omega max} T_{\omega max}}{\frac{N_s}{m} \left(\frac{D_r}{2}\right) L_h \frac{B_{sat}^2 l_g}{\mu_0}} + \frac{1}{2} \dots\dots\dots (3.30)$$

where $\alpha_{\omega max}$ is the ratio of the maximum torque to the average torque as described in section 3.2.2, and is defined as $\alpha_{\omega max} = T_{\omega max_max} / T_{\omega max}$ at the operating point (B). When $\alpha_{sat} > 1$, the motor is magnetically saturated; when $\alpha_{sat} \leq 1$, the motor is not magnetically saturated. In the condition without the magnetic saturation, the required current is expressed by Eq.(3.7) to Eq.(3.31).

$$I_{\omega max} = \frac{1}{N} \sqrt{\frac{2ml_g \alpha_{\omega max} T_{\omega max}}{N_r \mu_0 L_h \left(\frac{D_r}{2}\right)}} \dots\dots\dots (3.31)$$

The interlinkage flux at the commutation angle θ_c is expressed by Eq.(3.5), Eq.(3.31) to Eq.(3.32).

$$\Phi_{line}(I_{\omega max}, \theta_c) = N k_{sp} \beta_s \sqrt{\frac{N_s L_h D_r \mu_0 \alpha_{\omega max} T_{\omega max}}{ml_g}} \dots\dots\dots (3.32)$$

where k_{sp} is the ratio of the stator pole arc to the rotor pole arc at the commutation angle θ_c . In this thesis, k_{sp} is set to 2/3 from Ref.[3-1]. By solving $\Phi_{line}(I_{\omega max}, \theta_c) \leq \Phi_{max}$, the conditional equation for the number of turns N is derived as Eq.(3.33).

$$N \leq \frac{\frac{V_{dc}}{\omega_{max}} \frac{2\pi}{N_r} d_{\omega max}}{k_{sp} \beta_s} \sqrt{\frac{ml_g}{N_s \alpha_{\omega max} T_{\omega max} \mu_0 L_h D_r}} \equiv N_{(B)line} \dots\dots\dots (3.33)$$

The maximum number of turns that satisfies the condition is defined as $N_{(B)line}$. On the other hand, in the case of magnetic saturation, the required current is expressed by Eq.(3.8) to Eq.(3.34).

$$I_{\omega_{max}} = \frac{\alpha_{\omega_{max}} T_{\omega_{max}}}{\frac{N_s}{m} B_{sat} \left(\frac{D_r}{2}\right) L_h N} + \frac{1}{2} \frac{B_{sat} l_g}{N \mu_0} \dots\dots\dots (3.34)$$

The interlinkage flux at the commutation angle θ_c is expressed by Eq.(3.6) to Eq.(3.35).

$$\Phi_{sat}(I_{\omega_{max}}, \theta_c) = \frac{N_s}{m} B_{sat} L_h \left(\frac{D_r}{2}\right) k_{sp} \beta_s \dots\dots\dots (3.35)$$

By solving for $\Phi_{sat}(I_{\omega_{max}}, \theta_c) \leq \Phi_{max}$, the conditional equation for the number of turns N is derived as Eq.(3.36).

$$N \leq \frac{\frac{V_{dc}}{\omega_{max}} \frac{2\pi}{N_r} d_{\omega_{max}}}{\frac{N_s}{m} B_{sat} L_h \left(\frac{D_r}{2}\right) k_{sp} \beta_s} \equiv N_{(B)sat} \dots\dots\dots (3.36)$$

Note that the maximum number of turns that satisfies the condition is defined as $N_{(B)sat}$.

If the above conditions are satisfied, the desired output is obtained by the trapezoidal wave drive at the operating point (A) and single pulse drive at the operating point (B) for any number of turns. However, as shown in Eq.(3.31) and Eq.(3.34), the smaller the number of turns, the larger the required current. If the number of turns is reduced more than necessary, the current rating of the inverter will increase. Therefore, the maximum number of turns that simultaneously satisfies the conditions of Eq.(3.28), Eq.(3.33), and Eq.(3.36) should be selected. Here, the maximum number of turns for each condition is defined as the maximum number of turns $N_{(A)}$, which satisfies the condition that the velocity EMF becomes less than the supply voltage at the operating point (A) as Eq.(3.28), and the maximum number of turns $N_{(B)line}$, which achieves the desired interlinkage flux with a predetermined voltage application width at the operating point (B) as Eq.(3.33), and the maximum number of turns $N_{(B)sat}$, which satisfies the

condition that Eq.(3.36). If the larger one is chosen, the other condition cannot be satisfied. Therefore, the smaller number of turns N is chosen as the final number of turns. The number of turns N can be expressed as Eq.(3.37).

$$N = \begin{cases} \min(N_{(A)}, N_{(B)line}) & \alpha_{sat(B)} \leq 1 \\ \min(N_{(A)}, N_{(B)sat}) & \alpha_{sat(B)} > 1 \end{cases} \dots\dots\dots (3.37)$$

3.2.5 Decision method of rotor diameter D_r

This section presents how to determine the rotor diameter D_r . Since D_s , L_h , and N have been determined in the previous section to satisfy the operating points (A) and (B), the remaining degree of freedom D_r is used to reduce the size.

If the motor volume $V_{vol.}$ is assumed to be expressed as a cylindrical volume of stator diameter and axial length, it is expressed as Eq.(3.38) from Eq.(3.9), Eq.(3.18), and Eq.(3.26).

$$V_{vol.}(\alpha_{Tmax}, D_r) = \frac{\pi}{4} D_s^2 L_{all} = \frac{\pi}{4} D_s^2 (L_h + 2L_{end}) \dots\dots\dots (3.38)$$

where L_{all} is the axial length of the motor including the coil ends, which is expressed as the sum of the motor core thickness L_h and the length of the coil ends on both sides $2L_{end}$. D_s , L_h , and L_{end} in Eq.(3.38) are functions of D_r . At the same time, they are also function of α_{Tmax} , which is the adjustment parameter in this thesis. Therefore, first, each dimension of the motor is determined by searching D_r to minimize the Eq.(3.38) with an initial value of α_{Tmax} . Then, the parameters α_{Tmax} and $\alpha_{\omega max}$ are adjusted from the electromagnetic field analysis. Next, each dimension of the motor is determined by searching D_r to minimize the Eq.(3.38) with the updated value of α_{Tmax} . This process is repeated until the desired torque is obtained. The details are described in Section 3.2.6.

3.2.6 Parameter adjustment by simulation

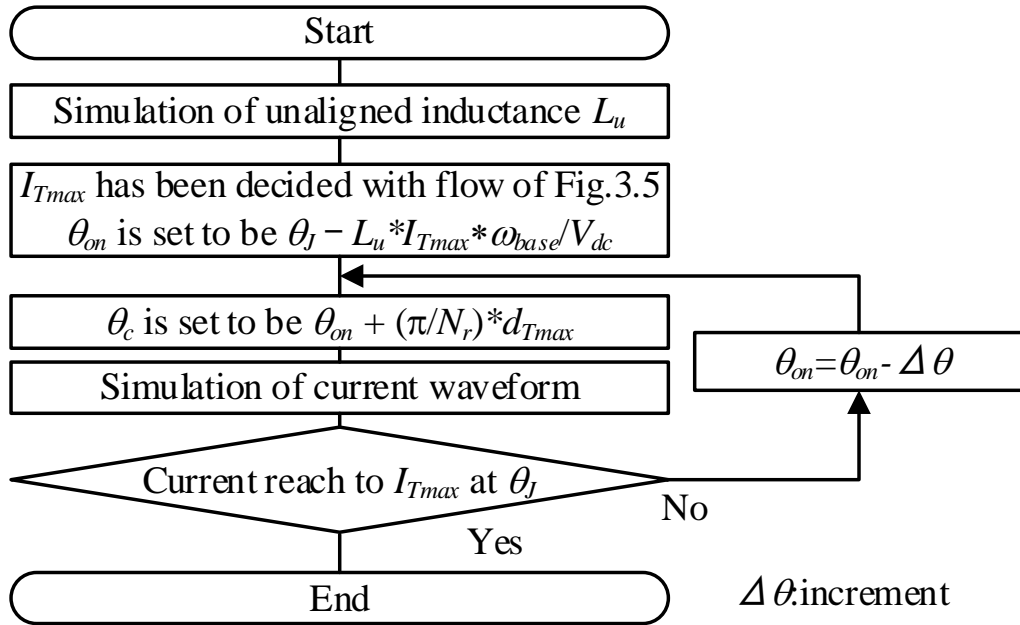
This section explains how to adjust the parameters α_{Tmax} , $\alpha_{\omega max}$, and α_{RMS} by the simulation.

As shown in Fig.3.5, in order to adjust the parameters α_{Tmax} , $\alpha_{\omega max}$, and α_{RMS} , first the approximated initial values $\alpha_{Tmax}[1]$, $\alpha_{\omega max}[1]$, and $\alpha_{RMS}[1]$ are given. Next, the motor parameters are derived according to the flowchart. Then, a simulation model based on the derived parameters are made. Finally, the average torque T_{max_ave} and the RMS current I_{RMS_sim} at the operating point (A) is analyzed. To adjust α_{Tmax} and $\alpha_{\omega max}$, the ratios of the desired torque T_{max} and $T_{\omega max}$ to the average torque T_{max_ave} and $T_{\omega max_ave}$, which are obtained from the simulation, are multiplied by the previous values $\alpha_{Tmax}[n-1]$ and $\alpha_{\omega max}[n-1]$. Similarly, the ratio of the current RMS I_{RMS} calculated from Eq.(3.11) to the current RMS I_{RMS_sim} obtained from the simulation is multiplied to the previous value $\alpha_{RMS}[n-1]$ for the adjustment of α_{RMS} . This procedure is repeated until the average torque obtained from the simulation becomes the desired torque and the current RMS value agrees with Eq.(3.11). Since the correction is based on the previous value, only a few repetitions are necessary.

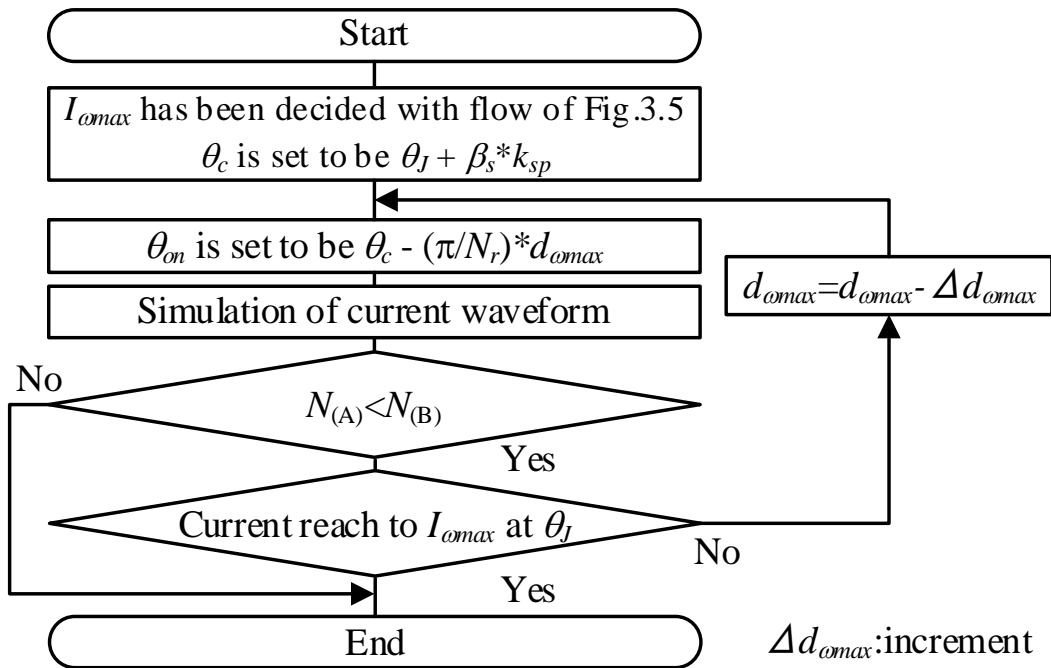
Fig.3.14 shows how to set the control variables during the analysis when adjusting the parameters α_{Tmax} , $\alpha_{\omega max}$, and α_{RMS} . The ratios d_{Tmax} and $d_{\omega max}$ of the electric period and pulse width dwell at the operating points (A) and (B) are given from the assumptions at the design. In addition, the ratio of the stator pole arc to the opposing part of the rotor pole arc k_{sp} at the commutation angle θ_c at the operating point (B) is also given as an assumption at the design. Therefore, the control variables are determined based on these values. Eq.(3.3) and Eq.(3.4) are used for the current command value in the simulation at the operating point (A). At operating point (B), Eq (3.31) or Eq.(3.34) are used depending on equation Eq.(3.30).

At the operating point (A), the applied voltage start angle θ_{on} is set so that the actual current rises to I_{Tmax} at θ_j . On the other hand, the commutation angle θ_c is set as $\theta_c = \theta_{on} + (\pi/N_r) * d_{Tmax}$. The angle required for the real current to rise to I_{Tmax} is estimated from the unaligned inductance L_u as

$L_u * I_{Tmax} * \omega_{base} / V_{dc}$ [3-13]. Therefore, the initial value of the applied voltage start angle θ_{on} should be $\theta_{on} = \theta_J - L_u * I_{Tmax} * \omega_{base} / V_{dc}$ based on the previously analyzed L_u . At the operating point (B), θ_c is set so that the ratio of the stator pole arc to the pole arc counterpart at θ_c is k_{sp} . On the other hand, θ_{on} is set as $\theta_{on} = \theta_c - (\omega / N_r) * d_{\omega max}$. As explained in section 3.2.4, when $N(A) < N(B)$ and $N(A)$ is adopted, the pulse width $d_{\omega max}$ for the required interlinkage flux at the operating point (B) becomes too large. In the case of $N(A) < N(B)$, the pulse width $d_{\omega max}$ should be shortened within the range where $N(A) < N(B)$ holds and the real current rises to $I_{\omega max}$ by θ_J .



(a) Operating point (A)



(b) Operating point (B)

Fig. 3.14. Procedure of setting control parameters

3.3 0.75kW SRM design example

Table 3.3 shows the required specifications of the motor to be designed. A motor with an output of 750 W, a base speed of 3000 min⁻¹, and a maximum speed of 5000 min⁻¹ will be designed. The air gap is set to 0.25mm, and the rotor pole arc and the stator pole arc are set to 10deg, which is the basic form of Corda triangle [3-2]. The torque at the base speed is $T_{max}=2.39\text{Nm}$ and the torque at the maximum speed is $T_{omax}=1.43\text{Nm}$. The input voltage V_{dc} is set to 48V and the magnetic saturation level α_{sat} is set to 1.6. The electromagnetic steel sheet is 35H300 and the saturation magnetic flux density B_{sat} is 1.64T from the value of B_{50} in the data sheet. This chapter performs the miniaturization design algorithm that satisfies the required N - T characteristics considering the magnetic saturation as shown in Fig.3.5. α_{Tmax} and α_{omax} are derived from the electromagnetic field analysis using the finite element method.

Table 3.3. Design requirements and constraints.

| Design requirements | | |
|----------------------------|-----------------|--|
| Output power | P_{out} | 0.75kW |
| Maximum speed | ω_{max} | 5000r/min ($T_{omax}=1.43\text{Nm}$) |
| Base speed | ω_{base} | 3000r/min ($T_{max}=2.39\text{Nm}$) |
| Input voltage | V_{dc} | 48V |
| Saturation level | α_{sat} | 1.6 |
| Max. electrical frequency | f_{e_max} | 2kHz |
| Max. current density | J_{rms_max} | 10A/mm ² |
| Max. copper loss | W_{c_max} | 75W ($W_{c_max}/P_{out}=0.1$) |
| Space factor | k_s | 50% |
| Sat. magnetic flux density | B_{sat} | 1.64T (35H300) |
| Design constraints | | |
| Airgap | l_g | 0.25mm |
| Stator pole arc | β_s | 10deg. |
| Rotor pole arc | β_r | 10deg. |

3.3.1 Decision of the number of phases and poles

In this design example, the maximum allowable electrical frequency is set to 2 kHz. This is because the sampling frequency is assumed to be 20 kHz and the maximum allowable electrical frequency is set with a margin of 1/10 of the sampling frequency. In this design example, the number of status lots N_s should satisfy $N_r \leq 24$ from Eq.(3.2). Therefore, this chapter designs a 3-phase 18/12 type SRM, according to Table 3.1, which is the limit of this design method.

3.3.2 Miniaturization design

Fig.3.15 shows the relationship between the rotor diameter D_r and the volume $V_{vol.}$ without and with consideration of the coil end. There is a point where the volume $V_{vol.}$ becomes minimum as the rotor diameter D_r is changed. First, the reason for that is discussed. As shown in Eq.(3.9), L_h is reduced as D_r is increased when the same torque is obtained. This is because the torque depends on the size of the rotor, which is the area of the gap. On the other hand, as shown in Eq.(3.26), the stator diameter D_s is outside the rotor diameter D_r . Therefore, as D_r is increased, the stator diameter D_s will

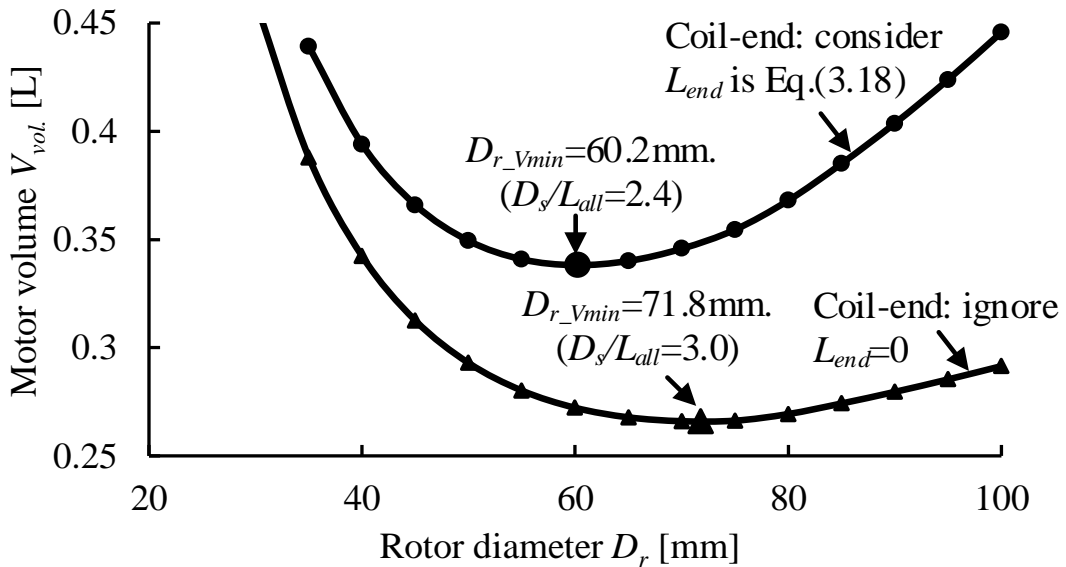
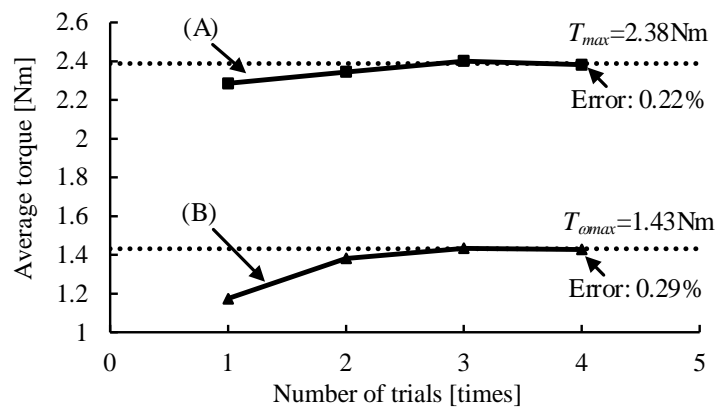


Fig. 3.15. Relationship between rotor diameter D_r and motor volume $V_{vol.}$

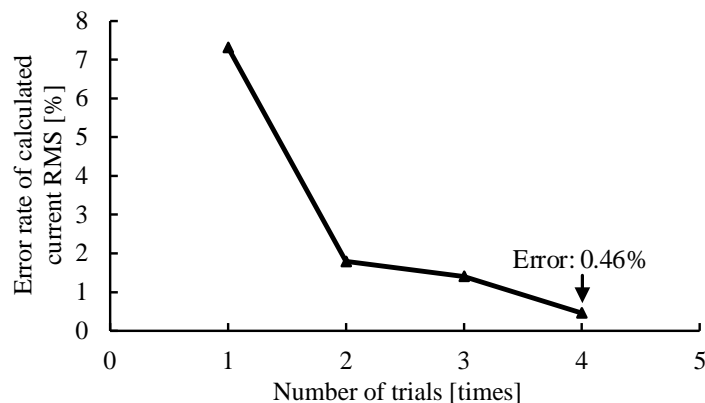
inevitably increase. Since there is a trade-off relationship between them, the volume V_{vol} is minimized at the point where they are balanced. In addition, the D_s/L_{all} ratio becomes smaller when the coil end is considered, which minimizes the volume; if the D_s/L_{all} ratio becomes large and the motor becomes flat, the axial length becomes longer due to the coil end, which results in larger volume of the motor. Therefore, the D_s/L_{all} ratio at the point where the volume V_{vol} becomes the minimum is smaller when the coil end is considered than when the coil end is not considered.

3.3.3 Adjustment with simulation

Fig.3.16 shows the error rates of (a) the average torque value and (b) the RMS current value when α_{Tmax} , $\alpha_{\omega max}$, and α_{RMS} are adjusted according to the algorithm shown in section 3.2.6. The initial values of α_{Tmax} and $\alpha_{\omega max}$ were set to 1.5, and the initial value of α_{RMS} was set to 1. From Fig.3.16(a), the average torque approaches the desired torque at each operating point as the number of trials increases, and finally converges. In addition, Fig.3.16(b) shows that the error rate of the current RMS value becomes smaller and smaller as the number of trials increases, and finally reaches zero. In the present case, the error rate agrees with less than 1% after four trials.



(a) Average torque



(a) Current RMS value

Fig. 3.16. Number of trials and average torque and current RMS value

3.3.4 Validation of designed motor

Table 3.4 shows the dimensions of the designed motor and Fig.3.17 shows the outline of the motor. The designed SRM has $m=3$, $N_s=18$, $N_r=12$, $D_s=96.3\text{mm}$, $D_r=58.1\text{mm}$, $L_h=35.2\text{mm}$, $N=91$ turns (1 series, 6 parallel). In this design, the current density was set to 10A/mm^2 , and the specifications were designed to allow the natural air cooling, which resulted in a large coil space and a flat shape.

Table 3.4. Design parameters

| Main parameters | | |
|---|------------|-----------------------------------|
| Number of phases | m | 3 |
| Number of stator poles | N_s | 18 |
| Number of rotor poles | N_r | 12 |
| Rotor diameter | D_r | 58.1 mm |
| Stator diameter | D_s | 96.3 mm |
| Thickness of motor core | L_h | 35.2 mm |
| Overall axial length | L_{all} | 43.0 mm |
| Number of turns | N | 91 turns ($\phi=0.65\text{mm}$) |
| Control parameters | | |
| Current amplitude at operating point (A) in Fig.1 | I_{Tmax} | 34.4 A |
| Current amplitude at operating point (B) in Fig.1 | I_{omax} | 28.5 A |

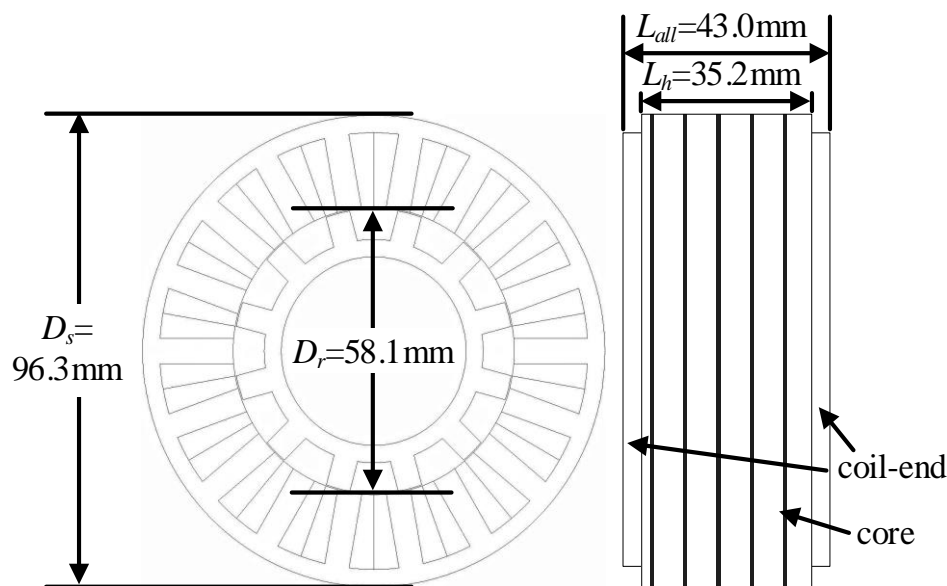


Fig. 3.17. Cross section of designed SRM

Fig.3.18 shows the back EMF waveform for each current value at the base speed of the designed motor. Note that the velocity EMF e_{emf} was calculated according to Eq.(3.39).

$$e_{emf}(i, \theta_m) = \frac{\partial \Phi(i, \theta_m)}{\partial \theta_m} \omega \dots\dots\dots (3.39)$$

For the validity of this study, the interlinkage flux is approximated by a Fourier series expansion with the parameter as a function of the current with reference from Ref.[3-1], which taking into account the magnetic nonlinearity. As shown in Fig.3.18, the speed EMF gradually increases as the current is increased until the magnetic saturation occurs. The back EMF hardly increases when magnetic saturation occurs. The back EMF at the ω_{base} of the designed motor is less than the input voltage V_{dc} at any current value. This is because the number of turns was determined so that the back EMF becomes less than the input voltage at the base speed as explained in section 3.2.4. When the speed EMF is less than the supply voltage, the current is controlled to a constant level by current hysteresis control. Therefore, the designed SRM is driven by the trapezoidal wave when the rotation speed is less than ω_{base} .

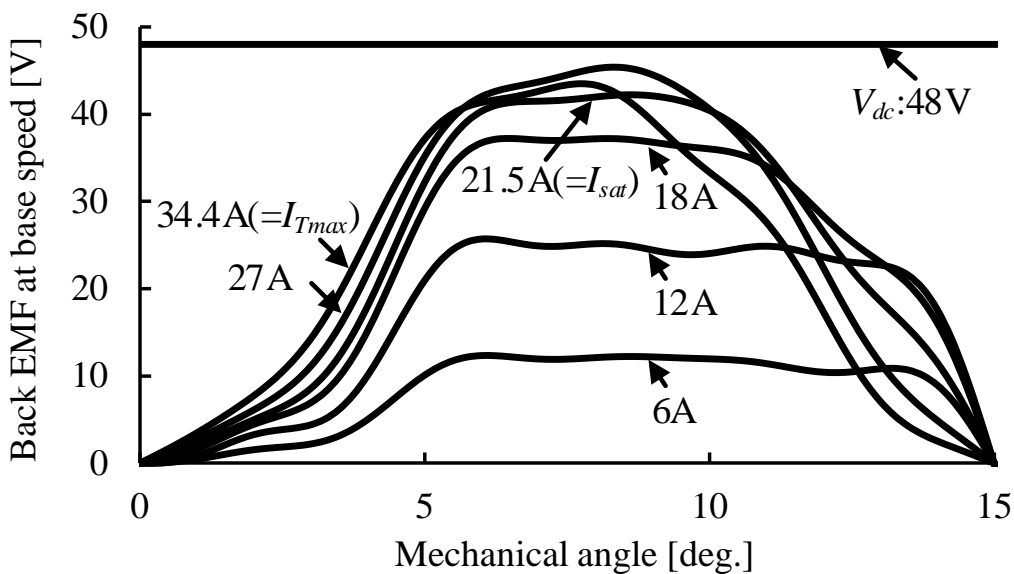
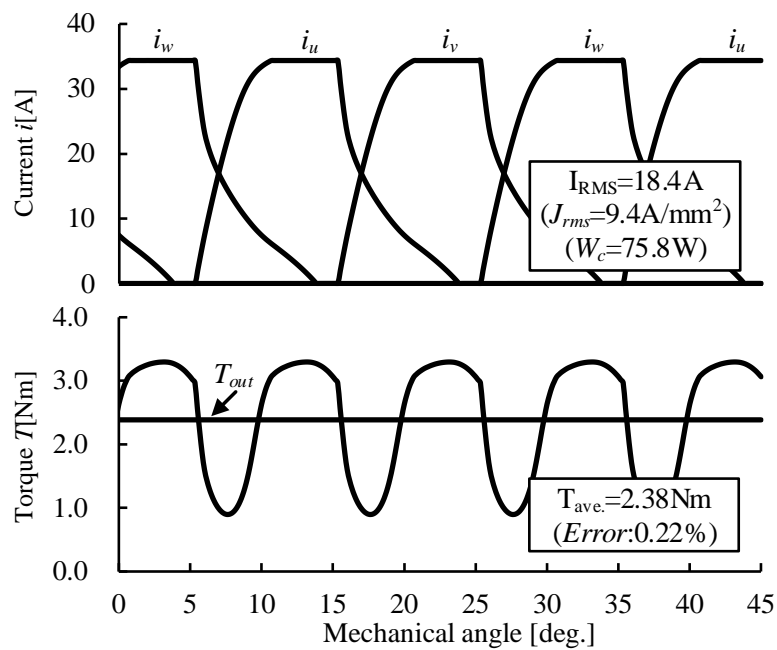


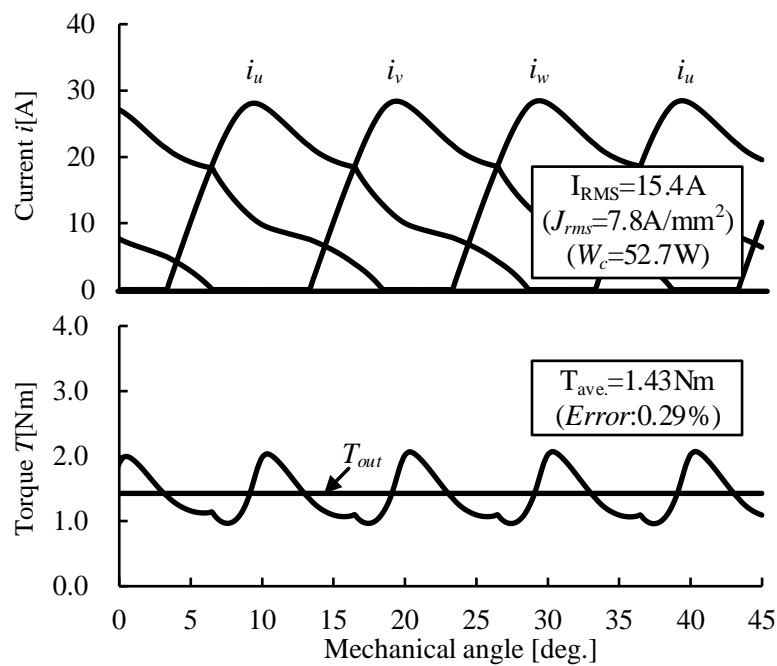
Fig. 3.18. Calculated back EMF of designed SRM at base speed

Fig.3.19 shows the results of the electromagnetic field analysis at the operating points (A) $[T_{max}, \omega_{base}]$ and (B) $[T_{\omega max}, \omega_{max}]$. At each operating point, it was confirmed that the desired torque is obtained with an error rate of 1% or less. In this design, the stator diameter was designed based on the constraint of the allowable maximum copper loss. An example of a design based on the constraint of the maximum allowable current density is found in Ref.[3-4]. The current density is $9.4\text{A}/\text{mm}^2$ whereas the reference value of $10\text{A}/\text{mm}^2$. The copper loss is 75.8W whereas the reference value of 75W , which are agree with the required specifications with an error of about 1%.

Fig.3.20 shows the current density map and the copper loss map. The rotation speed is given in 500 min^{-1} increments, and the current command is given in 5A increments. In addition, for all operating points, the applied voltage start angle θ_{on} is set so that the actual current rises to the current command by the time θ_j is reached. The commutation angle θ_c was set to $\theta_c = \theta_{on} + (\pi/N_r) * d_{T_{max}}$ when the rotation speed was below the base speed. On the other hand, when the rotation speed was higher than the base speed, θ_c was set so that the ratio of the stator pole arc to the pole arc counterpart at θ_c becomes k_{sp} . From Fig.3.20, the allowable maximum current density and allowable maximum copper loss are not exceeded at not only the operating points (A) $[T_{max}, \omega_{base}]$ and (B) $[T_{\omega max}, \omega_{max}]$ shown in Fig.3.19 but also within all N - T regions.

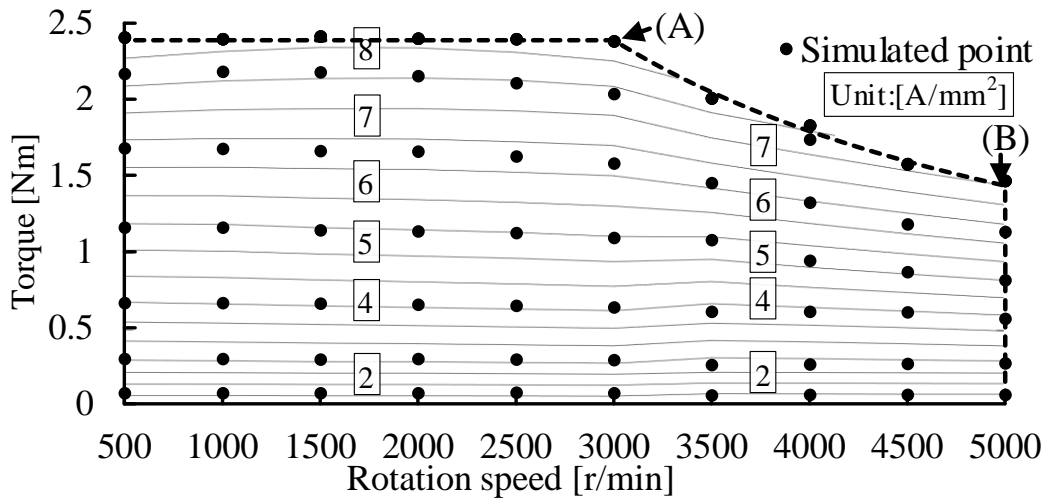


(a) Operating point (A)

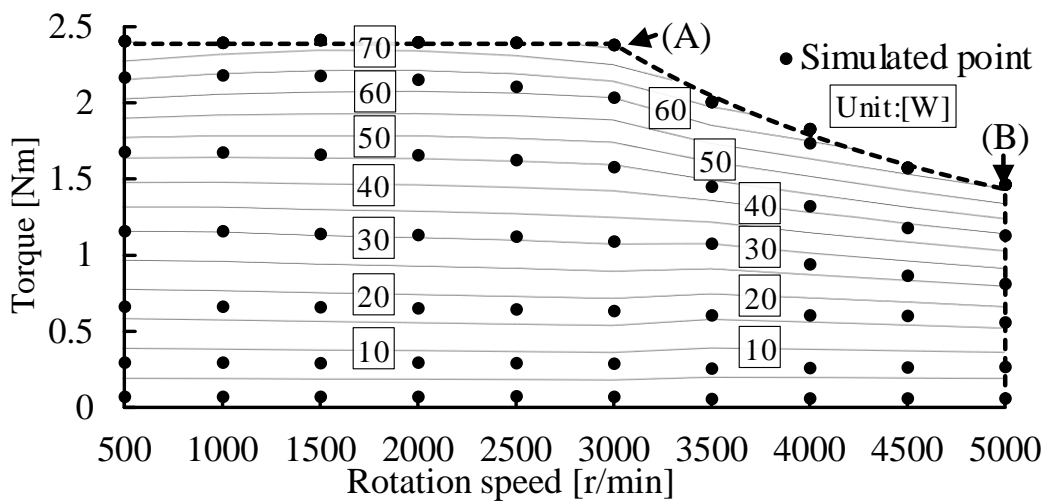


(b) Operating point (B)

Fig. 3.19. Simulation results of currents and torques at operating points (A) and (B)



(a) Current density



(b) Copper loss map

Fig. 3.20. Map of current density and copper loss.

3.3.5 Utility of magnetic saturation

Fig.3.21 shows the current trajectories in the magnetization characteristics at the operating point (A) [T_{max} , ω_{base}] and operating point (B) [$T_{\omega max}$, ω_{max}] when the magnetic saturation level α_{sat} is set to 1.2, 1.6, and 2.0. The current paths with the current condition at 1.2, 1.6, and 2.0 times the saturation current I_{sat} are drawn, respectively. Fig.3.21. indicates that the larger the magnetic saturation level α_{sat} leads that the deeper the magnetic saturation region can be used. Therefore, α_{sat} is a guideline for how much of the magnetic saturation region of the iron core material can be used. In order to use the vector control of SRM [3-12], which is not suitable to control the extremely nonlinearity, α_{sat} can be set to low at the motor design stage to mitigate the nonlinearity of SRM at the expense of the power density.

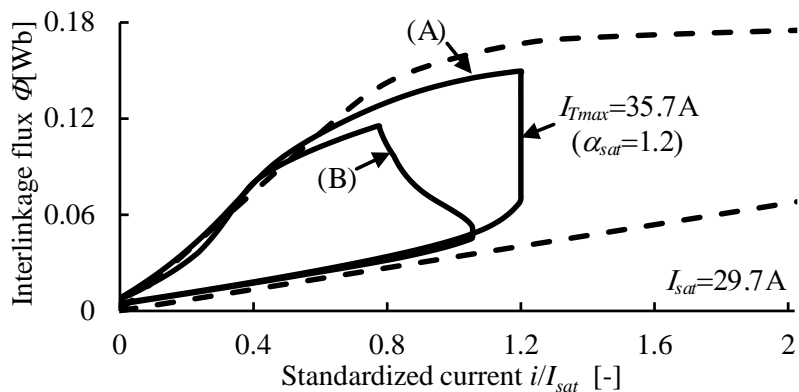
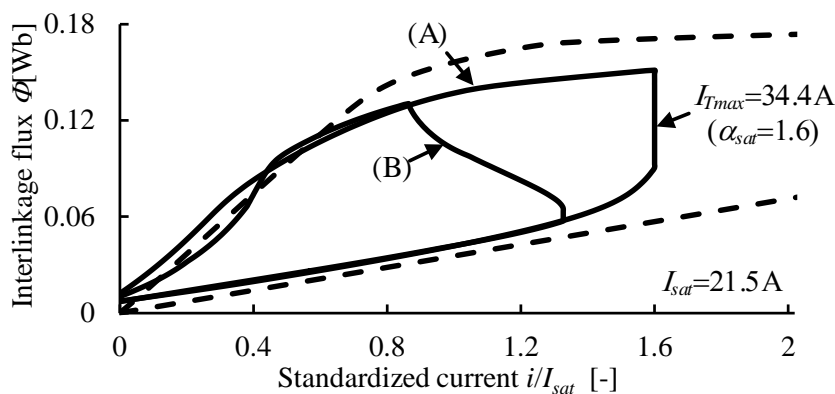
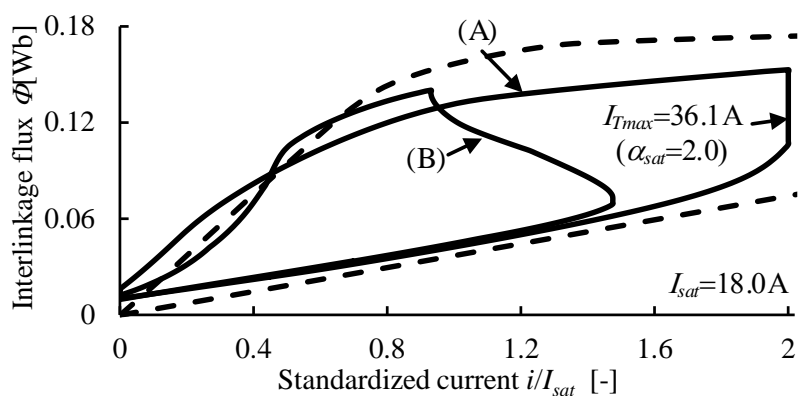
(a) magnetic saturation level $\alpha_{sat}=1.2$ (b) magnetic saturation level $\alpha_{sat}=1.6$ (c) magnetic saturation level $\alpha_{sat}=2.0$

Fig. 3.21. Current paths at operating point (A) and point (B) under different magnetic saturation level

Fig.3.22 shows the relationship between the magnetic saturation level α_{sat} and the motor volume. For each α_{sat} , the motor volume is minimized according to the algorithm. As shown in Fig.3.22 the volume decreases as the α_{sat} increases, when α_{sat} is less than 1.8. This is because the magnetic properties of the iron core material is effectively utilized by actively using the saturated region of the magnetic material, which results in the smaller iron core. On the other hand, the volume increases as α_{sat} increases, when α_{sat} is larger than 1.8. This is because the larger the D_s/L_{all} ratio due to larger α_{sat} leads flatter the motor and the longer the axial length due to the coil end. As a result, the motor becomes large. In other words, the effect of the coil ends making the motor larger was greater than the effect of making the motor smaller by utilizing the magnetic properties of the iron core material. It can be concluded that the SRM that satisfies the required N-T characteristics and minimizes the volume is achieved with $\alpha_{sat}=1.8$.

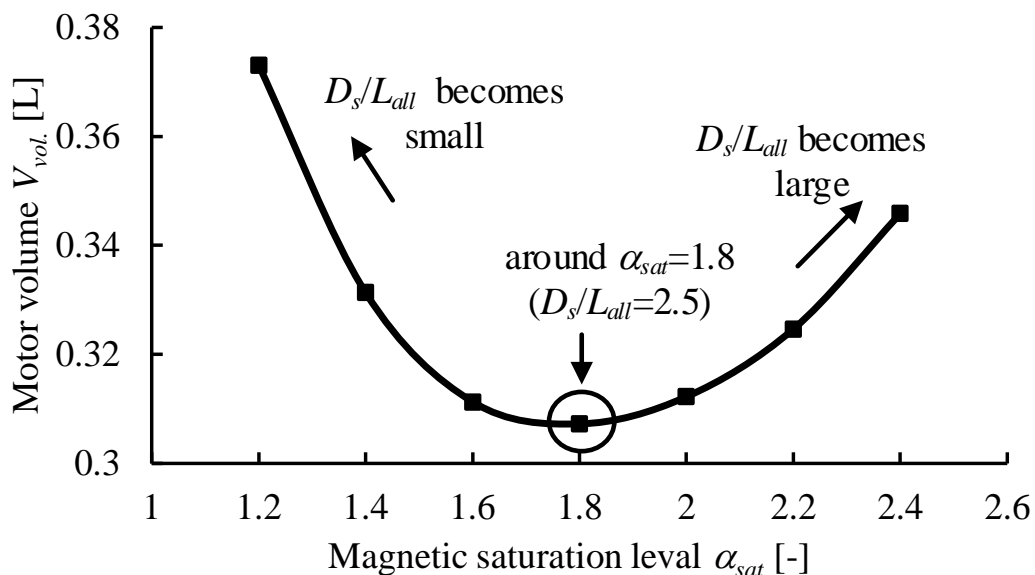


Fig. 3.22. Relationship between magnetic saturation level α_{sat} and motor volume.

3.3.6 Design in different iron core materials

3.4 Fig.3.23 shows the B-H characteristics of amorphous steel sheet (2605SA1), electromagnetic steel sheet (35JNE300), and 35H300 ($B_{sat}=1.64\text{T}$), which is a general electromagnetic steel sheet used in the previous section. The B_{sat} of amorphous steel sheet (2605SA1) is 1.53T, which is lower than that of the 35H300. On the other hand, the B_{sat} of the electromagnetic steel sheet (35JNE300) is 1.74T, which is higher than that of the 35H300. Assuming that these two iron core materials with different magnetic properties are used, the motor is designed as in the previous section.

Table 3.5 shows each dimension of the motor designed when using amorphous steel sheet (2605SA1) and electromagnetic steel sheet (35JNE300) as the iron core material. Note that the design specifications of the motor are the same as those shown in Table 3.3. In addition, the magnetic saturation level α_{sat} is determined so that the volume is minimized as shown in Fig.3.22. From Table 3.5, the motor using the electromagnetic steel sheet (35JNE300) with high B_{sat} is about 15% smaller in volume than the motor using the amorphous steel sheet (2605SA1) with low B_{sat} . This is because the higher the saturation magnetic flux density, the larger the interlinkage flux

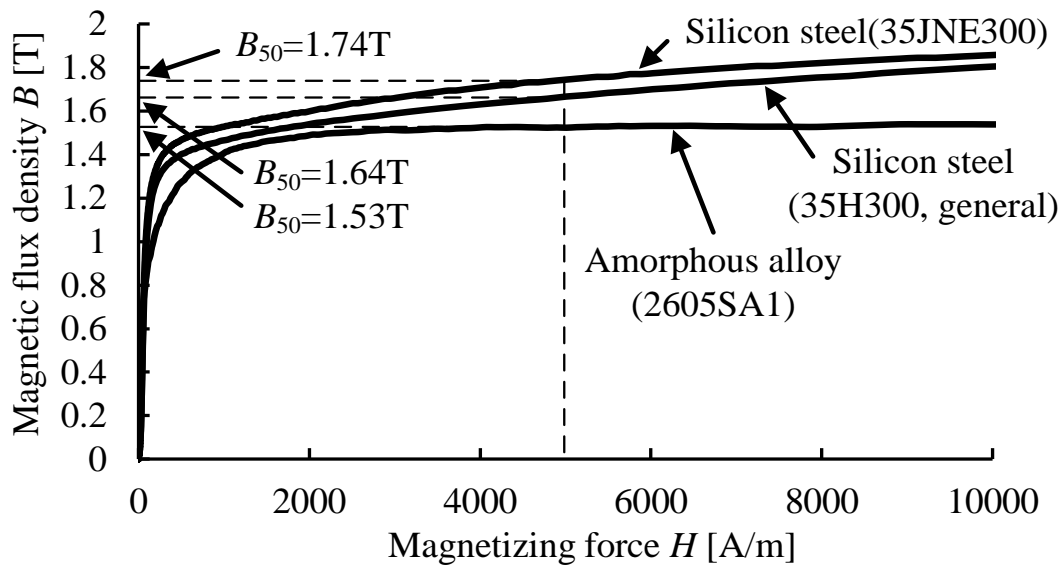
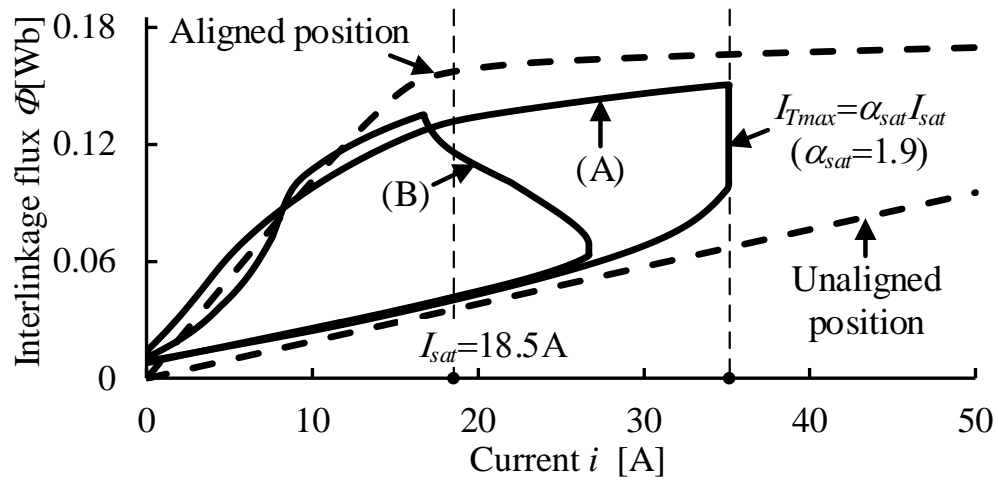


Fig. 3.23. B-H characteristics of 35H300, 2605SA1, and 35JNE300

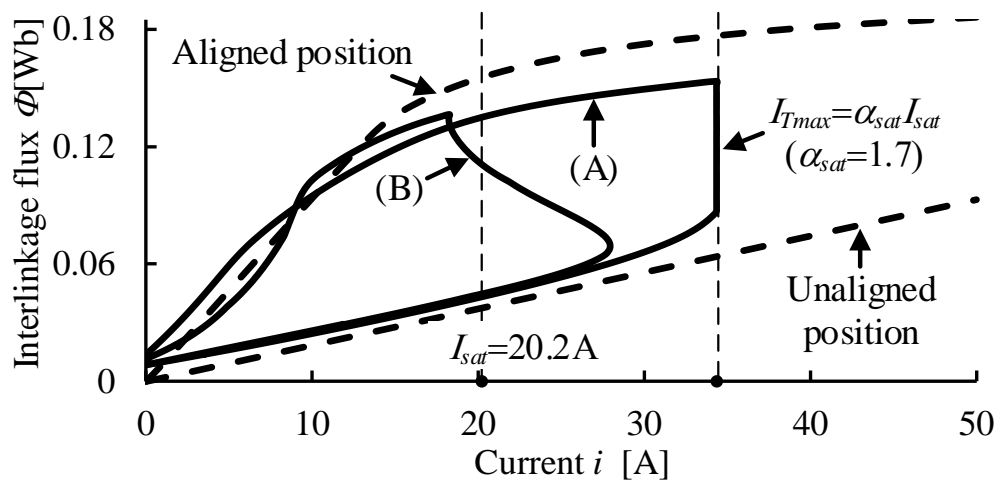
and the greater the torque as can be seen from Eq.(3.8). Fig.3.24 shows the current trajectory in the magnetization characteristics of the two motors designed. As shown in Table 3.5, the magnetic saturation level α_{sat} which the volume is minimized was $\alpha_{sat}=1.9$ for the amorphous steel sheet (2605SA1) with low B_{sat} and $\alpha_{sat}=1.7$ for the electromagnetic steel sheet (35JNE300) with high B_{sat} . In other words, the iron core material with lower B_{sat} has higher α_{sat} , and the point of stronger magnetic saturation for the iron core material achieved the smallest volume. As shown in Fig.3.24, the lower the B_{sat} , the lower the I_{sat} . From this result, the proposed method without independence on the reference values based on past examples, such as power density and power coefficient, which were used in conventional designs. In other words, the proposed design method achieved the design that matched the any magnetic properties of the iron core material. In addition, the algorithm is clear and allows the motor designer to design any motor desired.

Table 3.5. Design parameters

| | | 35H300 ($B_{50}=1.64\text{T}$) | 2605SA1 ($B_{50}=1.53\text{T}$) | 35JNE300 ($B_{50}=1.74\text{T}$) |
|---------------------------|----------------|--------------------------------------|--------------------------------------|---------------------------------------|
| Magnetic saturation level | α_{sat} | 1.8 | 1.9 | 1.7 |
| Rotor diameter | D_r | 58.6mm | 60.2mm | 57.4mm |
| Stator diameter | D_s | 99.7mm | 101.5mm | 98.2mm |
| Thickness of motor core | L_h | 31.3mm | 33.6mm | 29.8mm |
| Overall axial length | L_{all} | 39.4mm | 41.8mm | 37.7mm |
| Number of turns | N | 102turns ($\phi=0.65\text{mm}$) | 99turns ($\phi=0.66\text{mm}$) | 103turns ($\phi=0.68\text{mm}$) |
| Motor volume | V_{vol} | 0.307L | 0.338L | 0.286L |



(a) 2605SA1



(b) 35JNE300

Fig. 3.24. Current paths at operating point (A) and point (B) under different magnetic material

3.4. Conclusion

This chapter described an automatic design method for the high-efficiency motors with the consideration of the magnetic saturation using the B-H characteristic. First, the geometrical parameters and the input constants for the automatic design of the high-efficiency motor were explained. Next, the procedure to apply the proposed B-H characteristic into the permeance method was explained. Then, the torque and the loss are formulated as the functions of the shape parameters based on the proposed permeance method. The derived theoretical equations were summarized and the automatic design method using the rotor diameter as a degree of freedom was proposed and validated. In addition, the effect of the magnetic saturation considered by the BH characteristic was discussed. In order to confirm that the design method considers the material characteristics, the design examples using the materials with the different saturation magnetic flux densities were presented.

Bibliography

- [3-1] Miller T. J. E.: Switched reluctance motors and their control, pp.161-180, Magna Physics Publications and Oxford University Press (1993)
- [3-2] T. Kenjo: SR motor, pp.119-159, Nikkan Kogyo Shimbun, Ltd. (2012) (in Japanese)
- [3-3] K. Akatsu, S. Wakui, and M. Arimitsu: “Automatic Design Method for PM Motor which satisfies the Output NT Requirements”, IEEJ Journal Industry Applications, vol. 124, no. 9, pp. 946-955 (2004) (in Japanese)
- [3-4] T. Kumagai, J. Itoh, K. Kusaka, and D. Sato: “Optimum Design Method for Switched Reluctance Motor Satisfying the Requirements of N-T characteristic Considering Magnetic Saturation”, IEEJ, SA-20-016/RM-20-016, pp. 1-6 (2020) (in Japanese)
- [3-5] O. Ichinokura, K. Tajima, K. Nakamura, and Y. Yoshida: Dynamic analysis of electric motor using magnetic circuit model, p185, Kagakujiyoho shuppan Co., Ltd. (2016) (in Japanese)
- [3-6] H.C. Lovatt and J.M. Stephenson: “Influence of number of poles per phase in switched reluctance motors”, IEE Proceedings B - Electric Power Applications, Vol.139, No.4 pp.307-314 (1992)
- [3-7] Valeo Air Management UK Limited, Stephen Michael Knight, A STATOR ASSEMBLY FOR AN ELECTRIC SUPERCHARGER, Patent Application Publication, No. US 2015/0372553 (2015)
- [3-8] T. Kosaka, A. Kume, H. Wakayama, and N. Matsui: “Development of high torque density and efficiency switched reluctance motor with 0.1 mm short airgap”, in Proceedings of the IEEE European Conference on Power Electronics and Applications 2007, pp. 1–9 (2007)
- [3-9] H. Yamai, Y. Sawada, and K. Ohyama: “Applying Switched Reluctance Moor to Oil Hydraulic Pump Use”, IEEJ Journal Industry Applications, vol. 123, no. 2, pp. 96-104 (2014) (in Japanese)
- [3-10] E. Zhao, S. Song, Z. Ma, X. Zhang, L. Ning, and Y. Liu: “Design and initial testing of an integrated switched reluctance starter/generator system for unmanned aerial vehicle”, CES Transactions on Electrical Machines and Systems, Vol. 2, No. 4, pp. 377-383 (2018)

- [3-11] K. Kiyota, S. Nakano, and A. Chiba: “A Fast Calculation Method of Optimal Ratio of Outer Diameter and Axial Length for Torque Improvement in Switched Reluctance Motor”, IEEE Transactions on Industry Applications, vol. 54, no. 6, pp. 2303-2309 (2018)
- [3-12] K. Aiso and K. Akatsu: “High speed SRM using vector control for electric vehicle”, CES Transactions on Electrical Machines and Systems , Vol. 4, No. 1, pp. 61-68 (2020)
- [3-13] Miller T. J. E.: Electronic Control of Switched Reluctance Machines, pp.74-97, Newnes (2001)

Chapter 4

Design and Evaluation with Improved High Accuracy Iron Loss Calculation with FEM for High Efficiency Motor made by Blanking Amorphous Alloy Foil

4.1. Introduction

In this chapter, a method for accurate electromagnetic field analysis of iron loss using a B-H trajectory behavior model and a design method for high-efficiency motors based on the analysis are explained. In particular, by applying the method into a blanked amorphous material, the problem of degradation due to blanking is quantitatively demonstrated. First, an experiment using a ring core is performed to quantitatively show the effect of processing degradation due to blanking. Next, the B-H trajectory behavior model is multiplied by the algorithm implemented in the FEM software to realize highly accurate iron loss analysis. Using the accurate iron loss analysis, a high-efficiency motor utilizing blanked amorphous material is designed and prototyped. The efficiency and loss of the prototype motor are evaluated, and the superiority of the designed motor is explained. Finally, the accuracy of the iron loss analysis is verified to validate the proposed method.

4.2. Pre-experimental iron loss evaluation of ring cores

The B-H characteristics and the iron loss characteristics of the cores made by different material and different processing method are evaluated with ring cores as a preliminary step of the experimental evaluation with motor. Generally, the evaluation of the iron loss characteristic with ring core is more basic and more accurate.

4.2.1 Experimental preparation

Table 4.1 shows the specifications of the ring cores, whereas Fig.4.1 shows the photograph of the manufactured ring cores. Four ring cores are manufactured in order to evaluate the iron loss characteristics of the cores made by the different material and the different processing method. Two ring cores are made by the laser cutting after laminating (a) 20HX1300 of the high grade low-iron-loss silicon steel (0.20mm thickness) and (b) 2605SA1 of the amorphous alloy (0.025mm thickness), which are referred as “SS-C” and “AA-C” in this paper. The others are made by laminating after blanking (a) 20HX1300 and (b) 2605SA1, which are referred as “SS-B and “AA-B in this paper. The conductive elements of the laser cut surface of the manufactured SS-C and AA-C are removed with etching process in order to prevent the increase of the eddy current loss due to the short circuit between laminated steel sheets. Note that the lamination factor k_l is calculated from

$$k_l = \frac{m}{\rho_m V_{vol}} \dots\dots\dots (4.1)$$

where m is the mass of the ring core, ρ_m is the density of the material, and V_{vol} is the volume of the ring core. As shown in Table 4.1, the lamination factors of AA-C and AA-B are a little worse than that of SS-C and SS-B. This deterioration of the lamination factor will be due to the thinner and the higher number of layers of the amorphous alloy than these of the silicon steel.

Table 4.1. Specifications of ring-cores

| Name of Ring core | SS-C | SS-B | AA-C | AA-B |
|-------------------|---------------------------------|--------------------------------|---------------------------------|--------------------------------|
| Iron core | silicon steel (20HX1300) | | amorphous alloy (2605SA1) | |
| Steel Thickness | 0.20mm | | 0.025mm | |
| Processing Method | Wire cut* After Laminated | Laminated After Blanking | Wire cut* After Laminated | Laminated After Blanking |
| Lamination factor | 95.9% | 96.9% | 93.1% | 90.8% |

* The conductive elements of wire cut surface are removed with etching process



Fig.4.1. Photograph of ring-cores made with the processing methods as shown in Table 4.1.

Fig.4.2 depicts the diagrams of the measurement setup for the ring core. The primary and secondary windings are wound around the manufactured ring core. The magnetic flux density $B(t)$ and the magnetizing force $H(t)$ are expressed as

$$B(t) = \frac{1}{N_2 S_c} \int_0^t v_2(t) dt \dots\dots\dots (4.2)$$

$$H(t) = \frac{N_1 i(t)}{l} \dots\dots\dots (4.3)$$

where $v_2(t)$ is the voltage of the secondary winding, N_2 is the number of turns in the secondary winding, S_c is the effective cross-sectional area of the ring core, $i_1(t)$ is the current in the primary winding, N_1 is the number of turns in the primary winding, and l is the effective magnetic path length of the ring core. On the other hand, the iron loss W_i and the amplitude of magnetic flux density B_m are expressed as

$$W_i = \frac{1}{T} \int_0^T i_1(t) v_2(t) dt \dots\dots\dots (4.4)$$

$$B_m = \frac{\sqrt{2} V_{2_rms}}{2\pi f N_2 S_c} \dots\dots\dots (4.5)$$

where f is the frequency of the applied sinusoidal voltage, V_{2_rms} is the root

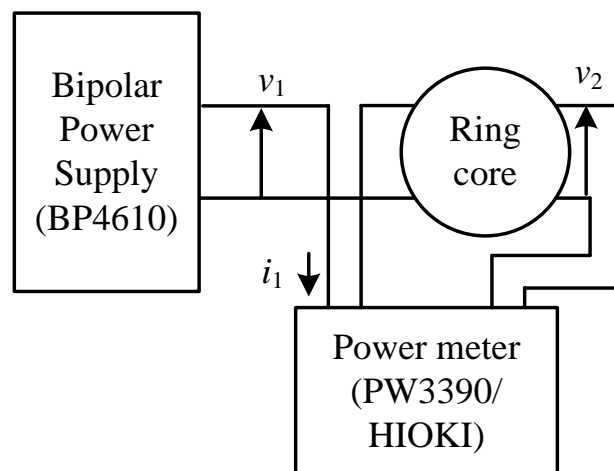
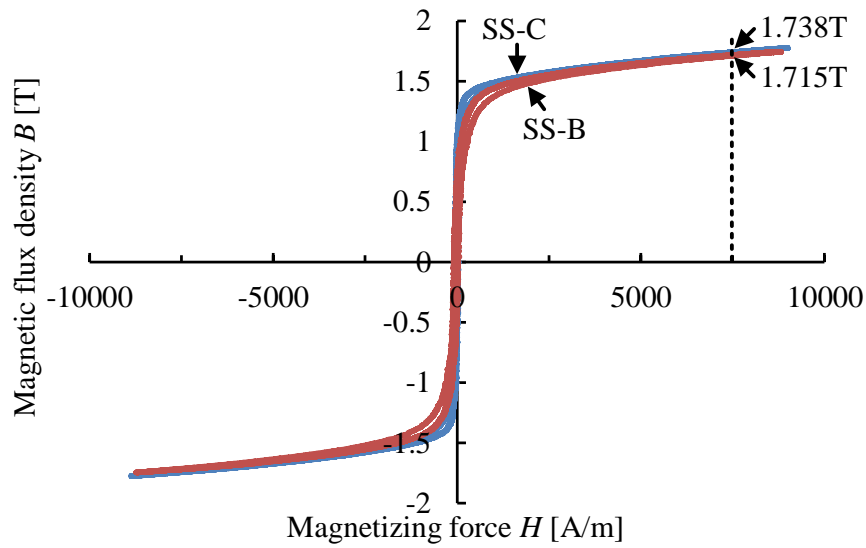


Fig.4.2. Diagrams of measurement setup for ring-core

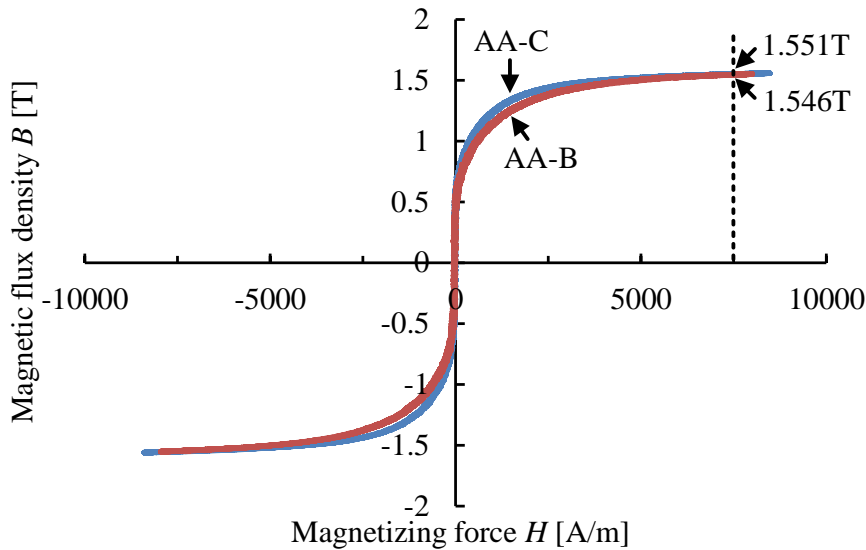
mean square value of $v_2(t)$ at no-load test. Note that $v_2(t)$ is not the value converted to the voltage of the primary winding, but the measured value of the voltage of the secondary winding. The active power measured by the power meter in Fig.4.2, i.e. the time average value of instantaneous power expressed by (4), is equal to the magnetic energy consumed by the iron core.

4.2.2 Measurement results of B-H characteristic

Fig.3 shows the measured B-H characteristics, whereas Table 4.2 shows the magnetic flux density at 7500A/m (which is defined as B75) and the permeability around 0A/m (which is defined as μ_i). The frequency of the applied sinusoidal voltage is low frequency of 50Hz in order to avoid the effects of the eddy current loss. B75 of AA-C and AA-B are 10.8% and 9.9% lower than that of SS-C and SS-B respectively in regard to the difference in the characteristics depending on the material. In addition, μ_i of AA-C and AA-B are 23.6% and 66.7% higher than that of SS-C and SS-B respectively. Therefore, the amorphous alloy has slightly lower magnetic flux density and higher permeability compared with the silicon steel. B75 of SS-B and AA-B are decreased by only 1.3% and 0.3% respectively compared with that of SS-C and AA-C in regard to the difference in the characteristics depending on the processing process. In addition, μ_i of SS-B and AA-B are decreased by 40.0% and 19.1% respectively compared with that of SS-C and AA-C. Therefore, the blanking process has little effect on the magnetic flux density, but it decreases the permeability. This decrease of the permeability will be due to the properties degradation with plastic strain and elastic strain generated at the end of the steel sheet during the blanking processes. However, μ_i of AA-B is still same level as that of SS-C in spite of the properties degradation.



(a) Silicon steel



(b) Amorphous alloy

Fig.4.3. Measured B-H characteristics at a frequency of 50Hz.

Table 4.2. Magnetic flux density at 7500A/m and permeability around 0A/m

| | B_{75} (=B at 7500A/m) | μ_i (=dB/dH around 0A/m) |
|------|--------------------------|------------------------------|
| SS-C | 1.738T | 0.0195H/m |
| SS-B | 1.715T | 0.0117H/m |
| AA-C | 1.551T | 0.0241H/m |
| AA-B | 1.546T | 0.0195H/m |

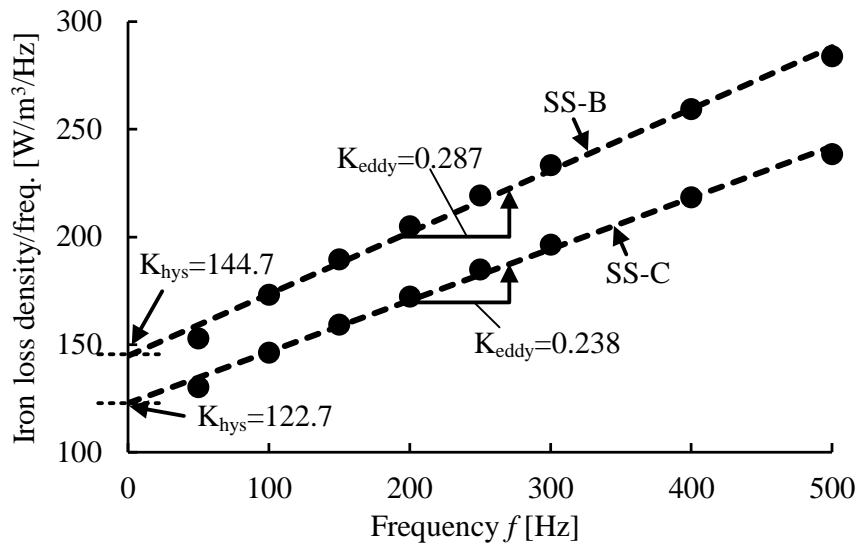
4.2.3 Experimental results of iron loss characteristic

Fig.4.4 shows the measured iron loss characteristic at 1.0T, whereas Table 4.3 shows the coefficients of the Steinmetz equation. The frequency of the applied sinusoidal voltage is low frequency of from 50Hz to 500Hz in order to evaluate the eddy current loss not including the skin effect which occurs in the high frequency region. The Steinmetz equation is expressed as

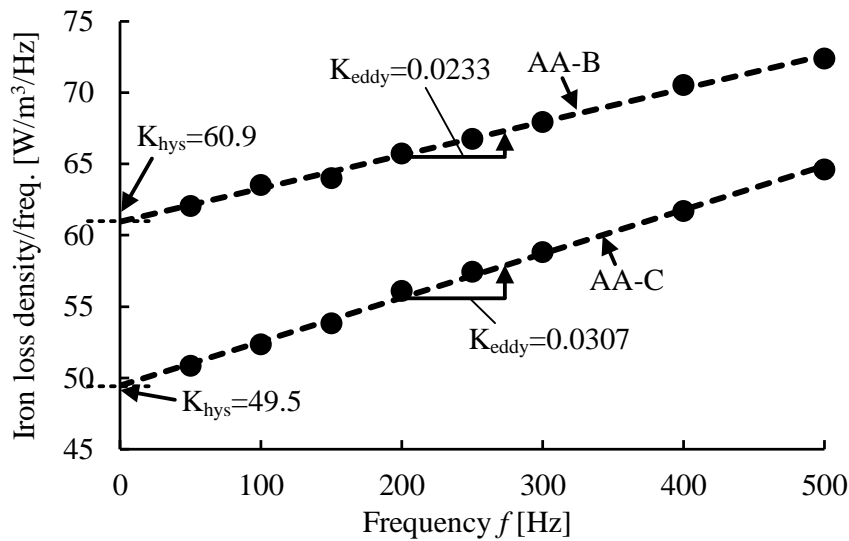
$$W_i = K_{hys} f B_m^{\alpha_{hys}} + K_{eddy} f^2 B_m^2 \dots\dots\dots (4.6)$$

where α_{hys} , K_{hys} and K_{eddy} represents the coefficients of the hysteresis loss and the eddy current loss. K_{hys} and K_{eddy} are calculated as the intercept and slope of W_i / f at $B_m = 1T$ as shown in Fig.4. K_{eddy} of AA-C and AA-B are 87.1% and 91.9% lower than that of SS-C and SS-B respectively in regard to the difference in the characteristics depending on the material. Therefore, the eddy current loss of the amorphous alloy is expected to be 1/10 of the silicon steel at the same f and the same B_m . In addition, K_{hys} of AA-C and AA-B are 59.7% and 57.9% lower than that of SS-C and SS-B respectively. Therefore, the hysteresis loss of the amorphous alloy is expected to be less than 1/2 of the silicon steel at the same f and the same $B_m = 1[T]$ (because of $B_m^{\alpha_{hys}}=1$). K_{eddy} of SS-B is increased by 20.6% compared with that of SS-C, whereas K_{eddy} of AA-B is decreased by 24.1% compared with that of AA-C in regard to the difference in the characteristics depending on the processing process. This will be due to the following two factor; (i) the increase of the eddy current loss due to the remaining conductive elements of the wire cut surface which could not be removed even by etching process in SS-C and AA-C and (ii) the properties degradation with the plastic strain and elastic strain generated at the end of the steel sheet during the blanking processes in SS-B and AA-B. In the silicon steel, the impact of (i) is greater than that of (ii). On the other hand the amorphous alloy, the impact of (i) is smaller than that of (ii). On the other hand, K_{hys} of SS-B and AA-B are increased by 17.9% and 23.0% compared with that of SS-C and AA-C. This will be due to the factor (ii). Therefore, the blanking process has little effect on the eddy current

loss, but it increases the hysteresis loss. This increase of the hysteresis loss is a problem in the electrical properties of the blanked material. Note that the eddy current loss dominates the iron loss of the high-speed motor. Therefore, the properties degradation due to blanking the amorphous alloy is not a serious problem in practical use.



(a) Silicon steel



(b) Amorphous alloy

Fig.4.4. Measured iron loss characteristics at 1.0T.

Table 4.3. Coefficients of the Steinmetz equation

| | $K_{hys.}$ | $K_{eddy.}$ |
|------|------------|-------------|
| SS-C | 122.7 | 0.238 |
| SS-B | 144.7 | 0.287 |
| AA-C | 49.5 | 0.0307 |
| AA-B | 60.9 | 0.0233 |

4.3. Improvement of accuracy of iron loss analysis in

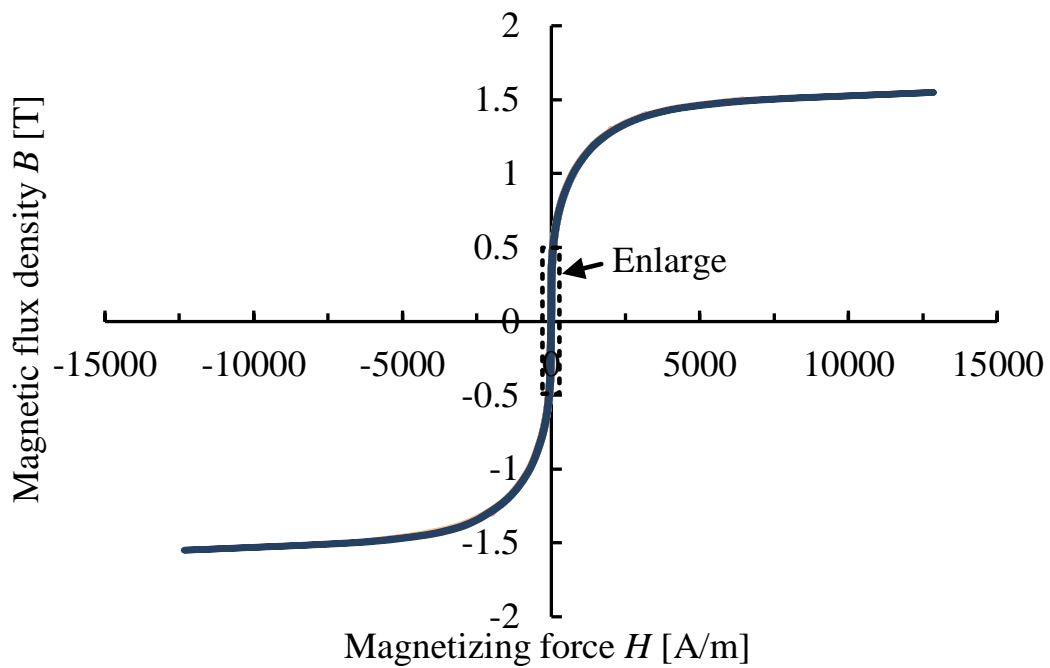
FEA

It was confirmed that the accuracy of FEA is low in the simple iron loss calculation algorithm based on the iron loss curve. This is because the analysis based on the iron loss curve is not applicable into the complicated magnetic flux waveforms of the SRM. In this paper, the hysteresis loss is analyzed based on Play Model [4-1][4-2], whereas the eddy current loss is analyzed by Homogenization method [4-3][4-4]. These methods are higher accuracy than that based on the iron loss curve thanks to the consideration of the DC bias characteristics of the hysteresis loss and the skin effect of the eddy current loss [4-5][4-6].

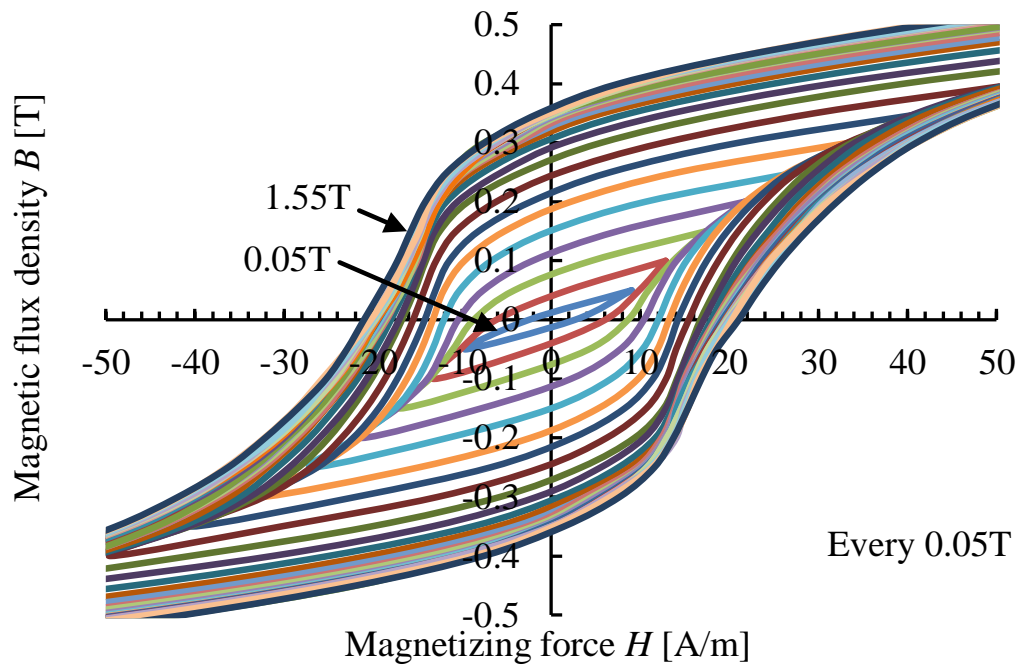
4.3.1 Preparation of Play model method based on measured B-

H trajectory behavior model

Fig.4.5 shows the measured B-H trajectory behavior model of AA-B, whereas Fig.4.6 shows the diagram of play model. The play model is the magnetization model which reproduces any minor loop. The hysteresis loss is calculated from the history of magnetization, i.e. the area of the B-H loop. This method is performed considering the DC bias characteristics of hysteresis loop. The play model is a magnetization model to represent an arbitrary minor loop. The play model is composed of hysterons and shape functions. The hysterons give a phase to the input magnetizing force H and create the elements of the minor loop. By combining several hysterons with different phase delays (i.e., different widths), various minor loops can be represented. However, the hysterons themselves do not have any material properties. The magnetization properties of a material are expressed by a shape function. The shape function is defined separately for each hysteron. It is a function of the respective hysteron value only. The shape function is defined by the nodal values on the hysterons and a linear interpolation function between them. Here, the nodal values are identified from the measured B-H trajectory behavior model. These B-H trajectory behavior model are measured by the method as explained in Subsection 2.2. The measurement range is from 0.05T to 1.90T for 20HX1300, and from 0.05T to 1.55T for 2605SA1. These measured data were implemented in JMAG Designer.



(a) Entire (± 15000 A/m, ± 2 T)



(b) Enlarge (± 50 A/m, ± 0.5 T)

Fig.4.5. Measured B-H trajectory behavior model of AA-B

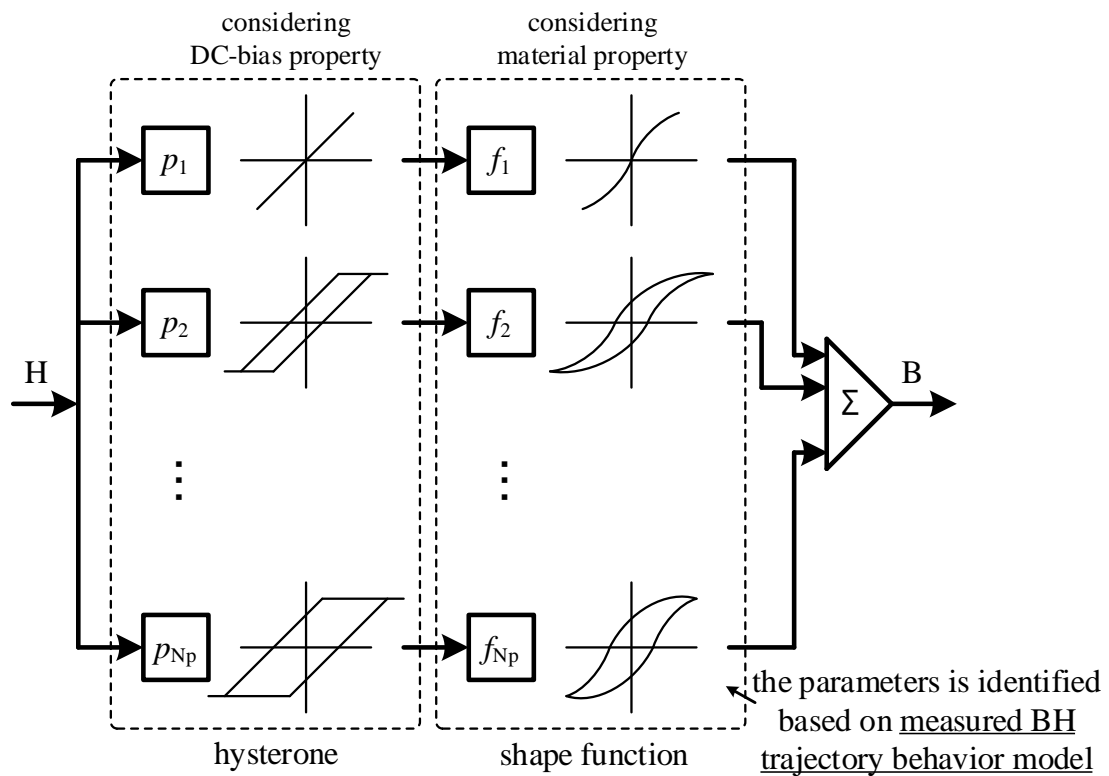


Fig.4.6. Diagram of play model

4.3.2 Preparation of Homogenization method

Table 4.4 shows the characteristic of 20HX1300 and 2605SA1. The classical eddy current loss W_{eddy_cla} is calculated from the thickness d and electrical resistivity ρ of the electrical sheet in the homogenization method. The values of d and ρ are the catalog value [4-7][4-8] in this paper. This method is performed considering the skin effect of the eddy current loss. Note that the classical eddy current loss calculated by the homogenization method does not include the excess loss such as anomalous eddy current loss. Therefore, the modified coefficient κ of the classical eddy current loss is defined as

$$\kappa = \frac{K_{eddy} f^2 B_m^2}{(\pi f d B_m)^2} = \frac{K_{eddy}}{6p} \dots\dots\dots (4.7)$$

where K_{eddy} represents the coefficients of the eddy current loss which does not include the skin effect as explained in Subsection 2.3. The eddy current loss W_{eddy} including the excess loss W_{eddy_ex} is expressed as

$$W_{eddy} = W_{eddy_cla} + W_{eddy_ex} = \kappa W_{eddy_cla} \dots\dots\dots (4.8)$$

Therefore, the eddy current loss is calculated by multiplying the analysis value of the classical eddy current loss by the modified coefficient κ . As shown in Table 4.4, the κ of the blanked silicon steel is 2.40, whereas the κ of the blanked amorphous alloy is 29.5. There is a pretty difference between the actual eddy current loss and the eddy current loss calculated by the physical property such as the thickness and electrical resistivity in the blanked amorphous alloy.

Table 4.4. Characteristic of 20HX1300 and 2605SA1

| | d [mm] | p [$10^{-6}\Omega m$] | K_{eddy} | κ |
|----------------|----------|---------------------------|------------|----------|
| 20HX1300(SS-B) | 0.2 | 0.55 | 0.287 | 2.40 |
| 2605SA1(AA-B) | 0.025 | 1.3 | 0.0233 | 29.5 |

4.4. Design and Manufacture of SRMs

Table 4.5 shows the specifications of the designed SRMs, whereas Fig.4.7 shows the photograph of the manufactured amorphous-allow- SRM. 70W SRMs (40mm thickness) are designed as first prototype. Two motor cores are made by blanking (a) 20HX1300 and (b) 2605SA1, which are referred as “SS-SRM” and “AA-SRM” in this paper. The detail of the employed innovative technology in blanking of the amorphous alloys is found in Ref.[3-9]. The comparative evaluation of the electrical characteristics of the different blanking technologies will be discussed in a future work. Note that the stator outer diameters of the blanked motor core are 40mm. There are problems of the material availability and the mold precision in order to blank larger motor core. The number of layers of SS-SRM is 200, whereas that of AA-SRM is 1600. These motors are manufactured by adhesively laminating the blanked steel sheets. Since it is difficult to laminate very thin steel sheets of the amorphous alloy with a caulking or a welding, an impregnation lamination is employed. There is a problem of the lower productivity due to the requirement of the manufacturing time for the adhesion process. In order to increase the effect of the iron loss reduction, a relatively high-speed motor is designed. In addition, the coil space is bigger than that of a general design [4-10] in order to increase the winding diameter. This results in low winding resistance and copper loss reduction. Furthermore, the airgap length is selected in order to achieve the highest efficiency within the mechanical constraint of 0.1 mm.

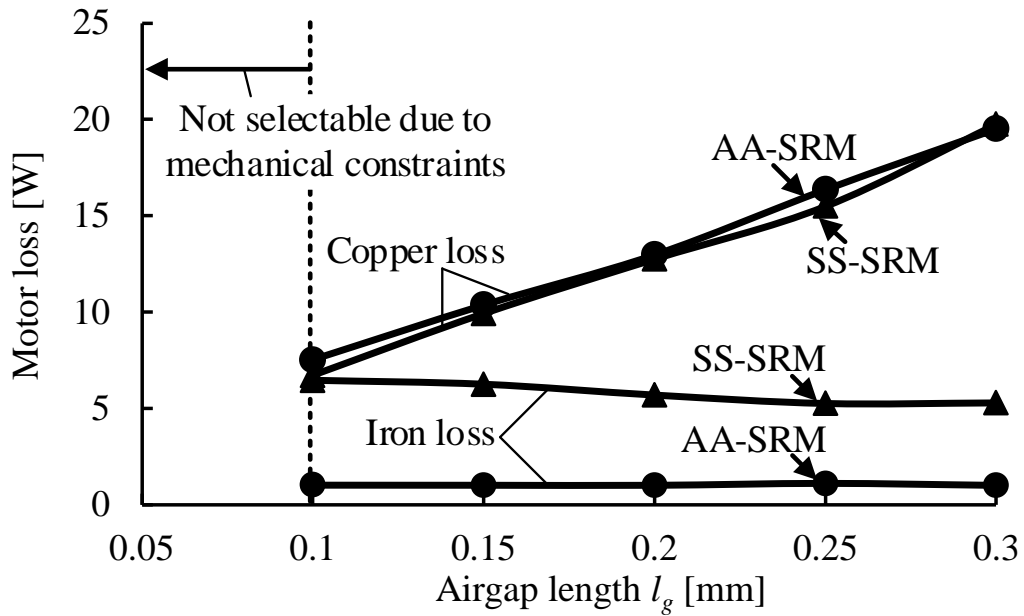
Table 4.5. Specifications of test SRMs

| Name of motor | SS-SRM | AA-SRM |
|----------------------|--|------------------------------|
| Iron core | 20HX1300 (high grade silicon steel) | 2605SA1 (amorphous alloy) |
| Number of layers | 200 (cal.) | 1600 (cal.) |
| Processing method | Laminated after Blanking | |
| Output power | 70W | |
| Maximum speed | 10000r/min | |
| Number of phases | 3 | |
| Number of poles | 6 (stator) / 4 (rotor) | |
| Motor size | 40mm × 40mm | |
| Airgap | 0.1mm | |
| Pole arc | 21deg. (stator) / 31deg. (rotor) | |
| Number of turns | 73turns | |
| Space factor of coil | 34% | |

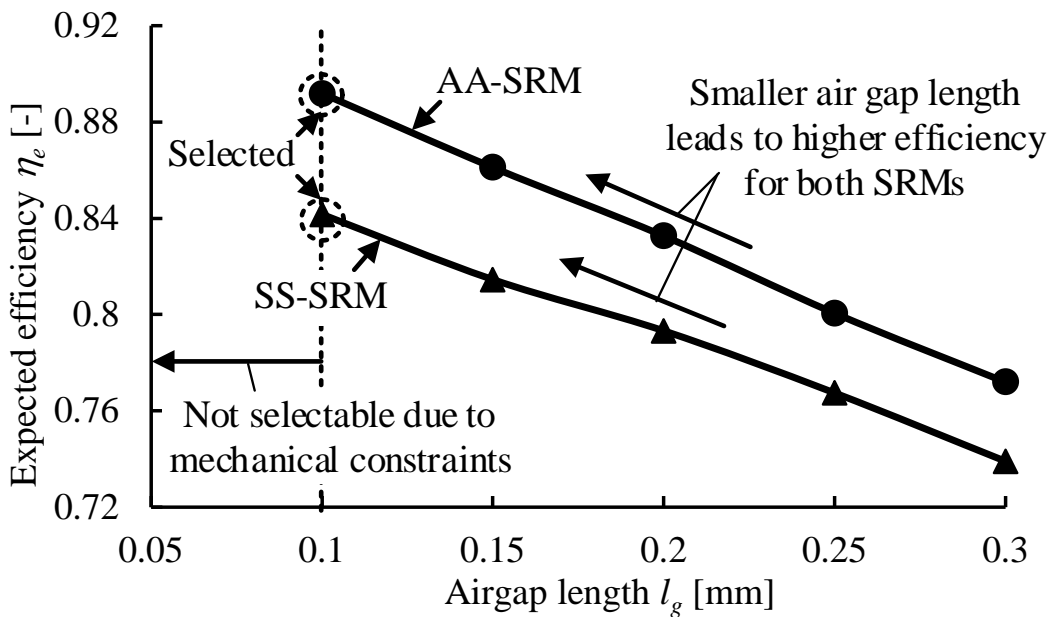


Fig.4.7. Photograph of 70W-SRM made of blanked amorphous alloy foil.

Fig.4.8(a) depicts the relationship between the airgap length and the motor loss, whereas Fig.4.8(b) shows the relationship between the airgap length and the motor efficiency. As shown in Fig.4.8(a), the large airgap extremely increases the copper loss. This is because the reluctance torque becomes small due to small change of the magnetic resistance with the change of the airgap length. The copper loss of AA-SRM remains almost the same to that of SS-SRM. Therefore, the high efficiency is not expected due to small effect of reducing the motor loss with the low iron loss characteristics of the amorphous alloy. In this paper, the airgap length in both SS-SRM and AA-SRM are selected to be 0.1mm in order to achieve the highest efficiency within the mechanical constraint.



(a) Motor loss



(b) Expected efficiency

Fig.4.8. Effect of airgap length

The information about the cost, structural strength, and heat-resistant are described. Note that the main subject of this paper is the evaluation of the electrical characteristics of the motors made by blanking the amorphous alloy. Therefore, the information about the cost and other are described as reference values.

Table 4.6 shows the cost comparison in the different processing methods excluding the cost of the molds and the manufacturing equipment. The cost reduction by the blanking of the silicon steel in the mass production is expected to be 1/30~1/50 compared with that of the wire cutting. On the other hand, that of the amorphous alloy is expected to be 1/10 due to the larger number of required sheets and the difficulty of processing of amorphous alloy.

Table 4.7 shows the cost comparison of blanking processing in the different materials. The material cost of the amorphous alloy is expected to be increased by 2 times compared with that of the silicon steel [4-11]. In addition, the jig tool cost is expected to be increased by from 3 times to 5

Table 4.6. Cost comparison in different processing methods excluding the cost of molds and equipment

| | Wire cure After Laminated | Laminated After Blanking |
|-----------------|---------------------------|----------------------------------|
| Silicon steel | K_{SS-B} | $K_{SS-B} \times 1/30 \sim 1/50$ |
| Amorphous alloy | K_{AA-B} | $K_{AA-B} \times 1/10$ |

Table 4.7. Cost comparison of blanking processing in different materials

| | Silicon steel | Amorphous alloy |
|-------------------|--------------------------|------------------------------|
| | Laminated After Blanking | |
| Material price | K_{SS-M} | $K_{SS-M} \times 2$ |
| Jig tool costs | K_{SS-J} | $K_{SS-J} \times 3 \sim 5$ |
| Re-polishing cost | K_{SS-R} | $K_{SS-R} \times 30 \sim 50$ |
| Assembly cost | K_{SS-A} | $K_{SS-A} \times 30 \sim 50$ |

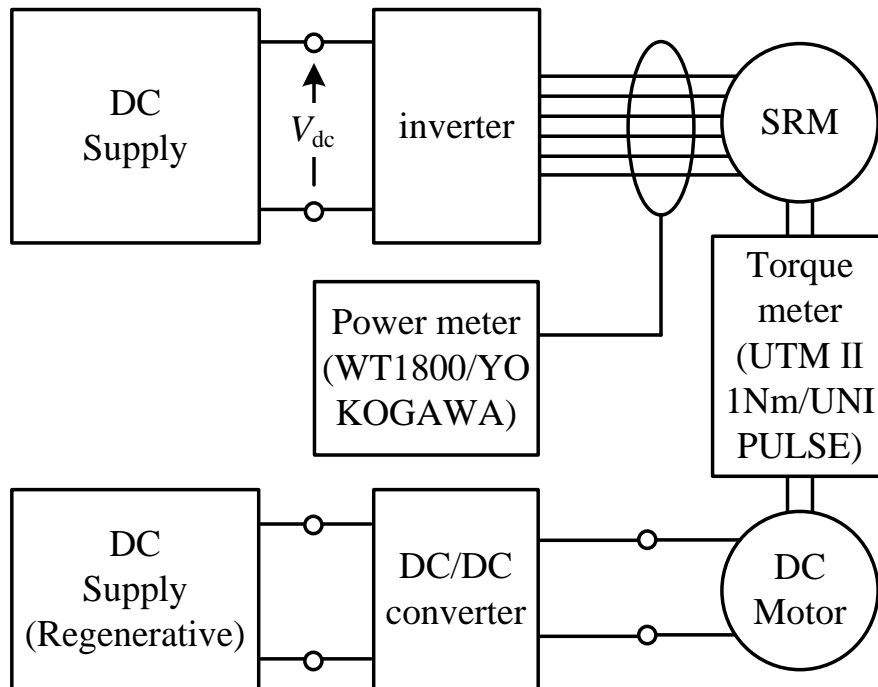
times. This is because the clearance of the jig tool is very small, and the required accuracy of the jig tools is very high. In addition, the re-polishing cost is expected to be increased by from 30 times to 50 times. This is because not only the number of required sheets is larger but also the tensile strength is high in the amorphous alloy. In addition, the assembly cost is expected to be increased by from 30 times to 50 times because of the large number of required sheets, more frequently re-polishing, and the manufacturing time for the adhesion process in the impregnation lamination.

The structural strength of the motor made by blanking the amorphous alloy is higher than that of the silicon steel. This is because the structural strength depends on the hardness of the core. The hardness of the amorphous is approximately 5 times higher than that of the silicon steel. On the other hand, the heat-resistant is expected to be same.

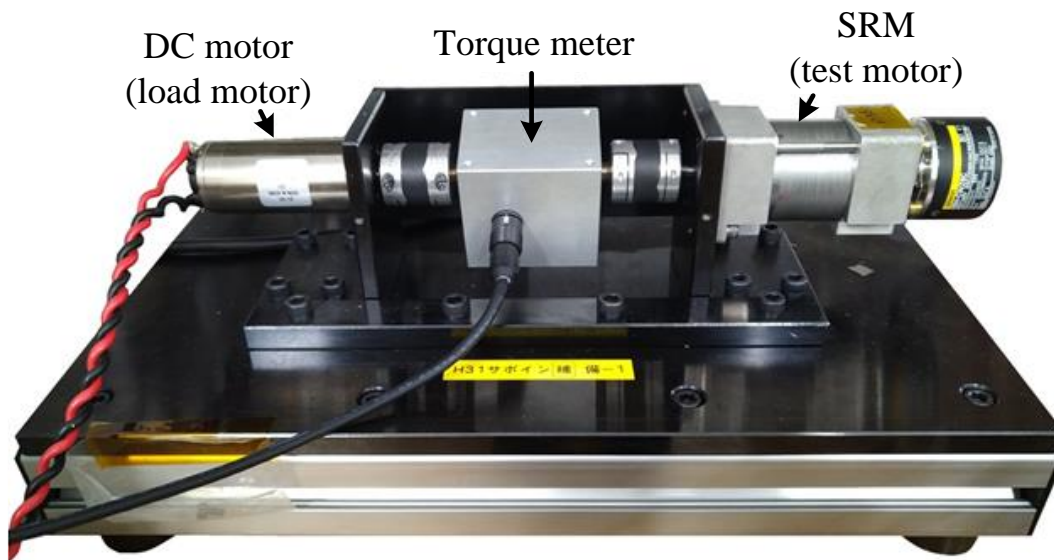
4.5. Experimental evaluation of SRMs

4.5.1 Test system configuration

Fig.4.9 (a) depicts the diagrams of the measurement setup for test motor, whereas Fig.4.9 (b) shows the photograph of the measurement bench. In particular, the motor efficiency characteristics and the iron loss characteristics of SS-SRM and AA-SRM are experimentally evaluated with the measurement bench. The input electric power and the root-mean-square (RMS) value of the winding current are measured with the power meter (PW3390, accuracy $\pm 0.04\%$, bandwidth 200kHz, HIOKI), whereas the torque is measured with the torque meter (UTMII-1Nm, accuracy $\pm 0.01\%$, bandwidth 1kHz, UNIPULSE). The winding temperature is measured by thermocouple built into the winding.



(a) Diagrams of measurement setup for test SRM



(b) Photograph of measurement bench
Fig.4.9. Measurement system for test SRM

The motor efficiency η_m is expressed as

$$\eta_m = \frac{P_{out}}{P_{in}} = \frac{T_{out} \omega_m}{P_{in}} \dots\dots\dots (4.9)$$

where P_{out} is the shaft output which is calculated as product of the measured torque T_{out} and the shaft angular velocity ω_m , whereas P_{in} is the input electric power which is measured by the power meter. According to the preliminary verification, the mechanical loss has large dispersion. In addition, there are individual differences of mechanical loss in SS-SRM and AA-SRM.

Therefore, it is impossible for the evaluation with Eq.(4.9) to make a fair comparison. In order to resolve the above problems, the efficiency η_e regarding the mechanical loss as a part of the shaft output is defined as

$$\eta_e = \frac{P_{out_m}}{P_{in}} = \frac{P_{out} + W_m}{P_{in}} = \frac{T_{out} \omega_m + T_{mech} \omega_m}{P_{in}} \dots\dots\dots (4.10)$$

where P_{out_m} is the shaft output when the mechanical loss W_m is regarded as shaft output. Note that W_m is the product of the measured torque T_{mech} and the rotational angular velocity ω_m when the DC motor drives the system with no SRM excitation. On the other hand, the iron loss W_i is calculated by subtracting P_{out} , W_m , and the copper loss W_c from P_{in} . Therefore, W_i is expressed as

$$\begin{aligned} W_i &= P_{in} - P_{out} - W_c - W_m \\ &= P_{in} - T_{out} \omega_m - \sum_{x=u}^w R_x(t_{temp}) I_{RMS_x}^2 - T_{mech} \omega_m \dots\dots\dots (4.11) \end{aligned}$$

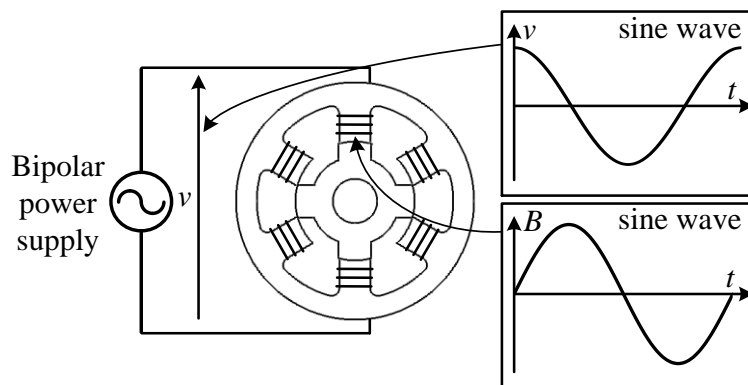
where $R_x(t_{temp})$ is the winding resistance of x -phase respectively at winding temperature t_{temp} , whereas I_{RMS_x} is the root-mean-square (RMS) value of the winding current of x -phase respectively.

4.5.2 Comparison of Analysis Accuracy

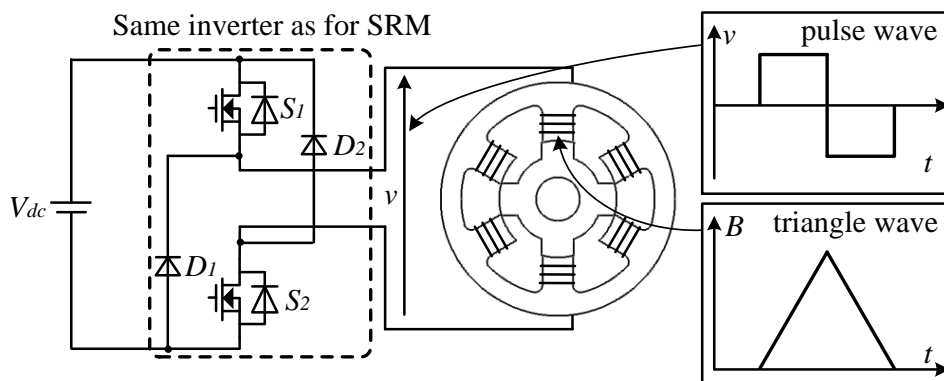
First, the analysis accuracy is compared between the analysis based on the iron loss curve and the analysis based on the B-H trajectory behavior model. In order to confirm the analysis accuracy of the iron loss with high accuracy, the iron loss in the completely stopped state is compared.

Fig.4.10 shows the diagrams of the measurement setup for the iron loss in the completely stopped state. When the one phase of the SRM is excited from the power supply, the rotor stops in a completely alignment state. Therefore, the iron loss in the completely stopped state can be measured by the continuous excitation into the one phase. Since it does not rotate ($\omega_m=0$), Eq.(4.11) becomes as follows.

$$W_i = P_{in} - R_u(t_{temp}) I_{RMS_u}^2 \dots\dots\dots (4.12)$$



(a) Excitation of sinusoidal waveform

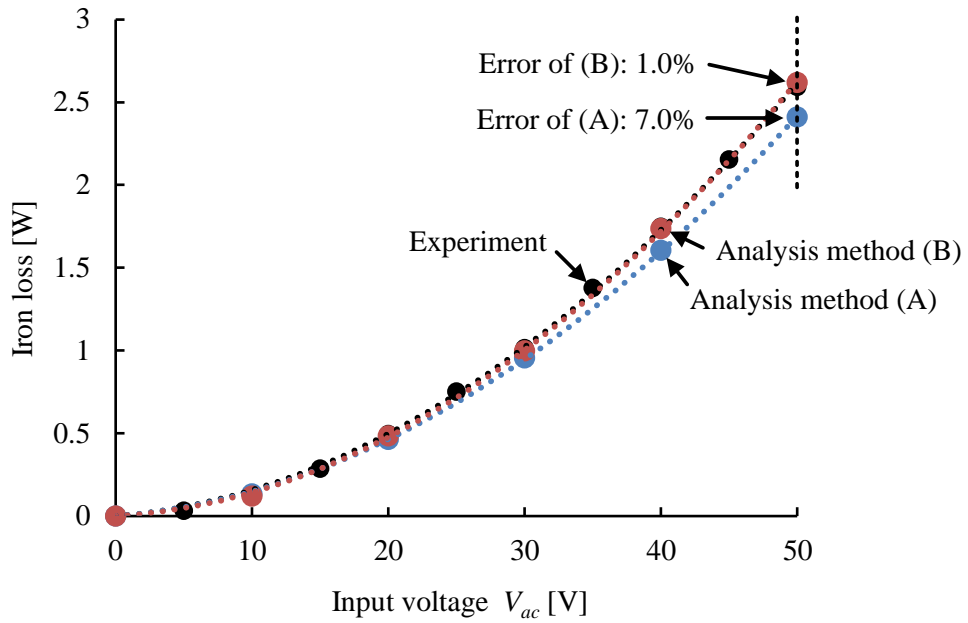


(b) Excitation of pulse waveform

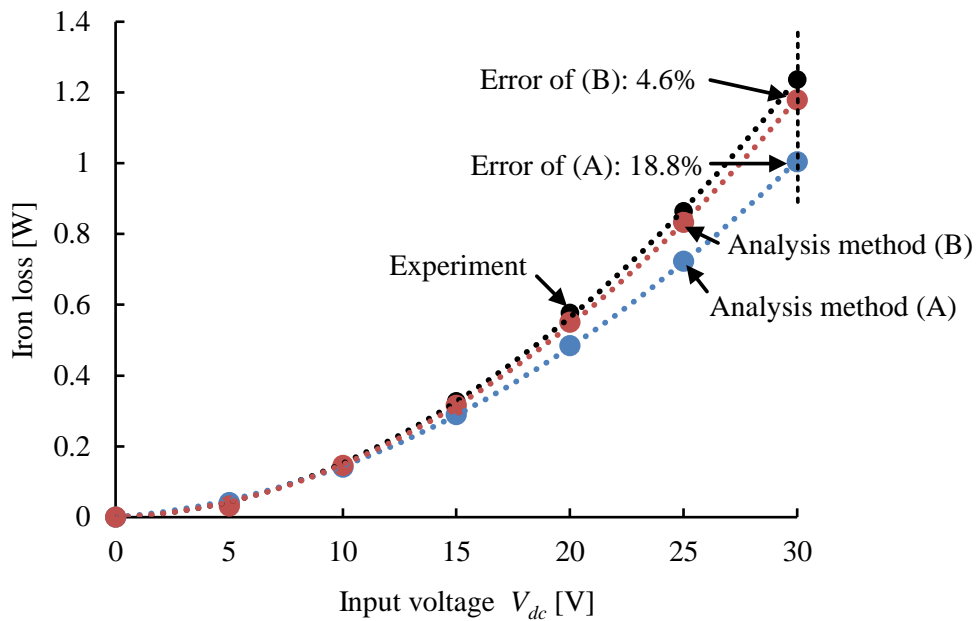
Fig.4.10. Diagrams of measurement setup for the iron loss in the completely stopped state

In this measurement method, it is possible to avoid the problem of mechanical loss, which generally has large variations. Therefore, the iron loss can be measured with high accuracy. In this study, (a) the case of the sine wave excitation using a bipolar power supply and (b) the case of the pulse wave excitation using an SRM asymmetric H-bridge circuit. In the case of the sine wave excitation, the magnetic flux density waveform is also a sine wave. Therefore, high analysis accuracy is expected regardless of the analysis method. On the other hand, in the case of the pulse excitation, the magnetic flux density waveform is a triangular wave (in other words, it has non-linear and DC superimposition). Therefore, the analysis accuracy is low in the analysis method based on the iron loss curve.

Fig.4.11 shows a comparison of the experimental and analytical values of the iron loss. Note that “Method A” is an analysis method based on the iron loss curve explained in Section 2.3.3 for both the hysteresis loss and the eddy current loss. The hysteresis loss is compensated for the loss of the minor loop by the method of counting the hysteresis loop explained in Section 2.3.4. On the other hand, “Method B” is the play model method using the B-H trajectory behavior model explained in Section 4.3.1 for the hysteresis loss and the homogenization method explained in Section 4.3.2 for the eddy current loss. In the case of the sinusoidal excitation, the method A has an error rate of 7.0% and the method B has an error rate of 1.0%. Therefore, the analysis accuracy is enough high regardless of the analysis method. This is because the magnetic flux density is sinusoidal, which has linearity. On the other hand, in the case of the pulse wave excitation, the method A has an error rate of 4.6% and method B has an error rate of 18.8%. Therefore, the analysis method based on the iron loss curve has low analysis accuracy. On the other hand, the analysis method based on the B-H trajectory behavior model has high analysis accuracy. This is because the magnetic flux density is triangular, which does not linearity. Therefore, the superiority of the analysis method based on the B-H trajectory behavior model were verified.



(a) Excitation of sinusoidal waveform



(b) Excitation of pulse waveform

Fig.4.11. Comparison of the experimental and analytical values of the iron loss.

4.5.3 Test procedure

The copper loss (winding resistance) depends on the winding temperature, whereas the mechanical loss depends on the bearing temperature. In particular, the bearing temperature cannot be measured in this system. Therefore, a warm-up operation is required in order to sufficiently warm the bearing.

Fig.4.12 shows the speed and the torque during the experiment (Step1~Step6), whereas Table 4.8 shows the operation of load motor and test motor at each step. At first, the motor is accelerated by load motor (Step1). Next, the load motor drives the system with no SRM excitation for a long time (Step2). In Step2, the mechanical loss becomes stable thanks to warm-up of bearing. Next, the test motor output the torque by controlling the current to the pulse current with the command amplitude (Step3). In Step3, the efficiency and iron loss are calculated from the average value of the measured value in this section. Next, the load motor drives the system with no SRM excitation again (Step4). In Step4, the mechanical loss is calculated from the average value of the measured value in this section. Finally, the motor is decelerated (Step5) and stop (Step6). The zero point of the torque meter is confirmed in the stopped state (Step6).

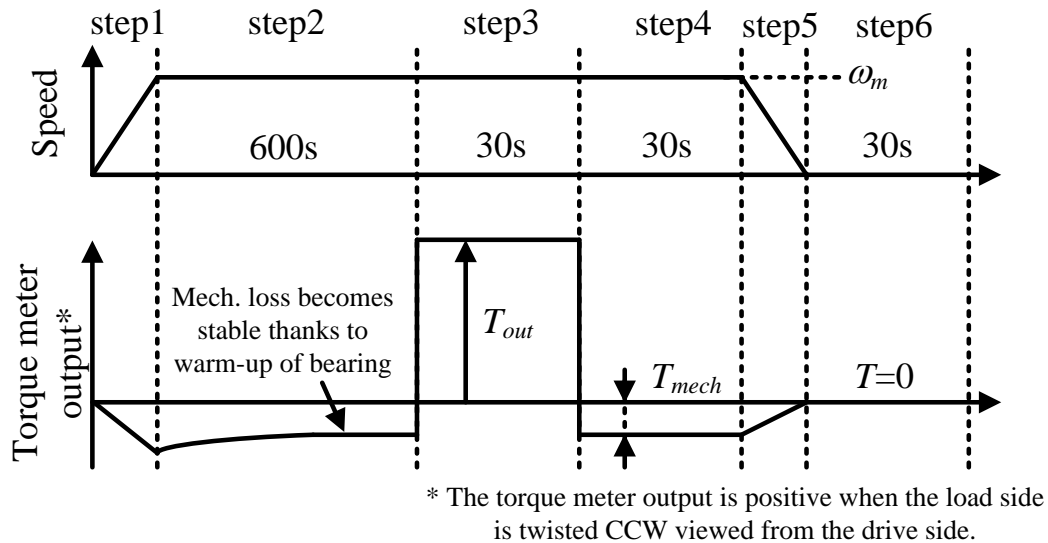


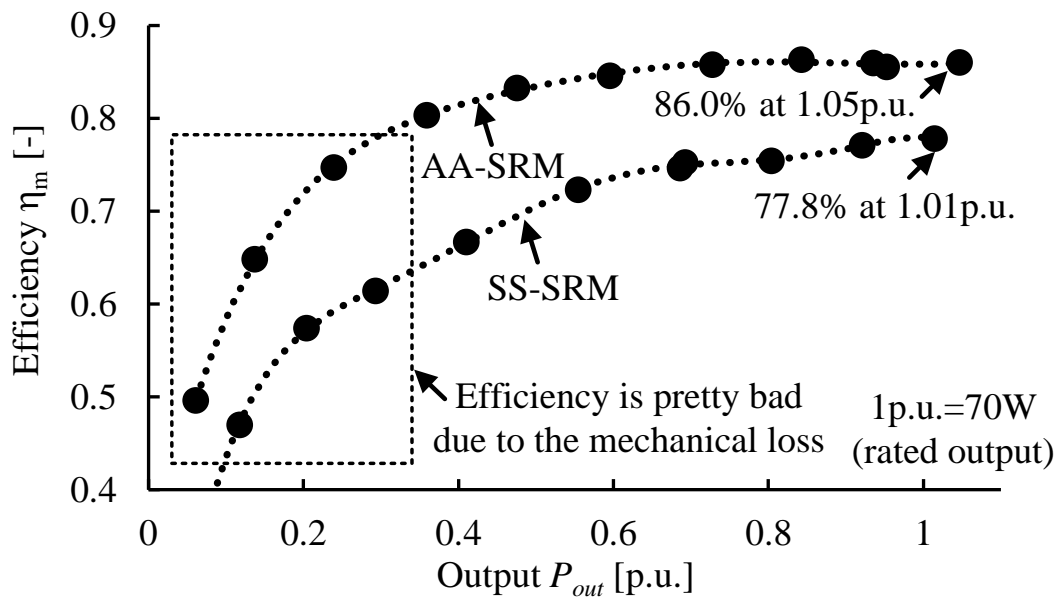
Fig.4.12. The speed and the torque meter output during the experiment (Step1~Step6)

Table 4.8. The operation of load motor and test motor at each step

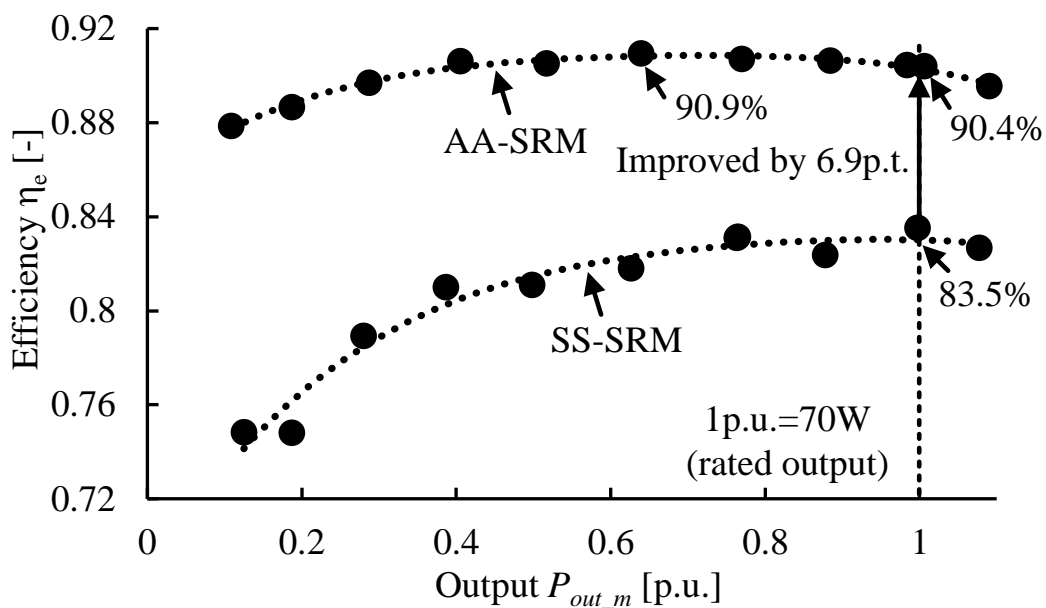
| | Load motor | Test motor | Purpose |
|-------|---------------|---------------|-------------------------|
| Step1 | Acceleration | No excitation | - |
| Step2 | ASR | No excitation | Warm-up of bearing |
| Step3 | ASR | ACR | Output measurement |
| Step4 | ASR | No excitation | Mech. loss measurement |
| Step5 | Deceleration | No excitation | - |
| Step6 | No excitation | No excitation | Zero point confirmation |

4.5.4 Measured characteristics of SS-SRM and AA-SRM

Fig.4.13 shows the motor efficiency characteristics of SS-SRM and AA-SRM at 10000r/min. The mechanical loss is not regarded as a part of the shaft output (i.e. use of Eq.(4.9)) in Fig.4.13(a), whereas the mechanical loss is regarded as a part of the shaft output (i.e. use of Eq.(4.10)) in Fig.4.13(b). As shown in Fig.4.13(a), the motor efficiency of AA-SRM is higher than that of SS-SRM in all output range. In addition, AA-SRM achieved the maximum motor efficiency of 86.0% at 1.05p.u. of rated power (70W). In the low torque region, the efficiency is pretty bad due to the mechanical loss. As shown in Fig.4.13(b), the motor efficiency of AA-SRM is approximately 90% in all output range. In addition, AA-SRM achieved the motor efficiency of 90.4% at rated power (70W). At this operating point, the motor efficiency of AA-SRM is improved by 6.9 p.t. compared with that of SS-SRM.



(a) Not regarding the mechanical loss as a part of the shaft output (Eq.(3.9))



(b) Regarding the mechanical loss as a part of the shaft output (Eq.(3.10))

Fig.4.13. Efficiency characteristics of SS-SRM and AA-SRM in all output range at 10000r/min.

Fig.4.14 shows the comparison results of (a) the copper loss and (b) the iron loss of SS-SRM and AA-SRM. As shown in Fig.4.14(a), the copper loss of AA-SRM is reduced by approximately 20% compared with that of SS-SRM. In addition, as shown in Fig.4.14(b), the iron loss of AA-SRM is reduced by approximately 75% compared with that of SS-SRM. Note that the increase in the iron loss of AA-SRM decreases at high output, i.e. W_i / P_{out_m} becomes low. This is because the increase of the magnetic density

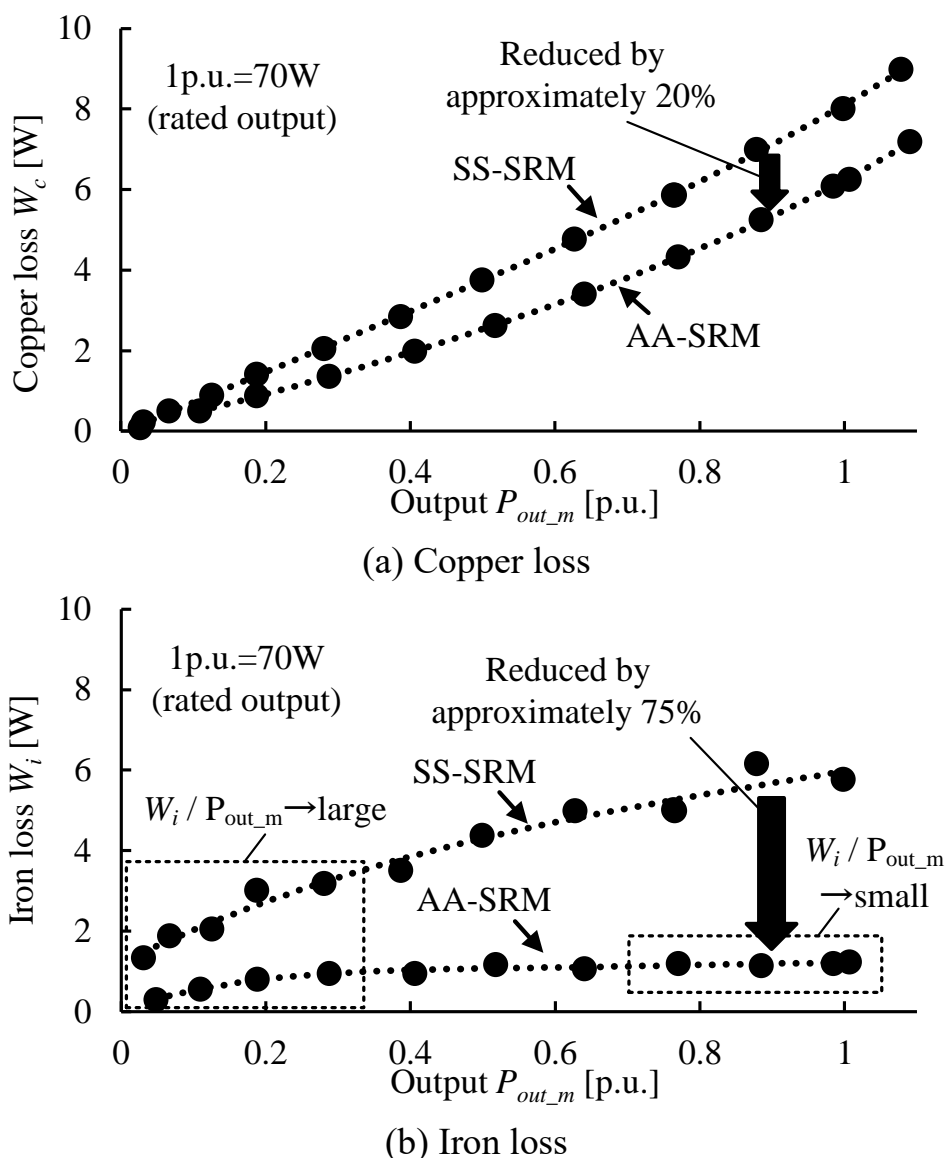


Fig.4.14. Motor loss comparison between SS-SRM and AA-SRM in all output range at 10000r/min.

decreases at high output due to the magnetic saturation of the amorphous alloy. In addition, the increase in the iron loss increases at low output, i.e. W_i / P_{out_m} becomes high. In the current hysteresis control with a constant hysteresis width, the iron loss due to the switching of the inverter is almost same, i.e. the influence becomes relatively large in the low output.

Fig.4.15 shows the comparison result of motor loss at rated power (70W). As shown in Fig.4.15, the copper loss of AA-SRM is reduced by 21.9% compared with that of SS-SRM. On the other hand, the iron loss of AA-SRM is reduced by 78.7% compared with that of SS-SRM. Therefore, it is confirmed that the iron loss reduction effect of the motor core with the amorphous alloy is high even in the blanked amorphous alloy.

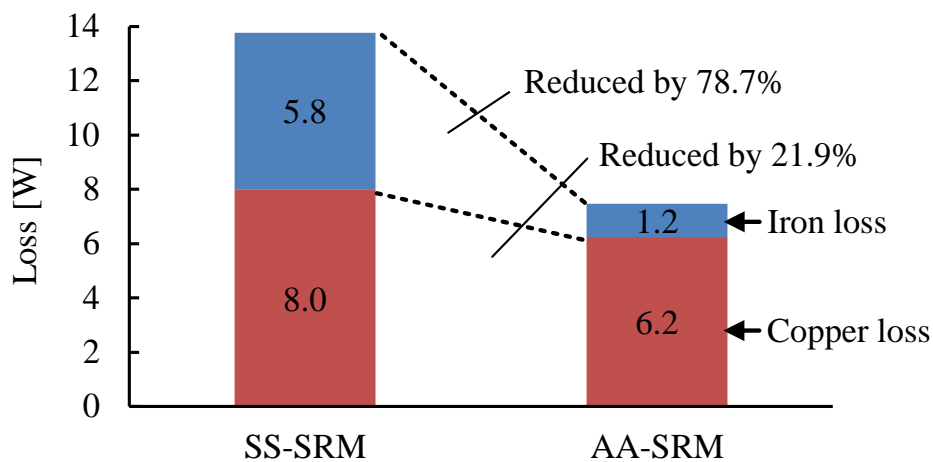
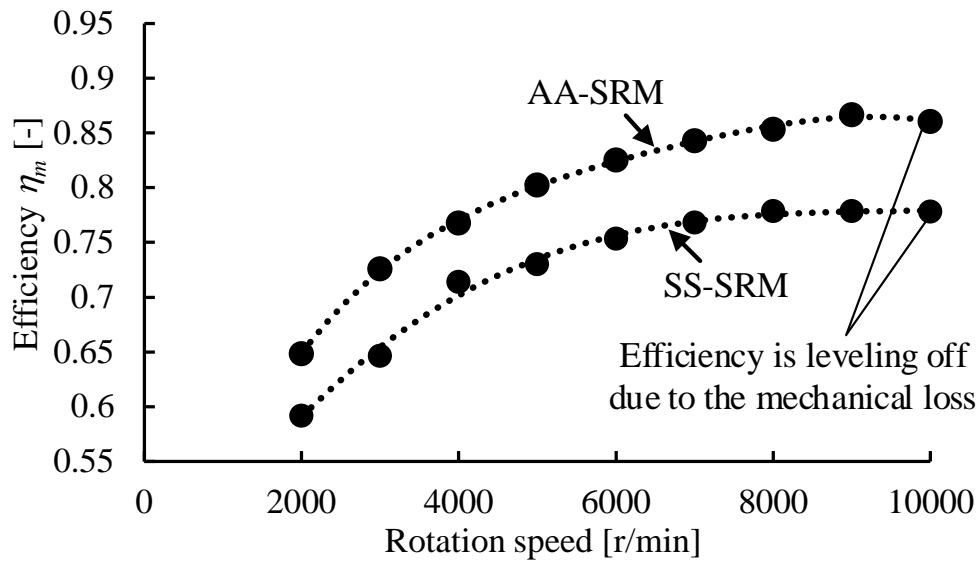
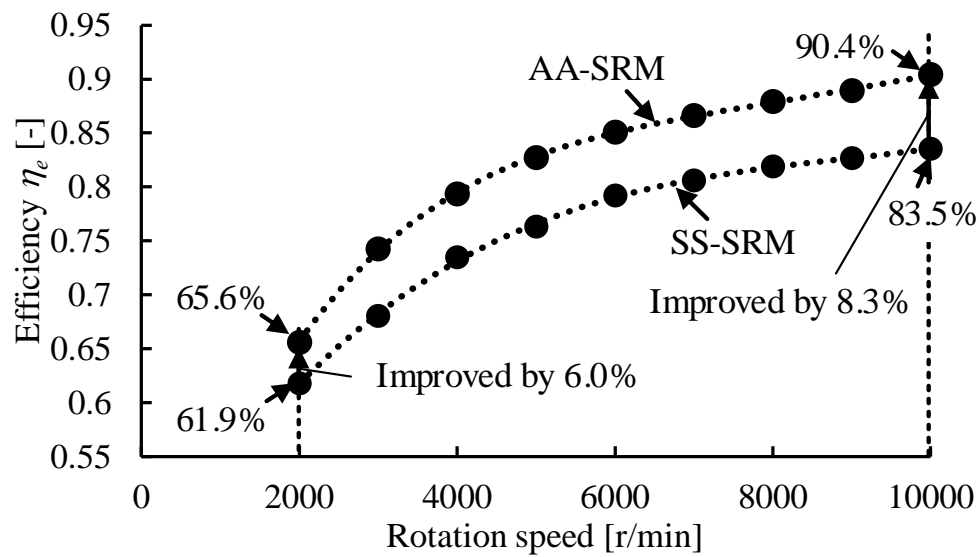


Fig.4.15. Motor loss comparison between SS-SRM and AA-SRM of rated power (70W) at 10000r/min.

Fig.4.16 shows the motor efficiency characteristics of SS-SRM and AA-SRM in all speed range at 1p.u. torque. The mechanical loss is not regarded as a part of the shaft output (i.e. use of Eq.(4.9)) in Fig.4.16(a), whereas the mechanical loss is regarded as a part of the shaft output (i.e. use of Eq.(4.10)) in Fig.4.16(b). As shown in Fig.4.16(a)(b), the motor efficiency of AA-SRM is higher than that of SS-SRM in all speed range. In addition, as shown in Fig.4.16(a), the motor efficiency is leveling off at approximately 10000 r/min due to the mechanical loss. As shown in Fig.4.16(b), the motor efficiency of AA-SRM is improved by 8.3% compared with that of SS-SRM at 10000r/min, while the motor efficiency of AA-SRM is improved by 6.0% compared with that of SS-SRM at 2000r/min. Therefore, the efficiency improvement thanks to the low iron loss characteristic of the amorphous alloy becomes greater at higher speeds.



(a) Not regarding the mechanical loss as a part of the shaft output (Eq.(3.9))



(b) Regarding the mechanical loss as a part of the shaft output (Eq.(3.10))

Fig.4.16. Efficiency characteristics of SS-SRM and AA-SRM in all speed range at 1p.u. torque.

Fig.4.17 shows the iron loss characteristics of SS-SRM and AA-SRM in all speed range at 1p.u. torque. The iron loss of AA-SRM is reduced by approximately 75% compared with that of SS-SRM in all speed range.

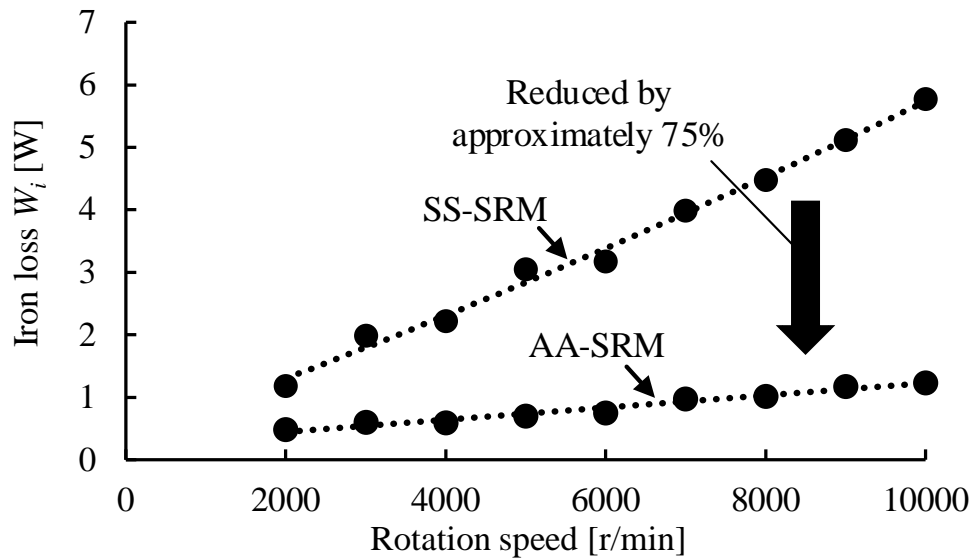
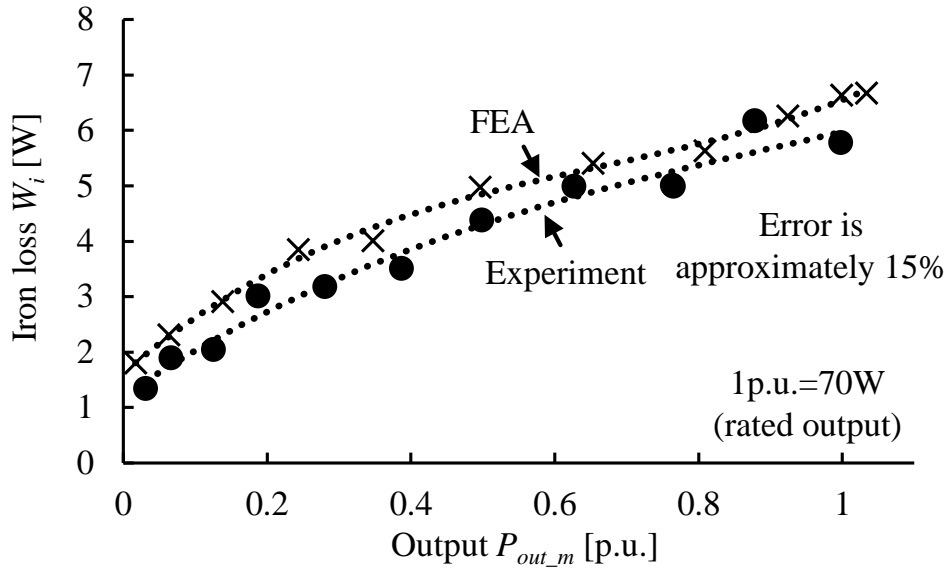


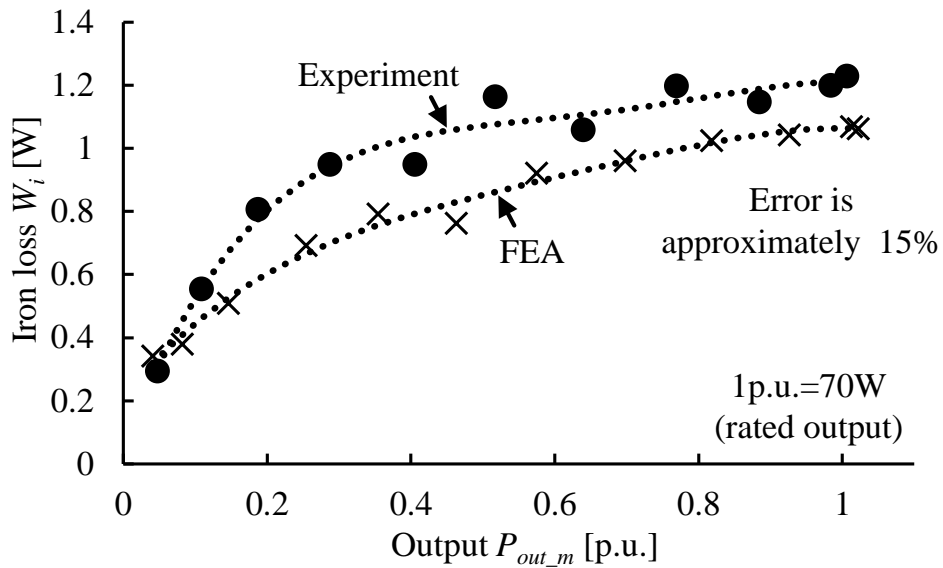
Fig.4.17. Iron loss characteristics of SS-SRM and AA-SRM in all speed range at 1p.u. torque.

4.5.5 Comparison results between measurement and FEA

Fig.4.18 shows the comparison between the measurement results and the FEA results of the iron losses of (a) SS-SRM and (b) AA-SRM. As shown in Fig.4.18, there is an error of approximately 15% between the measurement results and the FEA results in both SS-SRM and AA-SRM. These errors will be due to the accuracy of FEA analysis and the accuracy of measurement results. The characteristics of the blanked SRM is analyzed from the data of the characteristics of the blanked ring cores. However, the impact of the blanking process will be not always the same as that of the ring core, especially in complicated parts such as motor teeth. In addition, the iron loss in measurement results is the value calculated indirectly from other measured values by Eq.(4.11). However, there are errors in the value calculated iron loss due to the unconsidered loss such as the stray load loss and the AC copper loss.



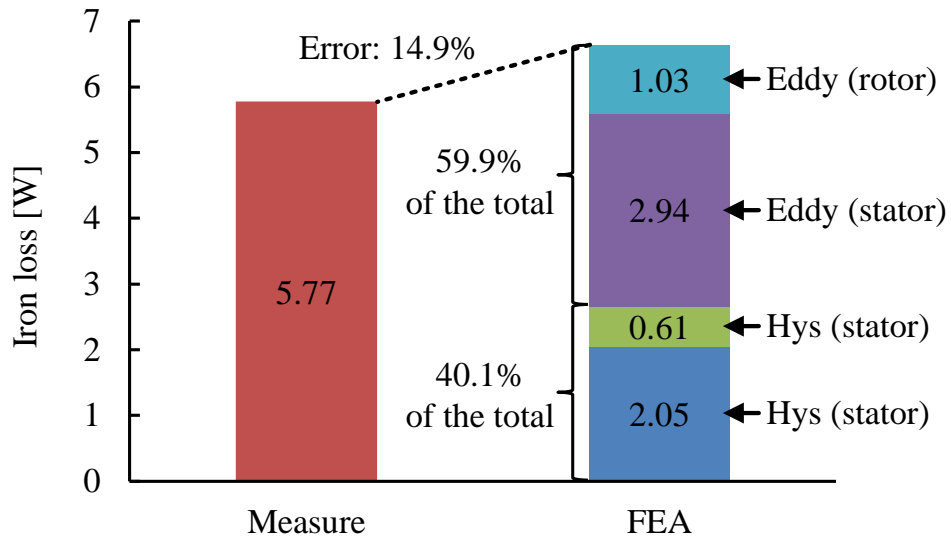
(a) SS-SRM



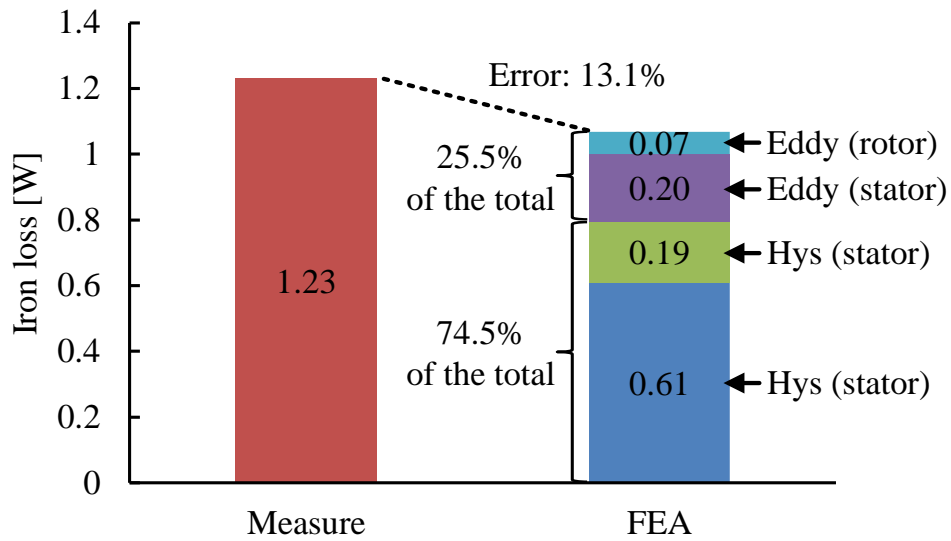
(b) AA-SRM

Fig.4.18. Comparison results of measurement and FEA in all output range at 10000r/min.

Fig.4.19 shows the separation results of the iron loss of (a) SS-SRM and (b) AA-SRM at rated power (70W). The errors between the measurement results and the FEA results are 15% or less in both SS-SRM and AA-SRM. In SS-SRM, the eddy current loss is 59.9%, whereas the hysteresis loss is 40.1% of 5.77W of the total iron loss. On the other hand, in AA-SRM, the eddy current loss is 25.5%, whereas the hysteresis loss is 74.5% of 1.23W of the total iron loss. Therefore, the eddy current loss dominates the iron loss in SS-SRM, whereas the hysteresis loss dominates the iron loss in AA-SRM. In general, the eddy current loss dominates the iron loss of the general high-speed motor as shown in Fig.4.19(a) since the eddy current loss is proportional to the square of the electrical frequency. In the amorphous alloy, the eddy current loss is 1/10 and the hysteresis loss is 1/2 compared with the silicon steel. Therefore, the dominant eddy current loss at high-speed motor is dramatically reduced.



(a) SS-SRM



(b) AA-SRM

Fig.4.19. Iron loss separation results of rated power (70W) at 10000r/min.

4.6. Conclusion

In this chapter, a method for accurate electromagnetic field analysis of iron loss using a B-H trajectory behavior model and a design method for high-efficiency motors based on the analysis were explained. In particular, by applying the method into a blanked amorphous material, the problem of degradation due to blanking during mass production was quantitatively demonstrated. First, a simple experiment using a ring core was performed to quantitatively show the effect of processing degradation due to blanking. Next, the B-H trajectory behavior model was multiplied by the algorithm implemented in the electromagnetic field analysis software to realize highly accurate iron loss analysis. Using the accurate iron loss analysis, a high-efficiency motor utilizing blanked amorphous material was designed and prototyped. The efficiency and loss of the prototype motor were evaluated, and the superiority of the designed motor was explained. Finally, the accuracy of the iron loss analysis was verified to validate the proposed method.

Bibliography

- [4-1] T. Matsuo, D. Shimode, Y. Terada, and M. Shimasaki, “Application of stop and play models to the representation of magnetic characteristics of silicon steel sheet,” *IEEE Transactions on Magnetics*, Vol.39, no.3, pp.1361-1364 (2003)
- [4-2] T. Matsuo and M. Shimasaki “An identification method of play model with input-dependent shape function,” *IEEE Transactions on Magnetics*, Vol.41, no.10, pp.3112-43114 (2005)
- [4-3] O. Bottauscio, M. Chiampi, and D. Chiarabaglio, “Advanced model of laminated magnetic cores for two-dimensional field analysis,” *IEEE Transactions on Magnetics*, Vol.36, no.3, pp.561-573 (2000)
- [4-4] K. Yamazaki and N. Fukushima, “Experimental validation of iron loss model for rotating machines based on direct eddy current analysis of electrical steel sheets,” *2009 IEEE International Electric Machines and Drives Conference*, pp.851-857 (2009)
- [4-5] K. Narita, T. Asanuma, K. Semba, H. Sano, T. Yamada, K. Aiso, and K. Akatsu, “An accurate iron loss evaluation method based on finite element analysis for switched reluctance motors,” *2015 IEEE Energy Conversion Congress and Exposition*, pp. 4413-4417 (2020)
- [4-6] T. Hara and K. Akatsu, “Comparison between analysis and experimental result of iron loss in SRM,” *The 23rd International Conference on Electrical Machines and Systems, LS3D-4*, pp. 577-580 (2020)
- [4-7] NIPPON STEEL CORPORATION: NON-ORIENTED ELECTRICAL STEEL SHEETS, <https://www.nipponsteel.com/>
- [4-8] Hitachi Metals, Ltd.: AMORPHOUS ALLOY RIBBON Metglas, <http://www.hitachi-metals.co.jp/>
- [4-9] N. Koga, S. Okada, and T. Yamaguchi, “Effect of Various Blanking Conditions on Properties of Cut Surface of Amorphous Alloy Foil and Tool Life,” *Journal of Japan Society for Technology of Plasticity*, Vol.59, No.692, pp.176-180 (2018)
- [4-10] Miller T. J. E.: *Switched reluctance motors and their control*, pp.161-180, Magna Physics Publications and Oxford University Press (1993)

- [4-11] Y. Enomoto, K. Suzuki, S. Okita, K. Eto, and E. Katayama, "Evaluation of a Motor with an Amorphous Iron Core Punched by a Die," IEEJ Transaction on IA, Vol.141, No.5, pp.423-430 (2021)

Chapter 5

Optimum Pulse Pattern of iron loss for efficiency improvement for High-Speed IPMSM

5.1. Introduction

In this chapter, a highly efficient pulse pattern using the iron loss evaluation function derived from the BH behavior model is explained. First, the assumption of the pulse pattern is explained in order to optimize the pulse pattern. Next, the procedure to apply the proposed BH trajectory behavior model into the derivation of the iron loss evaluation function under PWM is explained. Then, the optimal pulse pattern is derived based on the proposed iron loss evaluation function. The validity of the derived pulse pattern is explained by experiments using an inductor and a motor. In addition, the current THD is also evaluated to explain that the proposed method is different from the conventional linear model-based method.

5.2. Pulse pattern for iron loss reduction in stator core

5.2.1 PWM pulse patterns

In this section, the characteristics of the PWM pulse patterns and the constraints on optimizing the switching timing are explained. Note that the switching frequency of the inverter approaches the output frequency of the motor at high speed rotation. For this reason, synchronous PWM is effective. Therefore, synchronous PWM is assumed in this paper. The number of pulses in one cycle is constant at the synchronous PWM. As a result, the symmetry of the waveform is maintained and even number harmonics are not generated. In addition, the synchronous PWM has fewer switching cycles. As a result, the converter loss of the synchronous PWM is smaller than that of the asynchronous PWM.

Fig.5.1 shows the voltage waveforms of the U-phase, V-phase, and U-V lines when the synchronous PWM is applied. The synchronous PWM is symmetrical at every $\pi/2$. Furthermore, it is linearly symmetric at $\theta = 0$. In addition, the point symmetry is achieved when θ is $\pi/2$ or $3\pi/2$. Also, let $\alpha_i (i= 0, 1, \dots, m)$ be the timing of switching. In particular, let $\alpha_0 = 0$ and $\theta_m = \pi/2$. No switching is assumed at α_0 . In addition, it is assumed that $\alpha_0 < \alpha_1 < \dots < \alpha_m$ is valid. In the case of N -pulse PWM, $m = N/2 + 1$ is valid.

One of the constraints on optimizing the switching timing is that the fundamental amplitude of the output voltage must match the voltage amplitude command value. In this method, the first switching timing α_1 is determined to satisfy this constraint. The fundamental amplitude E_f of the U-phase voltage in Fig.5.1 is obtained by Fourier series expansion. The fundamental amplitude E_f is normalized by the amplitude $(2/\pi)E_{dc}$ of the square wave voltage (which is K_e). As a result, K_e is expressed as Eq.(5.1)

$$K_e = \frac{E_f}{(2/\pi)E_{dc}} = 2 \sum_{i=1}^{m-1} (-1)^{i+1} \sin \alpha_i - (-1)^m \dots \dots \dots (5.1)$$

In order for the fundamental amplitude of the output voltage matches the voltage amplitude command value, α_1 must satisfy Eq.(5.2).

$$\alpha_1 = \sin^{-1} \left\{ \frac{K_e + (-1)^m}{2} - \sum_{i=2}^{m-1} (-1)^{i+1} \sin \alpha_i \right\} \dots\dots\dots (5.2)$$

From Eq.(5.2), α_1 is a dependent variable that is determined by the voltage amplitude command K_e and other switching timings. Therefore, the switching timing to be optimized is $\alpha_2 \sim \alpha_{m-1}$.

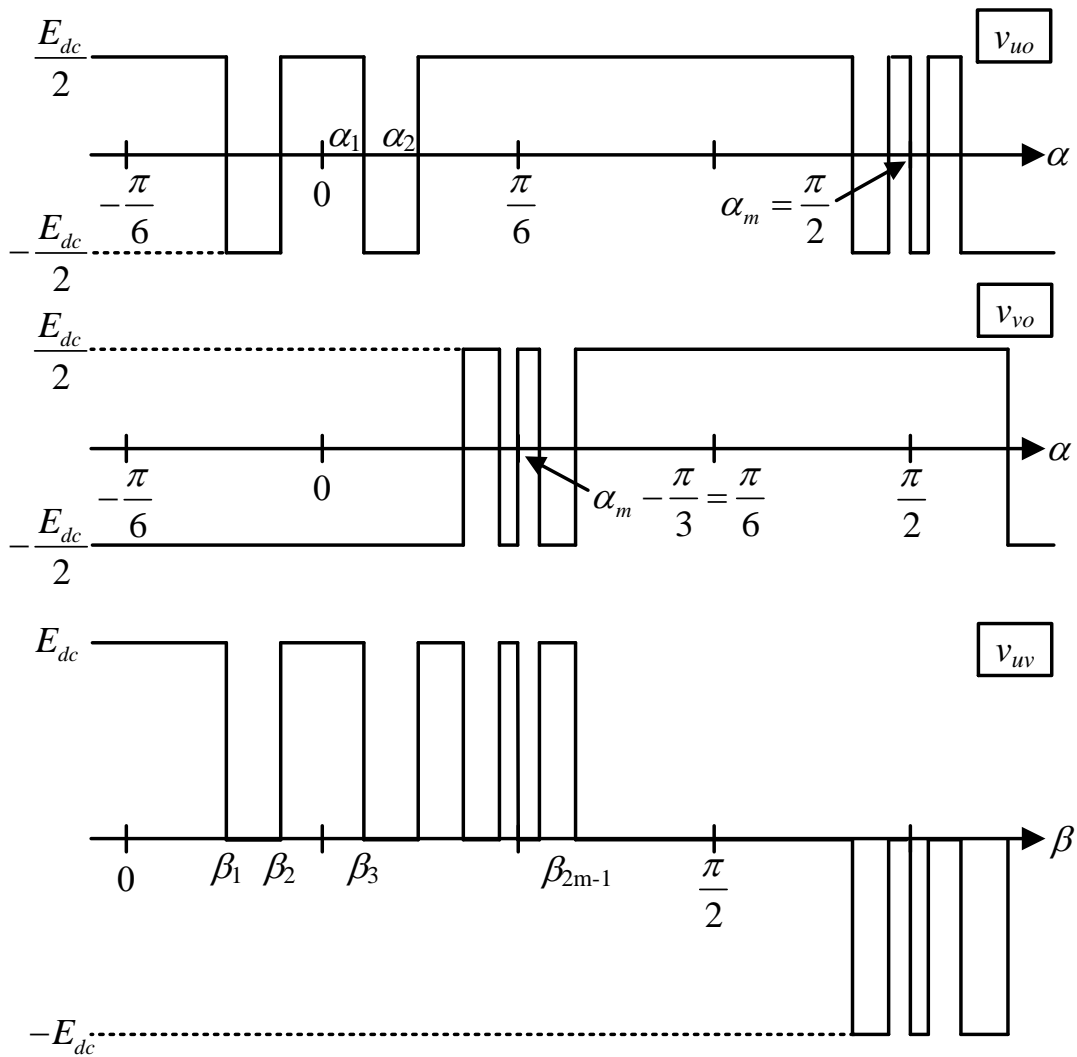


Fig.5.1. Phase voltage waveforms and line-to-line voltage waveform of synchronous PWM (1/4 cycle).

Fig.5.2(a) shows the basic vectors of the three-phase inverter, and Fig.5.2(b) shows the partitioned region of the space vector coordinates. The synchronous PWM has a symmetry of every 90 degrees. In addition, since it is a symmetrical three-phase system, the transition order of the output fundamental vectors is symmetrical every 30 degrees in the space vector notation. Therefore, the optimal switching timing is derived from the transition mode of the fundamental vectors in a 30-degree section. In Fig.5.2(b), the region of space vector is divided so that the number of switching is minimized. The other constraints for optimizing the switching timing are as follows.

1. Only one switching when the vector transitions.
2. The switching doesn't occur at 0 rad phase. Therefore, the switching state at 0 rad is limited to the vectors in Sector 6.
3. Switching occurs when phase is $\pi/6$ rad.
4. Non-zero vector is selected at $\pi/6$ rad because it is symmetric in front and back of this vector.

The switching timing that minimizes the objective function is calculated based on the switching transition mode satisfied these constraint condition.

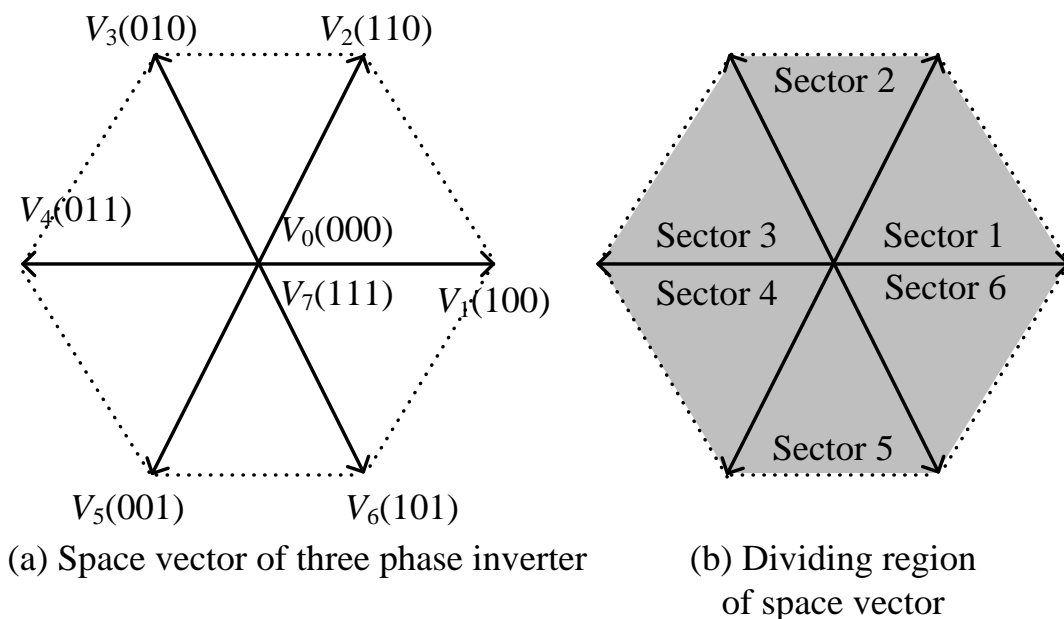
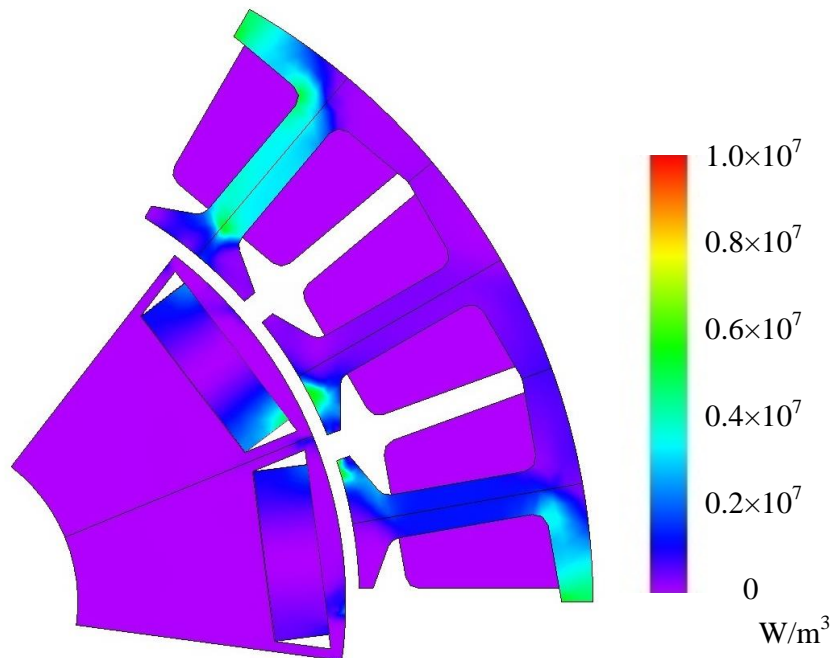


Fig.5.2. Transition modes of space vector.

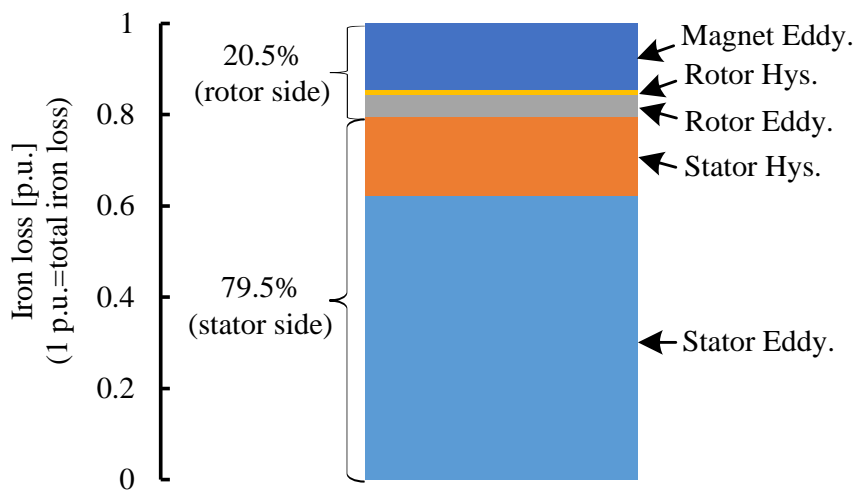
5.2.2 Iron loss evaluation function under PWM

This section explains the iron loss evaluation function of the stator iron core when the pulse pattern is applied. The proposed iron loss evaluation function calculates the iron loss from the magnetic flux density amplitude obtained by time integration of the output voltage. Note that, this function is an approximation iron loss evaluation function that does not directly calculate the iron loss. In this paper, the evaluation function is derived by focused on the stator iron loss, based on the assumption that the iron loss in the high-speed light load region is mainly due to the stator iron core.

Fig.5.3 shows the distribution and the separation results of iron loss at each location of the motor core under the high-speed light load. Time series data of the magnetic flux density at each location of the iron core is required to accurately calculate the iron loss of a motor. However, the optimization of the pulse pattern is not practical because it requires the optimization of multiple switching timings. Therefore, this section focuses on the iron loss distribution and separation results of the motor shown in Fig.5.3(a) and (b). In the high-speed light-load region, the iron loss in the stator iron core is larger than the iron loss in the rotor side, including permanent magnet eddy current loss. The loss accounts for about 80% of the total iron loss. This is because the change in the magnetic flux density of the stator teeth caused by the permanent magnet of the rotor increases in proportion to the rotation speed [5-1]. Therefore, the iron loss in the high-speed light-load region is estimated from the magnetic flux density in the stator teeth.



(a) Iron loss (eddy-current loss) distribution



(b) Iron loss separation

Fig.5.3. Iron loss distribution and separation

Fig.5.4(a) shows the relationship between the UV line-to-line voltage waveform and magnetic flux density with synchronous PWM is applied, whereas Fig.5.4(b) shows the relationship between the BH trajectory and switching timing. Eq.(5.3) is established for the voltage v_a , current i_a , armature resistance R_a , and armature chain crossing flux Φ_a in the armature.

$$v_a(t) = \frac{d\Phi_a(t)}{dt} + R_a i_a(t) \dots\dots\dots (5.3)$$

Eq (5.3) can be rewritten as Eq.(5.4), because the effect of voltage drop due to armature resistance is small in the high-speed light load region.

$$v_a(t) = \frac{d\Phi_a(t)}{dt} = NS \frac{dB_a(t)}{dt} \dots\dots\dots (5.4)$$

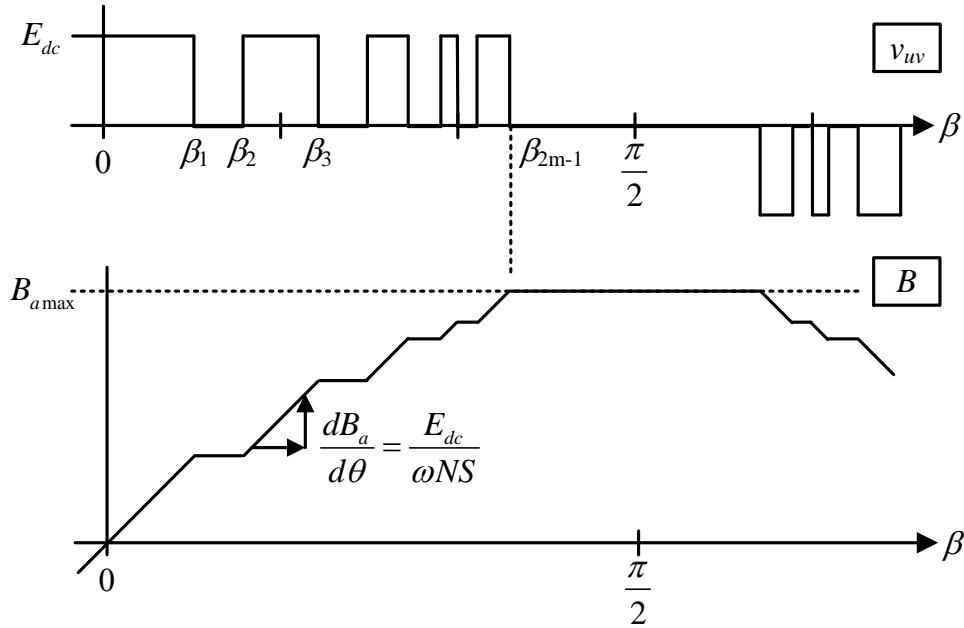
where N is the number of turns, S is the cross-sectional area of the teeth, and B_a is the magnetic flux density. Therefore, the magnetic flux density B_a is expressed by the following equation

$$B_a(t) = \frac{1}{NS} \int_0^t v_a(t) dt \dots\dots\dots (5.5)$$

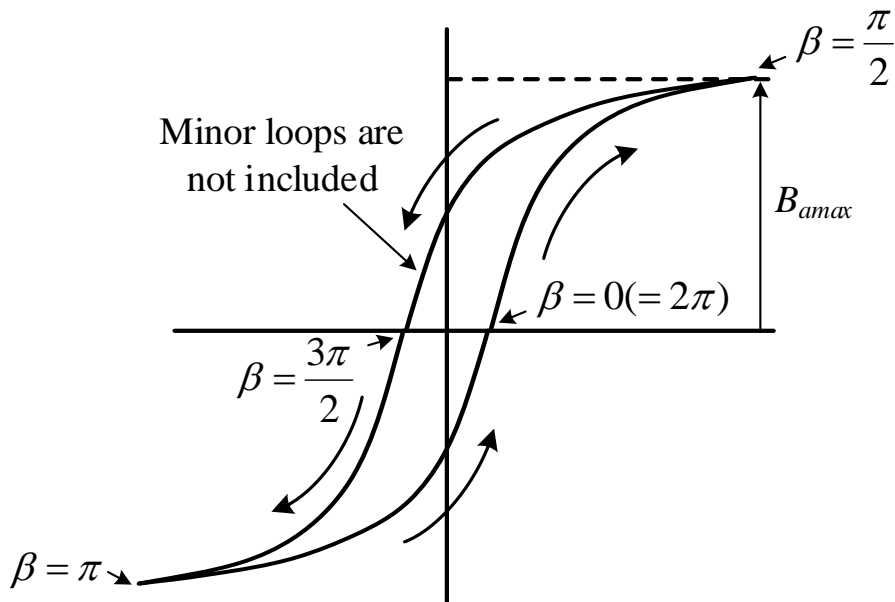
Here, the magnetic flux density B_a in Eq.(5.5) represents the magnetic flux density at the stator teeth where the coil is wound , because it is calculated from the armature chain flux. Therefore, the iron loss is possible to approximate by using the time function $B_a(t)$ of the magnetic flux density expressed in Eq.(5.5) instead of the time series data of the magnetic flux density at each location of the iron core. According to Figure 5.4(a), the line voltage of the synchronous PWM has the same polarity during the half cycle. Therefore, the minor loop is included in the hysteresis loop because the time variation of the magnetic flux density in the half cycle is ideally monotonically increasing or monotonically decreasing. As a feature of the BH trajectory behavior model, the hysteresis loss depends on the maximum flux density B_{amax} when there is no minor loop. B_{amax} in Fig.5.4 is expressed by Eq.(5.6), since it is the integral value of $[0, \pi/2]$ after the Eq.(5.5) is converted into a position function using $\omega=d\theta/dt$ (where ω is the electric angular velocity).

$$B_{a\max} = \int_0^{\pi/2} \frac{dB_a(\theta)}{d\theta} d\theta = \frac{1}{NS\omega} \int_0^{\pi/2} v_{uv}(\theta) d\theta \dots\dots\dots (5.6)$$

The output line voltage of the inverter is used for the evaluation function the line voltage is easier to calculate than the phase voltage from the motor



(a) Relationship between line-to-line voltage waveform and magnetic flux density waveform.



(b) Relationship between BH trajectory and switching timing

Fig.5.4. Relationship between line-to-line voltage waveform and magnetic flux density waveform and BH trajectory.

neutral point in three-phase, three-wire applications such as motor drive systems [5-2].

From the above discussion, the maximum flux density B_{amax} is adopted as the evaluation function for the hysteresis loss. On the other hand, the iron loss includes the eddy current loss. Therefore, improved generalized Steinmetz equation (iGSE) has to be used for calculation of the eddy current loss as well.

In this case, even if the magnetic flux density waveform is non-sinusoidal, as shown in Fig.5.4, the iron loss is calculated by applying the iGSE[5-2][5-3]. The time average iron loss per unit volume is expressed as Eq.(5.7) by using the iGSE,

$$P_V = \frac{1}{T} \int_0^T k_i \left| \frac{dB_a(t)}{dt} \right|^\alpha (\Delta B_a)^{\beta-\alpha} dt \dots\dots\dots (5.7)$$

where ΔB_a is the peak-peak value of the magnetic flux density. Also, k_i is expressed as Eq.(5.8),

$$k_i = \frac{k}{(2\pi)^{\alpha-1} \int_0^{2\pi} |\cos\theta|^\alpha 2^{\beta-\alpha} d\theta} \dots\dots\dots (5.8)$$

where k , α , and β are the coefficients that is calculated from the iron loss curves. The iron loss curves are obtained by the catalog data for iron core materials. Eq.(5.7) is converted to a position function and the integration range is rewritten to $[0, \pi/2]$ from the symmetry of the synchronous PWM. As a result, Eq.(5.7) is rewritten as Eq.(5.9),

$$P_V = k_i \omega^\alpha \frac{(\Delta B_a)^{\beta-\alpha}}{\pi/2} \int_0^{\pi/2} \left(\frac{dB_a(\theta)}{d\theta} \right)^\alpha d\theta \dots\dots\dots (5.9)$$

The peak-peak value of the magnetic flux density ΔB_a in Eq.(5.9) is $2B_{amax}$ due to the symmetry of the synchronous PWM. On the other hand, the definite integral term in Eq.(5.9) has the same range of integration compared to Eq.(5.6), and the slope of the voltage application time ($v_{uv}=E_{dc}$) (Fig.5.4) is $(dB_a/d\theta)^{\alpha-1}$ times larger than the original. Therefore, The definite integral term becomes the $(dB_a/d\theta)^{\alpha-1}$ times value of B_{amax} expressed in Eq.(5.6).

Therefore, Eq.(5.9) is rewritten as Eq.(5.10),

$$\begin{aligned}
 P_V &= k_i \omega^\alpha \frac{(2B_{a \max})^{\beta-\alpha}}{\pi/2} \left(\frac{dB_a}{d\theta} \Big|_{v_{uv}=E_{dc}} \right)^{\alpha-1} B_{a \max} \dots\dots\dots (5.10) \\
 &= k_i \omega^\alpha B_{a \max}^{\beta-\alpha+1} 2^{\beta-\alpha} \frac{2}{\pi} \left(\frac{E_{dc}}{\omega NS} \right)^{\alpha-1}
 \end{aligned}$$

In Eq.(5.10), all the terms except B_{amax} are determined by the experimental parameters and the characteristics of the iron core material. Therefore, the iron loss is reduced by optimizing the pulse pattern so as to minimize the term including B_{amax} . As an evaluation function for reducing iron loss, it is sufficient to use only B_{amax} instead of $B_{amax}^{\beta-\alpha+1}$. For this reason, B_{amax} expressed in Eq.(5.6) is used as the evaluation function. The UV line voltage v_{uv} in Eq.(5.6) is leaded by 30 degrees compared to the phase of the U phase voltage. Therefore, A new switching timing β_k ($k=0, 1, \dots, 2m+1$) is defined as the interline voltage reference. In addition, β_0 is 0 rad and β_{2m+1} is $\pi/2$ rad. The switching occurs at $\pi/3$ rad because the 90 degrees in the V-phase voltage is included. Furthermore, all the switching other than 0, $\pi/3$, and $\pi/2$ rad are obtained by α_i , and Eq.(5.11) to Eq.(5.14) are obtained.

$$\beta_k = \frac{\pi}{6} - \alpha_i \left(\alpha_i < \frac{\pi}{6} \right) \dots\dots\dots (5.11)$$

$$\beta_k = \alpha_i - \frac{\pi}{6} \left(\alpha_i > \frac{\pi}{6} \right) \dots\dots\dots (5.12)$$

$$\beta_k = \alpha_i + \frac{\pi}{6} \left(\alpha_i < \frac{\pi}{3} \right) \dots\dots\dots (5.13)$$

$$\beta_k = \frac{5}{6}\pi - \alpha_i \left(\alpha_i > \frac{\pi}{3} \right) \dots\dots\dots (5.14)$$

The amplitude of the line voltage takes the value of the DC voltage E_{dc} or 0 in $0 < \beta_k < \pi/2$ Therefore, the line voltage is expressed as Eq.(5.15),

$$v_{uv} = \begin{cases} E_{dc} & (\beta_k < \beta < \beta_{k+1}) \quad k : \text{even} \\ 0 & (\beta_k < \beta < \beta_{k+1}) \quad k : \text{odd} \end{cases} \dots\dots\dots (5.15)$$

The integral of the line voltage for each section is expressed as Eq.(5.16),

$$\int_{\beta_k}^{\beta_{k+1}} v_{uv}(t) d\theta = \begin{cases} E_{dc}(\beta_{k+1} - \beta_k) & (\beta_k < \beta < \beta_{k+1}) \quad k : \text{even} \\ 0 & (\beta_k < \beta < \beta_{k+1}) \quad k : \text{odd} \end{cases} \dots (5.16)$$

Therefore, Eq.(5.6) is rewritten as Eq.(5.17) from Eq.(5.16),

$$B_{a \max} = \frac{1}{NS\omega} \sum_{k=0}^{2m} \int_{\beta_k}^{\beta_{k+1}} v_{uv}(\theta) d\theta = \frac{E_{dc}}{NS\omega} \sum_{k=0}^{2m-1} (-1)^{k-1} \beta_k \dots\dots\dots (5.17)$$

Since the coefficient $E_{dc}/NS\omega$ is constant regardless of the pulse pattern, the evaluation function f_i of iron loss is obtained by normalizing Eq.(5.17) and expressing only the pulse pattern as follows,

$$f_i = \sum_{k=0}^{2m-1} (-1)^{k-1} \beta_k \dots\dots\dots (5.18)$$

Eq.(5.18) is expressed as the sum of the values calculated from each switching timing. In addition, Eq.(5.18) doesn't have to use the complex function, like the evaluation function for the RMS value of motor harmonic current under PWM Therefore, the iron loss is reduced by using Eq.(5.18) and obtaining each switching timing so that the evaluation function is minimized.

5.3. Experimental Verification

In this section, the results of the experiments using inductors and the high-speed IPMSMs are presented to confirm the effectiveness of the proposed method. The proposed evaluation function is an approximated iron loss evaluation function that does not directly calculate the iron loss. Therefore, the validity of the proposed evaluation function was evaluated by creating 12 random PWM patterns with the same amplitude of the fundamental component and deriving the correlation coefficient between the iron loss evaluation value calculated by Eq.(5.18) and the measured iron loss value. The effectiveness of the proposed method was evaluated from the comparison among (a) carrier asynchronous PWM: the zero-crossing point of the triangular wave carrier and the zero-crossing point of the voltage command do not coincide, (b) carrier synchronous PWM: the zero-crossing point of the triangular wave carrier and the zero-crossing point of the voltage command always coincide, and (c) proposed PWM: the evaluation function is minimized. In both the inductor and the high-speed IPMSM verifications, nine PWM pulses are used. The input voltage E_{dc} is 180 V and the modulation factor K_e is 0.785 (equivalent to the maximum output of the triangular wave comparison PWM method).

5.3.1 Verification in inductor

Fig.5.5 shows the experimental configuration. The inverter is a two-level inverter and IGBT (2MBI150U2A-060, 600 V, 150 A, Fuji Electric) is used as the switching device. A regenerative bi-directional DC power supply (RP7951A, Keysight Technologies) is used as the power supply for the inverter and the input voltage is set to 180 V. The power was measured using a power meter (PW3390, accuracy $\pm 0.04\%$, bandwidth 200 kHz, HIOKI).

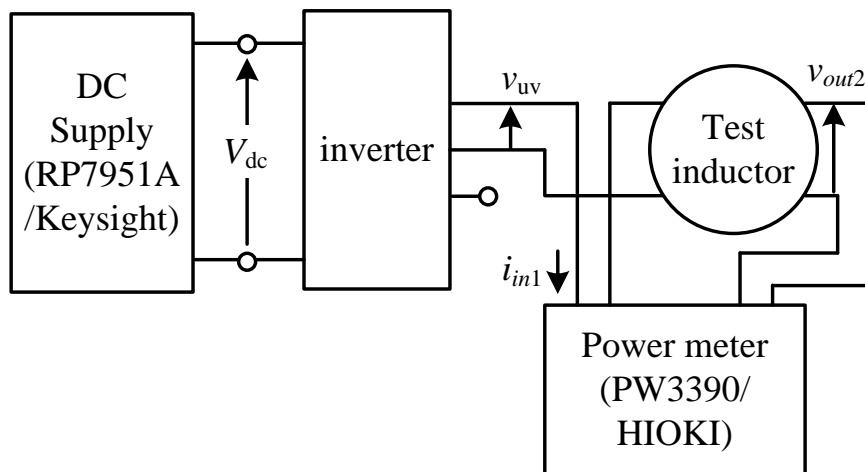


Fig.5.5. Configuration of the system to measure iron loss of test inductor.

Fig.5.6 shows a photograph of the fabricated inductor, and Table 5.1 shows its specifications. The auxiliary winding is wound on the secondary side and the iron loss is calculated from the primary side current and the secondary side voltage when PWM is applied. Although transformers are usually manufactured by the oriented electromagnetic steel sheets, the non-oriented electromagnetic steel sheets are used since this study assumes the iron loss in a motor.

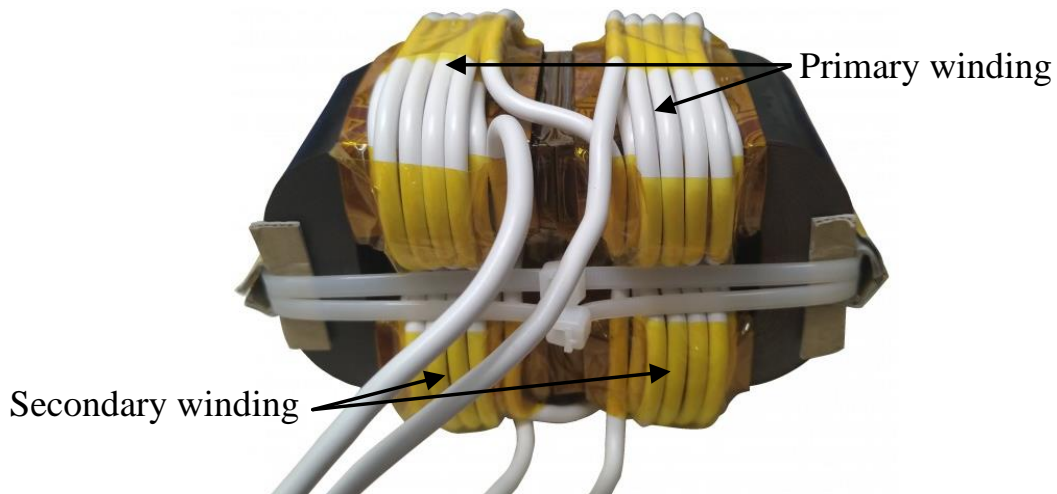


Fig.5.6. Photograph of inductor.

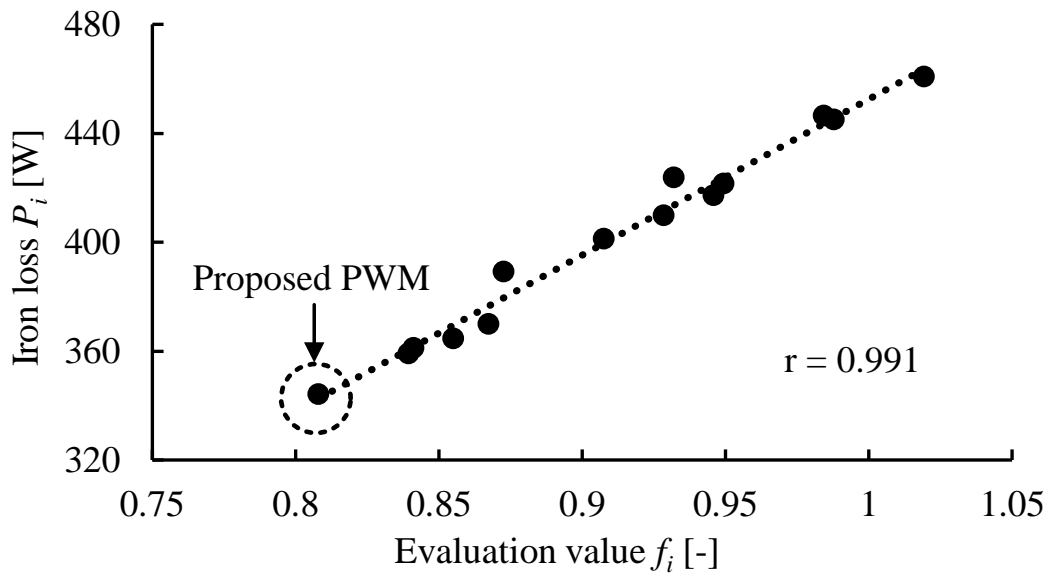
Table 5.1. Specifications of test inductor.

| | |
|----------------------|----------------------------|
| Core material | 35JN440 |
| Cross sectional area | 95cm ² |
| Gap length | 0.52mm |
| Number of turns | 21 |
| Core volume (weigh) | 262cm ³ (1.9kg) |

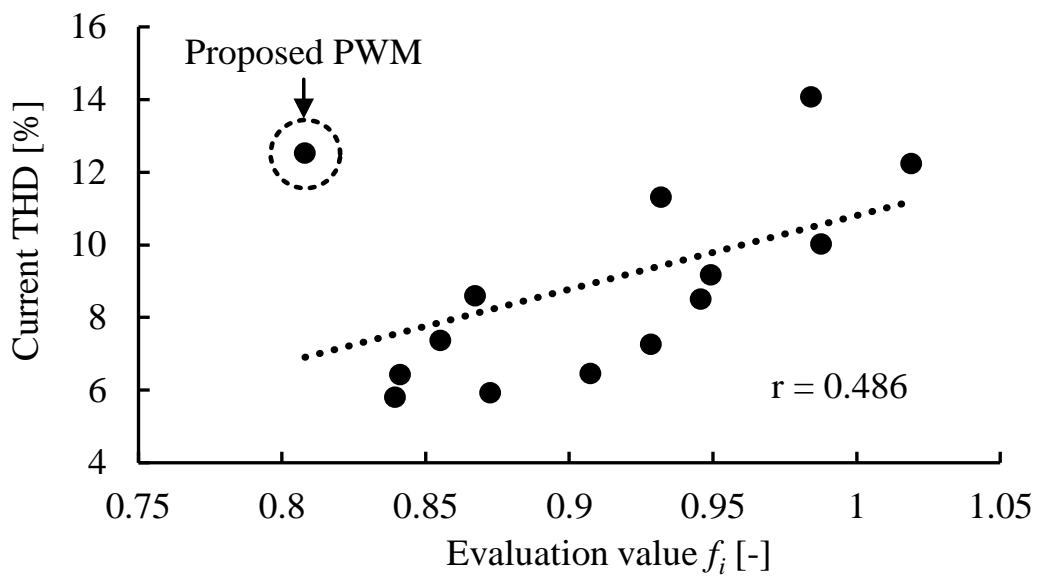
Fig.5.7 shows the results of the iron loss and the current distortion factor (THD) of the inductor when PWM is applied and the evaluation value by Eq.(5.18). Note that 12 patterns of random PWM voltages and the proposed PWM, which is derived so that the Eq.(5.18) is minimized, are applied to the inductor. The correlation coefficient r of these data was calculated from the following equation.

$$r = \frac{\frac{1}{n} \sum_{n=1}^n (f_{i_n} - \bar{f}_i)(P_{i_n} - \bar{P}_i)}{\sqrt{\frac{1}{n} \sum_{n=1}^n (f_{i_n} - \bar{f}_i)^2} \times \sqrt{\frac{1}{n} \sum_{n=1}^n (P_{i_n} - \bar{P}_i)^2}} \dots\dots\dots (5.19)$$

where n is the number of data, (f_{i_n}, P_{i_n}) are the n -th evaluation value and iron loss, and the bars are the respective average values. In general, the closer the correlation coefficient is to 1, the stronger the correlation, i.e., the stronger the linear relationship and the more accurate the evaluation function. From Fig.5.7(a), the iron loss and the evaluation value by Eq.(5.18) have a correlation coefficient of 0.991, which is a very high correlation. Therefore, the iron loss generated in the inductor driven with an arbitrary pulse pattern is calculated from Eq.(5.18). In addition, the proposed PWM, which is derived so that Eq.(5.18) is minimized, has smaller iron loss than any other pulse patterns. On the other hand, Fig.5.7(b) shows that the correlation coefficient between the current THD and the evaluated value by Eq.(5.18) is 0.486, which is a low correlation. In other words, although the evaluation function used in this iron loss reduction method has a very high correlation with iron loss, it has a low correlation with current THD. This indicates that the proposed method is different from the conventional method for reducing current THD.



(a) Evaluation value and iron loss



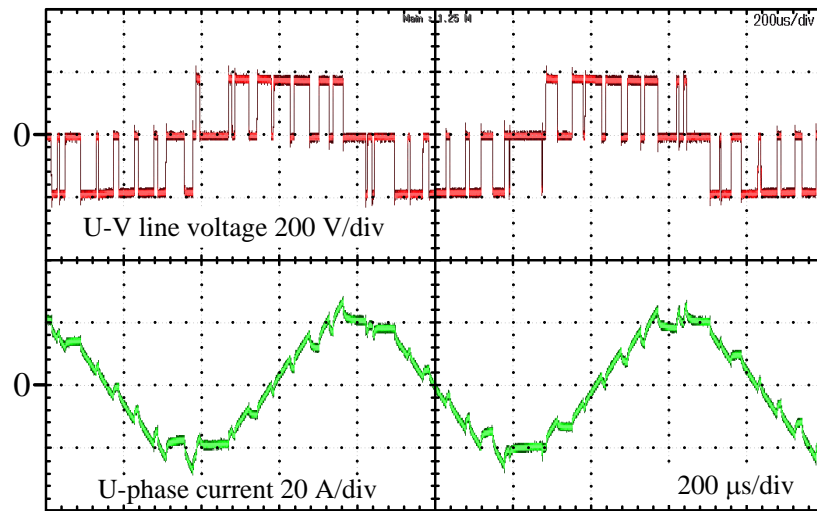
(b) Evaluation value and current THD

Fig.5.7. Correlation coefficient between evaluation value and iron loss, current THD of test inductor.

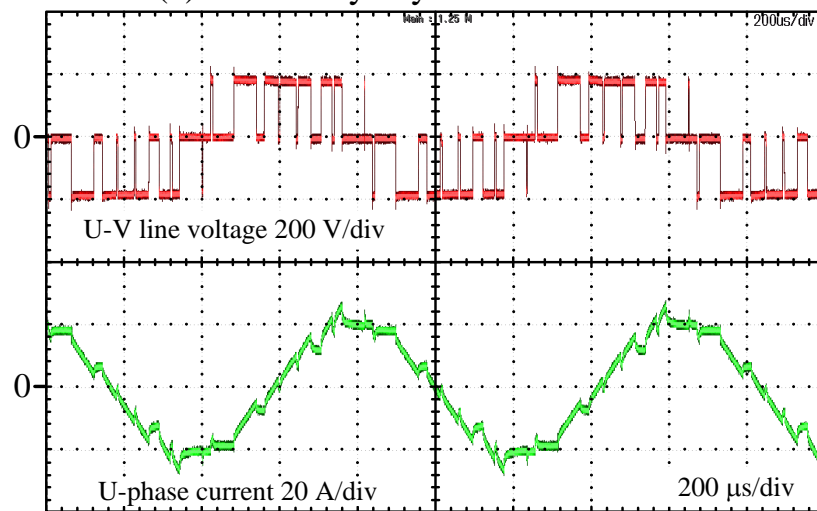
Table 5.2 shows the switching timing of the carrier-synchronous PWM and the proposed PWM with respect to the line voltage. Fig.5.8 shows the line voltage and the line current waveforms when (a) the carrier-asynchronous PWM, (b) the carrier-synchronous PWM, and (c) the proposed PWM are applied. Comparing the line voltages in Fig.5.8(b) and Fig.5.8(c), the proposed PWM is almost symmetric synchronous PWM, although there is an effect of dead time. The number of pulses of the proposed PWM tends to decrease because of the short pulses, whereas the line voltage of the carrier asynchronous PWM and the carrier synchronous PWM has nine pulses. This is because the proposed method tries to reduce iron loss by making the shape of the magnetic flux trapezoidal wave and keeping the maximum flux density amplitude B_{amax} low. As a result of the reduced number of pulses, the current waveform was closer to a trapezoidal wave rather than a sinusoidal wave compared to the carrier-synchronous PWM. In addition, the details of the experimental current waveform in Fig.5.8 have maxima and minima. That is different from the waveform shown in Fig.5.4, where the time variation of the current during the half cycle is monotonically increasing or monotonically decreasing. This is because the magnetic flux cannot be expressed simply as a product of the inductance value and the current due to the iron loss generated as an instantaneous value.

Table 5.2. Switching patterns of carry-synchronous PWM and proposed PWM in test inductor

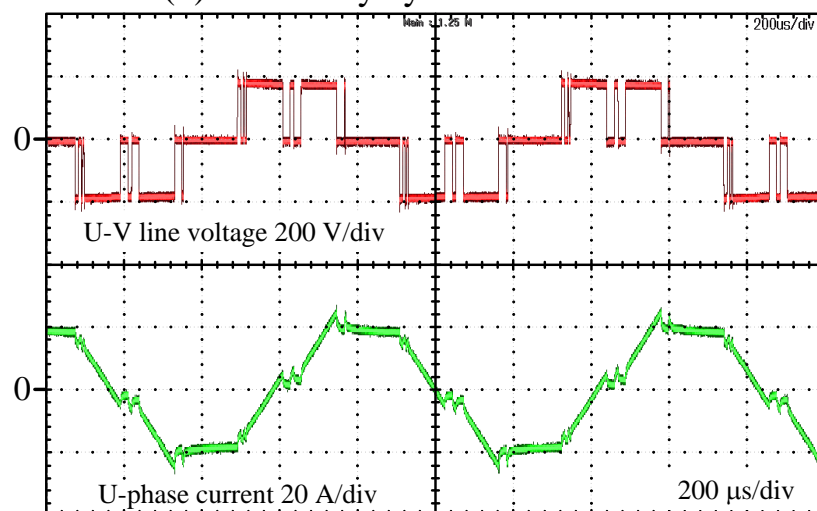
| Switching pattern | Carry-syn PWM | Proposed PWM |
|-------------------|---------------|--------------|
| β_1 | 0.163 rad | 0.044 rad |
| β_2 | 0.184 rad | 0.114 rad |
| β_3 | 0.448 rad | 0.124 rad |
| β_4 | 0.627 rad | 0.171 rad |
| β_5 | 0.863 rad | 0.876 rad |
| β_6 | 0.884 rad | 0.924 rad |
| β_7 | 1.047 rad | 0.934 rad |
| β_8 | 1.467 rad | 1.004 rad |
| β_9 | 1.495 rad | 1.047 rad |



(a) With carry-asynchronous PWM



(b) With carry-synchronous PWM



(c) With proposed PWM

Fig.5.8. U-V line-to-line voltage and phase current waveforms.

Fig.5.9 shows the iron loss generated by applying the carrier asynchronous PWM, the carrier synchronous PWM, and the proposed PWM. The proposed PWM reduces the iron loss by 7.6% and 5.6% compared to the carrier asynchronous PWM and the carrier synchronous PWM. Therefore, the proposed PWM reduces the iron loss in the inductor.

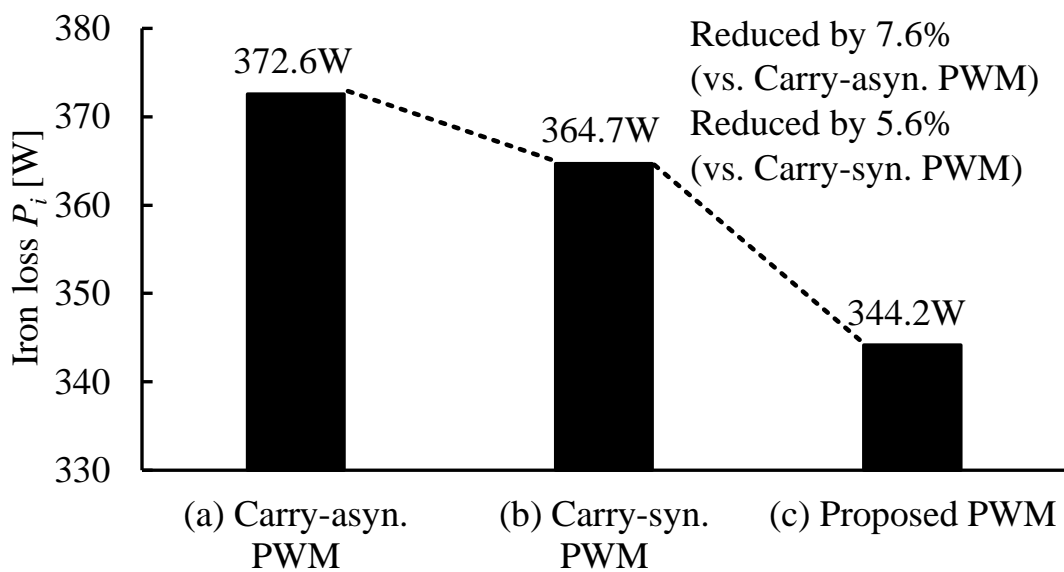


Fig.5.9. Iron loss of test inductor.

5.3.2 Verification in High-speed IPMSM

Fig.5.10 shows the experimental configurations. The input power of the test motor is measured with a power meter and the shaft output of the test motor is measured with a torque meter (TH2105, Ono Sokki). A resistive load is connected to the load motor with Y-connections and the load torque is applied. The iron loss was calculated by subtracting the output and primary copper loss from the input. The mechanical loss is not separated from the iron loss and is included in the iron loss in this study because it is considered to be the same regardless of the pulse pattern. Before measuring the iron loss, the warm-up operation was performed because the deviation of the measurement results occurs due to the mechanical loss and the temperature dependence of the coil winding so that the winding temperature is within the range of 30°C to 35°C.

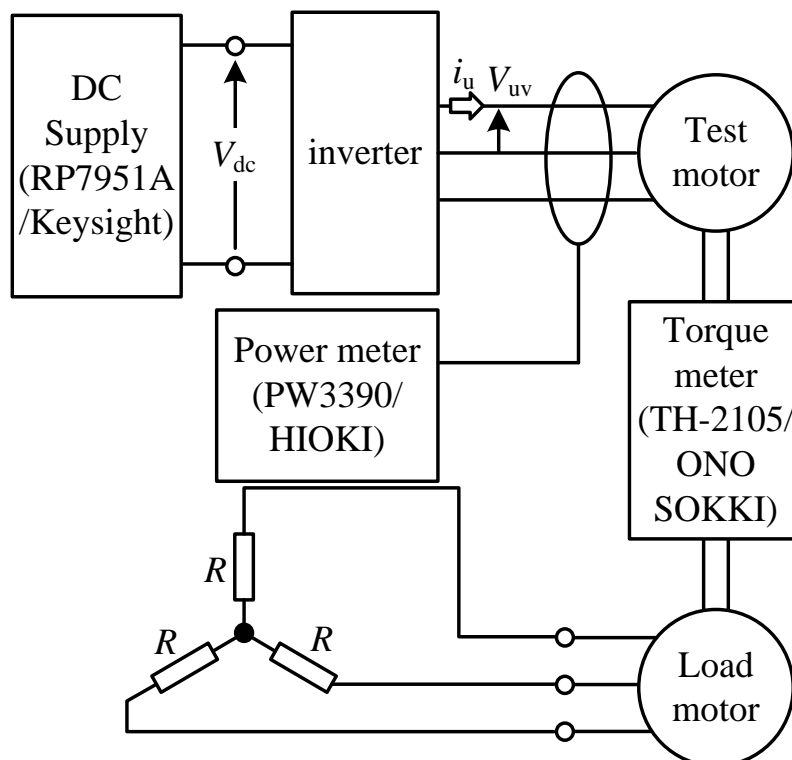


Fig.5.10. Configuration of IPMSM drive system.

Fig.5.11 shows the model of the test motor used in this thesis and Table 3 shows the motor parameters. The motor is a concentrated winding IPMSM with the rated power of 3 kW and the maximum speed of 12000 r/min. First, the test motor is driven using the V/f control and the speed is increased to the rated speed using the carrier asynchronous PWM. After the motor speed reaches the rated speed, the pulse pattern is switched to the specified PWM pulse pattern. The experimental conditions were set at 12000 r/min and 0.22 Nm, assuming a high-speed light load.

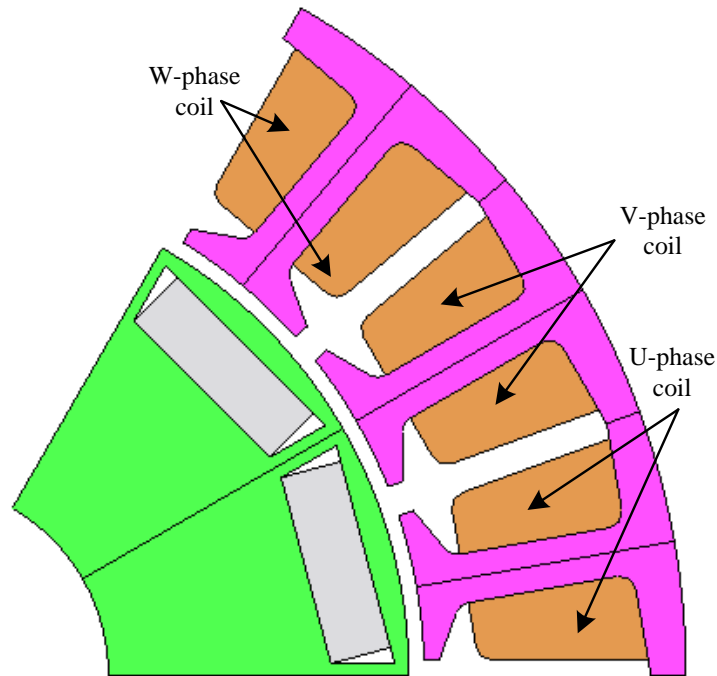
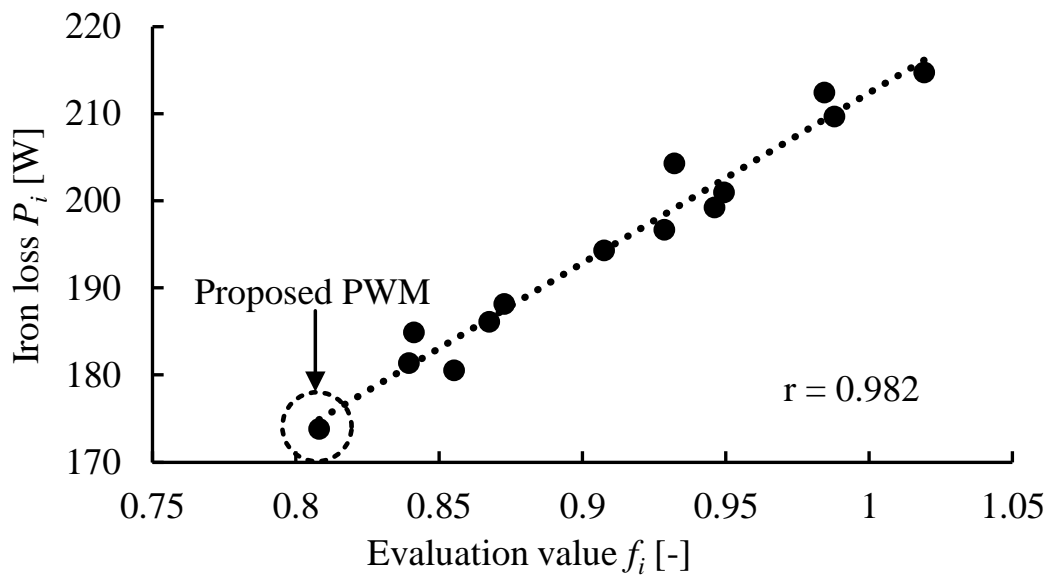


Fig.5.11. Model of test motor: concentrated winding IPMSM.

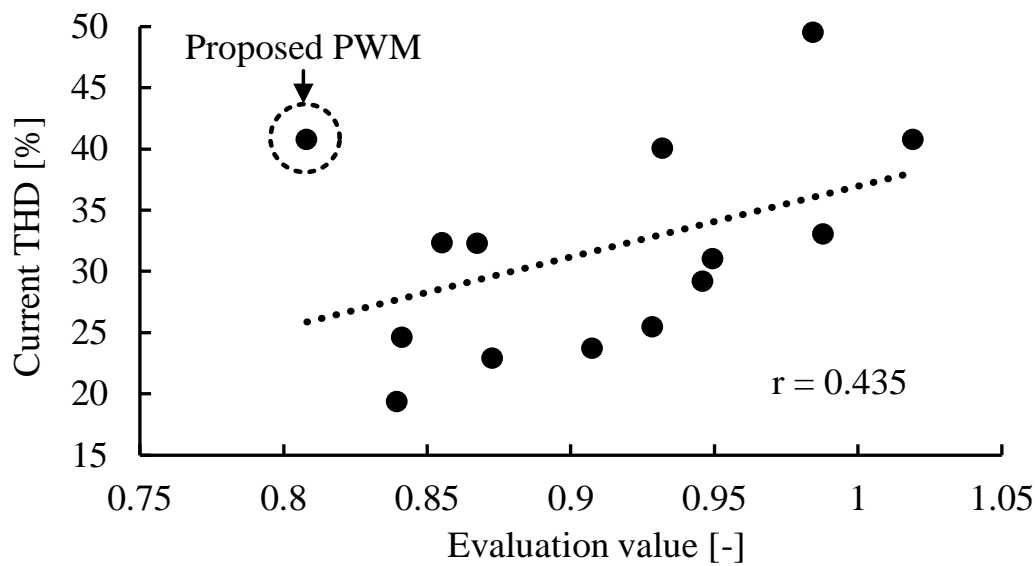
Table 5.3. Specifications of test motor.

| | |
|-------------------------|-----------------|
| Maximum power | 3 kW |
| Maximum torque | 4 Nm |
| Base speed | 7200 r/min |
| Maximum speed | 12000 r/min |
| Armature pairs of poles | 6 |
| d-axis inductance | 0.389 mH |
| q-axis inductance | 0.556 mH |
| Winding resistance | 0.0557 Ω |
| Back-EMF coefficient | 0.0189 Vs/rad |

Fig.5.12 shows the results of the iron loss, the total harmonic distortion (THD) of the current of the high-speed IPMSM, and the evaluated values by Eq.(5.18) under PWM excitation. Note that 12 patterns of the random PWM voltages and the proposed PWM derived so that Eq.(5.18) is minimized are applied to the motor. From Fig.5.12(a), the iron loss and the evaluation value by Eq.(5.18) have a correlation coefficient of 0.982, which is a very high correlation. Therefore, the iron loss generated in the motor driven with an arbitrary pulse pattern can be calculated from Eq.(5.18). In addition, the proposed PWM has the lowest iron loss of any pulse patterns. On the other hand, Fig.5.12(b) shows that the correlation coefficient between the current THD and the evaluation value by Eq.(5.18) is 0.435, which is a low correlation. In other words, the evaluation function used in this iron loss reduction method has a very high correlation with the iron loss. However, it does not have a low correlation with current THD. This result indicates that the proposed method is different from the conventional method for reducing the current THD.



(a) Evaluation value and iron loss



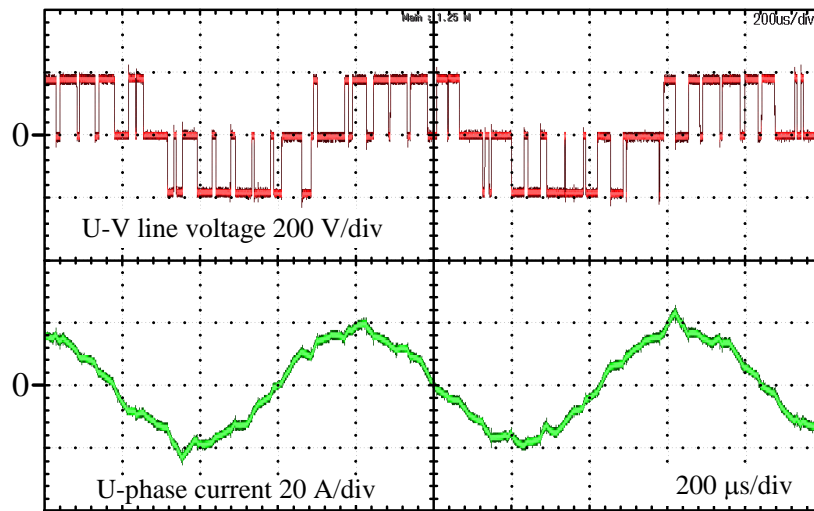
(b) Evaluation value and current THD

Fig.5.12. Correlation coefficient between evaluation value and iron loss, current THD of test motor.

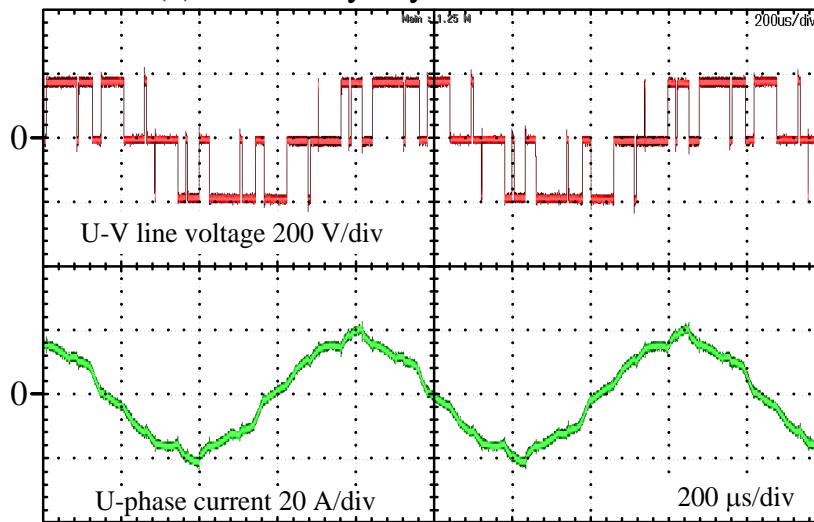
Table 5.4 shows the switching timing of the carrier-synchronous PWM and the proposed PWM with respect to the line voltage. Fig.5.13 shows the line voltage and the line current waveforms when (a) the carrier asynchronous PWM, (b) the carrier synchronous PWM, and (c) the proposed PWM are applied. The line voltage waveform is almost the same as that of the inductor experiment. This is because the pulse patterns were derived under the same conditions as for the inductor, as shown in Table 2 and Table 4. On the other hand, the phase current of the motor in the proposed PWM is almost a sinusoidal waveform as shown in Fig.5.13(c) while the that of the inductor is almost the trapezoidal waveform as shown in Fig.5.8(c). The magnetic flux in the stator teeth is the sum of the flux generated by the permanent magnets and the flux generated by the current flowing in the windings. In the proposed PWM, the current flows so that the sum of these fluxes becomes a trapezoidal wave shape. Therefore, even if the magnetic flux waveform in the stator teeth is trapezoidal, the current waveform can be not trapezoidal due to the spatial distribution of the magnetic flux caused by the permanent magnets.

Table 5.4. Switching patterns of carry-synchronous PWM and proposed PWM in test motor

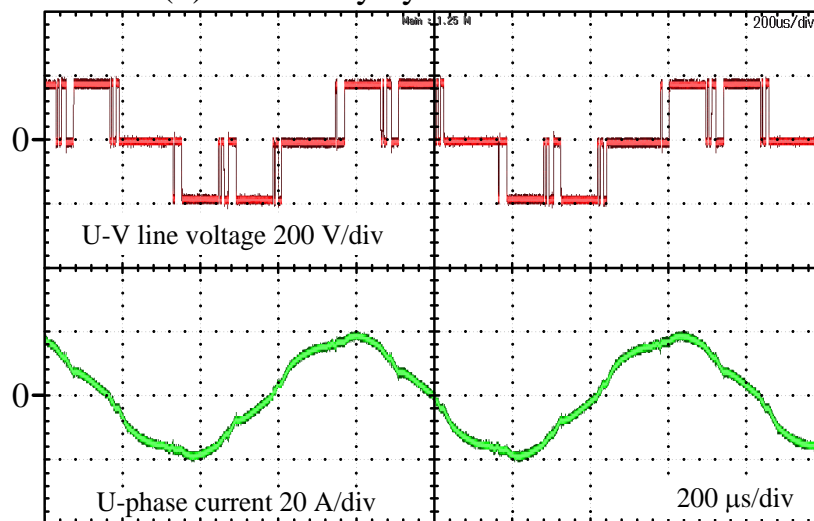
| Switching pattern | Carry-syn PWM | Proposed PWM |
|-------------------|---------------|--------------|
| β_1 | 0.163 rad | 0.044 rad |
| β_2 | 0.184 rad | 0.114 rad |
| β_3 | 0.448 rad | 0.124 rad |
| β_4 | 0.627 rad | 0.171 rad |
| β_5 | 0.863 rad | 0.876 rad |
| β_6 | 0.884 rad | 0.924 rad |
| β_7 | 1.047 rad | 0.934 rad |
| β_8 | 1.467 rad | 1.004 rad |
| β_9 | 1.495 rad | 1.047 rad |



(a) With carry-asynchronous PWM



(b) With carry-synchronous PWM



(c) With proposed PWM

Fig.5.13. U-V line-to-line voltage and phase current waveforms.

Fig.5.14 shows the iron loss generated when carrier asynchronous PWM, carrier synchronous PWM, and proposed PWM are applied. Note that 10 experiments were conducted for each of them and the mean values and the standard deviations of the iron loss are shown. The proposed PWM reduces the iron loss by 8.5% and 3.7% compared to the carrier asynchronous PWM and the carrier synchronous PWM. Therefore, the proposed PWM reduces the iron loss in the motor.

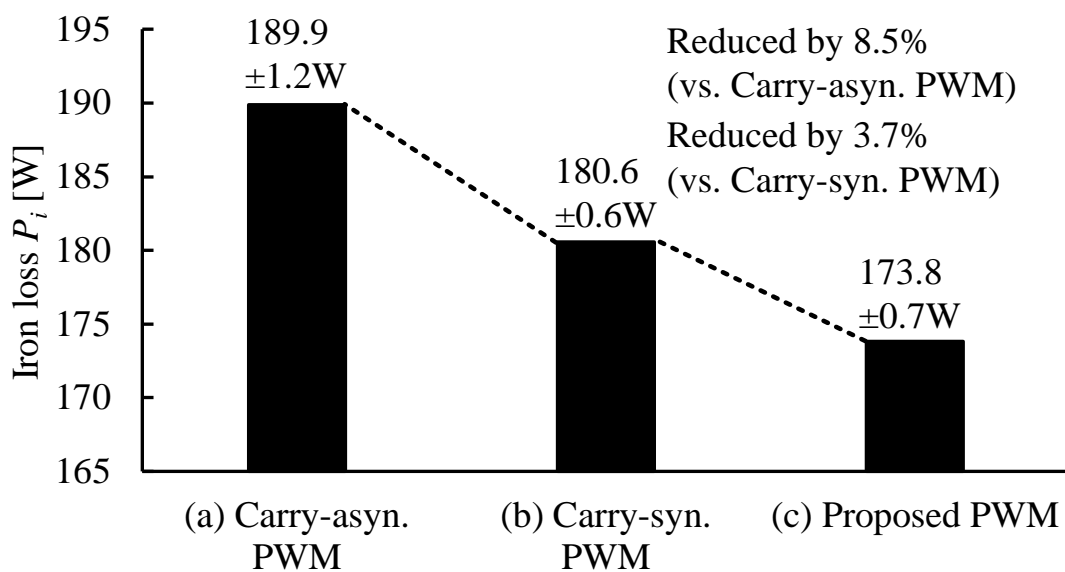


Fig.5.14. Iron loss of test motor.

5.4. Conclusion

In this chapter, a highly efficient pulse pattern using the iron loss evaluation function derived from the BH characteristic was explained. First, the assumption of the pulse pattern was explained in order to optimize the pulse pattern. Next, the procedure to apply the proposed BH characteristic to derivate the iron loss evaluation function under PWM excitation. Then, the optimal pulse pattern was derived based on the proposed iron loss evaluation function. The validity of the derived pulse pattern was verified by the experiments using the inductor and the motor. In addition, the current THD was also evaluated to explain that the proposed method was different from the conventional linear model-based methods.

Bibliography

- [5-1] T. Hiroaki, W. Jiabin, and H. David: “Analysis of Motor Loss in Permanent Magnet Brushless Motors”, JFE Technical report, no. 8, pp. 17-21 (2005) (in Japanese)
- [5-2] N. Yousefpoor, S. H. Fathi, N. Farokhnia, and H. A. Abyaneh: “THD Minimization Applied Directly on the Line-to-Line Voltage of Multilevel Inverters”, IEEE Transactions on Industrial Electronics, vol.59, no. 1, pp. 373-380 (2012)
- [5-3] J. Li, T. Abdallah, and C. R. Sullivan, “Improved calculation of core loss with nonsinusoidal waveforms,” in Proc. Ind. Appl. Conf., 36th IEEE IAS Annu. Meeting, vol. 4, pp. 2203–2210 (2001)

Chapter 6

Conclusion

6.1 Discussion

In order to improve the motor efficiency with limited resources (i.e., materials) by considering the magnetic saturation and iron loss in the materials, the BH trajectory behavior model has been proposed. The BH trajectory behavior model estimated and calculated the magnetic saturation and iron loss generated in the core material from the BH trajectory that the core material followed when excited from the outside. The application of the BH trajectory behavior model varied depending on the purpose of application (simplicity or accuracy). However, all methods of applying the BH trajectory behavior model considered the material properties more accurately than the conventional methods.

Chapter 2 described the efficiency improvement in synchronous motors with concentrated stator windings based on BH trajectory behavior model. This chapter began with a basic explanation of torque and loss, which affect the efficiency of motors. It also explained the conventional linear model-based efficiency improvement technology based on the explained torque and loss fundamentals. After that, the problems in handling magnetic saturation and iron loss based on the linear model were explained in detail. The

proposed BH trajectory behavior model estimates and calculates the torque under magnetic saturation, where linearity is lost, and the hysteresis loss, where frequency superposition is not valid, by considering the material properties in detail. Finally, a comparison was conducted between the conventional high efficiency technology based on the linear model and the proposed high efficiency technology based on the BH trajectory model to show the position of this paper.

Chapter 3 described an automatic design method for high-efficiency motors with consideration of magnetic saturation using the BH trajectory behavior model. First, the geometrical parameters and input constants for the automatic design of the high-efficiency motor were explained. Next, the procedure to apply the proposed BH trajectory behavior model into the permeance method was explained. Then, the torque and loss are formulated as functions of the shape parameters based on the proposed permeance method. The derived theoretical equations were summarized, and an automatic design method using the rotor diameter as a degree of freedom was proposed and validated. In addition, the effect of magnetic saturation considered by the BH trajectory behavior model was discussed. In order to confirm that the design method considers the material characteristics, design examples using materials with different saturation magnetic flux densities were presented.

Chapter 4 proposed accurate electromagnetic field analysis of iron loss using a BH trajectory behavior model and a design method for high-efficiency motors based on the analysis were explained. In particular, by applying the method into a blanked amorphous material, the problem of degradation due to blanking during mass production was quantitatively demonstrated. First, a simple experiment using a ring core was performed to quantitatively show the effect of processing degradation due to blanking. Next, the BH trajectory behavior model was multiplied by the algorithm

implemented in the electromagnetic field analysis software to realize highly accurate iron loss analysis. Using the accurate iron loss analysis, a high-efficiency motor utilizing blanked amorphous material was designed and prototyped. The efficiency and loss of the prototype motor were evaluated, and the superiority of the designed motor was explained. Finally, the accuracy of the iron loss analysis was verified to validate the proposed method.

Chapter 5 proposed a highly efficient pulse pattern using the iron loss evaluation function derived from the BH behavior model. First, the assumption of the pulse pattern was explained in order to optimize the pulse pattern. Next, the procedure to apply the proposed BH trajectory behavior model into the derivation of the iron loss evaluation function under PWM was explained. Then, the optimal pulse pattern was derived based on the proposed iron loss evaluation function. The validity of the derived pulse pattern was explained by experiments using an inductor and a motor. In addition, the current THD was also evaluated to explain that the proposed method was different from the conventional linear model-based method.

6.2 Future Works

In the automatic design method, magnetic saturation was considered based on the BH trajectory behavior model. However, in the design phase, iron loss is neglected. Due to the high magnetic flux density reached, iron loss is expected to be large. Therefore, an automatic design method that takes iron loss into account will be considered in the future.

In the FEM analysis of iron loss, the physical properties of the punched amorphous material were quantitatively evaluated. However, it is unclear which elements of the punching affected the physical properties of the amorphous material. In the future, when punching of amorphous materials will be put to practical use, it is important to know which processes affect the physical properties and to what extent. Therefore, the influence of the process will be studied in the future.

In the optimal pulse pattern, we derived a pulse pattern that reduces iron loss. However, depending on the operating point, it is necessary to consider the balance with copper loss. Therefore, the optimum pulse pattern that achieves the highest efficiency will be studied in the future.

List of Achievements

Publication Papers related to the Dissertation

Publication Journals

- [1] Takahiro Kumagai, Takeshi Ito, Kodai Nishikawa, Jun-ichi Itoh, Kazuki Yamane, Nobuaki Yamada, Masamichi Nawa: "Reduction of Iron Loss in Stator Core using an Optimum Pulse Pattern for High-Speed IPMSM", in *IEEJ Journal of Industry Applications*, Vol. 141, No. 4, pp. 313-323, 2021
- [2] Takahiro Kumagai, Jun-ichi Itoh, Keisuke Kusaka, Daisuke Sato: "Automatic Design Method of Typical Parameters of a Switched Reluctance Motor Focusing on Magnetic Saturation", in *IEEJ Journal of Industry Applications*, Vol. 141, No. 12, pp. 962-975, 2021
- [3] Takahiro Kumagai, Hirotaka Sakurai, Taisuke Shioi, Hirotaka Kato, Jun-ichi Itoh, Keisuke Kusaka, Takashi Yamaguchi, Masayuki Nakagawa, Daisuke Sato: "Experimental Evaluation of Switched Reluctance Motor Made by Blanking Amorphous Alloy Foil", in *IEEJ Journal of Industry Applications*, Vol. 11, No. 1, pp. 117-127, 2022

International Conference Proceedings (Peer-reviewed)

- [1] T. Kumagai, J. Itoh, K. Kusaka, D. Sato: ""Miniaturization Design for SRM Satisfying the Requirements of N-T characteristic Focusing Magnetic Saturation"", The 23rd International Conference on Electrical Machines and Systems, No. LS2D-3, pp. 269-274 (2020)
- [2] T. Kumagai, H. Sakurai, J. Itoh, K. Kusaka, T. Yamaguchi, M. Nakagawa, D. Sato: "Experimental Evaluation of Characteristic of Switched Reluctance Motor Made by Blanking Amorphous Alloy Foil", The 23rd International Conference on Electrical Machines and Systems, No. LS2D-1, pp. 258-262 (2020)

Bibliography

Publication Journal

- [1] T. shioi, T.Kumagai, K. Kusaka, J. Itoh: "Low vibration stopping method for the compressor driving motor", IEEJ Transactions on Industry Applications, Vol. 142, No. 3, pp. 198-205 (2021)

International Conference Proceedings (Peer-reviewed)

- [1] T. Kumagai, D. Sato, J. Itoh: "Torque Ripple Reduction Method for SRM based on Mathematical Model considering Voltage Limitation", EPE2017, Vol. DS1g, No. 0392 (2017)
- [2] T. Kumagai, K. Kusaka, J. Itoh: "Torque Ripple Reduction Method with Minimized Current RMS Value for SRM Based on Mathematical Model of Magnetization Characteristic", 20th European Conference on Power Electronics and Applications, Vol. LS2d, No. 368 (2018)
- [3] T. Kumagai, K. Kusaka, J. Itoh: "Reduction Method of Current RMS Value, DC Current Ripple, and Radial Force Ripple for SRM based on Mathematical Model of Magnetization Characteristic", IEEE INTERNATIONAL FUTURE ENERGY ELECTRONICS CONFERENCE IFEEEC2019, No. 1123 (2019) **【Best Paper Award】**
- [4] T. Kumagai, J. Itoh, K. Kusaka: "Reduction Method of Torque Ripple, DC Current Ripple, and Radial Force Ripple with Control Flexibility of Five-Phase SRM", Energy Conversion Congress and Exposition

2020 (2020)

- [5] T. Yasuda, T. Kumagai, M. Miyashita, K. Kusaka, J. Itoh: "Input Current Balancing Control Method under Imbalanced Load for Three-phase Multi-port Converter based on Modular Multilevel Converter", IPEMC2020-ECCE Asia (2020)
- [6] T. Shioi, T. Kumagai, K. Kusaka, J. Itoh: "Reduction Method of Stopping Vibration for Compressor in Home Appliances", ECCEurope, No. 221 (2021)
- [7] K. Tokui, T. Kumagai, J. Itoh: "Torque Ripple Suppression Method based on FOC for SRM without FEM Analysis", ECCEurope (2021)

National Conference Proceedings

- [1] T. Kumagai, D. Sato, J. Itoh: "Torque Ripple Reduction Method for SRM based on Mathematical Model considering Voltage Limitation", JHES2016, No. A3-20 (2016)
- [2] T. Ito, K. Nishizawa, T. Kumagai, J. Itoh: "Simulation model of concentrated winding IPMSM with non-sinusoidal inductance distribution", JHES2017, No. A3-19 (2017)
- [3] T. Kumagai, J. Itoh: "Simultaneous Reduction Method of Torque Ripple and Current Value for SRM based on Mathematical model of Magnetization Characteristics", NGT2017, No. NGT-17-208 (2017)
- [4] R. Ishibashi, T. Kumagai, N. Takaoka, H. N. Le, K. Kusaka, J. Itoh: "Control Method of Flying Capacitor Operating in Discontinuous Current Mode", SPC, No. SPC-18-048, MD-18-048 (2018)
- [5] T. Kumagai, J. Itoh: "Torque Ripple Reduction Method with Minimized Current RMS Value for SRM Based on Mathematical Model of Magnetization Characteristic", IEEJ Annual meeting (2018) **【IEEJ Excellent Paper Presentation Award】**

- [6] T. Kumagai, J. Itoh: "Reduction method of current RMS value and DC current ripple under zero torque ripple based on mathematical model of magnetization characteristics for SRM", JIASC2018, No. 3-14, pp. III-134 (2018)
- [7] M. Naito, T. Kumagai, H. Watanabe, J. Itoh: "Examining Reduction Method of Speed Ripple Based on V/f Drive", JHES2018, pp. A-23 (2018)
- [8] M. Naito, T. Kumagai, J. Itoh: "A method for reducing the periodic velocity ripple of PMSM driven by 120 degree energization", NGT2018 (2018)
- [9] T. Kumagai, J. Itoh, K. Kusaka: "Radial Force Ripple Formulation and Reduction Method for SRM Based on Mathematical Model of Magnetization Characteristic", SPC, No. SPC-19-052, MD-19-052 (2019)
- [10] M. Naito, T. Kumagai, H. Watanabe, J. Itoh: "Reduction of Speed Ripple Based on V/f control for SPMSM with Periodic Load Fluctuation", SPC/MD, No. SPC-19-030, MD-19-030 (2019)
- [11] T. Kumagai, J. Itoh, K. Kusaka: "Reduction Method of Current RMS value, DC Current Ripple, and Radial force ripple under zero torque ripple for SRM based on Mathematical Model of Magnetization Characteristics", IEEJ Annual meeting, (2019)
- [12] T. Kumagai, K. Kusaka, J. Itoh: "Reduction Method of Torque ripple and Current RMS value for SRM based on Mathematical Model of Magnetization Characteristics", JIASC2019, No. 3-2, pp. III-137 III-140 (2019)
- [13] K. Kiri, T. Kumagai, K. Kusaka, J. Itoh: "Temperature measurement inside PM motor applying wireless sensing", JIASC2019, No. Y-112, pp. Y-112 (2019)
- [14] K. Nishikawa, T. Kumagai, J. Itoh, K. Yamane, N. Yamada, M. Nawa: "A Study on Evaluation Function to Minimize Harmonic Iron Losses for Motor", JIASC2019, No. Y-40, pp. Y-40 (2019)

- [15] T. Ito, T. Kumagai, K. Nishikawa, J. Itoh, K. Yamane, N. Yamada, M. Nawa: "Experimental verification of PWM pattern evaluation function to minimize harmonic iron losses for high speed IPMSM", SPC/MD, No. SPC-19-129, MD-19-095, pp. 25-30 (2019)
- [16] K. Tokui, T. Kumagai, J. Itoh: "Consideration on trade-off between current effective value and torque ripple reduction of concentrated winding IPMSM", JHES2019, pp. A3-6 (2019)
- [17] M. Naito, T. Kumagai, H. Watanabe, J. Itoh: "Experimental Verification of Reduction of Speed Ripple Based on V/f control for PMSM with Periodic Load Fluctuation", SPC/MD, No. SPC-19-130, MD-19-096 (2019)
- [18] T. Yasuda, T. Kumagai, M. Miyashita, K. Kusaka, J. Itoh: "Power Distribution Method in Arm for Multi-port Converter with Cascaded Chopper Cell", NGT2019, No. NGT-19-053 (2019)
- [19] M. Naito, T. Kumagai, H. Watanabe, J. Itoh: "Sensorless Control of PMSM with Estimated System to Reduce Estimated Error Focusing Periodic Load Fluctuation", SPC/HCA/VT, No. SPC-19-186, HCA-19-065, VT-19-039 (2019)
- [20] K. Tokui, T. Kumagai, J. Itoh, K. Yamane, N. Yamada, M. Nawa: "Experimental verification of harmonic iron loss and harmonic copper loss caused by optimum PWM for high speed IPMSM", SPC/MD, No. SPC-20-027, MD-20-027, pp. 73-78 (2020)
- [21] K. Tokui, T. Kumagai, J. Itoh, K. Yamane, N. Yamada, M. Nawa: "Verification of pulse pattern to minimize harmonic iron loss and harmonic copper loss for high speed IPMSM", IEEJ Annual meeting (2020)
- [22] M. Naito, T. Kumagai, J. Itoh: "Sensorless vector control with position estimation error compensation using periodicity for PMSM", IEEJ Annual meeting (2020)
- [23] T. Kumagai, J. Itoh, K. Kusaka: "Reduction method of Torque ripple, DC current ripple, and Radial force ripple with five-phase SRM",

- IEEJ Annual meeting, No. 5-075, pp. 120-121 (2020)
- [24] T. Kumagai, J. Itoh, K. Kusaka, Daisuke Sato: "Optimum Design Method for Switched Reluctance Motor Satisfying the Requirements of N-T characteristic Considering Magnetic Saturation", SA/RM, No. SA-20-016, RM-20-016, pp. 1-6 (2020)
- [25] H.Sakurai, T. Kumagai, J.Itoh, T.Yamaguchi, M.Nakagawa, D.Sato: "Experimental Evaluation of Characteristic of Switched Reluctance Motor Made by Blanking Amorphous Alloy Foil", JHES2020 (2020)
- [26] K. Kawai, T. Kumagai, H. Watanabe, J.Itoh: "Reduction method of start-up acoustic noise for permanent magnet synchronous motor (PMSM)", IEEJ/IAS (D) Online Technical Meetings 2020 (DOTeM 2020), Vol. , No. SPC-20-159 HCA-20-052 VT-20-048 (2020)
- [27] T. Shioi, T. Kumagai, J. Itoh: "Fundamental investigation of the cause of vibration at stop for compressor motor", NGT2020, No. NGT-20-018 (2020)
- [28] K. Tokui, T. Kumagai, H. Watanabe, J. Itoh: "Average torque control for SRM with magnetic saturation", NGT2020, No. NGT-20-018 (2020)
- [29] T. Shioi, T. Kumagai, J.Itoh: "Reduction Method of Vibration at Motor Stop for Compressor", SPC/HCA/VT, No. SPC20-0228, HCA-20-078, VT-20-083 (2020)
- [30] K. Tokui, T. Kumagai, J. Itoh: "Torque Ripple Suppression Method for SRM with Harmonic Current based on Mathematical Model", SPC/HCA/VT, No. SPC20-239, HCA-20-089, VT-20-094 (2020)
- [31] K. Kawai, T. Kumagai, H. Watanabe, T. Shioi, J. Itoh: "A current-source control method for reduction start-up acoustic noise of permanent magnet synchronous motor (PMSM)", SPC, No. SPC-21-02 (2021)
- [32] K. Kawai, T. Kumagai, T. Shioi, J. Itoh: "Stability analysis and design method of $i_d=0$ control of V/f control for permanent magnet synchronous motor (PMSM)", MD/HCA, No. MD-21-068HCA-21-

008 (2021)

- [33] T. Kumagai, J. Itoh, K. Kusaka, M. Kato: "V/f control for Switched Reluctance Motor", IEEJ 2021, No. 5-105, pp. 179-180 (2021)
- [34] T. Shioi, T. Kumagai, K. Kusaka, J. Itoh: "Estimation Method of Load Torque Characteristics and Mechanical Parameter for Reciprocating Compressor Considering Pressure variation", 2021 IEE-Japan Industry Applications Society Conference, No. 4-4, pp. IV-95 (2021)
- [35] H.Kato, T. Kumagai, K.Kusaka, J.Itoh: "Improvement of Iron Loss Evaluation Equation for Amorphous Alloys", 2021 IEE-Japan Industry Applications Society Conference (2021)
- [36] K.Tokui, T. Kumagai, K.Kusaka, J.Itoh: "Torque Ripple Suppression Method for SRM based on Torque / Current Ratio in Magnetic Saturation and Linear Region", 2021 IEE-Japan Industry Applications Society Conference (2021)
- [37] T. Kumagai, K.Kusaka, J.Itoh, M. Kato: "High Performance V/f control Method for Switched Reluctance Motor", 2021 IEE-Japan Industry Applications Society Conference, Vol. 3, No. 37, pp. III 271-III276 (2021) **【Excellent Paper Presentation Award A (IEEJ Industry Applications Society Conference)】**
- [38] H.Sakurai, T. Kumagai, J.Itoh, K. Kusaka, T.Yamaguchi, M.Nakagawa, D.Sato: "Experimental Evaluation of Switched Reluctance Motor Made by Blanking Amorphous Alloy Foil", 2021 IEE-Japan Industry Applications Society Conference (2021)
- [39] G.Tanaka, T.Yasuda, T.Kumagai, K. Kusaka, J. Itoh: "Comparison of Loss of Space Vector Method Schemes for Six-Phase Motors", Joint Conference of Hokuriku Chapters of Electrical and Information Societies 2021 (2021)
- [40] H.Kato, K.Tokui, T. Kumagai, K. kusaka, J. Itoh: "A Method of Reducing DC Current Ripple by Allowing Torque Ripple for SRM", Joint Conference of Hokuriku Chapters of Electrical and Information Societies 2021 (2021)

- [41] K.Tokui, T. Kumagai, J.Itoh: "Applicable Speed Expansion of Torque Ripple Suppression Method for SRM with Harmonic Current", IEEJ Annual meeting (2022)
- [42] T.Shioi, T. Kumagai, J.Itoh: "Low-vibration Stopping Method for Compressor using DC Side Current Detection", IEEJ Annual meeting (2022)